Optical anisotropy and vibrational properties of Sn, In, and Cs nanowires

vorgelegt von
Diplom-Physiker

Karsten Fleischer

Berlin

Fakultät II – Mathematik und Naturwissenschaften

der Technischen Universität Berlin

zur Erlangung des akademischen Grades
Doktor der Naturwissenschaften
Dr. rer. nat.

genehmigte Dissertation

Promotionsausschuss:

Vorsitzender:	Prof. Dr. E. Sedlmayr
Berichter/Gutachter:	Prof. Dr. W. Richter
Berichter/Gutachter:	Prof. Dr. C. Thomsen
Berichter/Gutachter:	Priv. Doz. Dr. N. Esser

Tag der wissenschaftlichen Aussprache: 29. Juni 2005

Berlin 2005

D 83

Parts of this work have been already published

K. Fleischer, S. Chandola, N. Esser, W. Richter, and J. F. McGilp,
Reflectance anisotropy spectroscopy of Si(111)-(4×1)-In,
phys. status solidi (a) **188**, 1411 (2001).

K. Fleischer, S. Chandola, N. Esser, W. Richter, and J. F. McGilp,
Phonon and polarized reflectance spectra from Si(111)-(4×1)In: Evidence for a charge-density-wave driven phase transition,
Phys. Rev. B **67**, 235318 (2003).

K. Fleischer, G. Bussetti, C. Goletti, W. Richter, and P. Chiaradia,
Optical anisotropy of Cs nanostructures on III-V(110) surfaces,
J. Phys.-Condes. Matter **16**, S4353 (2004).

K. Fleischer, S. Chandola, N. Esser, W. Richter, J. F. McGilp, W. G. Schmidt, S. Wang, W. Lu, and J. Bernholc,
Atomic indium nanowires on Si(111): the (4×1)-(8×2) phase transition studied with reflectance anisotropy spectroscopy,
Appl. Surf. Sci. **234**, 302 (2004).

X. Lopez-Lozano, O. Pulci, C. Noguez, K. Fleischer, and W. Richter,
Electronic structure and reflectance anisotropy spectrum of InAs(110),
Phys. Rev. B **71**, 125337 (2005).

Contents

1. Introduction

In the last few decades the size of electronic devices, particularly integrated circuits, has decreased rapidly. It is already foreseeable that in the decades to come the lateral size of such structures will reach the scale of a few nanometers. Nowadays gate lengths of transistors in integrated circuits can be as small as 65 nm, the thickness of oxide layers in certain transistor types is already around 2 nm. The smaller the structures get, the more often new problems occur due to the different physics in low dimensions. To get reliable working devices new materials had to be introduced, such as high *k* dielectrics. Apart from the problems within the semiconductor devices itself there are also new problems arising from contacts to these structures. The size of integrated circuits is already to some extend limited by the size of the metallic contacts. Manufactures have undergone changes in the production process to use metals with higher conductance such as copper instead of gold or aluminium in order to shrink the sizes of on-chip interconnects down to 100 nm [1]. The question arises where the size limit of such wires will be without losing their metallic properties. As will be discussed in section 2.3 a truly one-dimensional conductor with one metallic band is unstable and will become semiconducting [2]. On the other hand there are already chain systems only 4 atoms wide reported, which show one-dimensional conductance [3, 4]. It is obvious that investigations about the conductance of such small metallic wires are essential for future applications. In chapter 2 I will give a short review about known 1D conductors, examples how they can be prepared and an introduction how to describe the electronic properties of low dimensional metallic structures as well as possible non-metallic phases which occur for 1D structures.

Not only the electronic properties of nanowires but also their optical properties are of importance. Conductance measurements on wires of atomic sizes, though possible, are very complicated and not easy to use within production processes. Optical techniques are already in use as monitoring probes for production purposes. I will therefore focus on optical measurements of metallic nanowires and in what sense the spectra can be correlated to electronic properties of these wires. In principle optical techniques can also probe buried structures – an important aspect since protective caps are needed to include nanowires in structures stable at ambient conditions. The investigation of the optical properties of on-surface structures as performed in this work is the first step in this direction.

In this work I will present mainly measurements of anisotropies in the free electron absorption but also interband transitions by reflectance anisotropy spectroscopy (RAS). Additionally the vibrational modes of the system were investigated by Raman spectroscopy (RS). Both techniques can be used *in-situ* during the formation of nanowires and are therefore suitable to monitor wire properties during production. The techniques will be introduced in chapter 3.

There are numerous systems with quasi one-dimensional properties. Necessar-

ily this work can only discuss a few. Only wires prepared by self-organisation on semiconductor surfaces, consisting of only one type of atoms. Indium, tin, lead and caesium are the metals of choice – all bulk metals. Since substrate, growth temperature, flux and deposition time are varied, the morphology of the wires investigated here still cover a wide range of possible geometries. The wire formation itself will be discussed in detail for the individual systems. The investigated structures range from comparably large systems such as the tin wires on InAs(110) (≈ 20 nm wide, chapter 4) to indium wires on Si(111) (≈ 1 nm wide, chapter 5) to already semiconducting Cs chains on GaAs(110) ($\approx 1-2$ nm wide, chapter 6).

In this work it will be shown in what way optical spectroscopy provides direct information on the conductance anisotropy of such structures. But also in the cases where the conductance anisotropy is small or the nanowires are already semiconducting it will be shown that with optical techniques the formation of the wires can be monitored. Similarly optical techniques can give insights to the metal insulator transition occurring for the indium wires on silicon for low temperatures.

2. Low dimensional metal structures

The subject of this work will be the optical properties of metallic nanowires. Consequently structures which are usually called nanowires must be introduced. The obvious definition that it is a wire with a width in the region of nanometres needs to be specified. Only few examples of free standing cylindrical wires exist with widths in the nanometre region. The term nanowire is applied to many more systems as long as the dimension in two directions is in the low nanometre regime and the length considerably larger. Depending on their preparation such structures are found on surfaces, in liquid solution or embedded in solids. In the first section I will therefore briefly review the methods of preparation commonly used.

As the focus of this work is on metallic nanowires, it is therefore important to understand in what way the classical description of a metal, particularly the description of the conducting properties in terms of a free electron gas, needs to be modified if the width of a conductor is drastically reduced. The second part of this introductional chapter will therefore be dedicated to the description of electrons in 1D structures.

2.1 Preparation of nanowires

The width of structures which are called nanowires ranges from about 100 nm to a few Ångström. Apart from these variations in diameter, changes in length and lateral arrangement are even greater, depending on the preparation method. Some commonly used techniques will be reviewed here.

Lithography

Lithography is the method of choice for today's production of integrated circuits (IC), where the lateral arrangement of the material is the most crucial point. Today's conventional lithographic methods use UV light from excimer lasers. The structure size is limited by the wavelength of the laser light (currently $\lambda = 193\,\text{nm}$ or 157 nm). The width which is realised in today's commercially available ICs is about 65 nm - already below the diffraction limit of $\lambda/2$. This can only be achieved by an enormous precision in the manufacturing steps and huge effort in the mask designs.

Other lithographic methods such as electron beam lithography, or the direct scratching of the photo resist using an atomic force or scanning tunnelling microscope can produce much smaller structures, but not in large quantities or on large areas as required for current device production [5].

The most promising approach to reduce the structures with conventional lithographic techniques is the EUV-lithography (extreme ultraviolet, 13 nm), currently developed in joint ventures of the industry but also research institutes worldwide.

It is planned to be introduced in mass production in 2009, though there are still numerous problems involving the plasma lamps, and the need to introduce ultra high vacuum conditions to the production process (details can be found in [6]).

Electrochemical deposition

Metallic nanoparticles themselves are even commercially produced by electrochemical methods. Metallic nanowires can also be produced in such way. One technique is electrochemical deposition of metals in structured membranes which are then dissolved in later production steps [7–10]. The width of wires produced in such a way is determined by the pores of the membrane and the length by its thickness. It was shown that gold or silver particles can be produced which are only 20 nm wide but 5 μm long [11].

There are numerous other methods such as the electrodeposition on cathodes with electrolytes doped with trace elements such as Sn or Pb [12]. Other methods are described in [10, 13]. For most of the electrochemical processes the nanowires are prepared in a liquid and are randomly oriented. Hence single wires or wire arrays need to be set up by a manual rearrangement, which so far is not easily possible.

Self-organised growth on structured or stepped surfaces

One elegant way for the preparation of isolated but oriented metallic nanowires is the deposition of the metal on stepped surfaces. Depending on the type of adsorbate and substrate, adsorption on step edges can be the favoured mechanism [14]. It is therefore possible to form single atomic chains on step edges. For vicinal surfaces this was demonstrated on a variety of adsorbate/substrate combinations such as Ag/Pt(997) [15], Ga/Si(112) [16], Au on Si(335),Si(557),Si(5 5 12) [17, 18], or Ag/Si(5 5 12) [19] surfaces. In all these cases the adsorption takes place on single atomic steps. The step separation can be varied only by changing the offcut angle. On Si(111) it was shown that very regular single atomic step arrays can be prepared as templates for such adsorption experiments [20, 21]. By utilising step bunching, higher and more separated steps can also be prepared. In this case the step height and terrace width not only depend on the offcut angle but also on the conditions upon preparation [14, 20, 22–24].

The formation of nanowires on surface steps may provide the best way to combine current processing techniques based on lithography, which is used to create the template structure. The wire formation by the adsorption of the metal is then the second step.

Metal atom surface reconstructions

Single (or multiple) atom wide chains can be prepared not only by step decoration, but also on clean flat surfaces. Many adsorbate terminated surfaces have reconstructions consisting of single atomic rows, dimer rows, or even larger structures [4]. Some of these anisotropic surface reconstructions are known to show quasi 1D metallic properties such as the Si(111)-In:(4×1) [3], Si(111)-Au:(5×2) [25, 26] or InAs(110)-Bi:(1×2) [27] surface. Other chains of metal adsorbates also show one-dimensional surface states but are found to be semiconducting. Examples are caesium or sodium rows

on III-V(110) surfaces (see chapter 6), GaAs-Sb:(1×1) [28], Si(111)-(K,Li,Na,Ag):(3×1) [4, 29, 30].

These surfaces are ideal test cases for the investigation of electronic properties of extremely narrow (2-5 atoms wide) metallic wires. The whole surface is covered by identical wires and a wider range of experimental techniques can be used, since no high spatial resolution is required as in the case of individual wires. This holds particularly true for optical surface science techniques which can be used to investigate electronic but also vibrational properties of nanowires (see chapter 3). Furthermore such surfaces can be calculated by *ab-initio* techniques which makes direct comparison of calculations to measured properties possible (see 3.5).

For these reasons one of the best investigated surfaces the Si(111)-In:(4×1) reconstruction, was chosen as the main test system for the investigations of the optical properties of metallic nanowires (see chapter 5). Measurements on this surface are the major aspect of this work.

Anisotropic island growth

Adsorption of a larger quantity of metal atoms on surfaces can lead to the formation of islands. The shape of the islands formed not only depend on the adsorbate and substrate material itself but also on the surface orientation and reconstruction before adsorption. In some cases it is possible to grow larger anisotropic islands. Examples are the formation of tin islands on InAs(110) or lead islands on Si(335) [31] as will be discussed in chapter 4. In these systems the island size (and also shape) is determined by the amount of metal deposited. The width, height and length of the island and also the ratio of width/length changes when more material is deposited.

The orientation of nanowires prepared in this way is predetermined by the substrate orientation and therefore does not vary, even on larger samples, though in comparison to the step adsorption or reconstructed surfaces the individual nanowires do vary in shape and size. Nevertheless the whole surface is covered in similar islands, which makes these structures ideal test cases for studies of the properties of the metal nanowire with respect to its shape.

Other methods

The methods described so far are the ones most commonly used for the preparation of metal nanowires. Semiconductor nanowires can be prepared with comparable methods, while for another type of nanowires – carbon nanotubes – other methods such as arc discharge deposition or chemical vapour phase epitaxy are used [32]. In particular, carbon nanotubes can show one-dimensional metallic properties as well. Nevertheless for the investigations of the metallic properties of nanowires I will limit myself to structures composed of purely metal atoms only, focusing on anisotropic metal islands and reconstructions involving metal adsorbates.

The choice of preparation methods presented here is naturally selective. For a broader view I refer to some review articles [33, 34].

2.2 Description of a Fermi liquid

The description of the conductance of metals dates back to the work of Paul Drude [35] in 1900. The model assumes that all valence electrons of a material act as conduction electrons and the positive ion core is screened by the core electrons leaving the valence electrons unaffected. Hence the name free electron model. One inherent problem of the description was that on the one hand the conduction electrons were assumed to be free but a phenomenological scattering rate $1/\tau$ is needed to explain the finite resistance of metals. Also the occurrence of insulating materials is impossible to explain in this model.

As the nature of electrons was better understood, particularly since electrons were found to be spin-half particles and therefore follow the Fermi-Dirac distribution function, the shortcomings of the model could be overcome by Sommerfeld [36], Bloch [37] Wilson [38]. In particular the electron-ion interaction was treated properly and for instance the scattering rates $1/\tau$ could be calculated. For a complete review of the possibilities of this model I would like to refer to common textbooks [39–41]. One important result for my work is that the original formulation of the free electron absorption in the Drude model is still valid. Only the electron mass m_e must be replaced with an effective mass m^* taking the periodicity of atom cores (ion-electron interaction) into account. Also the effective scattering rate $1/\tau$ has a defined physical meaning though different scattering mechanisms such as impurity scattering or phonon scattering contribute. In this work the optical response of these electrons will often be termed free electron response, since the formulas used are similar. This is somewhat misleading and a more appropriate term “the independent electron” response should be used [39]. Nevertheless the infrared absorption of metals is commonly called the Drude free electron absorption or Drude tail and I will therefore continue to use it.

The independent electron formulation still has many problems in describing real measurements, since electron-electron interactions are still neglected. The principle problem is that an N-electron system cannot be treated exactly. Based on Landaus discussion of He^3 [42] one approach to solve such an N-electron system was applied to the more complicated metallic systems. In this form it is nowadays known as Fermi liquid theory. Its principle idea is that for electrons at the Fermi edge the one electron wavefunctions of the independent electron picture ψ_i are good first approximations for weakly interacting electrons. By an “adiabatic increase” of the interaction there is a one-to-one correspondence of the one-electron wavefunction ψ_i and the N-electron wavefunction ψ_{N_i} having the same quantum numbers. The latter can be calculated with perturbation theories from the independent electron picture. The N-electron wavefunction ψ_{N_i} does not represent a single electron, though still has a particle like nature and is therefore termed quasi-particle. The Fermi liquid picture is nowadays applied when dealing with many electron systems. The simpler pictures are still good approximations as long as one keeps in mind that one does not deal with “free” electrons but N-electron quasi-particles.

2.3 Instability of a 1D Fermi liquid

The Fermi liquid picture can describe the properties of bulk metals very well. For a two dimensional system new phenomena such as the fractional quantum Hall effect can occur. The interaction between electrons is already larger in the 2D case but the mathematical description of a Fermi liquid still works well [4, 43].

If the Fermi liquid picture is applied to a strictly 1D system the mathematical description breaks down. While in 3D and 2D the electron Greens function has one pole at the quasi particle excitation energy, in 1D two solutions evolve which invalidate the single particle assumption of the Fermi picture. No single electrons or alternative fermionic quasiparticles can be described in a strict 1D formalism. The whole mathematical formalism used to describe interacting electrons in 3D and 2D hence does not work in the 1D case [43].

There are many intuitive pictures to visualise this problem. The easiest is the one to assume two electrons at the Fermi surface with wavevector k_F and $-k_F$ "collide". In 2D and 3D k is a vector and scattering leads to small changes in the electrons "direction". In 1D the only possible scattering is the full momentum transfer. Hence interactions between single electrons are expected to be much larger than in the 2D and 3D case.

Another more detailed argument is the one given by R. E. Peierls. For a strictly 1D metal a model of the band structure and the Fermi surface is shown in Fig. 2.1a) Assuming the band is crossing the Fermi level at half of the Brillouin zone it can be seen that any periodic distortion with a periodicity of 2 unit cells will lead to a backfolding of the band at the new zone boundary. This is always accompanied with an energy gain of electrons at the Fermi surface of ΔE_P due to the opening of a gap as depicted in Fig. 2.1b). The figure displays the situation of a band crossing at half the Brillouin zone ($k_F = ½\pi/a$). The argument can be similarly formulated for any k_F, though the distortion then involves more than two unit cells. Peierls and Fröhlich discussed this phenomena in terms of the electron-phonon interaction. The periodic lattice distortion of $2k_F$ leads to the energy gain and a periodic modulation of the charge called a charge density wave (CDW) [2, 44]. This instability of the 1D metallic band against CDWs accompanied with periodic lattice distortions (or vice versa) is now known as Peierls instability.

For the description of electrons in 1D any many-body interaction which causes a $2k_F$ distortion would lead to a more stable configuration than the metallic band. Repulsive electron-electron interaction would lead to similar problems and CDWs (see Mott transition later in this chapter). Also a periodic modulation of the spins – a spin density wave (SDW) – would lead to an energetically favoured configuration and an opening of a pseudogap at k_F. In addition the for the 3D case well-known BCS-singularity (Bardeen, Cooper and Schrieffer [45]) can also occur in 1D and hence Cooper pair formation and superconductivity [43]. Calculations are therefore additionally complicated since the formation of a static CDW leading to an insulating ground state and Cooper pairs leading to superconductivity are competing processes. Usual mean field theories can only describe one of them. All these problems stimulated the development of a more consistent picture for 1D fermions – the Luttinger liquid which will be described later.

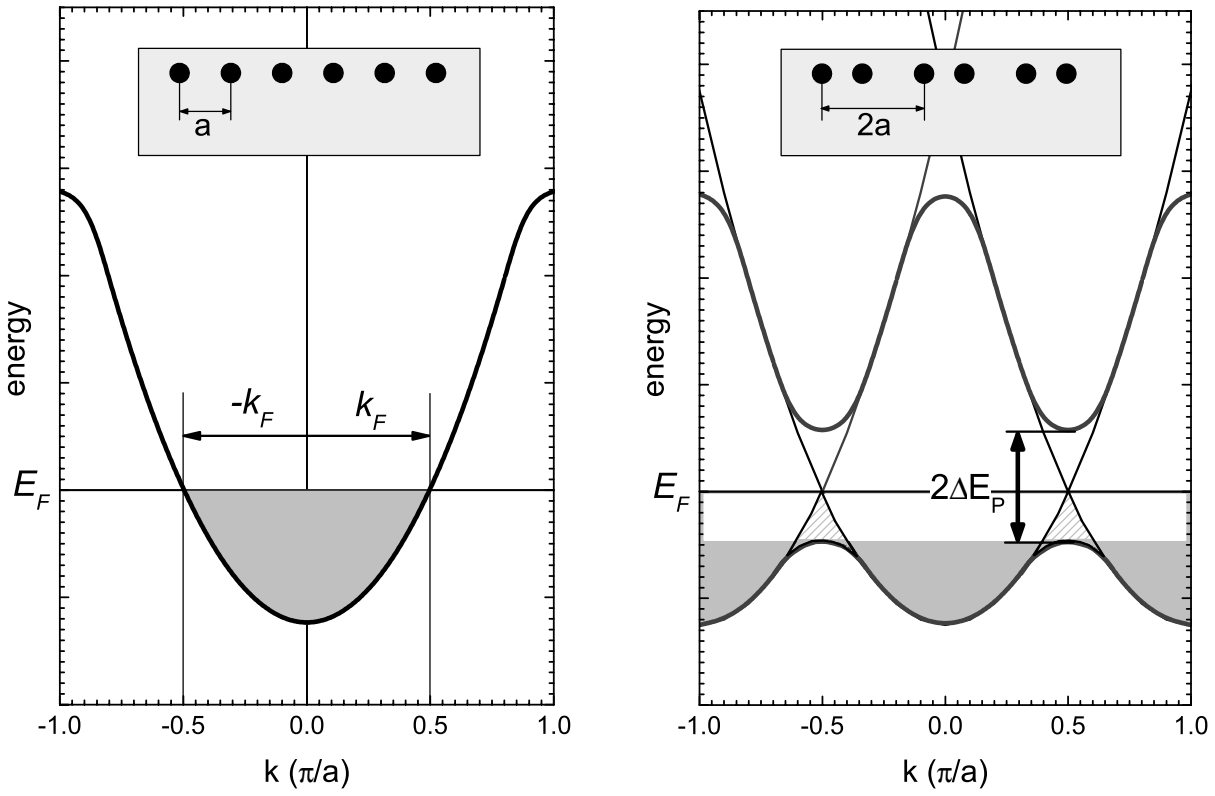

Figure 2.1: *Graphical explanation of the energy gain at the Peierls transition. A system with a parabolic metallic state with $k_F = ½\pi/a$ can gain energy by a distortion of periodicity 2a. The backfolding of the bands leads to a gap opening at $½\pi/a$ with a Peierls gap (ΔE_P). Since no filled states exist above the new found valence band the system gains energy as depicted by the shaded area. The total energy gain though depends on the density of states in the area around the Fermi vector k_F.*

Quasi one-dimensional metallic systems

The question arises whether this break-down of the Fermi picture in 1D is a real phenomenon or just an artefact of the mathematical technique. Or in other words can real physical structures be approximated by strictly 1D models at all.

In recent years the preparation of very narrow metallic chains can be controlled with growing accuracy and as conducting wires get smaller the question arises whether the conductance will be affected by the formation of CDWs long before the physical size limit of single atomic rows. One of the smallest structures known to be metallic are indium rows on top of a Si(111) surface – the Si(111)-In:(4×1) reconstruction [3]. In Fig. 2.3 the bandstructure and Fermi surface of an ideal 1D structure is compared with the measured band structure and Fermi surface of the Si(111)-In:(4×1) surface. For this particular surface one finds more than one metallic band and some of them do show a dispersion along the wire direction. The situation is close to the one described by the strictly 1D model only for the band labelled m_3. Such systems, where the dispersion of metallic bands along the wire direction is

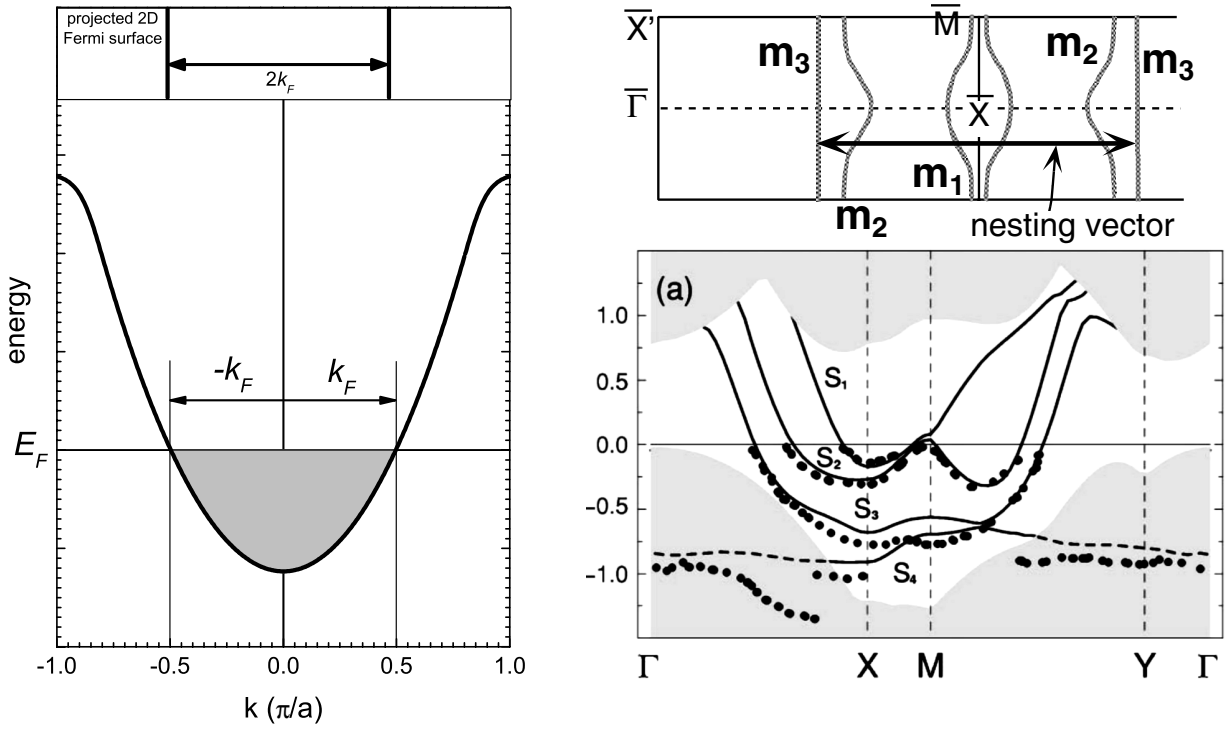

Figure 2.2: *Comparison of the bandstructure and Fermi surface of an ideal 1D metal (left) and the quasi-1D structure of the Si(111)-In:(4×1) surface (right). For the real structure more than one metallic band is found and the sheets of the 2D Fermi surface cannot be nested by a single distortion $2k_F$ due to the small dispersion along the chain direction. The bandstructure calculation was taken from [46], measured filled states and Fermi surface from [47].*

measurable but small or only some of the bands do show 1D properties are called quasi one-dimensional structures.

Are such systems unstable against distortions of $2k_F$ e.g charge or spin density waves as predicted by the Peierls argument? For the system introduced here the answer is quite controversial. The surface does undergo a phase transition below 120 K which does show a characteristic doubling of the unit cell along the chain direction and an opening of electronic gaps which can be attributed to charge density waves. Nevertheless alternative explanations exist [46, 48]. The controversy and how the optical measurements performed here indicate that indeed a CDW is formed will be extensively discussed in chapter 5.

Quasi one-dimensional bulk metallic systems

The preparation of free standing or surface adsorbed nanowires is a recent development. Quasi one-dimensional systems though have been known for a much longer period. Various inorganic materials are known for which large conductance anisotropies are found and metallic bands show only a small dispersion along certain crystallographic directions. The materials where such properties are found include

the so called blue bronze $K_{0.3}MoO_3$ and transition metal chalcogenides such as TaS_3 or $NbSe_3$ and are known since the early 1970s. A extensive review of these materials as well as properties related to the formation and dynamics of the collective mode (the CDW) can be found in the book of Gor'kov and Grüner [49].

Another prominent class of bulk anisotropic conductors are organic metals. The first one investigated, also in the early 1970s was tetrathiafulvalene–tetracyano-p-quinodimethane (TTF-TCQN), though many more are known today. Some of these organic compounds even show superconductivity and many show low temperature properties which are explained with CDW and SDW formation. Again I would like to omit a more detailed description at this point and will instead refer to the book of Wosnitza [50].

In most of these bulk quasi one-dimensional systems the conductivity drops at low temperatures. The transition temperature, changes in diffraction pattern, and transport properties can be described using the random phase approximation (RPA), neglecting any local field effects and also using one set of interactions, electron-phonon interaction (superconductivity, CDW, SDW) or repulsive electron-electron interaction (Mott: CDW) [43, 49, 51, 52]. Although these approaches are criticised by Voit [43] in favour of the Luttinger liquid description, I will use some of these results for comparison with the measurements in the following chapters.

2.4 The Luttinger liquid

So far I have sketched the arguments that the classic Fermi liquid picture of an electron does not work for a 1D system. In the few last years a lot of effort went into formulating a theoretical description of one-dimensional fermionic quasiparticles. The pioneering work in this field is the work of Tomonaga [53] and Luttinger [54, 55]. The theory is rather complex and comparison to the experiments done in this work is not possible due to the lack of explicit calculations for the materials investigated. Therefore only the principle ideas will be sketched here. For a comprehensive review of various aspects of the Luttinger liquid and recent extensions to systems with more than one metallic band or coupling between individual wires, which are necessary in understanding real systems (see the example of Si(111)-In:(4×1) above), I would like to refer to the review article of Voit [43].

2.4.1 General approach

In the Luttinger picture the collective density fluctuations are described in a particle like way by defining a Hamiltonian describing two branches of Fermions c_{rks} with momentum k, spin s and $r = \pm 1$ for the individual branches. The Fermions are not described individually but instead the fluctuations of the density $\rho_{r,s} = \sum_k c^\dagger_{r,k+p,s} c_{rks}$ (spin or charge density) are particle like. In its original form the dispersion of the two Fermion branches is linear $\varepsilon_r(k) = v_F \cdot (rk - k_F)$ and only two interactions with coupling constants g_2 and g_4 for forward scattering on different and the same branch respectively are considered. In this simplified picture (linear dispersion, no backward scattering) the model can be solved exactly [43].

2.4.2 Some results

In its original form the Luttinger model predicts unusual properties such as spin-charge separation. If electrons are removed (e.g. in photo emission experiments) the spin and charge excitation by the formation of a hole will be dispersed differently leaving a spinon (collective spin excitation) and holon (collective positive charge excitation) branch in the band structures. Such effects are discussed for some experiments [18, 56, 57] and calculations [58].

More relevant for the discussion in this work are extensions to the Luttinger picture which include backward scattering of 1D Fermions. By including additional terms the Luttinger Hamiltonian ceases to be exactly solvable, but to describe coupling to phonons or impurity scattering such terms are needed. Since the formalism is quite complicated again, I will omit a discussion here and will only discuss one result of such a description from [43]. In Fig. 2.3 a "phase" diagram is shown, relating the dominating fluctuation to the coupling parameter of the electron-electron interaction for backward scattering $g_{1\perp}$ and a renormalised parameter K_ρ which is a function of g_2, g_4 and v_F. Further details are found in [43]. What can be seen in this model is that charge and spin density waves (CDW, SDW) as well as superconducting phases (SS, TS) are stable solutions of 1D electron systems if treated in the more sophisticated way. This is not possible in the Fermi liquid picture as shown above. Qualitatively superconductivity or CDW formation can be described by the theory. Nevertheless there are problems to determine the coupling parameters in a predictable way.

CDWs are valid solutions already for 1D-systems if electron-electron interaction is considered. Peierls' argument primarily considered electron-phonon interaction and a periodic lattice distortion. If the latter is the main driving force the CDWs are often called "driven by a Peierls instability". For systems where electron-electron interaction dominates, the insulating phase is usually called Mott or Mott-Hubbard state (see below). In both cases the electron density does change periodically and

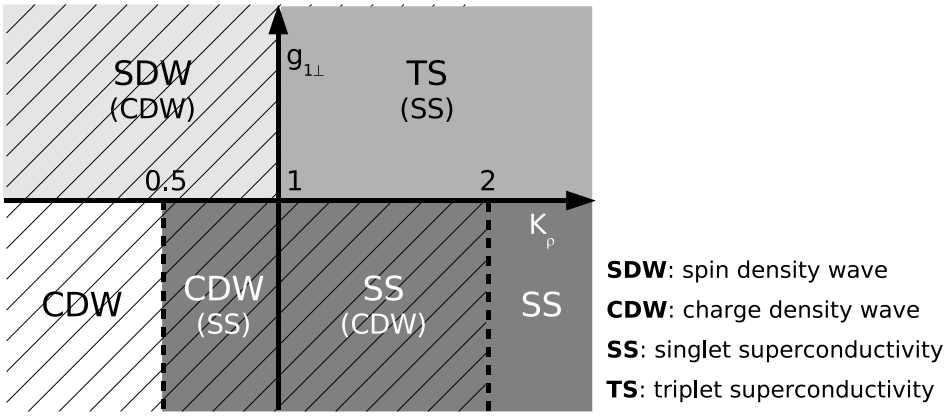

Figure 2.3: *Phase diagram of a 1D electron system derived by evaluation of the Luttinger liquid solution to an additional interaction – here electron-electron backward scattering (taken from [43].)*

the term CDW can be applied. This already shows the problem of the theoretical predictions since both interactions will be present in real systems. Although there is a lot of progress in the calculational methods using the Luttinger liquid theory so far only qualitative descriptions of metallic nanowire systems exist. Experimental results and calculations are compared directly and quantitative only in a few cases [58]. For the quasi one-dimensional bulk materials the situation is different, though most calculations were done in mean field pictures and perturbation theories based on the Fermi liquid picture despite its principle problem in a 1D formalism [43, 49]. In the future much progress is expected in the description of metallic nanowire systems particularly since the preparation can be better controlled and systems are known where, for instance, the chain distance and therefore inter-chain interactions can be varied in a controlled way [59]. Also improvements in experimental techniques, namely the increase in resolution of angle resolved photo electron spectrometers at third generation synchrotron light sources will stimulate detailed calculations of such systems.

2.4.3 The Mott transition

A different mechanism which can transform a metal into a semiconducting state is the so called Mott-Hubbard transition. Formulated by Mott in 1949 it explained why certain bulk metals showed nonconducting liquid phases [52, 60]. It was shown by Mott that assuming half filled metallic bands, the opening of a pseudo gap becomes favourable if the average electron distance d is enlarged above a critical value d_0. In later years the problem was studied also by Hubbard [61, 62] which is why the metal-insulator transitions driven by this mechanism are nowadays known as the Mott-Hubbard transition.

The basic idea is that for a metallic system the positive charge of the core is screened by the presence of all free electrons. If the density of the electrons and therefore also the screening length is reduced below a critical value, it becomes possible for an electron to form a bound state with the core atom. In the case of the alkaline atoms as originally discussed by Mott each core atom provides only one electron and the electron density is hence directly linked to the lattice constant d. An increase in lattice constant above a critical value d_0 which depends on the electron-electron interaction can therefore reduce the electron density below the critical limit.

The Mott argument is independent from the dimensionality and can be formulated in 3D, 2D and 1D. In the original work of Mott half filled bands were discussed, but the principle argument holds true also for other band fillings. Instead of discussing changes in the average electron distance d one can also discuss the screening itself, which depends on the electron-electron interaction parameter U – the repulsion of two electrons at the same site. If U is positive the ground state will be semiconducting showing first spin fluctuations, and for even larger U charge fluctuations. In this formulation the Mott-Hubbard model is just a special case of the more general Luttinger description [43].

The Mott-Hubbard model is commonly used to explain insulating ground states for organic or inorganic systems which should be metallic by electron counting but have small electron densities (see for example [63–65]). For the system discussed

in chapter 6 – caesium wires on III-V(110) surfaces the insulating properties of the surface are explained with the Mott-Hubbard model [4, 66, 67]. Although the consequences of the Mott argument and the Peierls argument in 1D (CDWs, SDWs) are quite similar there is a conceptual difference. The Peierls instability is a 1D phenomenon only, originally formulated for an electron-phonon interaction, while Mott's argument can be applied in 3D and considers electron-electron interaction. In strictly 1D systems both electron-electron and electron-phonon interaction lead to the conceptual problems as pointed out by Peierls and an accurate description needs calculations in the Luttinger picture.

2.5 Other consequences of the size reduction

The effects of size reduction for the metallic properties of nanowires are manifold. The most drastic – a complete suppression of the conductance due to the Peierls instability – was already discussed separately. Apart from that there are many other effects expected.

Electron confinement

Due to the reduced size, confinement effects are expected which change the density of states but also the energy of the bands itself. Therefore the properties will differ greatly from the properties of the bulk metal. For instance optical interband transitions are expected to be shifted. Nevertheless for the systems investigated here there is no need to address these effects. For the adsorbate induced reconstructions the width of the wires is already too small to compare the electronic structure with the bulk material and there is no way to change the width of the nanowire. For larger systems such as the anisotropic islands the spectra are dominated by the free electron response and, for instance, interband transitions were too weak to be analysed in terms of energetic shifts with island diameter. I will therefore omit a more detailed discussion of confinement effects and refer to textbooks instead [40, 41, 68].

Quantisation of conductance

Due to the reduced size the number of electrons in an individual wire is much lower than in bulk materials. Consequently it is expected that the charge quantisation is also seen in conductance experiments. The ultimate limit of the conductance is an one-electron conductor. In experiments where the conductance is measured in wires, which are pulled or etched to get narrower wires, it was observed that the conductance is reduced in steps of $2e^2/h$ [69, 70]. This behaviour is well understood for ballistic transport and calculations also show that, at least for cylindrical wires, not only a quantisation of conductance occurs but also that certain "magic configurations", namely wire radii, are found to be more stable similarly for atomic nuclei or clusters [71].

Since all the measurements were performed with wire arrays on surfaces with either varying widths, or if the wire width is uniform, it is fixed at defined values and is unchangeable, it is not expected that the quantisation of the conductance can be measured here.

3. Optical response of one-dimensional structures

Within this chapter the experimental methods used in the study of the metallic nanowires, namely reflectance anisotropy spectroscopy (RAS) and Raman spectroscopy will be introduced. Before the techniques itself are discussed some general concepts needed for the description of optical spectra such as the dielectric function will be discussed. The description will be limited to models needed for the analysis of RAS and Raman spectra of these wires.

3.1 The dielectric function

The interaction of light with matter is usually discussed within Maxwell's theory with the light described by plane waves. The presence of a time varying electric field $\mathbf{E} = \mathbf{E}_0 e^{i(\mathbf{kr}-\omega t)}$ introduces a polarisation $\mathbf{P} = \varepsilon_0 \underline{\underline{\tilde{\chi}}} \mathbf{E}$ within the medium. The complex electric susceptibility tensor $\underline{\underline{\tilde{\chi}}}$ reflects the properties of the material. Alternatively these properties can also be expressed with the dielectric tensor $\underline{\underline{\tilde{\varepsilon}}}$ which connects the electric field with the electric displacement vector $\mathbf{D} = \varepsilon_0 \underline{\underline{\tilde{\varepsilon}}} \mathbf{E}$. Both quantities $\underline{\underline{\tilde{\chi}}}$ and $\underline{\underline{\tilde{\varepsilon}}}$ are therefore equivalent descriptions and can be calculated from each other: $\underline{\underline{\tilde{\varepsilon}}} = 1 + \underline{\underline{\tilde{\chi}}}$.

In the case of isotropic materials or materials with cubic symmetry the off-diagonal tensor components of $\underline{\underline{\tilde{\varepsilon}}}$ will vanish and the diagonal components $\tilde{\varepsilon}_{xx}$, $\tilde{\varepsilon}_{yy}$ and $\tilde{\varepsilon}_{zz}$ will be equal to the same scalar function $\tilde{\varepsilon}$, which is called the dielectric function of the material. In general $\tilde{\varepsilon}$ will be energy dependent. All optical properties of a material such as the refractive index n, the extinction coefficient κ, the penetration depth of light l_P, the reflectance R of a semi-infinite medium, or the complex reflectivity r can be calculated from the dielectric function. Similarly the dielectric function can be determined by measuring a set of optical properties such as the reflectivities r_s and r_p for p- and s-polarised light by ellipsometry [72, 73]. Since the measurement of an ideal semi-infinite medium is virtually impossible, because of the natural roughness of the material and inhomogeneities in real samples the dielectric function derived from such measurements is usually called the effective dielectric function $<\tilde{\varepsilon}>$. By minimising the surface roughness and improving the crystal quality of bulk crystals the measured effective dielectric function is a good approximation of the true bulk property. Nowadays the dielectric functions for common materials are known and tabulated [74, 75].

If the bulk dielectric function of individual materials is known, the effective dielectric function of layered or inhomogeneous samples can be modelled by calculating $<\tilde{\varepsilon}_{\mathrm{model}}>$ of a given structural model. By comparison with the measured $<\tilde{\varepsilon}>$ model parameters, such as the thickness of overlayers or the roughness of a sample can be derived [73, 76, 77].

From a microscopic picture contributions to the dielectric function can be understood in terms of the different possible absorption mechanisms for light. The imaginary part of the dielectric function reflects the absorption properties of a medium. The most dominant contributions are the free carrier absorption, interband transitions, lattice absorption and core-level excitations. The latter two will be neglected in the following, since for the materials investigated they do not contribute in the measured spectral region. Lattice absorption is of importance for infrared spectroscopy where the energy of the light is of the order of the phonon energies (<0.2 eV), while core level excitation become important for deep UV measurements above 10 eV.

3.1.1 Contribution of interband transitions

For semiconductors the most important contribution to the dielectric function in the visible spectral range are interband transitions. In Fig. 3.1 $\tilde{\varepsilon}$ is shown for silicon. The maxima in $\tilde{\varepsilon}$ can be attributed to certain transitions within the electronic band structure as shown in the right graph of Fig. 3.1. The absorption and also Im($\tilde{\varepsilon}$) are large whenever the the joint density of states (JDOS) is maximised [72]. This is the case for parallel bands as in the case of the E_1 transition of silicon or if the bands are flat as is the case for the E_2 transition. The maxima in the JDOS or Im($\tilde{\varepsilon}$) are usually called critical point energies.

For the discussion of the optical properties of nanowires there are two important points regarding the interband transitions. *(i)* since no free standing nanowires are in-

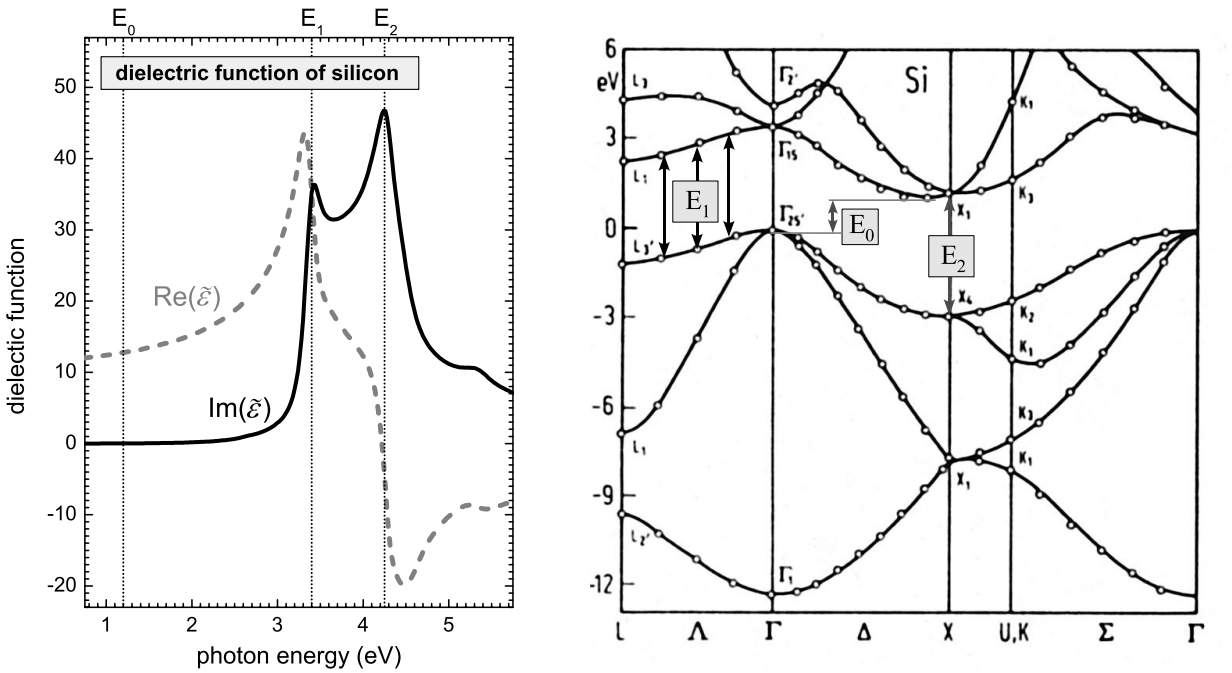

Figure 3.1: *The dielectric function of silicon is shown in the left part (solid line: imaginary part, dotted line: real part). In the right image the main transitions contributing to the bulk critical points are depicted by arrows in the bulk band structure.*

vestigated, the reflectivity of the substrate will influence optical measurements. The substrates of choice in this study were semiconductors, with well known $\tilde{\varepsilon}$. Nevertheless optical models will have to be developed to relate structures in the measured spectra to the wires itself. *(ii)* regards interband transitions within the electronic bands of the wire itself: Depending on the size of the wire they are expected to be different from the bulk material. The dielectric function of these wires will therefore be unknown. In order to relate structures in the optical spectra to the properties of the wires models have to be developed involving effective media theories (see 3.3.2), comparison to *ab-initio* calculations (see 3.5), or even the simplest approximation of single harmonic oscillators.

3.1.2 Contribution of intraband transitions

Another mechanism which contributes to the dielectric function of metallic nanowires are intraband transitions, also called the free electron response. They can be described within the Drude model which describes the absorption of a free electron gas.

$$\tilde{\varepsilon} = \varepsilon_\infty - \frac{4\pi N_c e^2}{m^*(\omega^2 + i\omega\omega_\tau)} \tag{3.1}$$

N_c denotes the charge density, m^* the effective mass and ω_τ the scattering rate which is related to the inverse scattering time τ. By defining the plasma frequency $\omega_p^2 = 4\pi N_c e^2/(m^*\varepsilon_\infty)$ the real and imaginary part of the Drude dielectric function can be expressed in terms of ω_p and ω_τ [72].

$$\mathrm{Re}(\tilde{\varepsilon}) = \varepsilon_\infty\left(1 - \frac{\omega_p^2}{\omega^2 + \omega_\tau^2}\right) \qquad \mathrm{Im}(\tilde{\varepsilon}) = \frac{\varepsilon_\infty\omega_p^2\omega_\tau}{\omega(\omega^2 + \omega_\tau^2)} \tag{3.2}$$

As was already discussed in section 2.2 the Drude model of noninteracting electrons is a rather crude model. Nevertheless the agreement with the IR response of metals and also doped semiconductors is astonishing if the electron mass is replaced by the effective mass, which reflects interactions of the electrons with the screened core potentials. In Fig. 3.2 $\mathrm{Im}(\tilde{\varepsilon})$ is shown for several metals. The deviations from the Drude dielectric function can be attributed to the already discussed interband transitions. In the Drude model the scattering rate of the electrons itself cannot be directly explained, since the electrons are assumed to be noninteracting. In the Fermi liquid picture introduced earlier this is changed. The electron-electron and electron-phonon interactions can be included in this model and the scattering rate quantitatively described [39, 41]. The Drude function for the free carrier absorption remains valid.

On surfaces or other two-dimensional structures the Fermi liquid picture can still be applied, though the reduced dimensionality and the vacuum-metal interface leads to a reduction of the plasma frequency at the surface. The effect has already long been known for metal surfaces. It was extensively discussed by Ritchie [78] for thin metal films, showing that the surface plasma frequency can be approximated as $\omega_{p,s} = \omega_p\sqrt{2}$. This was confirmed by numerous experiments involving electron loss

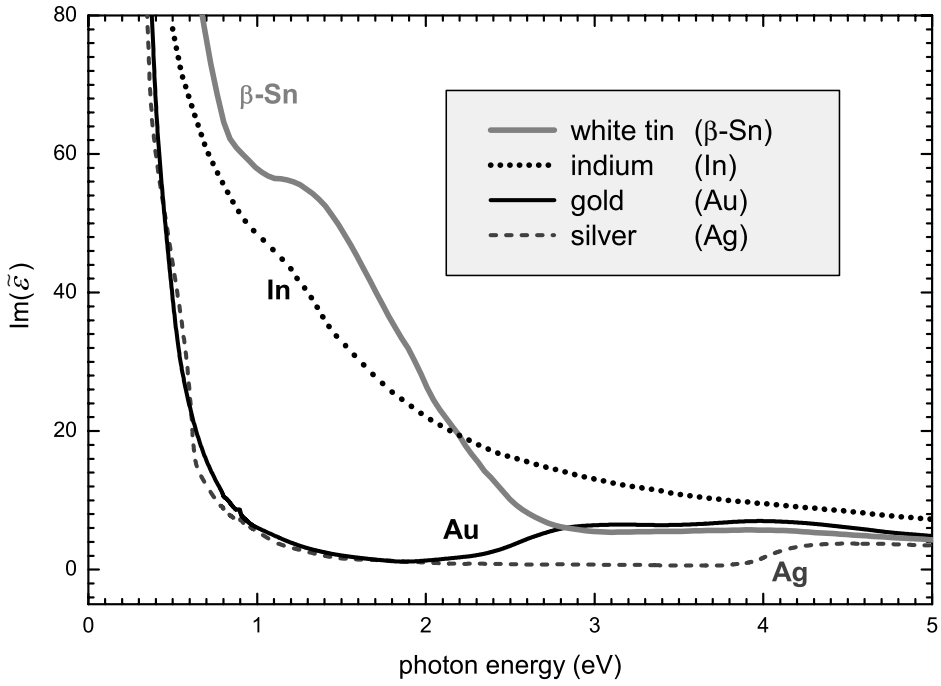

Figure 3.2: *Imaginary part of the dielectric function for various metals. For all metals the characteristic Drude tail of the free carrier absorption is observed in the infrared. Additional structures arise from interband transitions – most prominent for β-tin between 1 and 2 eV.*

spectroscopy and adapted to other geometries such as spheres. An excellent review of surface and interface plasmons can be found in [79]. Surface plasmons at surfaces are found to be particularly important for resonant enhancement in second harmonic generation (SHG) [80]. Surface plasma excitations are also discussed in linear optics for the absorption of metallic nanoparticles [81], the RAS of metal surfaces [82] and also extensively for scanning near-field optical microscopy (SNOM) [83]. All these measurements dealt with either isotropic clusters or surfaces. For the case of nanowires on surfaces the description is more complicated and no general approach is currently available.

Conductivity tensor

One aspect of this work will be the determination of anisotropies in conductance and not primarily the absorption of individual nanoparticles. In general the conductance is expressed as the conductivity tensor $\underline{\underline{\tilde{\sigma}}}$ which connects the current density **j** with the electric field. It can be related to the dielectric tensor as follows [72, 84]

$$\underline{\underline{\tilde{\varepsilon}}} = \varepsilon_\infty + i\underline{\underline{\tilde{\sigma}}}/\varepsilon_0\omega. \tag{3.3}$$

If one now neglects all interband contributions to $\tilde{\varepsilon}$ and assumes ε_∞ to be zero, the discussion is then limited to the free electron contribution only and can be expressed

for the isotropic case in terms of the two Drude parameters ω_p and ω_τ:

$$\sigma = \frac{\varepsilon_0 \omega_p^2}{\omega_\tau - i\omega} \tag{3.4}$$

If measured dielectric functions can be approximated by a Drude dielectric function one can directly relate the fit parameters ω_p and ω_τ to the conductance. By extrapolating the measurements to zero frequency the DC conductivity can be approximated as well, though measurements usually vary systematically from such extrapolation due to other transport mechanisms neglected by this simple model.

The description of the conductance by a Drude dielectric function is based on the assumption of electron like fermionic quasiparticles. In section 2.3 it was shown that this model fails in a strict 1D case. Nevertheless for larger wires, as will be described in chapter 4, the Drude model can be successful even in the cases of reduced dimensionality, although values for ω_p and ω_τ will differ from bulk values of the material.

3.2 Reflectance anisotropy spectroscopy

So far $\underline{\underline{\tilde{\varepsilon}}}$ was assumed to be isotropic and the discussion reduced to a scalar dielectric function. At surfaces, interfaces and also one-dimensional structures, for symmetry reasons, the isotropic description is invalid. By probing the optical anisotropy one can get signals which are specific to the areas of reduced symmetry. If samples were rotated changes in the reflectivity were noted [85, 86]. Much later a technique was developed by Aspnes and Studna and independently by Berkovits et al. which directly measures these anisotropies – reflectance anisotropy[1] spectroscopy (RAS) [87, 88]. RAS probes the difference in the reflectance between two perpendicular axes of a sample in normal incidence.

$$\frac{\Delta R}{R} = 2\frac{R_x - R_y}{R_x + R_y} \tag{3.5}$$

Hexagonal surfaces or other samples with threefold symmetry as well as randomly oriented domains do not show RAS signals. For the investigation of nanowires this limits the use of RAS to ordered wire systems with a defined wire direction. The incoming light is linearly polarised with an angle of 45° degrees towards the anisotropy axis as shown in Fig. 3.3 for the case of indium wires on Si(111). The components necessary for determining the polarisation state of the reflected light are shown as well. With the setup utilising two polarisers and a photo-elastic modulator, not only the real reflectance difference $\Delta R/R$ is measured but the anisotropy of the complex reflectivity $\tilde{r}$. Both the real and imaginary part can be probed, the first by analysing the signal at $2\omega_0$, the latter at ω_0, the frequency of the polarisation modulation of the PEM. For a detailed analysis of the measurement I refer to the analysis of Aspnes et al. [89] as well as Salvati and Chiaradia [90].

[1] The technique is also known as reflectance difference spectroscopy (RDS)

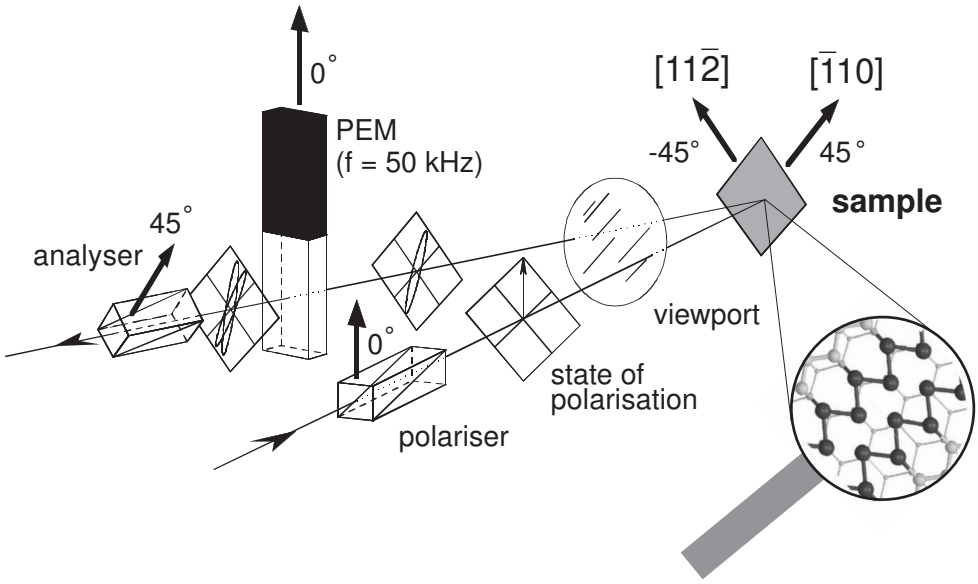

Figure 3.3: *One possible setup for determining the reflectance anisotropy is shown here. The light of the lamp is polarised and reflected by the sample surface. The sample is oriented such that the main axes are rotated 45° to the light polarisation. The reflected light is usually elliptically polarised. The combination of the photo-elastic modulator (PEM) and analyser can probe the tilt of the ellipse with respect to the incoming polarisation as well as the phase shift. It is therefore suited to measure both real and imaginary part of the complex reflectivity $\tilde{r}$. Simpler setups, using only one polariser or rotating polarisers instead of the PEM can only probe the real reflectance $R = |\tilde{r}|^2$. Details about various configurations for RAS spectrometers can be found in [89, 90].*

The fact that for simpler RAS setups only $\Delta R/R$ is measured while for those following the design of Aspnes $\mathrm{Re}(\Delta\tilde{r}/\tilde{r})$ and $\mathrm{Im}(\Delta\tilde{r}/\tilde{r})$ can be measured sometimes leads to some confusion when comparing absolute values of the RAS signal since $R = |\tilde{r}|^2$. For small amplitudes the two quantities differ by a factor of 2, $\Delta R/R \simeq 2\mathrm{Re}(\Delta\tilde{r}/\tilde{r})$. In this work all RAS spectra will be expressed in terms of the complex reflectivities, hence $\mathrm{Re}(\Delta\tilde{r}/\tilde{r})$ will be shown and for simplification the indication for the complex number $\tilde{r}$ will be omitted and the term $\mathrm{Re}(\Delta r/r)$ is used.

3.2.1 Surface dielectric anisotropy

The normal reflectance of a semi-infinite isotropic bulk sample in vacuum is directly related to the dielectric function:

$$R = |(\tilde{n} - 1)/(\tilde{n} + 1)|^2 \tag{3.6}$$

with the complex refractive index $\tilde{n} = \tilde{\varepsilon}^2$. In the case of anisotropic samples the diagonal elements of the dielectric tensor will differ and the description in terms of

the scalar dielectric function must be dropped. Instead the tensor components $\tilde{\varepsilon}_{xx}$, $\tilde{\varepsilon}_{yy}$, and $\tilde{\varepsilon}_{zz}$ have to be discussed. In the ideal case of normal reflectance the electric field vectors of the light are within the x, y plane. The component $\tilde{\varepsilon}_{zz}$ therefore does not influence the measurements[2]. For such bulk anisotropic samples where $\tilde{\varepsilon}_{xx} \neq \tilde{\varepsilon}_{yy}$ RAS can probe the difference in the reflectance R_x and R_y and can be directly calculated from the tensor components $\tilde{\varepsilon}_{xx}$, $\tilde{\varepsilon}_{yy}$ using (3.6) and (3.5).

The measurement of bulk anisotropies is but a special case of application. The system of anisotropic surfaces or wires on top of an isotropic bulk have to be treated differently since the isotropic bulk is influencing the measurements as well. For a more general description one assumes an anisotropic surface layer of thickness d between the semi-infinite isotropic bulk with a bulk dielectric function $\tilde{\varepsilon}_b$ and above, another semi-infinite ambient layer with the dielectric function $\tilde{\varepsilon}_a$. The anisotropy of the surface layer is expressed again by the two different diagonal tensor components of the dielectric function $\tilde{\varepsilon}_{xx}$ and $\tilde{\varepsilon}_{yy}$. In this so called three layer model the RAS spectra is described as follows [87]

$$\frac{\Delta r}{r} = \frac{4\pi i d}{\lambda} \frac{\tilde{\varepsilon}_{xx} - \tilde{\varepsilon}_{yy}}{\tilde{\varepsilon}_b - \tilde{\varepsilon}_a} \tag{3.7}$$

Since $\tilde{\varepsilon}_b$ and $\tilde{\varepsilon}_a$ are usually known this relates the RAS signal to the properties of the surface layer. The term $d \cdot (\tilde{\varepsilon}_{xx} - \tilde{\varepsilon}_{yy})$ is called the surface dielectric anisotropy (SDA). With this quantity the anisotropy of a surface can be directly discussed in terms of a dielectric function of the surface layer. For interpretation of RAS spectra this is quite useful since the influence of the bulk reflectivity to the spectra is removed in the SDA and therefore similar adsorbate structures on different substrates can be better compared. On the other hand (3.7) enables simulations of RAS spectra with optical models. By comparing such models to the measurements model parameters can be fitted, similar to common practise for the analysis of ellipsometric measurements.

3.2.2 Applications of RAS

RAS is commonly used as an *in-situ* probe of semiconductor surface and interface reconstructions. RAS has become more important, in particular for growth in gaseous environments, such as for metal organic vapour phase epitaxy (MOVPE) where electron based analysis does not work.

Currently it is used for the determination of surface reconstructions during growth, monitoring of the growth rate by monolayer oscillations, and even the determination of doping levels is possible. RAS spectra of samples of multilayers as they are used in semiconductor devices get more complex, since all layers and interfaces within the penetration depth are probed. Nevertheless such spectra can nowadays be modelled, though more complex models have to be applied other then the three layer model discussed above [91].

The contribution of free electrons to the RAS spectra was, until now, not discussed mainly due to the limited spectral range of the standard optics. In the next sections I will therefore discuss in detail how anisotropies in the conductance can be measured with RAS as well.

[2] by measuring different surface planes of the sample e.g (xy0) and (x0z) all three diagonal components can be probed

3.2.3 Anisotropy in optical conductance

As shown above the dielectric function is related to the optical conductance. Since in RAS the difference of the dielectric tensor components can be measured, RAS, in principle, is also able to measure conductance anisotropies. Using (3.7), (3.3) and defining a conductance anisotropy $\Delta\sigma = \sigma_{xx} - \sigma_{yy}$ it can be easily seen that the reflectance anisotropy is directly related to $\Delta\sigma$:

$$\frac{\Delta r}{r} = \frac{2d}{\varepsilon_0} \frac{\Delta\sigma}{\tilde{\varepsilon}_b - 1} \tag{3.8}$$

If $\tilde{\varepsilon}_b$ is constant, as is the case for silicon below 1 eV, the RAS signal is therefore proportional to the conductance anisotropy. This was not discussed in analyses of RAS spectra so far, since usual semiconductor surfaces are not metallic, and for the RAS of bulk metals the RAS signal vanishes in the IR due to the strong rise in $\tilde{\varepsilon}_b$. For metallic nanowires on semiconductor surfaces however this contribution will become important.

3.2.4 Technical implementation of an IR enhanced RAS

So far technical details of the RAS spectrometer were not discussed. Since considerable work went into the design of a spectrometer capable of measuring in the infrared, I would like to discuss the modifications necessary to achieve this. As we will see in the next section the contribution of a free carrier anisotropy to the RAS signal of metallic nanowires is mostly expected in the infrared region. Conventional RAS spectrometers utilise silicon detectors and are therefore only capable of measurements above 1.2 eV. It was recently demonstrated by Goletti et al. that by using a special CaF_2 PEM and an InSb liquid nitrogen cooled detector, RAS measurements down to 0.3 eV are possible [92]. One drawback is that with such a single detector setup and foil polarisers the overall measurement range is reduced to 0.3 - 1 eV. In order to extend that range into the visible and UV range other concepts such as multiple detectors but also multiple monochromators have to be used as demonstrated by Herrmann [93]. The IR-VIS setup shown in Fig. 3.4 utilises MgF_2 polarisers which operate between 0.2 to 9 eV, a CaF_2 PEM which fully modulates the polarisation between 0.25 eV and 5 eV, a double grating monochromator, one for the IR and one for the NIR to UV range and three detectors: one liquid nitrogen cooled InAs detector for measurements between 0.45 and 0.9 eV, one InGaAs photo diode for 0.75 to 1.5 eV and a Si photo diode for measurements above 1.3 eV. The detectors were chosen to provide sufficient overlap in order to compare and calibrate the response of all detectors more easily. With these components the effective range is 0.5 eV to 5 eV. For some measurements it was beneficial to use a tungsten lamp instead of the usual Xe high pressure lamps in order to improve the signal to noise ratio in the IR, although in this case only measurements up to 3 eV were possible.

At present the monochromator gratings as well as the detectors have to be switched manually which makes automated measurements of the full range impossible. The spectra have to be taken by three separate measurements, though a readjustment of the system is limited to the adjustments of the detector positions.

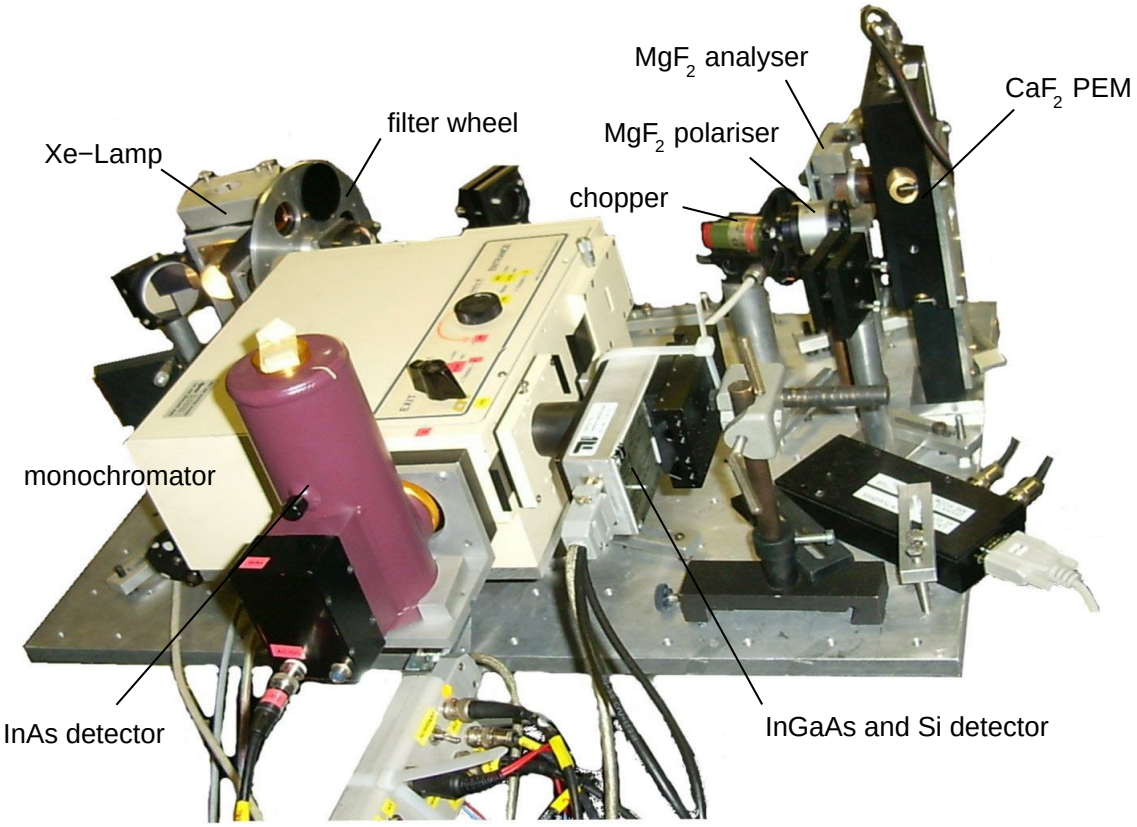

Figure 3.4: *Photograph of the infrared enhanced RAS. The main parts of the RAS are labelled and described in detail within the text.*

This could not prevented, since the two gratings are not aligned perfectly. For the larger Si detector these small changes in the focal point were not important, but for the smaller InAs and InGaAs this caused problems. Unfortunately IR detectors which are fast enough to detect the 114 kHz[3] modulated signal of the RAS have to be small. Additionally the sensitivity of the InAs diode is two magnitudes smaller than for the Si diode. For this reason the noise in the IR measurements is comparably large which limits the sensitivity of the RAS to $0.5 \cdot 10^{-3}$ for a single measurement and integration times of 500 msec. For the other detectors the sensitivity is better than $1 \cdot 10^{-4}$ even for faster data acquisition with 100 msec integration time.

The need for fast IR detectors principally limits the spectral range of the RAS setup using polarisers and PEM. For a further extension into the IR other concepts have to be applied. Possible approaches are the use of FTIR-ellipsometers in normal incidence [94] or the implementation of simpler setups such as rotating polariser systems [89]. In both cases the measurement time will increase, which will render these systems useless for any *in-situ* monitoring of processes with timescales in the order of seconds.

[3]The PEM is operated with 57 kHz. Re($\Delta r/r$) is measured at 2ω

3.3 Models for the optical anisotropy of nanowires

So far the discussed application areas of RAS involved mainly semiconductor surfaces and interfaces. In this section I will introduce different models, which can be used to describe the signals of the one-dimensional metallic structures. In order to simulate RAS spectra of these structures the three layer model of (3.7) will be used. The main point is therefore the determination of the actual values for $\tilde{\varepsilon}_{xx}$ and $\tilde{\varepsilon}_{yy}$ which describe the problem most accurately. Apart from the different three layer models a short introduction is given to more general *ab-initio* calculations which were available for some of the investigated systems.

3.3.1 Bulk metal approximation

The most simple approximation of the optical anisotropy of nanowires is to assume the optical response for light polarised along the wires corresponds to the bulk metal dielectric function ($\tilde{\varepsilon}_{xx} = \tilde{\varepsilon}_{\text{metal}}$). Vacuum ($\tilde{\varepsilon}_{yy} = 1$) is assumed for the response for light polarised perpendicular to the wire. Using (3.7) the RAS spectrum can then be calculated. In Fig. 3.5 such a calculation is shown for several metals on silicon. Due to the simplicity of this model the agreement to real measurement is expected to be poor, though principle structures in the RAS of metal wires on semiconductors can be

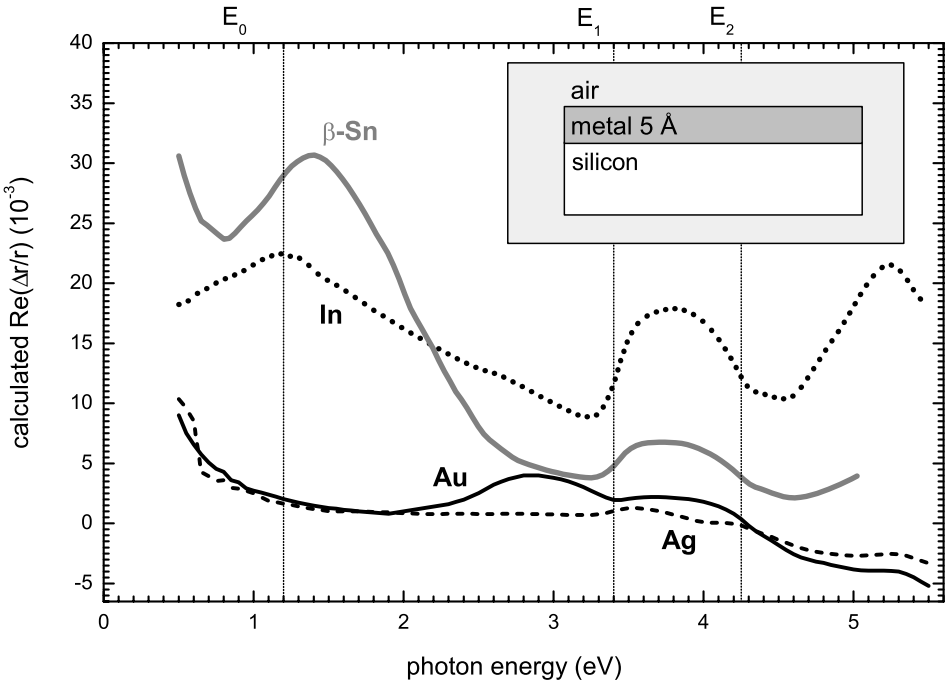

Figure 3.5: *Model calculations of RAS spectra of metal wires on silicon using (3.7) and only the bulk dielectric functions of the metals (see Fig. 3.2 and silicon. Due to the $1/\lambda$ term in (3.7) the increase in the IR is less dramatic than for the dielectric function itself but can still be found. Using the same thickness for all materials the strongest RAS spectra is expected for tin and indium.*

already seen, in particular an increase of the RAS in the infrared is predicted. Using the dielectric function of the metal and silicon only, the calculation also shows that the $1/\lambda$ term in (3.7) is partly compensating the rise of $\mathrm{Im}(\tilde{\varepsilon}_{\mathrm{metal}})$ seen in Fig. 3.2. If the surface dielectric anisotropy can be approximated by a Drude dielectric function where $\mathrm{Im}(\tilde{\varepsilon}) \sim \omega^{-3}$ the RAS should still increase in the far infrared since for long wavelengths this term will always dominate. For the near infrared region the rise in the RAS signal can nevertheless be less pronounced if interband transitions from the adsorbate or substrate dominate the RAS. For example in the case of indium the slope of the Drude tail is not steep enough and the RAS decreases again for smaller energies. The SDA and λ are not the only factors influencing the RAS spectra – the underlying isotropic bulk contributes as well. The discussion so far is only valid if the bulk dielectric function remains constant in the IR. For metal substrates, when also $\varepsilon_b \sim \omega^{-3}$ the RAS will vanish in the IR. Consequently in RAS measurements of anisotropic metal surfaces (clean [95, 96] or vicinal [97] or patterned [98]) no RAS signal in the IR has been measured so far, though calculations of the SDA reveal strong anisotropies [96]. On semiconductors where ε_b is constant or decreasing in the IR (at least in the region above the Drude tail due to dopants and the phonon frequencies), the bulk metal approximation shows that RAS signals in the IR are expected.

3.3.2 Anisotropic effective medium approximation

The second model which I want to discuss is an anisotropic effective medium approximation. The RAS spectra will be calculated again with (3.7). The effective dielectric tensor components $\tilde{\varepsilon}_{xx}$ and $\tilde{\varepsilon}_{yy}$ will be replaced by model dielectric functions from effective media approximations (EMA). With EMAs the optical response of media consisting of two or more components can be modelled from the optical properties of the components if the inclusion size is smaller than λ and the geometry as well as volume fraction of the inclusions is known. EMAs date back to the work of Maxwell Garnett where the transmission spectra of coloured glass windows were explained by spherical inclusions of gold within the glass matrix [99, 100]. Using the scalar dielectric function of isotropic media $\tilde{\varepsilon}$ a general description is nowadays used [73, 76, 101]. It starts from the basic assumption of spherical inclusions and dipole interactions with particles much smaller than the wavelength. The effective medium $\tilde{\varepsilon}_{\mathrm{ema}}$ for various inclusions $\tilde{\varepsilon}_{a,b,\ldots}$ within a host medium $\tilde{\varepsilon}_h$ can then be written as:

$$\frac{\tilde{\varepsilon}_{\mathrm{ema}} - \tilde{\varepsilon}_h}{\tilde{\varepsilon}_{\mathrm{ema}} + 2\tilde{\varepsilon}_h} = f_a \frac{\tilde{\varepsilon}_a - \tilde{\varepsilon}_h}{\tilde{\varepsilon}_a + 2\tilde{\varepsilon}_h} + f_b \frac{\tilde{\varepsilon}_b - \tilde{\varepsilon}_h}{\tilde{\varepsilon}_b + 2\tilde{\varepsilon}_h} + \ldots \tag{3.9}$$

The factors $f_a, f_b, \ldots$ denote volume fraction of the inclusion and are called structure factors. Since all metallic wires discussed in this work consist of only one material this is reduced to one inclusion. Equation (3.9) is then simplified to:

$$\frac{\tilde{\varepsilon}_{\mathrm{ema}} - \tilde{\varepsilon}_h}{\tilde{\varepsilon}_{\mathrm{ema}} + 2\tilde{\varepsilon}_h} = f_a \frac{\tilde{\varepsilon}_a - \tilde{\varepsilon}_h}{\tilde{\varepsilon}_a + 2\tilde{\varepsilon}_h} \tag{3.10}$$

In this form the approximation is called Maxwell Garnett approximation.

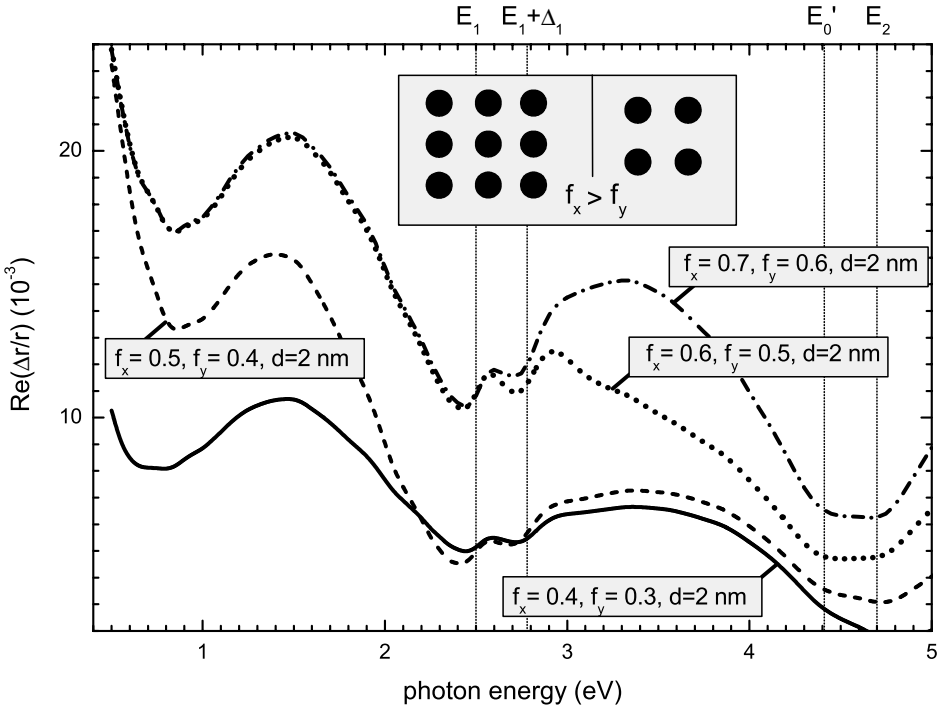

Figure 3.6: *Model calculations of RAS spectra of tin wires on InAs using (3.7) and different effective media dielectric functions for the two perpendicular axes and a thickness of the anisotropic layer of 2 nm. (solid curve:* $f_x = 0.4$, $f_y = 0.3$*; dashed curve:* $f_x = 0.5$, $f_y = 0.3$*; dotted curve:* $f_x = 0.6$, $f_y = 0.5$*; dash-dotted curve:* $f_x = 0.7$, $f_y = 0.6$*)*

For the case of the wires on top of bulk samples the host medium is vacuum or air which further simplifies the problem:

$$\frac{\tilde{\varepsilon}_{\text{ema}} - 1}{\tilde{\varepsilon}_{\text{ema}} + 2} = f_a \frac{\tilde{\varepsilon}_a - 1}{\tilde{\varepsilon}_a + 2} \tag{3.11}$$

This special case of the Maxwell Garnett approximation is also called Lorentz-Lorenz approximation.

The Lorentz-Lorenz and Maxwell Garnett approximation work well for small volume fractions, but if there is as much medium as host ($f_a \approx 0.5$) other approximation have to be used. Following the work of Bruggeman one approach is to assume the host medium is the effective medium $\tilde{\varepsilon}_{\text{ema}} \approx \tilde{\varepsilon}_h$ For one type of inclusion in vacuum (3.9) can then be written as:

$$0 = f_a \frac{\tilde{\varepsilon}_a - \tilde{\varepsilon}_{\text{ema}}}{\tilde{\varepsilon}_a + 2\tilde{\varepsilon}_{\text{ema}}} + (1 - f_a) \frac{1 - \tilde{\varepsilon}_{\text{ema}}}{1 + 2\tilde{\varepsilon}_{\text{ema}}}. \tag{3.12}$$

With the known optical properties for the inclusion $\tilde{\varepsilon}_a$ – in this case the metal – effective media dielectric functions can now be calculated using (3.12) or (3.11). In order to simulate an RAS spectrum the calculation of one effective medium dielectric function is not enough, since two different $\tilde{\varepsilon}$ are needed for the two perpendicular directions. Again the most simple approach is to use the same EMA but different

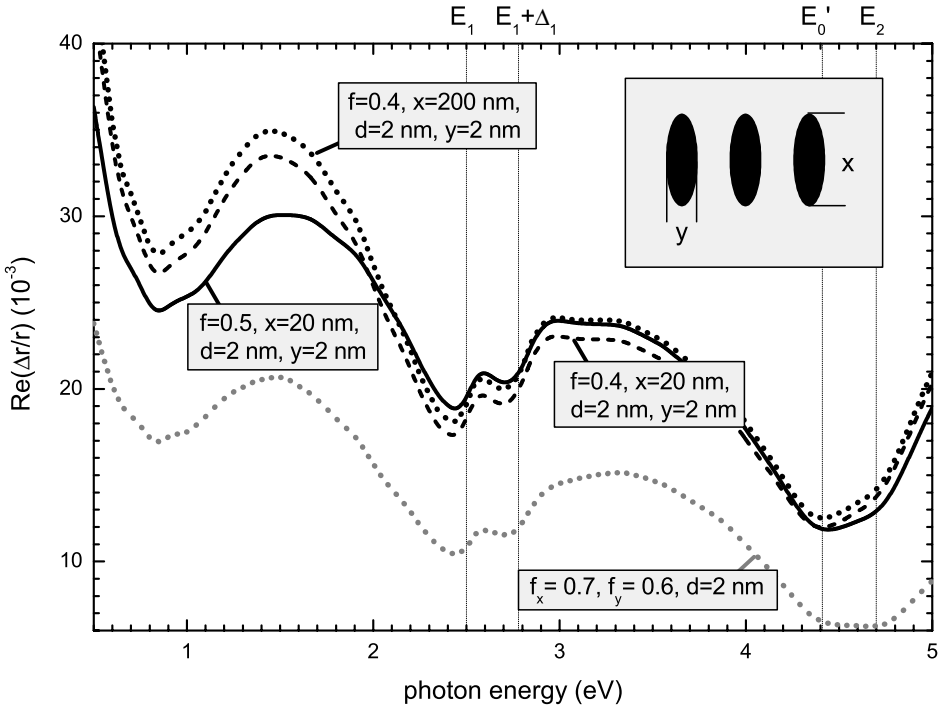

Figure 3.7: *Model calculations of RAS spectra of tin wires on InAs using (3.7) and a modified Bruggeman model with ellipsoid inclusions. The anisotropy arises from the anisotropy of the ellipsoid. Again a 2 nm thick anisotropic layer was assumed. (solid curve: $f = 0.5, x = 20\,nm$, $y = 2\,nm$; dashed curve: $f = 0.4, x = 20\,nm$, $y = 2\,nm$; dotted curve: $f = 0.4, x = 200\,nm$, $y = 2\,nm$) The grey dotted line shows one of the curves of Fig. 3.6 for comparison ($f_x = 0.7$, $f_y = 0.6$). calculation from Fig. 3.6*

volume fractions for the two directions. In Fig. 3.6 model spectra are shown for tin on InAs using the Bruggeman EMA. The already discussed bulk metal approximation is the borderline case of this model using $f_x = 1$, $f_y = 0$.

So far the effective medium was derived for isotropic spherical inclusions. For geometrical reasons this is a bad approximation for nanowires. For better agreement anisotropic effective media theories have to be used. One approach is to use a modified Bruggeman model where the spherical inclusions are replaced by ellipsoids with one long axis z and two equal short axes x, y. Both the Maxwell Garnett and the Bruggeman approximation can be extended that way, although the resulting equations cannot be solved analytically and a numerical solution has to be used [102]. The procedure is also described in [103] and will not be explained here[4]. Figure 3.7 shows a model calculation for the same system as in Fig. 3.6.

The EMAs described here are just a small selection of possible approaches. There are numerous other EMAs used particular for the description of metal clusters de-

[4] All effective media dielectric functions were calculated using a program for modelling of linear optical spectra (Lay_TEX 2.0) [77]. RAS spectra and the simple model dielectric functions were calculated using a standard spreadsheet (Microcal Origin 7)

scribed in the literature [81]. For simple geometries such as the wires there are other analytical solutions for the effective media. Aspnes for instance provided a solution for terrace structures in order to explain the RAS spectra of rough surfaces. In this case – similar to all other EMAs discussed – the bulk properties of the wire material is used to determine the dielectric anisotropy of the wires. Although details differ the main RAS structures which can be explained were always similar. For this reason the discussion will be reduced to the models which can be calculated more easily. As one will see in chapter 4 all these EMA models only work for rather large wires dominated by bulk properties of the metal. For the more interesting case of small wires other models had to be used.

Another weak point of such effective media theories is the fact that the inclusions are assumed to be non-interacting. By analysing single particles, it was already shown that the spectrum of two individual nanorods is influenced by their distance [105]. Until now such particle interactions have not been included in any effective media theories. One interesting point in comparing the measured anisotropies of nanowire assemblies is therefore whether effective media approximations can be used to describe the spectra at all and where the limits of these models are.

3.3.3 Free electron gas approximation

For the smallest wires investigated here the bulk metal approximation as well as the EMA based models discussed probably do not agree well with measurements, since chains of single atoms can hardly be approximated by bulk properties of the corresponding metal. Full calculations of the dielectric response of such a small systems, though possible, are very time consuming and involve a full analysis of the surface in slab calculations within the density functional theory (DFT, see below). An alternative, straight forward approach is to focus on the properties of the free electron gas. If one neglects all contributions of interband transitions the model is reduced to the intraband terms, which can be expressed as a Drude dielectric function (3.2). To model the optical anisotropy one just uses two Drude dielectric functions with different scattering rates $\omega_{\tau,x}, \omega_{\tau,y}$ and plasma frequencies $\omega_{p,x}, \omega_{p,y}$. In figure 3.8 a calculation of $\tilde{\varepsilon}_{xx}$ and $\tilde{\varepsilon}_{yy}$ as well as the difference of them is shown in units of ω_0 (an arbitrary frequency). To simulate real structures one can use measured values or values derived from *ab-initio* calculations as parameters for the Drude dielectric function. Figure 3.9 gives an example of the expected RAS spectra of an anisotropy in the plasma frequencies along and perpendicular to the wire axis. Apart from the rise in the infrared structures can arise at the bulk critical points of the substrate (in this case silicon). In what way this model can be used to get information about the properties of the wire system – most importantly quantitative information about an anisotropy in the conductance – remains to be seen. In principle if the measured RAS spectra can be described with curves such as the one shown in Fig. 3.9 the DC conductance anisotropy can be measured by interpolating the measurements to zero frequency. For carbon nanotubes and conducting polymers it was already shown with dielectric (or impedance) spectroscopy measurements in the FIR and microwave regime, that only 50% of the DC conductance arises from free carrier transport. Other mechanisms such as ballistic transport or e^- inter-chain movement

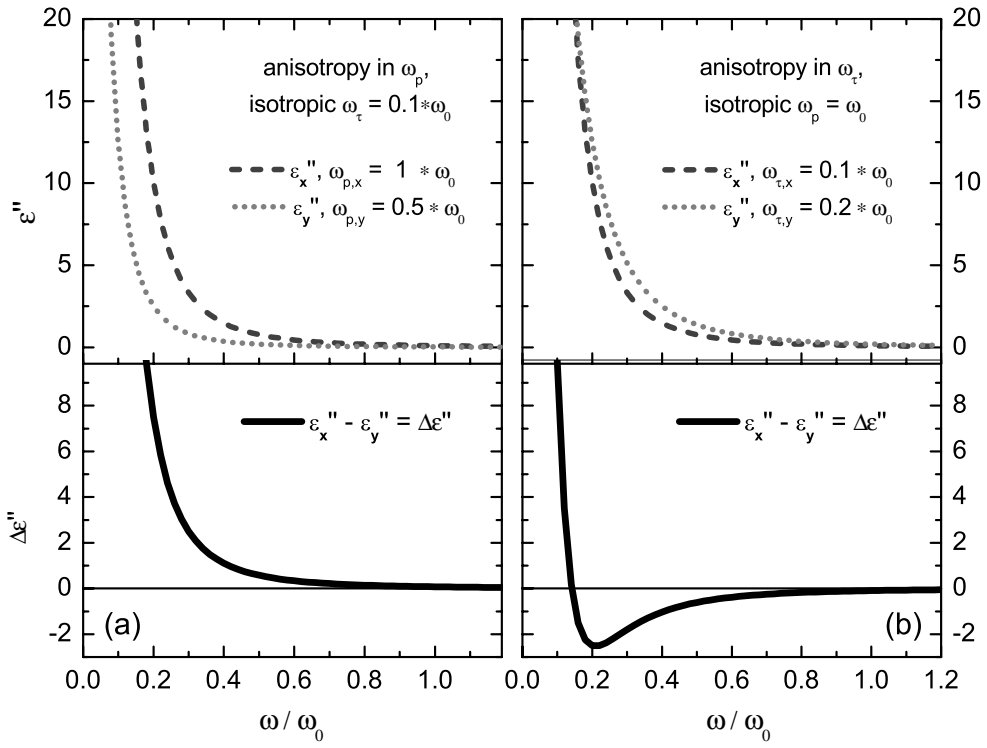

Figure 3.8: *Different Drude dielectric functions (dashed and dotted curves) and their differences (solid curve). In a) ω_τ was kept constant while ω_p was changed. b) shows the difference in the case where ω_τ was changed. In this case the SDA (and RAS) can change its sign. If only anisotropies in ω_p are considered the RAS is either all positive or all negative.*

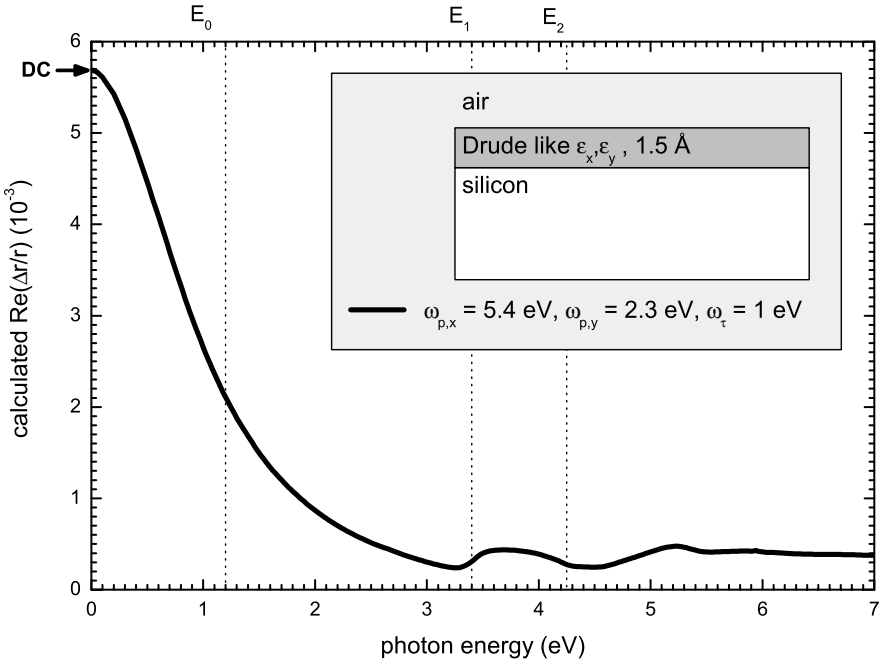

Figure 3.9: *Model calculation of a RAS spectra assuming an anisotropic metal layer on top of silicon. In this case only the ω_p was assumed to be anisotropic. If only free electrons contribute to the DC conductance the conductance anisotropy can be extrapolated from the RAS spectra for $\omega \to 0$.*

lead to an additional frequency independent conductance [106].

It remains to be seen whether RAS measurements in the NIR and visible energy range will lead to comparable results, which is one aspect of this work. Measurements using different wire systems will be presented in chapter 4. The systems were chosen to cover a wide range of wire sizes in order to determine limits of this Drude type model. However, it was already shown in section 2.3 that the free electron picture cannot, in principle, be applied to an ideal one-dimensional system. In particular for the smallest investigated system, the indium wires on silicon, this is of importance and will be separately discussed in chapter 5.

3.4 Raman spectroscopy and nanowire phonon modes

Apart from information about the electronic transitions and related anisotropies, there are optical techniques which can also probe vibrational properties of a nanowire. Two such techniques are commonly used: Fourier transform infrared spectroscopy (FTIR) and Raman spectroscopy. The latter was used in this study and will therefore be introduced here.

Light can be scattered either elastically or inelastically when it passes through matter. One inelastic scattering process is called Raman scattering after C. V. Raman who first experimentally confirmed and identified this process in organic liquids [107]. The effect itself was also independently seen in quartz by Landsberg and Mandestam [108]. For more detailed description of the process and technical implementation I would like to refer the reader to several reviews and books [73, 109–111]. Here only a brief review of some relevant aspects is given. The Raman process itself is a transfer of energy to or from the incident light wave of frequency ω_i leading to a scattered light wave ω_s. The energy is transferred by elementary excitations such as phonons or coupled plasmon-phonon modes. By analysing the frequency of the scattered light the energies of the elementary excitation Ω_j can be determined since energy and momentum conservation applies.

$$\hbar\omega_s = \hbar\omega_i \pm \hbar\Omega_j; \quad \mathbf{k}_s = \mathbf{k}_i \pm \mathbf{q}_j \tag{3.13}$$

If ω_s is lower than ω_i due to the generation of, for example a phonon, the process is called Stokes process and in the opposite case, Anti-Stokes.

In this work only scattering processes involving phonon modes are of interest. With Raman spectroscopy it is possible to determine phonon frequencies of individual atomic arrangements. In simple models such as a linear chain it can be shown that the phonon frequency not only depends on the mass of the vibrating atoms but also on the coupling constant k such that $\omega_s \sim \sqrt{k/m}$. Since k is determined by the bonding configuration of the atoms, changes in the measured frequencies, for instance at a phase transition, can give insight into the nature of such a transition.

Not only the frequency of the phonon modes but also the intensity of the scattered light can be analysed. The intensity of the scattered light wave I_s can be given by

$$I_s = I_i \frac{\omega_s^4 V}{(4\pi\varepsilon\varepsilon_0)^2 c^4} |\mathbf{e_s}\tilde{\chi}(\omega_i, \omega_s)\mathbf{e_i}|^2 \tag{3.14}$$

Here V is the scattering volume, $\mathbf{e}_i$ and $\mathbf{e}_s$ the unit vector of the polarisation for incident and scattered light. $\tilde{\chi}(\omega_i, \omega_s)$ is the generalised dielectric susceptibility. The latter is usually expressed by a Taylor expansion of its tensor components in terms of lattice distortions Q_j by the phonon [73]. The first term in this expansion is the static susceptibility and equivalent with the already discussed dielectric function:

$$\chi^0_{\alpha\beta} = \varepsilon_{\alpha\beta} - 1 \tag{3.15}$$

For single phonon scattering without deformation gradients and static electric fields only the second term in the expansion $\sum_j Q_j(\partial\chi_{\alpha\beta}/\partial Q_j)$ is relevant. If only this term is considered the tensor is usually called the first order Raman tensor $\underline{\underline{R}}$ and the intensity of the scattered light is then given as:

$$I_s = I_i \frac{\omega_s^4 V}{(4\pi\varepsilon\varepsilon_0)^2 c^4} \left|\mathbf{e}_s \underline{\underline{R}} \mathbf{e}_i\right|^2 \tag{3.16}$$

3.4.1 Selection rules

Raman tensors depend on the symmetry of the crystal lattice under consideration and are known for all symmetries [110]. For certain polarisation configurations $\mathbf{e}_i$ and $\mathbf{e}_s$ the term $\mathbf{e}_s \underline{\underline{R}} \mathbf{e}_i$ in (3.16) can become zero. In this case the mode is called Raman forbidden. The measured intensity of certain modes is therefore dependent on the scattering configuration. To denote a certain configuration the Porto notation will be used here $\mathbf{k}_i(\mathbf{e}_i, \mathbf{e}_s)\mathbf{k}_s$ giving the polarisation vector and wave vector of incident and scattered light. From the disappearance of certain modes upon polarisation changes the symmetry of the phonon mode can be derived.

3.4.2 Resonant Raman scattering

Apart from these polarisation dependent changes in the intensity of the scattered light, the energy of the incident light itself also has an influence. In general due to the ω_s^4 dependence, the scattered intensity increases with incident photon energy. Additionally the dielectric function and therefore also the susceptibility itself is a function of ω_i. In a microscopic quantum mechanical picture using time dependent third order perturbation theory the susceptibility can be expressed as

$$\chi_{\alpha\beta}(\omega_i, \omega_s) = \frac{e^2}{m_0^2 \cdot \omega_s^2 V} \sum_{e,e'} \frac{\langle 0|p_\alpha|e'\rangle\langle e'|H_{E-L}|e\rangle\langle e|p_\beta|0\rangle}{(E_{e'} - \hbar\omega_s)(E_e - \hbar\omega_i)}. \tag{3.17}$$

The scattering process is described by a virtual electronic transition from the ground state $|0\rangle$ to an excited state $|e\rangle$ followed by the scattering into a second excited state $|e'\rangle$ via an electron-phonon interaction (H_{E-L}). Finally the scattered light is reemitted by the transition from $|e'\rangle$ to the ground state $|0\rangle$. From (3.17) it can be easily seen that $\chi_{\alpha\beta}$ and therefore also I_s is particularly large if the incident or scattered light energy matches the energies of real states and if the excitation or annihilation probability ($\langle e|p_\beta|0\rangle$ or $\langle 0|p_\alpha|e'\rangle$) is large [73]. For this reason the Raman efficiency can be increased by several orders of magnitudes if the incident light energy is close

to critical point energies. The resonance of bulk phonon modes is well investigated and known for many semiconductors [112–115].

Resonances can be also understood within the classical description of Raman scattering. Details can be found, for instance, in [73]. One interesting result of these considerations is that the Raman cross section S is proportional to the squared absolute value of the first derivative of $\tilde{\varepsilon}$ with respect to the frequency $|\partial\tilde{\varepsilon}/\partial\omega|^2$. For bulk semiconductors this gives reasonable agreement [112–115] and inversely by measuring the resonance one can gain information about $\tilde{\varepsilon}$ with Raman spectroscopy in addition to the vibrational properties.

3.4.3 Surface phonons

So far only Raman scattering involving bulk phonon modes was discussed. Due to the symmetry break at the surface macroscopic surface phonon modes are expected. This phenomena was already described by Lord Rayleigh [116]. Such macroscopic surface modes decay exponentially into the bulk. Similar to the bulk case coupled modes such as surface polaritons can also exist. In this work no such modes were found so I will not describe such macroscopic modes here. Instead the reader is referred to other work [117–119].

The atomic geometry of a surface or, more relevant for this work, adsorbates on a surface varies significantly from the bulk material. For this reason different vibrational modes exist at the surface. In contrast to the macroscopic modes the displacement pattern of such modes only includes atoms in the very first atomic layers. Such surface phonons are therefore called microscopic modes. Microscopic phonon modes were already predicted by Wallis [120]. The detection of such surface phonons only became possible in the last decade. With Raman spectroscopy clean surface phonon modes were found for InP(110) surfaces [121] and for adsorbate terminated surfaces such as Sb/InP(110) [122], Sb/InAs(110) [123] or H/Si(111) [124]. There are two main problems in the detection of microscopic surface phonons. First the scattering volume is small compared to the bulk case. Since the lateral size of the scattering volume is determined by the focal area of the incident light and therefore the same for bulk and surface only the depth d has to be considered. For bulk phonons d can be approximated by the penetration depth l_P of the incident light. Using silicon as an example and an incident photon energy of 2.41 eV, l_P is about 600 nm. The scattering volume for microscopic surface modes instead is limited to the first atomic layers and therefore of the order of 1 nm. This leads to signals several orders of magnitude lower than bulk mode signals. By using light with higher energy the absolute scattering rate can be increased (ω_i^4 dependence) and since l_P is decreased the ratio can be improved, but bulk phonons will always be much stronger than the microscopic surface modes. Figure 3.10 shows the spectrum of an indium terminated Si(111) surface in (4×1) reconstruction taken with an incident laser energy of 2.41 eV. It is obvious that bulk phonons dominate the spectra. Due to a resonant enhancement of the surface phonons the intensity ratio of bulk to surface phonon is around 100 – smaller than the 600 as expected from the penetration depth discussion above.

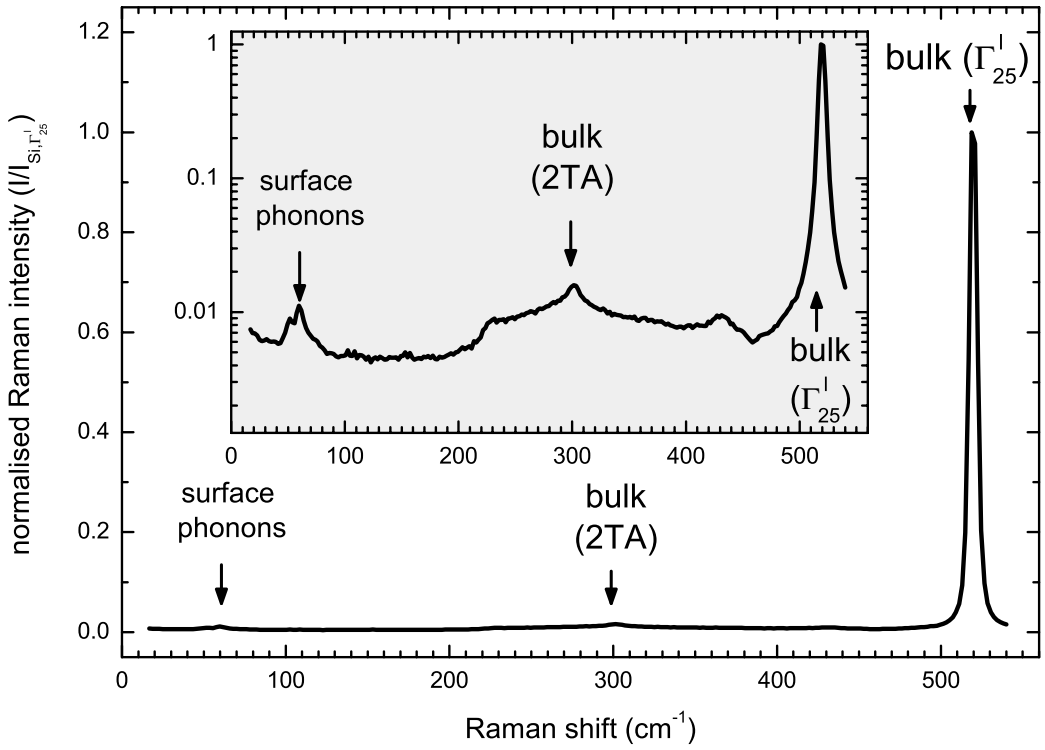

Figure 3.10: *Raman spectra of a Si(111)-In:(4×1) surface using incident laser light of 2.41 eV (514 nm) and* $\mathbf{e}_s \parallel \mathbf{e}_i \parallel [\bar{1}10]$. *The bulk silicon* Γ_{25}' *mode is dominating the Raman spectra. At low energies additional surface modes can be seen (logarithmic plot in the inset).*

3.4.4 Resonant Raman scattering on surface phonons

Similar to resonant Raman scattering in bulk samples, surface modes can also be resonant. Following (3.17) these resonances occur at energies where transitions within the surface band structure are likely. By analysing the resonance behaviour of surface modes not only vibrational properties of the surface (or nanowire) but also – indirectly – information about surface critical point energies can be gained. This again can give complementary information to the RAS spectra, where anisotropies in surface critical points are measured.

If scattering intensities are to be compared one has to carefully consider all influences to the measured Raman intensity. If fully evaluated, the scattered intensity depends on the incident laser power P_i and frequency ω_i, reflectivity $r(\omega_i)$ of the sample, collection aperture $\Delta\Omega$, temperature T, absorption coefficient $\alpha(\omega_i)$ and a volume independent quantity termed "Raman susceptibility" S which is related to the differential scattering cross section [113]. In addition to these principal dependencies technical aspects such as transmittance of the monochromator, sensitivity of the detector and precision of the focus influence the measured signal. If one wants to analyse the electronic properties of the sample only the Raman susceptibility is of interest. Since absolute measurements of all other values are normally not possible

or the resulting error of the measurement is too large, only relative measurements can be done. In the case of the surface phonons the best approach is to normalise the measured spectra by dividing the measured intensity I_{surf} by the measured intensity of the bulk phonon mode I_b. I_{surf}/I_b is now independent of all technical parameters since the same configuration is used. If the small energetic difference between $\omega_{s,s}$ and $\omega_{s,b}$ is neglected I_{surf}/I_b only depends on the Raman susceptibility of the bulk phonon S_b, Raman susceptibility the surface phonon S_{surf} and the scattering volume for surface and bulk phonon, since they are not the same. The scattering volume for the surface phonon is independent of ω_i since only the first atomic layers contribute while for the bulk phonons V_b is proportional to the penetration depth of the incident light $l_P(\omega_i)$. The penetration depth in the bulk material as well as S_b are usually well known. By analysing

$$\frac{I_{surf}}{I_b} \cdot S_b \cdot l_P(\omega_i) \sim S_{\mathrm{surf}} \tag{3.18}$$

a quantity can be calculated which is proportional to the desired Raman susceptibility of the surface modes S_{surf}. The change of this quantity with ω_i can now be directly related to the resonance of the surface phonon mode to transitions within the surface electronic band structure.

3.4.5 Determination of phonon line widths and phonon energies

The measured Raman shift was so far discussed as the phonon energy and the measured intensity was related to the Raman cross section which is in a simple model proportional to $|\partial\tilde{\varepsilon}/\partial\omega|^2$. Corrections to get reliable information of the intensities were also discussed already. For simple spectra with only one or two separate peaks the interpretation of Raman spectra is straight forward. The line shape of a phonon mode in Raman spectroscopy is Lorentzian in the ideal harmonic case. Due to the limited resolution of the measurement the measured peak is additionally broadened. The resulting line shape is therefore a convolution of Gaussian and Lorentzian but can be approximated by a Voigt profile[5].

If the spectra are more complicated, showing many phonon modes within a small spectral region, the peak position and intensity of individual modes can only be derived by a fitting procedure. As for any best fit procedure the number of parameters should be kept as small as possible. The Gaussian broadening is therefore kept constant for all peaks since it is caused by the setup itself.

The broadening of the setup itself can be determined either by a line shape analysis of very narrow emission lines, such as the laser line itself or by a fit of the strong bulk modes for each incident photon energy since the resolution of the setup is energy dependent. One test of the fit routine is the determination of the Lorentzian width of the bulk phonon. The result should be independent of the laser energy. Fixing the Gaussian width in this way, this leaves only the peak position, Lorentzian broadening and amplitude as free parameters for the other modes of interest. Particularly at low frequencies the background arising from elastic scattering has to be treated as well.

[5] $y(x) = y_0 + A\frac{2\ln 2}{\pi^{3/2}}\frac{w_L}{w_G}\int_{-\infty}^{\infty}\frac{e^{-t^2}}{\left(\sqrt{\ln 2}\frac{w_L}{w_G}\right)^2+\left(\sqrt{4\ln 2}\frac{x-x_c}{w_G}-t\right)^2}dt$

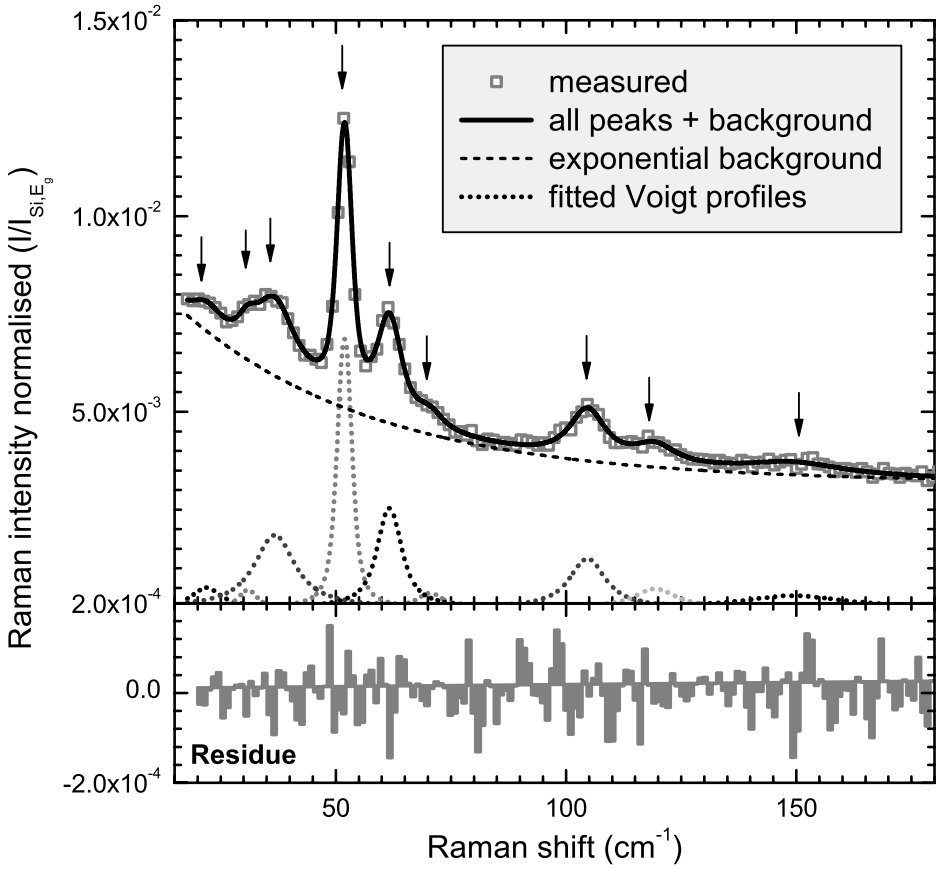

Figure 3.11: *Example fit of the Si(111)-In:(4×1) Raman spectra by 8 Voigt profiles and an exponential background. The residue (difference of measurement and fit) shows no remaining structure. The arrows indicate the peak positions.*

In Fig. 3.11 an example of such a fit is given for the Raman spectra of Si(111)-In:(4×1) taken with an incident laser energy of 1.93 eV and A' symmetry. It can be seen that if only phonon modes contribute to the spectrum such a peak analysis can reproduce the measured spectrum very well.

3.4.6 Second order Raman scattering

If the Taylor expansion of the susceptibility is extended beyond the first order, several other details seen in Raman spectra can be understood. This involves first order forbidden processes, where phonon modes which are disallowed by the selection rules can be seen due to the presence of electric fields at the surface or for instance two phonon processes. The latter need to be discussed in more detail, since two phonon scattering at acoustical phonons occurs in the same energy region where surface phonon modes are expected. In first order scattering acoustical phonon modes cannot be seen, since the maximum momentum transfer of light in the visible energy range is small compared to the inverse lattice constant $1/a_0$. Therefore only

phonons around the Γ-point of the Brillouin zone can be measured. The energy of acoustical phonons approaches zero at Γ and cannot be measured with Raman spectroscopy. For a scattering process with for instance two acoustical phonons with momentum around k and $-k$ the sum of the momentum is again close to zero and can therefore be provided by an incident photon. This two phonon scattering leads to broad structures in the Raman spectra with line shapes following the density of states of the acoustical or optical phonons [125]. For example in silicon two phonon scattering with acoustical phonons leads to a structure between 200 and 450 cm^{-1} as shown in the measurement in Fig. 3.10.

If surface phonons exist in the same energy region energy transfer between bulk acoustical phonon modes and the surface mode are possible. Although such a mode can be localised at the surface it will resonantly introduce vibrations within the bulk. Such modes are therefore called surface resonances. Since an adsorbate can also increase the scattering intensity of bulk phonons by introducing roughness or an electric field, it is not easy to attribute structures in the region of the two phonon bulk scattering to microscopic surface modes. This can only be safely done in regions where bulk phonons do not exist. For some III-V semiconductors such as InP for instance, surface modes were found above twice the highest acoustical phonon energy and below the lowest optical mode – within the so called phonon gap. For silicon there is no such phonon gap. Consequently adsorbate induced phonons can only be assigned to microscopic modes in regions with vanishing second order scattering, here below 200 cm^{-1}.

3.4.7 Size effects

The last point I want to address here is the so called size effect. If the volume of a scatterer is decreased, for instance in reducing the average crystal size of micro-crystalline samples or more relevant here, in reducing the width of wires, changes in the measured phonon frequencies are expected. In the microscopic model of Raman scattering the effect can be easily understood. If the phonon is localised within a crystallite of the dimension L the localisation of the wave function in space leads to a broadening of the wavefunction in momentum. The modified wave function of the phonon can be treated as a superposition of wave functions with different wave vectors $\mathbf{q}$. Therefore a contribution of areas of the Brillouin zone with $|\mathbf{q}| \neq 0$ (Γ-point) exist. Depending on the phonon dispersion around the Γ-point several possibilities exist. For a minimum at the Γ-point a blue shift of the phonon frequency accompanied with a broadening is expected – for a maximum a broadening and red shift. Details of this model are described by Andrzejak [126]. It was shown that in the case of Si with an average crystallite dimension of 100 Å Raman frequency shifts by about 1-2 cm^{-1} can be observed (the actual shift depends also on the shape of the crystallites). In the case of nanowires such size effects were already found in semiconducting nanowires or nanoparticles of ZnO, GaN, graphite or Si [127–130]. Of course other effects such as smearing of the $\mathbf{q}$ vectors due to disordering, can have a similar effect [131].

3.4.8 Raman spectroscopy on metallic nanowires

To summarise this section I would like to list the properties of metallic nanowires which can be, in principle, measured with Raman spectroscopy. For larger wires these are mostly shifts in the bulk phonon frequency of the metal due to size effects. For the smallest wires new modes, which are related to the individual atomic geometry of the metal atoms, can occur. Changes in the phonon frequencies of such modes will lead to information about changes within the atomic arrangement upon the wire formation or at possible metal-insulator transitions. The analysis of Raman resonances in this case will additionally provide information about the electronic structure of the wire. As we will see in chapter 5 the latter two aspects are important in the understanding of structures where electron phonon coupling is strong.

3.5 First principle calculations

All calculations predicting properties of one-dimensional structures discussed in this chapter as well as in chapter 2 used simple models, in order to enable analytical solutions. On the other hand the models based on effective media approximation discussed in this chapter used measured bulk properties. For a comparison with measured samples both approaches are valuable in discussing possible effects on optical spectra. For a qualitative comparison only the latter approach gives reasonable agreement, but only for larger wire structures. It is therefore highly desirable to have parameter free calculations of smaller wire structures, preferably located at surfaces.

To some extent this can be done by *ab-initio* calculations based on density functional theory (DFT). For bulk materials or small molecules this technique has long been used to calculate not only the atomic structure but also band structures, vibrational properties and optical transitions. With today's computers more complex structures such as surfaces can be studied. Although wires with widths of the order of nm cannot be treated yet. The method works well for structures which can be approximated by a periodic continuation of a smaller unit cell. Since comparison to such calculations is a major point of the discussion of indium wires on silicon in chapter 5 and caesium wires on GaAs in chapter 6, a short summary of the possibilities of DFT calculations will be given here.

Structure

DFT dates back to the work of Hohenberg, Kohn and Sham [132, 133] and aims to determine the ground state of a many-body system in an effective independent particle picture. Starting with a many electron Hamiltonian one treats the kinetic energy, the Coulomb interaction of electrons and nuclei as external potential but replaces the interaction of individual electrons by the interaction of a single electron with the field generated by the total electron density of all other electrons in the system $n(\mathbf{r})$. Finally one includes an effective exchange and correlation potential $V_{XC}(\mathbf{r})$ treating the many body interactions. Although in this formulation the solution would be exact, it does not help for the calculation of real systems since $V_{XC}(\mathbf{r})$ itself is not known. In practise the exchange and correlation potential needs to

be approximated. Such an approximation is the local density approximation (LDA), where V_{XC} is assumed to be a function of the electron density $n(\mathbf{r})$ itself. Alternatively the generalised gradient approximation (GGA) is used, where V_{XC} depends on $n(\mathbf{r})$ and its gradient $\nabla n(\mathbf{r})$.

For structural calculations the model of a certain material is formulated using a set of electron wavefunctions $\psi(\mathbf{r})$. The core region is usually replaced by a pseudopotential simulating the positive nuclei screened by core electrons not considered in the calculation. Bulk materials can be calculated by using periodic continuations of a unit cell leading to periodic Bloch wavefunctions. Surfaces can be calculated by using the same procedure but replacing the unit cell by so called slabs which include the surface unit cell but also several layers of bulk layers below and vacuum layers above. These slabs are then again periodically continued. The total energy of a many electron system defined this way can then be calculated. In an iterative scheme the atom positions are modified until the total energy is minimised. If the found minimised total energy of different structural models is compared, the one with the lowest total energy is the most energetically favoured model. More details of this procedure can be found for instance in [134] and for each calculated system discussed here in later chapters. The atomic positions determined by this procedure can be compared directly to measurements.

Band structure

If the structural model is found, the band structure is calculated and compared to measurements, usually angle resolved photo emission (ARPES) and inverse photo emission. A common problem of all DFT-LDA or DFT-GGA based calculations is that the electronic gaps are underestimated. This is an artefact since DFT is a ground state theory, while in ARPES excited states (one electron removed) are measured. In a simple approach the calculated gaps are opened with the so called scissors operator, moving all empty states rigidly to higher energies to match the experiments.

A more accurate way as to how calculations can be corrected is the so called GW scheme. The name arises since the self energy of the excited state is determined using a Greens function method and the screened Coulomb potential W [135]. The GW term is just the first term in an expansion of the self energy with respect to the screened Coulomb potential. Hedin [135] already treated higher terms. The GW correction is rather time consuming but necessary to correctly describe gap positions. In rare cases uncorrected DFT-LDA calculations can even calculate a metallic ground state even though none is found in measurements. Examples are low bandgap semiconductors such as InAs, InSb and GaSb DFT-LDA calculates metallic ground states in clear contrast to measurements. By applying GW corrections this discrepancy is usually overcome [136, 137]. In a few cases such as the C(111)-(2×1) surface even the GW correction does not work and more sophisticated iterative GW schemes have to be used [138]. This problem is most troublesome in the discussion of the Si(111)-(4×1) surface and its low temperature (8×2) phase described in chapter 5. In this particular system the low temperature phase is experimentally found to be insulating, but DFT-GGA calculations based on the experimentally found structural model give a metallic ground state. It is unclear whether this is just an artefact of the gap problem or whether a charge density wave driven by a Peierls transition is responsible for

the insulating state. In the latter case DFT cannot describe the surface since electron-phonon interaction, which leads to the gap opening is not treated in the calculation.

Optical spectra

Optical spectra are calculated by evaluating the dielectric tensor components by summation of all possible optical transitions in the calculated bands [139]. Again the gap problem leads to an underestimation of the transition energies. Hence calculated optical spectra such as the dielectric function itself or RAS spectra are red shifted compared to measurements. By using the scissors operator this can be partly corrected. Preferably GW corrections should be done since only then relative energetic positions of structures can be properly reproduced. Although the GW corrections improve the agreement considerably, relative intensities of structures are usually not exactly reproduced.

A problem is that so called excitonic effects are not considered, which are critical for optical excitations since the electron is not removed as in ARPES but remains at an excited state within the material. Hence the electron-hole interaction needs to be treated.

In recent calculation further many-body corrections are applied by using higher terms in the expansion of the self energy given by Hedin [135]. Details of this procedure and also other recent developments to treat the many-body interactions in *ab-initio* calculated optical spectra can be found in [140, 141]

Phonons

Once the minimum energy structure is calculated within DFT-LDA, vibrational properties – the phonon modes can also be calculated. The common method for this is the frozen phonon approach [142, 143]. The structure is treated as a system of coupled harmonic oscillators with the atomic mass for each atom and force constants derived by the following procedure. The individual atoms in the calculated structure are displaced, the forces can be calculated driving it into the minimum position. In order to evaluate phonon modes each atom in the structure is displaced in each Cartesian direction and the corresponding force constant is calculated. With this the dynamical matrix is created and by diagonalisation and solving of the eigenvalue problem. The resulting eigenvalues correspond to the frequency of a phonon and the Eigenvectors give the displacement pattern of a phonon.

This scheme was successfully applied to bulk phonons [143, 144] and also for microscopic surface phonons of clean III-V(110), Sb/GaAs(110) or Si(111) surfaces [145–147].

4. Anisotropic optical conductance

In this chapter RAS measurements of systems showing an anisotropic conductance will be discussed in more detail. Measurements of the anisotropic conductance of several structured metal systems exist already. The scale ranges from very small systems like the four atom wide indium chains on silicon [148, 149] to large anisotropic silver islands on vicinal silicon [150]. There is also a wide range of organic one-dimensional conductors [50], the bulk anisotropy of high temperature superconductors, where also optical measurements have been performed [151, 152]. Another system, where 1D conductance was observed, are carbon nanotubes [32, 153]. For the latter two cases optical measurements of the anisotropy are rarely done, since the orientation of the crystallites or tubes is difficult.

In chapter 2 nanowires, grown on semiconductor surfaces by self organisation were introduced. Such highly anisotropic assemblies of bulk metals such as indium, tin or lead will be discussed in this chapter. The bulk dielectric function of these metals is dominated by the response of free electrons and explained in terms of Drude dielectric functions (see section 3.1.2). In what way the measured optical anisotropy of the nanowires also arises from such free carriers is the main subject of this chapter.

All structures investigated, were prepared by deposition of the metal on to clean surfaces in ultra high vacuum (UHV). Nevertheless the size and morphology of the resulting structures can be quite different. In the case of the indium wires on Si(111) (Fig. 4.1c) the structure consists of a double chain of indium atoms, separated by a

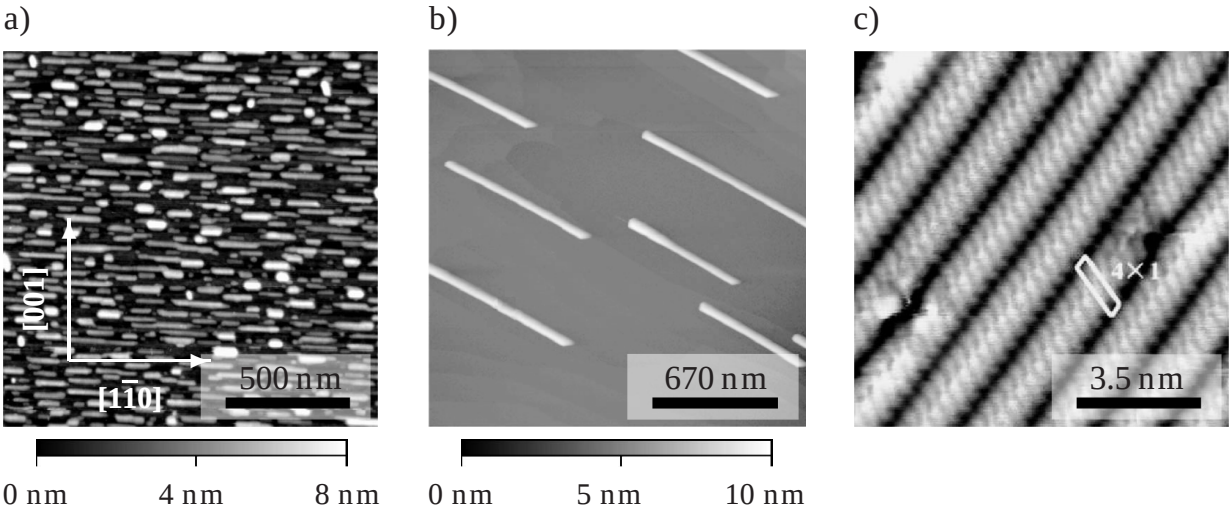

Figure 4.1: *Examples for the different wire geometries discussed: a) Tin islands on InAs(110) (AFM image of a 20 ML thick tin layer). b) Lead wires on Si(335). (STM image of 3 ML lead, taken from [31]). c) Indium wires on Si(111) ((4×1) reconstructed surface at ≈ 0.75 ML, taken from [47]).*

silicon zig-zag chain. The length of this structure is only limited by the quality of the silicon substrate and can be larger than several μm– the width of an individual chain is only about 0.8 nm.

More isolated wires occur for lead adsorption on the Si(335) surface. The wires are as high as wide and can be several μm long. In Fig. 4.1b an example for 3 ML coverage is shown. The width and height in this case is about 10 nm.

Dense arrays of nanowires occur for tin adsorption on InAs(110) (Fig. 4.1a). At higher coverages large anisotropic islands occur. But in particular, the smaller coverages are interesting in terms of the discussion of metallic nanowires, since then the islands are only about 25 nm wide but up to 400 nm long.

The three different systems are only a small selection of known metallic nanowires, though they represent all principle structures such as dense wire arrangements, isolated wires and anisotropic islands.

4.1 Tin on InAs(110)

Tin adsorption on III-V(110) surfaces has been previously studied, though with different points of interest. Tin occurs in two phases: the metallic phase (white tin or β-tin) and the semiconducting phase (grey tin, α-tin), which is only stable at temperatures below 13°C. The latter has a bandgap of almost zero and previous studies focused on stabilisation of this phase by choice of substrates, namely InSb. In these studies it was already noted that on InAs(110) the metallic phase occurs and elongated islands were observed [154, 155].

In Fig. 4.2 the morphology of two different samples is shown, one of 20 ML nominal thickness and one of 100 ML. It can be clearly seen that for the higher

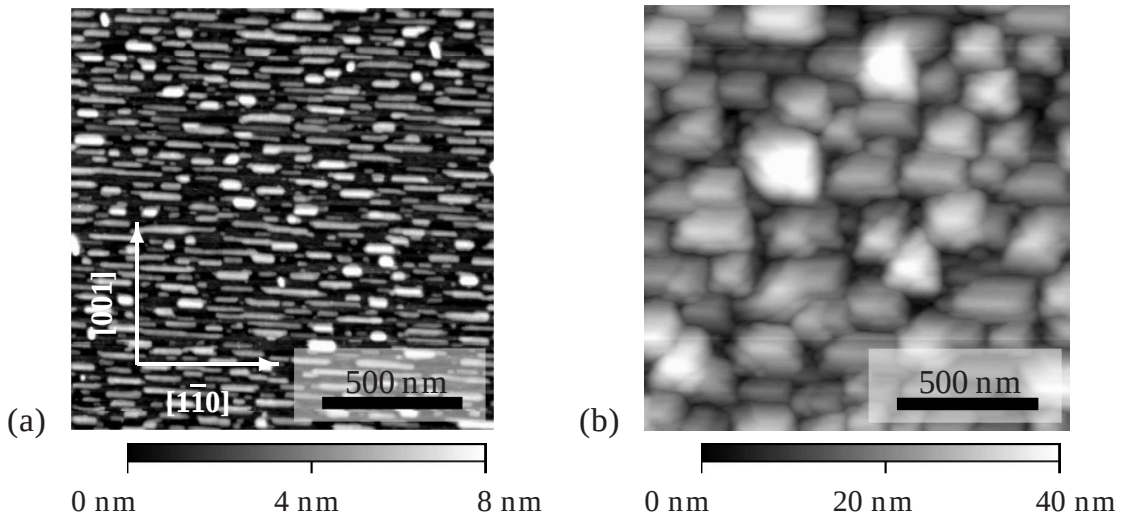

Figure 4.2: *AFM images of two different Sn coverages on InAs(110). a) shows a sample with 20 ML while b) shows one width 100 ML. For smaller coverages the tin islands are highly anisotropic with a long axis of up to 400 nm and a short one of only 25 nm. At higher coverages the islands are larger but less anisotropic (400 nm long, 100 nm wide).*

coverage the Sn islands are less anisotropic. The ratio between longer and shorter baseline was up to 20 for a 20 ML thick sample but only up to 2.5 for a 100 ML thick sample.

Thicker tin layers

Studies at high coverages (>20 ML) with Raman spectroscopy showed that those islands consist of the tetragonal β-tin, hence the metallic phase. For 20 ML thick samples the β-Sn bulk phonon was found 4 cm^{-1} above the reported bulk value of 42.4 cm^{-1}. At 100 ML it was still found 2 cm^{-1} above that value. The larger shift for the low coverages can be explained by size effects (see 3.4.7). The deviation from bulk values for larger coverages is most likely caused by strain within the islands. The orientation of the island could not been derived from measurements performed so far [155]. The size anisotropy of the large islands (see Fig. 4.2) suggests that the islands are oriented with different crystal axes along x and y. RAS spectra in this coverage region should therefore be dominated by the anisotropic bulk response of β-tin. In Fig. 4.3 RAS spectra of samples with 40 ML to 60 ML coverage are shown. It can be seen that the measured optical anisotropy can be explained by the bulk anisotropy only. In particular structures around the bulk interband transitions around 1 eV and 3 eV dominate the spectra in the infrared, while the free electron like response (see page 46 for details) gets smaller with increasing coverage.

Unfortunately the only available bulk dielectric function for β-tin was derived from randomly oriented crystallites of the material giving only an average of the dielectric tensor components of the anisotropic bulk material [156]. Since measurements of the dielectric tensor components were not available a simple model was applied to derive an approximation of the bulk anisotropy: $\tilde{\varepsilon}_{xx}$ was assumed to follow the published mean dielectric function of MacRae and Arakawa [156]. For $\tilde{\varepsilon}_{yy}$ the same function was shifted by 20 meV towards higher energies and additionally Gaussian broadened by 100 meV. The inset in Fig. 4.3 shows the expected bulk response (dotted line) and the response of a 5 nm thick β-tin layer on InAs. The measured spectra of the 60 ML thick layer can, in principle, be explained by a linear combination of both. In particular, the minimum structure around 1 eV is nicely reproduced by the anisotropic overlayer model. The width of the structures in the model RAS spectra is too broad, caused by the inherent broadening of the available data for $\tilde{\varepsilon}_{xx}$ (mixture of all components) and $\tilde{\varepsilon}_{yy}$ (mixture of all components + artificial broadening).

The third curve (dashed) shows the results of the bulk metal approximation, where the anisotropic layer is treated with the bulk dielectric function in x and vacuum in y. The RAS line shape of the thickest layer can be even better reproduced by this model, though the thickness used in this simulation is unreasonably small (here 0.25 nm vs. 8 nm real mean island height at 60 ML). Therefore further calculations were performed using better suited anisotropic effective media approximations as described in 3.3.2. Although the thickness derived from these calculations is closer to the AFM value and also the best agreement in line shape was achieved by the Bruggeman model with ellipsoid inclusions, no new insight can be gained by these models. That the structures around 1 and 3 eV arise from bulk like properties of the tin islands can already be seen in the bulk metal approximation and in this case the thickness of the layer was already known. Most problematic is the bulk dielectric

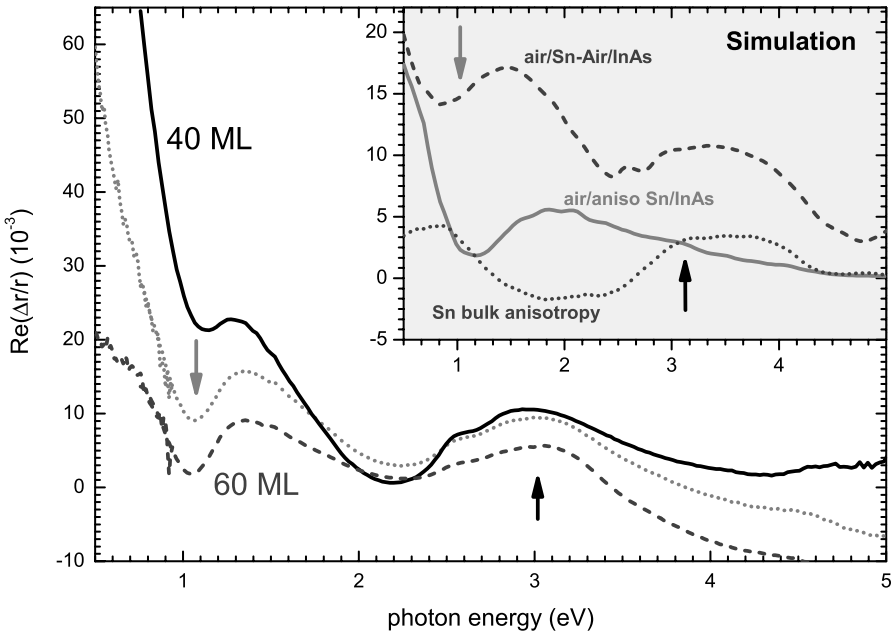

Figure 4.3: *RAS spectra of 40, 50 and 60 ML Sn on InAs(110). The anisotropy arises mainly from the bulk optical anisotropy of β-Sn (arrows). The inset shows calculations of the RAS with different models (*solid: *anisotropic Sn on InAs;* dotted: *Sn bulk anisotropy;* dashed: *bulk metal approximation). In all cases agreement can be found for thick samples, where the anisotropy in the free electron properties is small.*

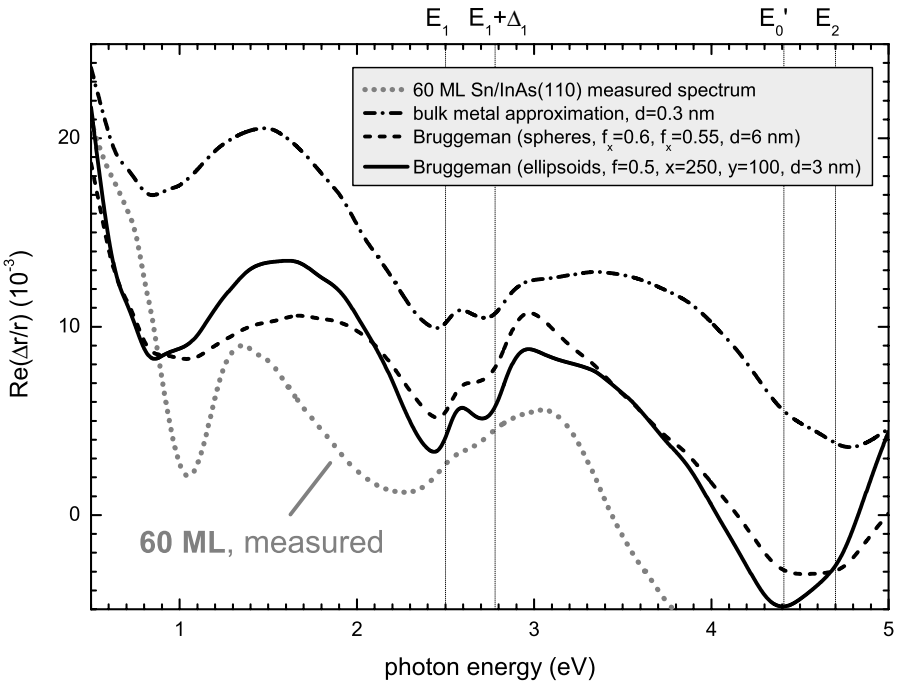

Figure 4.4: *Comparison of the RAS spectra of a 60 ML thick tin layer on InAs(110) with several models using anisotropic effective media approximations. For the two Bruggeman models the curve was lowered by 15 RAS units for better comparison with the measurement.*

function which had to be used in all these models, since $\tilde{\varepsilon}$ was already broadened by the measurement of arbitrarily oriented crystals. If the full dielectric tensor could be used the agreement should be much better. A similar analysis with the real dielectric function will therefore also show sharper anisotropies. The energy region above 3.5 eV can also not be explained with the three layer calculation since the island size is already of the order of the UV wavelength and additional strong anisotropies arise from Mie-resonances. They become much more important for even thicker layers. In a similar case of In islands on GaAs where Mie-resonance occur as well this strong anisotropy was already successfully simulated [157].

Initial growth

At low coverages (<5 ML) the tin layer consists not of the metallic phase, but at least partly of the semiconducting grey tin. One therefore expects only a quenching of the RAS spectra of the clean InAs(110) surface and a small anisotropy due to a possible interface anisotropy or strain in the substrate or in the pseudomorphic α-tin layer. Figure 4.5 shows the RAS spectra in that coverage region. The origin of the RAS of the clean spectra will be discussed in more detail for caesium wires on the same surface in chapter 6. For the moment it is enough to say that the structures of the clean surface are quenched upon tin adsorption. Although there is a considerable anisotropy in the region of 1.2 eV for 1 and 2 ML, an increase in the infrared was not found for such low coverages – consistent with an overlayer of the semiconducting α-tin. Above 4 ML this behaviour changes and an infrared anisotropy occurs.

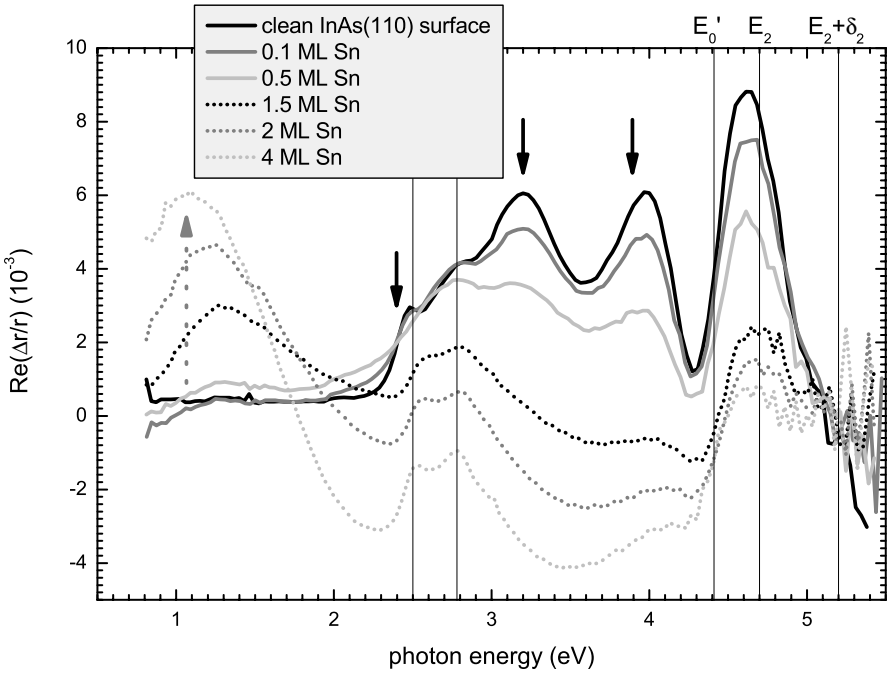

Figure 4.5: *RAS of initial tin growth on InAs (0-4 ML). The anisotropy of the clean InAs(110) surface (black arrows) is reduced, though structures remain at the bulk critical points of InAs (thin lines). In the infrared an anisotropy arises for the growing tin film (dotted arrow).*

Infrared anisotropy and the free electron model

As already seen in Fig. 4.2 the most interesting region for a possible conductance anisotropy of the Sn films on InAs is the region between 5 ML and 30 ML, where strongly anisotropic islands (up to 400 nm long, 25 nm wide) occur. Figure 4.6 shows RAS spectra in this coverage region. The most dominant structure is the anisotropy in the infrared. It evolves for coverages above 5 ML and is strongest at around 25 ML. Initially the rise of the RAS into the infrared is structureless and well described by an anisotropy in the mean free path and plasma frequency of the quasi-free electrons. Above 15 ML an additional contribution arises from the bulk anisotropy of β-Sn as already discussed for thicker layers. The calculated spectra in the inset of Fig. 4.6 agree not only the IR regime but in the region of the InAs bulk critical points as well. In Fig. 4.7 this will become even more clear. By calculating the surface dielectric anisotropy (SDA) the influence of the substrate can be removed from the RAS spectrum. The SDA for the coverages above 7 ML clearly shows the line shape expected for the Drude RAS-model. Figure 4.7 directly compares the SDA with line shapes calculated with two Drude dielectric function for x and y. A problem for such fits is the large number of free parameters for each individual spectrum, since the thickness of the layer d, the plasma frequencies $\omega_{p,x}$ and $\omega_{p,y}$, the scattering frequencies $\omega_{\tau,x}$ and $\omega_{\tau,y}$ and ε_∞ need to be determined. With 6 free parameters there are too many to give reliable values for all of them since the system is mathematically over-defined. To reduce the number of fit parameters ε_∞ was set to 1 for all fits and

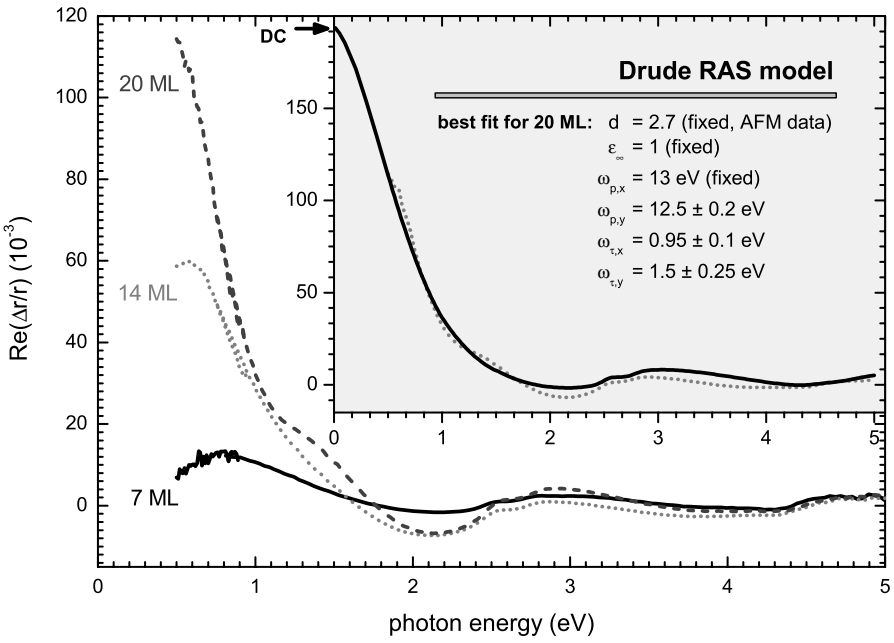

Figure 4.6: *In the coverage region above 5 ML the reflectance anisotropy of tin islands on InAs(110) is dominated by a strong infrared structure. The strongest anisotropy was found for a coverage of 25 ML. The inset shows the comparison to the Drude RAS-model. In contrast to the spectra of thicker layers the agreement with the measured data is very good.*

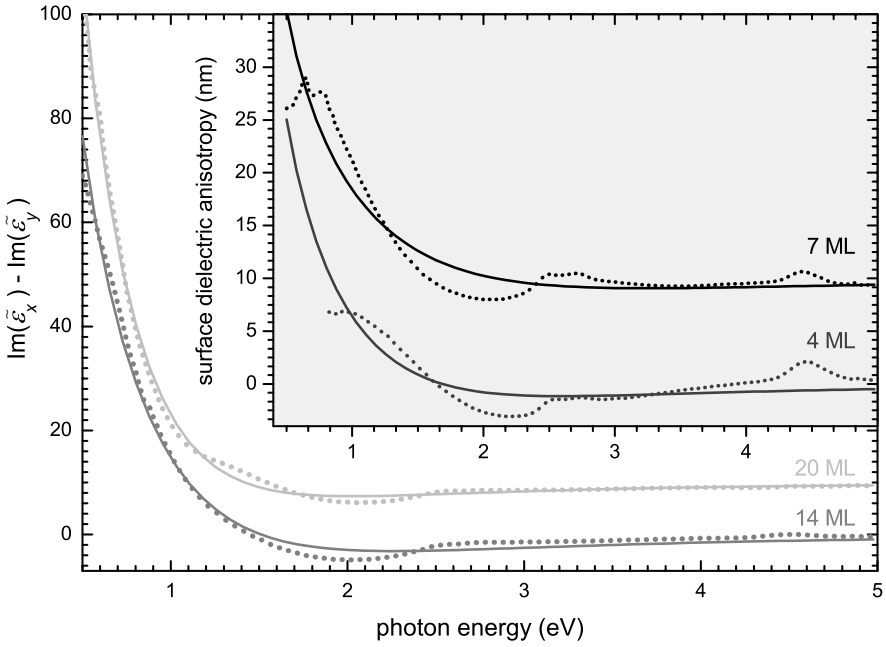

Figure 4.7: *The surface dielectric anisotropy (SDA) is calculated for various coverages (dotted curves). In the case of 20 and 14 ML the SDA was divided by the thickness of the layer and the spectra were stacked for better visibility. The solid lines show best fit calculated SDAs if they arise only from an anisotropy in the free electron properties. The values from these fits are given in Table 4.1. The Drude RAS model works well for layers well above the critical thickness of 5 ML.*

$\omega_{p,x}$ was set to the known bulk plasma frequency of 13 eV [156]. The thickness d can be derived from the islands' mean height, since the morphology for certain coverages was measured *ex-situ* with AFM. This leaves only three free parameters – few enough to derive mathematically sound fits. In the range from 7 to 40 ML, reasonably good and for 14 ML and 20 ML, very good agreement can be achieved. In Table 4.1 the derived parameters are given. One has to stress the point that in particular the absolute values for ω_p cannot be taken too seriously since $\omega_{p,x}$ was always kept constant. Nevertheless it can be seen that the anisotropy mostly originates in the anisotropy of the scattering frequency ω_τ and not in differences of ω_p. The ratio of 0.6 for $\omega_{\tau,x}/\omega_{\tau,y}$ shows that the mean free path of electrons differs by almost a factor of two between the two perpendicular axes. Furthermore the scattering frequency decreases for increasing layer thickness or island size, while the plasma frequency decreases. It remains to be seen if the same can be shown for the DC conductance of such films, which have not yet been performed. What can be done though, is the interpolation of the measured RAS spectra to zero frequencies as well as the calculation of the zero frequency response from the fitted Drude parameters. For NIR measurements of the dielectric function it is already known that an extrapolation of optical conductance measurements towards $\omega = 0$ can give comparable results to real DC measurements [106]. The fact that the interpolation of the measured RAS to $\omega = 0$ leads to different DC values can be also understood. It was already shown with EMA of metallic

	4 ML	7 ML	14 ML	20 ML	40 ML
fixed d	0.55 nm	0.95 nm	1.9 nm	2.7 nm	5.4 nm
fixed ε_∞	1	1	1	1	1
fixed $\omega_{p,x}$	13 eV	13 eV	13 eV	13 eV	13 eV
$\omega_{p,y}$	13.5±0.3 eV	13.4±0.2 eV	13.3±0.2 eV	12.5±0.1 eV	12.1±0.1 eV
$\omega_{\tau,x}$	1.7±0.2 eV	2.25±0.2 eV	1.3±0.1 eV	0.9±0.1 eV	0.6±0.05 eV
$\omega_{\tau,y}$	2.5±0.3 eV	3.0±0.3 eV	2.1±0.1 eV	1.5±0.05 eV	0.76±0.05 eV
$\omega_{p,x}/\omega_{p,y}$	0.96	0.97	0.98	1.04	1.08
$\omega_{\tau,x}/\omega_{\tau,y}$	0.67	0.75	0.60	0.63	0.78
$\Delta r/r\|_{\mathrm{DC,calc}}$	0.015	0.02	0.1	0.19	0.06
$\Delta r/r\|_{\mathrm{DC,meas}}$	0	0	0.05	0.13	0.08
$\mathrm{Re}(\Delta\sigma\|_{\mathrm{DC}})$	0.2±0.1 S	0.5±0.1 S	5±1 S	13±3 S	8±2 S

Table 4.1: *Free electron parameters derived by fitting the SDA for various coverages of Sn on InAs(110). Parameters which were kept fixed are marked. For 40 ML the region from 1 to 1.5 eV was excluded from the fit because of the strong influence of interband transition in this regime. The last values given are the RAS signal linearly interpolated to $\omega = 0$ ($\Delta r/r|_{\mathrm{DC,meas}}$) and the calculated value for $\omega = 0$ from the given Drude parameters ($\Delta r/r|_{\mathrm{DC,calc}}$). With (3.8) the expected DC conductance difference between the two axes was calculated for the Drude model only.*

inclusions in an insulating environment that below a certain percolation threshold where the first completely connected path through the metal inclusion occurs, the reflectivity can decrease again although the higher frequency range follows a Drude like function [158]. A similar reason can be responsible for the apparent decrease of RAS for $\omega \to 0$ at coverages below 15 ML. Since DC conductance measurements were not available, these interpolations remain somewhat speculative. If they can be confirmed, RAS can be used as a contactless probe of the conductance of nanowire assemblies. To be more accurate RAS can probe the difference in conductance of two perpendicular directions – absolute values cannot be gained.

So far it was shown that for the dense layer of anisotropic islands the RAS spectra can be used to determine anisotropies in the free electron like response as proposed in section 3.3.3. In the next section the same model will be tested for isolated anisotropic metal islands.

4.2 Lead on Si(335)

Another system with anisotropic islands, but where the term nanowires can be much better applied are lead wires on Si(335) surfaces. According to a study by Stròżak et al. Pb forms highly anisotropic islands with ratios of length to width of more than 60. Although this system was not yet measured by RAS, surface difference spectra (SDR) are available, where absolute changes in the reflectivity upon Pb adsorption were

measured for two perpendicular polarisations [31]. From these data one can calculate RAS spectra, assuming the surface before adsorption of Pb is isotropic: $R_{Si,x} = R_{Si,y}$. For silicon this should, at least, be the case in the IR energy region of interest. With the known SDR values for the two polarisations along and perpendicular to the wires

$$\left.\frac{\Delta R}{R}\right|_{SDR,x} = \frac{R_{Si+Pb,x} - R_{Si,x}}{R_{Si,x}} =: SDR_x \tag{4.1}$$

$$\left.\frac{\Delta R}{R}\right|_{SDR,y} = \frac{R_{Si+Pb,y} - R_{Si,y}}{R_{Si,y}} =: SDR_y \tag{4.2}$$

$$\Rightarrow R_{Si+Pb,x} = (SDR_x + 1)R_{Si,x}, \quad \text{and} \quad R_{Si+Pb,y} = (SDR_y + 1)R_{Si,y} \tag{4.3}$$

the RAS can be calculated:

$$2\mathrm{Re}\left(\frac{\Delta r}{r}\right) \approx \left.\frac{\Delta R}{R}\right|_{RAS} = 2\frac{R_{Si+Pb,x} - R_{Si+Pb,y}}{R_{Si+Pb,x} + R_{Si+Pb,y}} = 2\frac{SDR_x - SDR_y}{SDR_x + SDR_y} \tag{4.4}$$

In Fig. 4.8 the results of this calculation are shown for different Pb coverages on Si(335). Since data are only available for a few energies, range and resolution are both very poor compared to direct RAS measurements. However the general line shape of the spectra can already be seen. Again the spectra are dominated by a strong

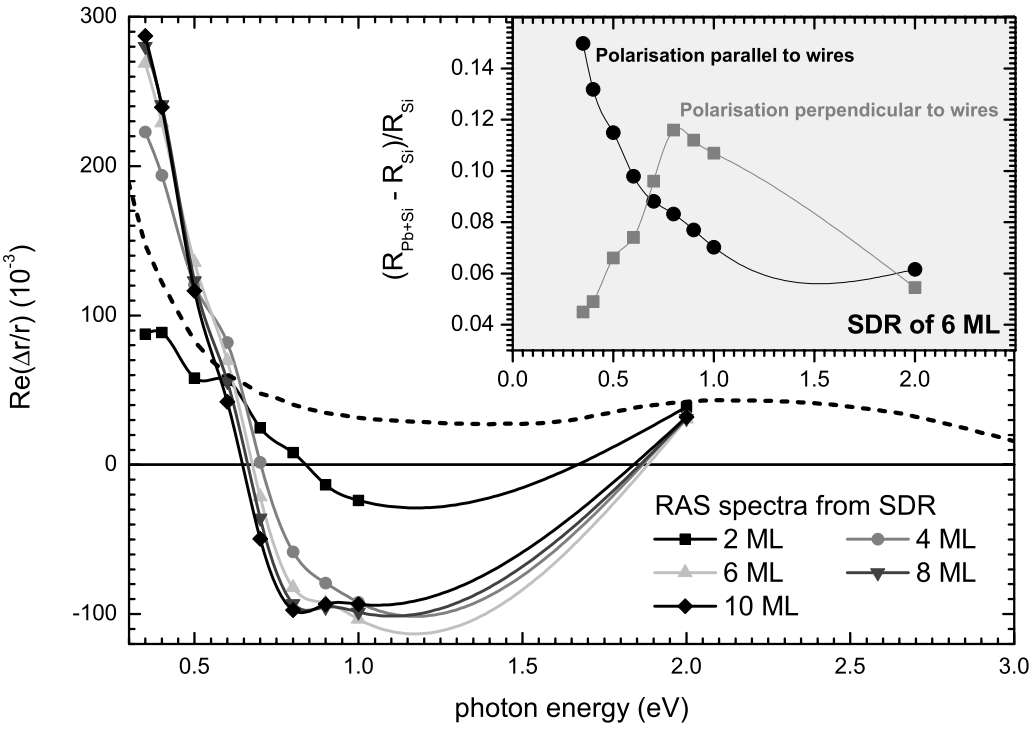

Figure 4.8: *RAS spectra of Pb on Si(335) calculated from SDR values of Stròżak et al. with (4.4). The inset shows the original SDR data for light polarisation along and perpendicular to the long wire axis. The increase of reflectivity is larger for light polarised along the wire axis. The dashed curve shows a calculation using the bulk metal approximation.*

infrared anisotropy comparable to the signals of tin islands on InAs. The RAS spectra show a rather large negative signal in the energy range above 0.7 eV, which means that the reflectivity perpendicular to the long axis of the lead wires is higher that the one along the wire. Such behaviour is expected for an anisotropy in the scattering frequencies (see Fig. 3.8) and was already seen for the tin islands on InAs (see Fig. 4.6 and 4.7). Still, the amplitude of almost -100 RAS units is surprisingly large. The other puzzling fact is that the RAS amplitudes seem to saturate above 8 ML, which means that the increase in length, height or amount of islands does not affect the effective optical anisotropy of the sample. Unfortunately data for coverages above 12 ML were not available. It would be interesting to see whether at higher coverages the IR anisotropy will decrease again similar to the behaviour of the Sn/InAs(110) system.

In Fig. 4.9 the surface dielectric anisotropy of 6 ML Pb on Si(335) is calculated from the RAS spectra of Fig. 4.8 and compared with a fit in the Drude RAS model. Again the general line shape can be reproduced. Since only a small number of points were available and the energy range of the data is limited a meaningful best fit of all

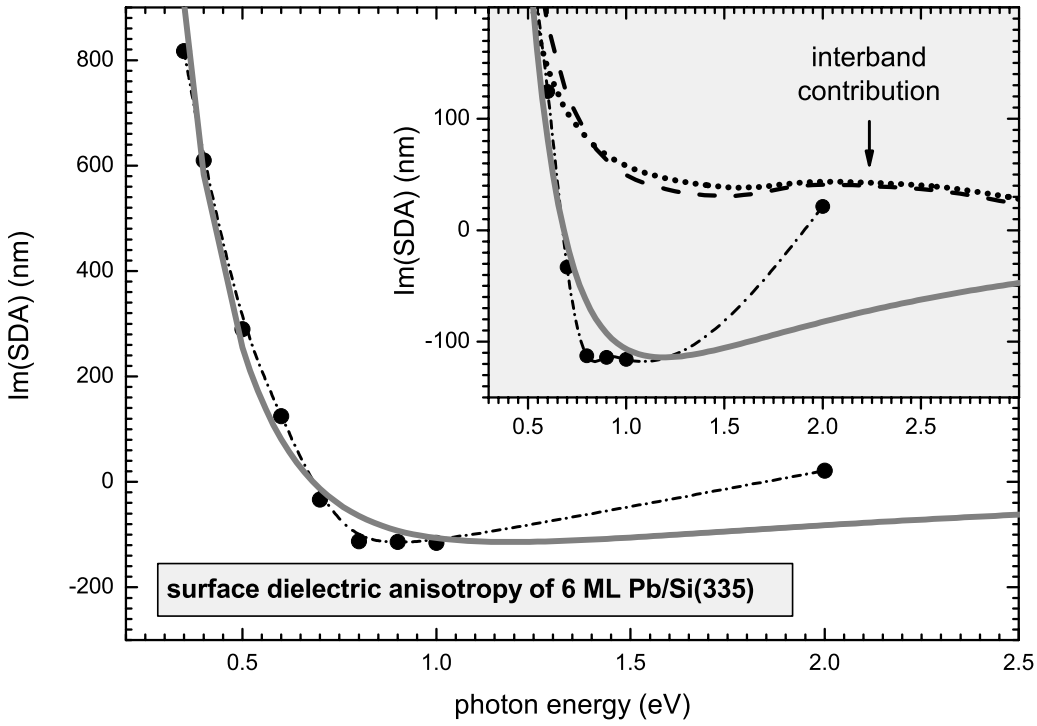

Figure 4.9: *Calculation of the surface dielectric anisotropy for the spectra of 6 ML Pb on Si(335). The dotted grey curve show a calculation using the model of the anisotropic free electron gas. In the inset the measurements are compared with two simulations using the bulk metal approximation (dotted curve) and Bruggeman EMA with ellipsoids (dashed curve, $f = 0.3, x = 100\,nm, y = 10\,nm, d = 5\,nm$). For comparison the anisotropic Drude fit is also shown ($\omega_{p,x} = 12\,eV$, $\omega_{p,y} = 20\,eV$, $\omega_{\tau,x} = 0.4\,eV$, $\omega_{\tau,y} = 4\,eV$, $d = 2.5\,nm$, $\varepsilon_\infty = 1$)*

free parameters ($\omega_{p,x}$, $\omega_{p,y}$, $\omega_{\tau,x}$, $\omega_{\tau,y}$, d and ε_∞) is not possible. As one could already see for the system Sn/InAs(110) the RAS spectra in the visible range is influenced by anisotropic interband transitions and deviations from the "Drude-like" line shape occur. If the energy range of the fits is limited and the number of points rather small, the influence of these interband transitions is too large for reliable fits. The simple bulk metal approximation shows, apart from the free electron contribution, an anisotropy arising from Pb interband transitions above 2 eV. Another problem can be the assumption inherent in the RAS calculation that there is no reflectance difference of the clean Si(335) surface. The data point at 2 eV is already much closer to the first bulk critical point of silicon (3.4 eV) where an anisotropy can be observed, for instance in the case of the Si(110) surface. The Si(111) surface however is isotropic. Since Si(335) samples were not available for this study the origin the positive RAS value for 2 eV remains unresolved.

An additional problem can arise from inherent anisotropies of the optical view ports. For instance the strong RAS signal at 2 eV (about 40 RAS units) is almost constant for all coverages and too large for a real anisotropies of the Si(335) surface. It is therefore probable that this signal arises from an anisotropy of the optical view port. For the RAS measurements this influence is minimised by the use of special strain reduced view ports. For the SDR studies no information concerning the effects of window strain was given in [31].

Although no explicit fitting of the parameters for the free electron gas could be performed, the analysis of the literature data of the optical anisotropy of isolated Pb wires on Si(335) again shows that the general line shape can be described by an anisotropy of the free electron gas. Any models based on anisotropic effective media approximations using the bulk properties of Pb cannot explain the negative RAS signal between 0.75 eV and $\sim$ 1.8 eV (see inset in Fig. 4.9). The model of the anisotropic electron gas can do this, assuming a strong anisotropy in the scattering frequency ω_τ. Again the absolute values of the free electron parameters cannot be extracted from RAS measurements alone. In the case of the lead wires it can be only mentioned that the crossing from positive to large negative RAS values can only be explained if the ratio $\omega_{p,x}/\omega_{p,y}$ is larger than 1.5 and the ratio $\omega_{\tau,x}/\omega_{\tau,y}$ is larger than 5. Furthermore fits for $\omega_{p,x} < 9$ eV cannot reproduce the line shape. This signifies that the DC anisotropy of this system should also be larger than the one of the tin islands on InAs(110), where the differences in ω_p as well as ω_τ are much smaller. A similar calculation for $\omega = 0$ with the parameters of the function shown in Fig. 4.9 results in a DC $\Delta r/r$ value of 0.6 which is three times larger than the anisotropy found in the Sn/InAs(110) system. The large value of ω_p in comparison with bulk values for lead of around 6 eV can be explained by confinement effects in the small structures [105, 159]. Due to the previously mentioned problems in the fitting process itself and since the preparation of the structures was not possible in our lab, a more detailed study of this point could not be done.

The last interesting point in comparison with the system of tin islands on InAs(110) is that even at small lead coverages of about 2 ML, the Drude like signal occurs – an encouraging result for investigating even smaller structures.

4.3 Indium on Si(111)

So far it was shown that the optical anisotropy of isolated or a dense package of elongated metallic islands can be explained by an anisotropic Drude like free electron response. In this section measurements of the optical anisotropy of a much smaller system of metallic wires will be shown. At a coverage of less than 1 ML of indium on Si(111), an anisotropic surface reconstruction occurs: the Si(111):In-(4×1) surface which will be extensively discussed in the next chapter. For the moment a short introduction is sufficient. The indium rows of this surface as seen in Fig. 4.1 consist of two indium zig-zag chains (bright regions) separated by a Si π-bonded zig-Ag chain. It was shown by Abukawa et al. that this surface is metallic with a strongly one-dimensional character. A more detailed study by Yeom et al. showed that there are three metallic surface states. One of them does not show any dispersion in the chain direction (see Fig. 5.6). This surface was therefore assumed to be an ideal test case for an one-dimensional conductor.

In contrast to the optical anisotropy of the metallic islands, the RAS spectra of the Si(111):In-(4×1) in the infrared spectral region is not dominated by the free electron like response. The most dominant structures arise from interband transitions between surface states around 2 eV. In Fig. 4.10 a typical spectrum of the (4×1) reconstructed

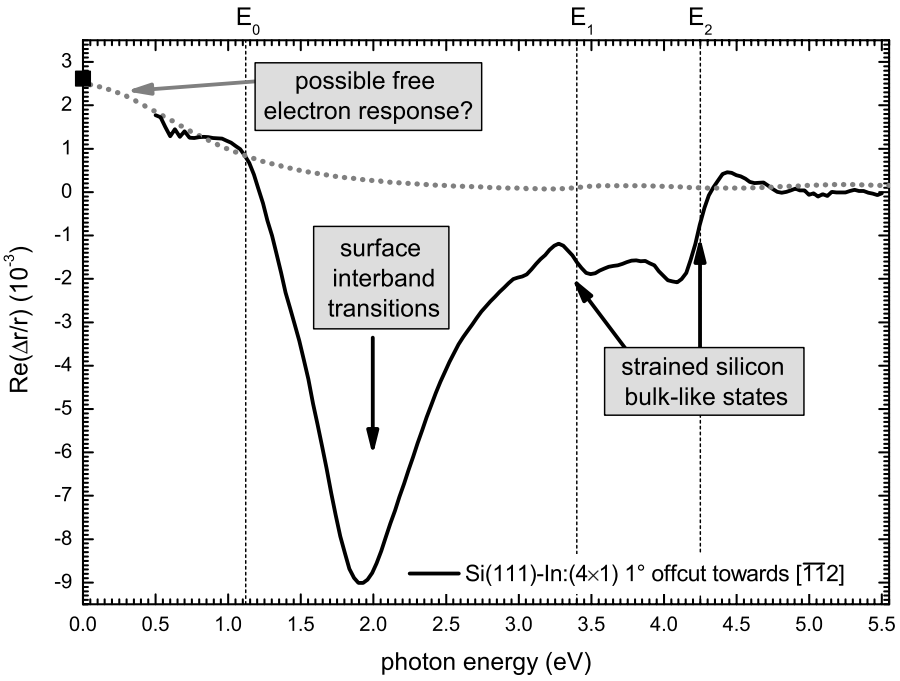

Figure 4.10: *RAS spectra of the Si(111):In-(4×1) reconstructed surface. The origin of the main structures is noted. A more detailed discussion of this surface follows in the next chapter. The grey dotted line shows the RAS expected from a free electron like response (parameters see text). The black box shows the expected DC anisotropy using the measured conductance values [148] and (3.8). It is obvious that in the case of the indium wires the RAS spectra is dominated by other contributions.*

surface is shown. The origin of most structures is labelled. In comparison a modelled RAS spectra of an anisotropic Drude free electron gas on silicon is shown, using similar model dielectric functions as for the other two materials above.

In the case of the Si(111):In-(4×1) surface measurements of the DC conductance anisotropy exist [148]. Using the values given there for $\sigma_{\parallel}$=7.2×10^{-4} S and $\sigma_{\perp}$=1.2×10^{-5} S, and a thickness of the conducting layer of 2Å, the expected RAS signal if extrapolated to zero frequency using (3.8) is only 2.6×10^{-3}, although the conductance is 60 times higher parallel to the wire. Fig. 4.10 also shows a simulation of the free electron response using values for $\omega_{p,x}$ = 4.5 eV, $\omega_{p,y}$ = 3 eV, $\omega_{\tau,x}$ = 1 eV, $\omega_{\tau,y}$ = 1.5 eV and d = 2Å. $\omega_{\tau,x}$ was taken from [148], where the average scattering time parallel to the wires was calculated using the measured conductivity and an analysis of the Fermi surface measured by ARPES. The ratio of $\omega_{p,x}/\omega_{p,y}$ was set to be fixed as well, motivated by the measured anisotropy in the effective masses m^*_x/m^*_y = 0.7 [160] and recent calculations of ω_p within DFT-LDA theory ($\omega_{p,x}$ = 7.3 eV, $\omega_{p,y}$ = 3.3 eV) [161]. The first estimation would result in an $\omega_{p,x}/\omega_{p,y}$ ratio of 1.2 the latter of 2.2. For the calculation here the ratio was set to be 1.5, a value between the two different literature results. The anisotropy in the scattering rate $\omega_{\tau,x}/\omega_{\tau,y}$ was assumed to be similar. This leaves only two free parameters for a fit d and $\omega_{p,x}$. The values for the plasma frequencies found by this fit ($\omega_{p,x}$ = 4.5 eV, $\omega_{p,y}$ = 3 eV) are in the same order as the recent calculations of this quantity within the DFT-LDA theory ($\omega_{p,x}$ = 7.3 eV, $\omega_{p,y}$ = 3.3 eV) [161].

It is obvious that the free electron contribution to the RAS spectra at least in the accessible spectral region is very small. Hence this model cannot describe the full optical response of wires this small. Nevertheless, as one can see in the next chapter, the optical anisotropy below 1 eV can at least be partly understood in terms of such a free electron like response.

4.4 Validity of the free electron model

In this section one has seen so far that the RAS of different metallic nanowires does show structures in the infrared region. The RAS response can be easily explained by anisotropic properties of the free electron response only in the case of “thicker” wires such as the tin or lead anisotropic islands. One problem is the determination of the parameters of the two Drude dielectric functions needed to quantitatively explain the RAS spectra. If the contribution of interband transitions to the RAS spectra is small, as in the case of the tin islands on InAs(110) at coverages between 10 and 30 ML, only three parameters can be obtained by fits of the RAS spectra or SDA. The remaining parameters had to be approximated by known bulk values and additional *ex-situ* measurements such as the thickness of the layer. The fits for the system of lead wires – though more problematic due to the small number of measured points – confirm, that if ω_τ gets strongly anisotropic a transition from positive RAS values at 0.5 eV to negative in the NIR range occurs.

With some technical improvements the current RAS setup can be modified to measure the reflectivity of the samples and the surface differential reflectance. If this can be achieved, the problems mentioned in the determination of the Drude parame-

ters can be reduced since absolute mean values for ω_p and ω_τ can be derived from the reflectance data. This leaves only the ratio of $\omega_{p,x}/\omega_{p,y}$ and $\omega_{\tau,x}/\omega_{\tau,y}$ to be fitted with the RAS spectra. Such a more accurate determination might lead to more insights about confinement mechanisms if e.g. the parameters can be derived for wires with varying length to width ratio. In cases where the RAS spectra are dominated by interband transitions (In/Si(111)) meaningful fits of the Drude parameters cannot be done.

Apart from that, one main issue remains unaddressed so far – in what way the measured optical anisotropic conductance can be used to determine the electrical DC or AC conductance for such nanowires. Studies where both optical and electrical conductance is measured for such systems remain to be done. In the case of the indium wires electrical measurements exist [148, 149], but the performed optical measurements give no clear indication of an anisotropic response of the free electrons as stated above. In the case of the tin islands as well as the lead islands no electrical measurements exist. However for bulk materials it has long been known that the optical conductivity can be related to the DC conductivity. Also for thin films it was already shown that the measured optical conductivity can be extrapolated to zero frequency and compare well with measured DC values [84]. For this extrapolation mid-IR-transmittance spectra were used, hence much closer to the zero frequency than possible with a conventional RAS setup. For higher energies it was also shown that the DC conductivity can show a similar behaviour to the optical conductivity derived from SDR measurements at 0.4 or 0.5 eV [162], which is accessible with the RAS setup as well. It is therefore reasonable that the measured anisotropy in optical conductance will also occur for DC measurements and therefore RAS can be used to monitor such anisotropies *in-situ* and without contact.

5. The Peierls transition of Si(111)-In

As we have seen in the general discussion of 1D conductors in Section 2.3 an ideal 1D conductor has an inherent instability: the so called Peierls instability. In the following chapter I want to show how the formation of a charge density wave (CDW) driven by this instability is affecting optical spectra of such a system. The test system of choice is the indium terminated Si(111) surface. Under specific preparation conditions the surface shows a quasi one-dimensional metallic structure – the (4×1) reconstructed surface. As we will see this metallic surface undergoes a phase transition with typical characteristics of the formation of a charge density wave. Although the nature of this transition is still under discussion [46, 47, 163–166]. I will show in this chapter that all the optical measurements performed support the CDW model. As we have seen in the previous chapter the free electron response in the RAS is small for this particular system. Nevertheless I will show that changes in the strong interband transitions upon the phase transition can also help to understand the nature of the phase transition. In the following I will first introduce the Si(111)-In:(4×1) surface in detail followed by a discussion about the phase transition at low temperatures. Reflectance anisotropy spectroscopy (RAS) and Raman spectra of both phases will be discussed with respect to the conflicting models for the nature of the phase transition. Critical for understanding the nature of both phases are experiments where the surfaces are deliberately perturbed by adsorbates. This will be discussed in detail in a separate section. To summarise this chapter a model of the surface and its phase transition will be presented which is in accordance to all measurements performed so far.

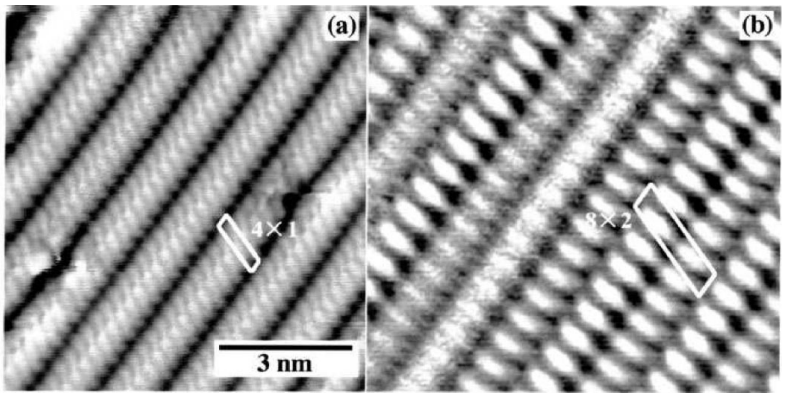

Figure 5.1: *STM images and low temperature STM images of the (4×1) reconstructed indium terminated Si(111) surface. Below 120 K a change of symmetry is obvious. Yeom et al. interpreted this phase transition as a development of a charge density wave (CDW). (Image taken from [47])*

5.1 Si(111)-In:(4×1) introduction to the surface

The indium induced reconstructions of the Si(111) surface were already investigated by Lander and Morrison in 1964 [167]. With electron diffraction techniques, several ordered surfaces were observed ranging from a $(\sqrt{3} \times \sqrt{3})$ – $(\sqrt{31} \times \sqrt{31})$ – (4×1) – (1×1)R30° with increasing indium coverage. Although the (4×1) structure was quite often investigated in later years, no successful microscopic model of the surface could be developed [167–175]. The (4×1) surface itself occurs at a coverage of around 1 ML of In. The symmetry of the (4×1) surface is lower than the three fold symmetry of the Si(111) surface. Therefore three domains of the (4×1) reconstruction usually occur, rotated by 120°. This made investigations of the anisotropy of this lower symmetry surface impossible. The first measurements which showed the anisotropy in real space were STM measurements by Nogami et al. [171, 172]. These STM studies newly stimulated discussions about the microscopic structure [173–175]. In Fig. 5.2 two such models are shown. Although Stevens et al. [174] did not derive the present established model by their combined STM and ICISS (impact-collision ion-scattering spectrometry) measurements, they were the first to be able to prepare a single domain (4×1) surface by using vicinal Si(111) surfaces.

Further interest in the (4×1) surface was stimulated by Abukawa et al. in 1995 [3]. Again by using vicinal Si(111) surfaces, single domain surfaces were investigated and it was shown by angle resolved photo-electron spectroscopy (ARPES) that the surface is quasi one-dimensional metallic. Three metallic surface states exist on the surface and at least one of them is almost dispersionless along the chain direction. This confirmed earlier studies where indications of metallic behaviour were found by high resolution electron energy loss spectroscopy (HREELS) [177].

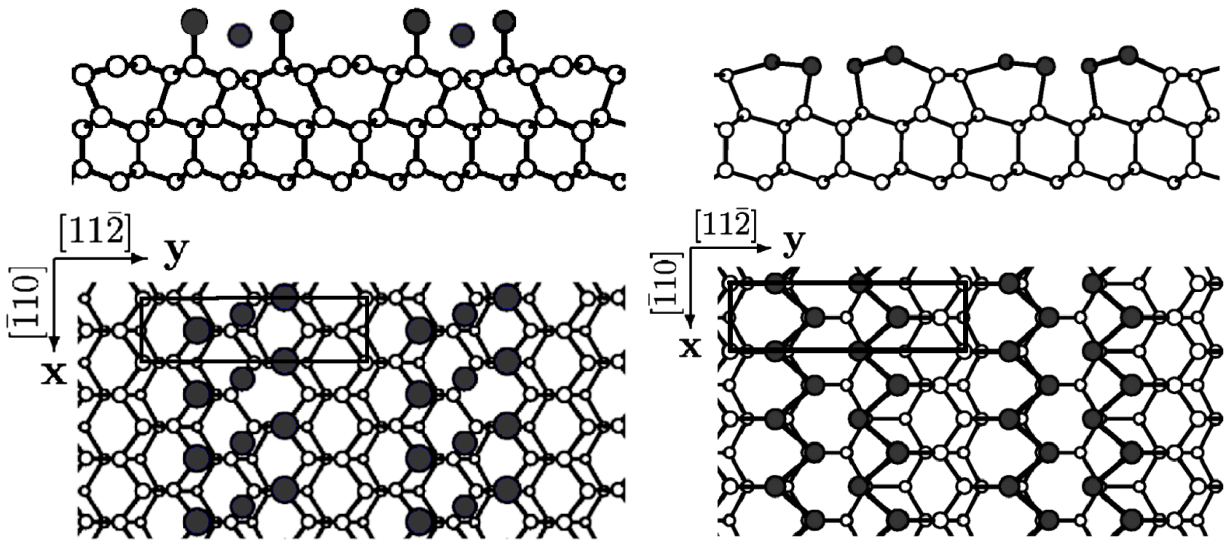

Figure 5.2: *Calculated atomic positions for two different models of the (4×1) surface. The open circles depict Si atoms, the full circles In. On the left side the original model of Saranin et al. [175]. On the right side the now accepted model with double zig-zag chains of indium. (Images taken from [176])*

The (4×1) surface is a model system of a one-dimensional metallic structure and can be prepared in a single domain by using vicinal Si(111) surfaces. It is therefore an ideal test system for 1D conductors. Experimentally it was shown in recent years that the surface undergoes a phase transition (see Fig. 5.1) at low temperatures accompanied with changes in the conductance [149]. Furthermore the geometric structure of this surface was analysed experimentally with grazing incidence x-ray diffraction (GIXRD) [48, 178]. With theoretical work, utilising *ab initio* calculations within density functional theory (DFT), different microscopic models of the surface were compared to the measurements. The structural models by Baba et al. [179], Stevens et al. [174] and later Saranin et al. [175] could not be confirmed. The model derived from the GIXRD studies [178] was found to be the most energetically favourable (4×1) model [46, 176]. Since the double chain model can reproduce the measured bandstructure and STM images [46] and also RAS spectra [176], it is by now the accepted model. In Fig. 5.2 the calculated atomic positions of the (4×1) structure are shown. The (4×1) surface therefore consists of an In double chain, spaced by a Si π-bonded chain – with 4 indium and 2 silicon atoms in the top layer unit cell. Before the phase transition at low temperatures will be discussed, I will describe the results of optical studies on the room temperature (4×1) phase.

5.1.1 Reflectance anisotropy

RAS spectra of the Si(111)-In:(4×1) surface were measured by Pedreschi et al. already in 1998 [180]. Fig. 5.3 shows a comparison of the spectra derived in this work and the one of Pedreschi et al.. Since no calculation of the RAS spectra was done until 2003 the spectrum had to be discussed phenomenologically. The dominant structure is a large minimum at 2 eV caused by a higher reflectance for light polarised perpendicular to the In chains than for light polarised along the chains. It was therefore proposed that the transitions involved in this structure are located more at the In-Si back bond than in the In-In bonds of the chains itself. The work of Pedreschi et al. was performed on samples with a 4° degree offcut towards the $[11\bar{2}]$ direction. In order to investigate in what way steps and possibly indium on step edges contribute to the RAS spectra I will compare studies performed on similar samples and those done on samples with only 1° offcut towards the $[\bar{1}\bar{1}2]$ direction. The RAS spectra of the clean (7×7) surface differed for both kinds of samples. The (7×7) is structurally isotropic and the RAS only arises from regions with broken symmetry – the step edges. The larger offcut angle leads to a higher number of steps or smaller terraces. Consequently any step induced structure will be more pronounced in the 4° offcut samples. The spectra of the clean surface in Fig. 5.3 was measured with the 4° offcut samples. Samples with only 1° offcut did not show any anisotropy. In contrast to steps on the Si(001) surface [181] the step induced RAS signal on the Si(111) surface is very small. Since almost no signal arises from the Si(111) surface the preparation of this surface could not be directly monitored with the RAS. But for the preparation of single domain Si(111)-In:(4×1) surfaces the quality of the original clean surface is of utmost importance. I will therefore continue with a more detailed description of this process.

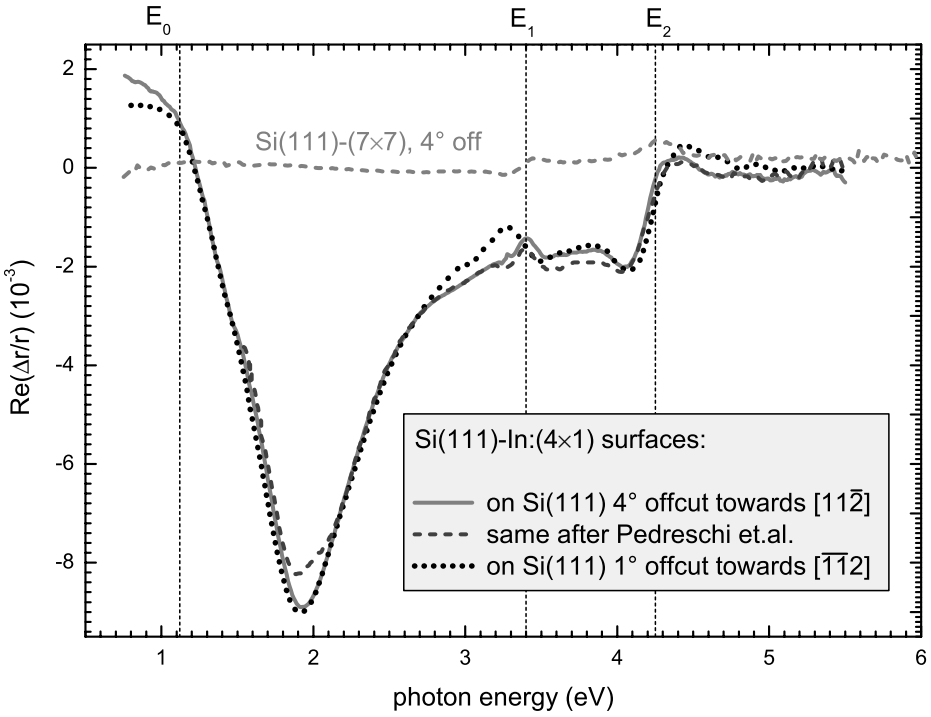

Figure 5.3: *Comparison of RAS spectra of the Si(111)-In:(4×1) surface measured by Pedreschi et al. [180] and this work on silicon samples with different offcut angles and directions. There is only an amplitude difference, since the literature data had to be divided by 2. Apart from that the agreement is very good. The most dominant structure of the RAS spectra is the minimum at 2 eV. Smaller structures are seen around the Si bulk critical points of silicon. A spectrum of the clean Si(111)-(7×7) surface is given for comparison.*

5.1.2 Preparation of the single domain Si(111)-In:(4×1) surface

As it was already discussed the adsorption of indium onto the Si(111)-(7×7) reconstructed surface leads to different reconstructions. The first one occurring is the $(\sqrt{3}\times\sqrt{3})$ at a coverage of about 0.3 ML. Above half monolayer coverage a $(\sqrt{31}\times\sqrt{31})$ surface appears. Both surfaces have a hexagonal symmetry and can therefore not be measured with RAS. The (4×1) surface, which starts to form above 0.75 ML coverage, though anisotropic, normally also cannot be measured with RAS, since three equivalent domains are formed. They are rotated by 120° from each other and therefore the RAS signal from such 3-domain surfaces completely cancels out. By using vicinal silicon surfaces this problem can be overcome. The regular step pattern reduces the symmetry of the Si(111) surface and a single domain surface with In chains parallel to the step edges can be preferably formed. In the first STM studies on vicinal substrates no preferred orientation of the chains was found [171, 172]. The single domain surface can be stabilised only on samples with small step roughness. For achieving smooth steps the Si(111) sample has to be carefully heat treated. Using Si(111) with an offcut towards the [11$\bar{2}$], it was demonstrated by Viernow et al. [21]

that repeated flash heating the Si(111) samples to 1100°C for 10 seconds, followed by a slow temperature decrease to 960°C and than a rapid cooling leads to the formation of well defined terraces. On Si(111) with an offcut towards [$\overline{1}12$] and the same procedure, the step array was found to be even more regularly [20]. For this study the procedure was slightly modified, since no controlled ramping of the heating was possible. Instead samples were heated at 1100°C for 10 sec, at 1000°C for another 10 sec and than rapidly cooled. Although by this procedure one will not achieve such a good order as shown by Viernow et al., the surface is good enough to assure a single domain surface. There are two critical points in the preparation. *(i)* the annealing temperature has to be above 950°, because otherwise step bunching is energetically more favourable. *(ii)* in order to avoid sample contamination, the pressure during the whole procedure does not exceed 2-5 10^{-9} mbar. Otherwise no preparation of single domain surfaces was possible afterwards.

The actual indium deposition and formation of the single domain Si(111)-In:(4×1) surface was controlled with the RAS setup. In Fig. 5.4 two examples of RAS-transients taken at 2 eV are shown. Without an *in-situ* probe the preparation of a one-domain is rather critical, since the preferential growth of a single domain surface depends on sample temperature and indium flux. The sample temperature can be varied between 400 and 450°C but the range for deposition time or indium flux needed to achieve a single domain surface is rather small. Following the procedure used in [3], first more indium is deposited than needed for the (4×1) and the sample is

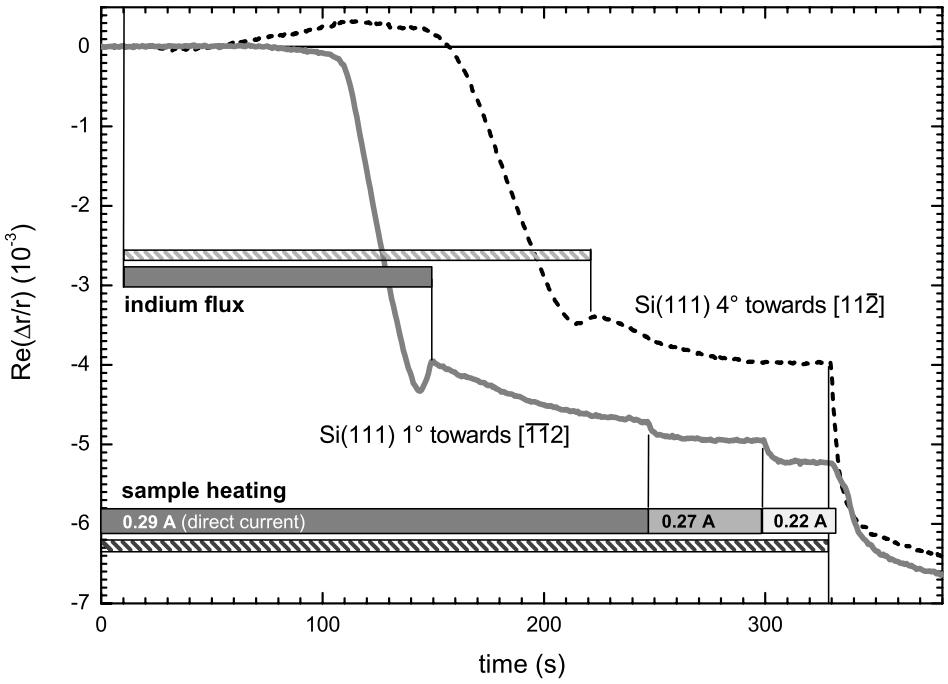

Figure 5.4: *RAS transients during the deposition of In on Si(111) surfaces. Two transients are shown – one from a Si(111) sample with 4° offcut towards the direction (dashed) and another with only 1° offcut towards the* [11$\overline{2}$] *direction (solid line). The indium flux and consequently the deposition time for 1 ML varied.*

annealed afterwards until enough In is desorbed. During the whole procedure the RAS at 2 eV is monitored. Since all other reconstructions like the $(\sqrt{3} \times \sqrt{3})$ or the three domain (4×1) are optically isotropic, the RAS amplitude is directly proportional to the surface area in the (4×1) reconstruction. The actual indium flux and heating current was therefore individually optimised for each sample. The indium shutter was closed after the RAS amplitude was decreasing again and the annealing was stopped when the desorption of the excess indium saturated. Furthermore it was found that a gradual decrease in annealing temperature after the indium deposition leads to a better surface quality. The other significant difference between the two preparations shown in Fig. 5.4 is the positive signal around 0.5 ML coverage for the sample with 4° offcut. This behaviour was not observed in the other set of samples with only 1° offcut. So far the origin of this behaviour is not clear. Possibly the anisotropy originates from indium at step edges, since it is not seen on the 1° sample where the average number of steps is about 4 times smaller.

5.2 The phase transition

The preparation of the single domain (4×1) reconstructed surface was the first step in the investigations of the surface. The surface undergoes a phase transition at 120 K into a (8×2) surface, first reported by Yeom et al. in 1999. Originally the low temperature phase was reported to have a (4×2) symmetry derived from RHEED images and STM. Later this was corrected by LEED studies, where defined 8× spots could be seen. The ×2 spots were always reported to be streaky and never clearly defined. In Fig. 5.5 typical LEED measurements of samples prepared in this work for the two phases are shown. Not all 8× spots can be seen and in the other direction

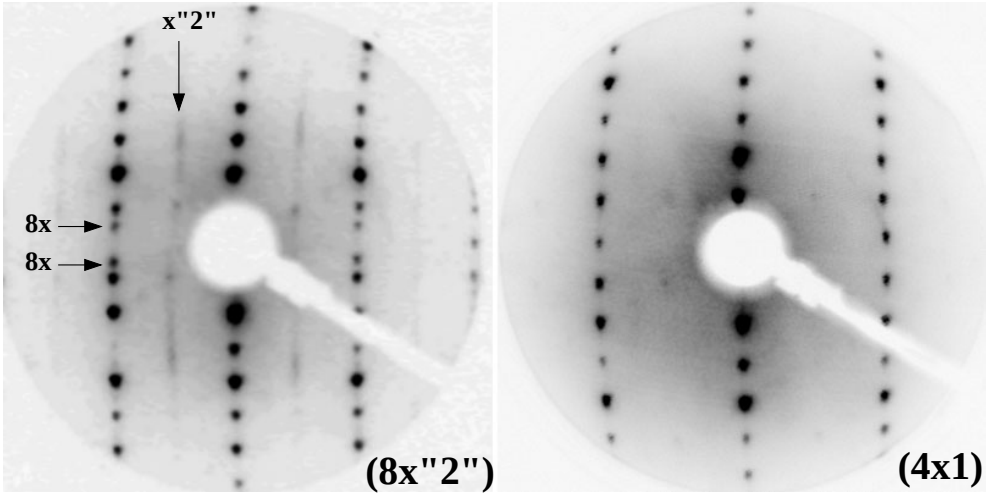

Figure 5.5: *LEED images of the single domain Si(111)-In:(4×1) surface above and below the phase transition. The low temperature phase is called (8×2) although the "×2" spots are streaky and not all "8×" spots can be seen at this electron energy (90eV).*

almost no defined ×2 pattern occurs – only streaks. This is consistent with all other measurements based on electron diffraction. Usually this surface should therefore be referred to as "(8×2)", (8×"2") or even (8×1). Nevertheless for clarity the low temperature phase will be labelled (8×2) through this work.

In the low temperature STM images by Yeom et al. in Fig. 5.1 the ×2 symmetry is well observed in real space. With angle resolved photo-electron spectroscopy (ARPES) it was reported that the spectral weight at the Fermi edge is drastically reduced upon the phase transition [47]. This was interpreted as a metal – insulator transition as is expected if a CDW is formed. In the model proposed by Yeom et al. the formation of the CDW is driven by the Peierls instability. This concept was already discussed in detail in section 2.3. In a strictly one-dimensional metallic system energy can be gained by the formation of a periodic modulation of charge with real space periodicity $c/b \cdot a_0$ if the metallic band is crossing the Fermi level at $b/c \cdot 2\pi/a_0$ of the first Brillouin zone. In Fig. 5.6 the Fermi surface of the Si(111)-In:(4×1) surface is shown as determined by Yeom et al. [47]. The surface is only quasi-one-dimensional, since only one of the surface states is dispersionless in the chain direction. Nevertheless this band (labelled m_3) is crossing the Fermi level at ½ of the surface Brillouin zone ($\bar{\Gamma} \rightarrow \bar{X}$). Hence for this metallic band the situation can be described by the simple 1D-model and the band should therefore be unstable against a periodic modulation. The observed periodicity upon the phase transition is consistent with a CDW of real space periodicity of $2 \cdot a_0$ as expected by the Peierls model. It is by now also confirmed that the phase transition leads to a gap opening [47, 164, 182] Therefore, Yeom et al. concluded that a CDW driven by a Peierls instability of the m_3 state occurs for this surface [47].

This model was questioned by work from Kumpf et al. with grazing incidence x-ray diffraction (GIXRD) [48]. Upon cooling of the surface a change of the atomic positions of the outer chain indium atoms was observed – doubling the surface unit

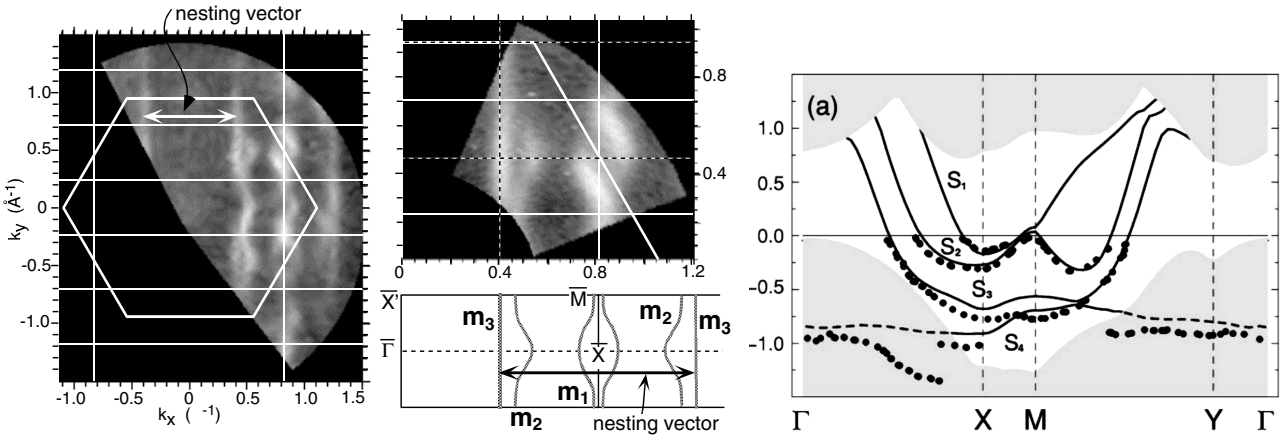

Figure 5.6: *Fermi surface of the Si(111)-In:(4×1) surface measured by ARPES and the model Fermi surface derived from these data. The metallic state m_3 has almost no dispersion and crosses the Fermi level about halfway between $\bar{\Gamma}$ and $\bar{X}$. (Image taken from [4]) On the right side is the surface bandstructure as calculated by Cho et al.. The three measured metallic surface bands are nicely reproduced (Image taken from [46]).*

cell in the direction perpendicular to the wires leading to a 8× symmetry. This change however was perpendicular to the chain direction, hence challenging the assumption that only the electron density is changed and the symmetry is ×2. With GIXRD it was also noted that the shift of atomic positions is along the chain direction. The results were interpreted as trimer formation and a resulting surface in (8×2) symmetry due to a change of reconstruction.

Based on these findings DFT-GGA calculations were performed by Cho et al. to find surfaces of minimal total energy testing models in (4×1), (4×2) and (8×2) symmetry [46] (see also Fig. 5.7). It was found that the (8×2) is the minimum energy structure reproducing the atomic position of Kumpf et al., though without changes in the nature of the bonding within the chains. From that Cho and coauthors suggested that the phase transition is not caused by a CDW formation but by a disorder–order transition similar to other dimerised surfaces [183, 184]. The (4×1) room temperature surface would be a thermal mixture of (8×2) or (4×2) unit cells. In contrast to the measurements the calculated surface structures were found to be metallic even in the case of the (8×2) surface. Recent calculations also found semiconducting (8×2) models with small modifications in the underlying (8×2) model [166, 185]

From an experimental point though the disorder–order model was doubted since the originally calculated bandstructures for the (8×2) and (4×2) surfaces did not reproduce measured data as well as similar calculations for the (4×1) model [163]. In any case later electron diffraction experiments always confirmed an (8×2) symmetry of the low temperature surface in agreement with the GIXRD data and calculation. Other calculations also confirmed the (8×2) as the most energetically favourable

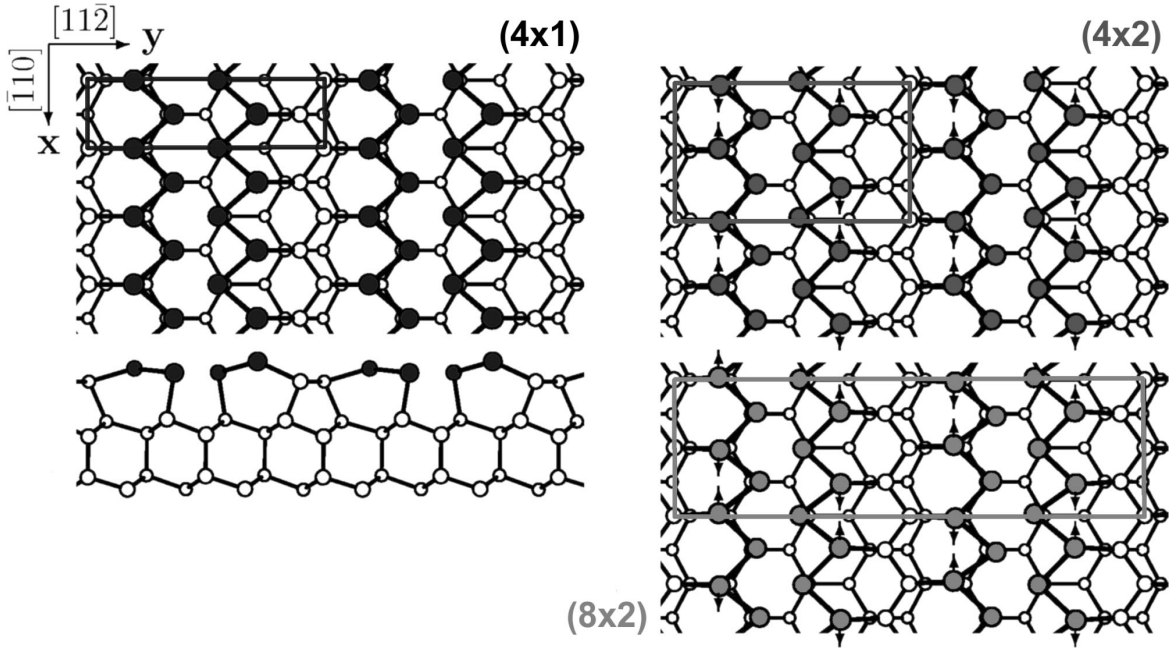

Figure 5.7: *Calculated atomic positions for the (4×1), (4×2) and (8×2) surface. The change in the position for the (4×2) and (8×2) surface is shown in comparison to the (4×1) surface by the arrows. (taken from Wang et al. [176])*

[176, 186] and also provided qualitative agreement with the optical properties of this surface above 1 eV as will be shown later in this chapter. All these findings supported the (8×2) as the minimum energy surface.

Apart from the RAS study of Pedreschi et al. [180] no further optical measurements were performed for the room temperature phase and none for the low temperature phase prior to this work. As it was described in chapter 3 anisotropies in the electronic transitions as well as anisotropies in the conductance of surfaces can be probed with RAS. With another optical technique – Raman spectroscopy – vibrational modes of the atomic arrangement can be probed. For the Si(111)-In:(4×1) and (8×2) surface it was therefore expected that new insights in the nature of the phase transition can be gained by comparing the spectra of both phases. Particularly the vibrational properties of the surface should change if the atomic positions are changed. In the next part I will first present the RAS measurements and discuss the changes observed in terms of the conflicting models.

5.3 RAS of the (4×1) and (8×2) surface

The room temperature spectrum of the indium terminated surface was already introduced in Fig. 5.3 on page 58. The most prominent features are the large minimum around 2 eV (S_1) and two smaller structures around the bulk critical points of silicon (E_1, E_2). The latter two are most likely caused by strain introduced in the near surface bulk region. Since they were independent of the reconstruction (4×1) or (8×2) I will not discuss them here. For all measurements presented here the RAS was optimised for infrared measurements by using a tungsten lamp. For this reason the spectra are limited to energies below 3 eV.

At elevated temperatures all optical spectra usually broaden and structures show a red shift. This can be explained by the lattice expansion and electron-phonon interaction [187, 188]. In the case of Si(111)-In one needs to compare room temperature data with measurements below 100 K. In order to distinguish between the “normal” changes of the spectra and any changes introduced by the phase transition, spectra were taken for many temperatures between room temperature and 120 K. In this temperature region the RAS spectra show a considerable increase in amplitude. Also more details in the minimum structure can be resolved, namely an additional shoulder around 1.4 eV (S_2). The expected blue shift of the structure is very small about 40 meV. In comparison the blue shift of comparable structures on GaAs and InP clean surfaces show a shift of 240 and 150 meV respectively [189, 190]. The reason could be the 1D nature of the states involved in the transition.

In Fig. 5.8 some spectra, recorded during the cooling process below 120 K, are shown. To monitor the phase transition one can, alternatively, measure transients at specific energies to monitor the phase transition. Fig. 5.8b) shows such transients taken at the energies of the structures of the (4×1) surface (S_1 at 1.9 eV, S_2 at 1.4 eV) and one at 2.4 eV. In both graphs it can be seen that the first irregular changes (decrease in RAS amplitudes) occur around 120 K ± 5 K in good agreement with other reported transition temperatures. Particularly in the transients it can be seen that the change towards the (8×2) spectrum is gradual. To be more quantitative: assuming that the

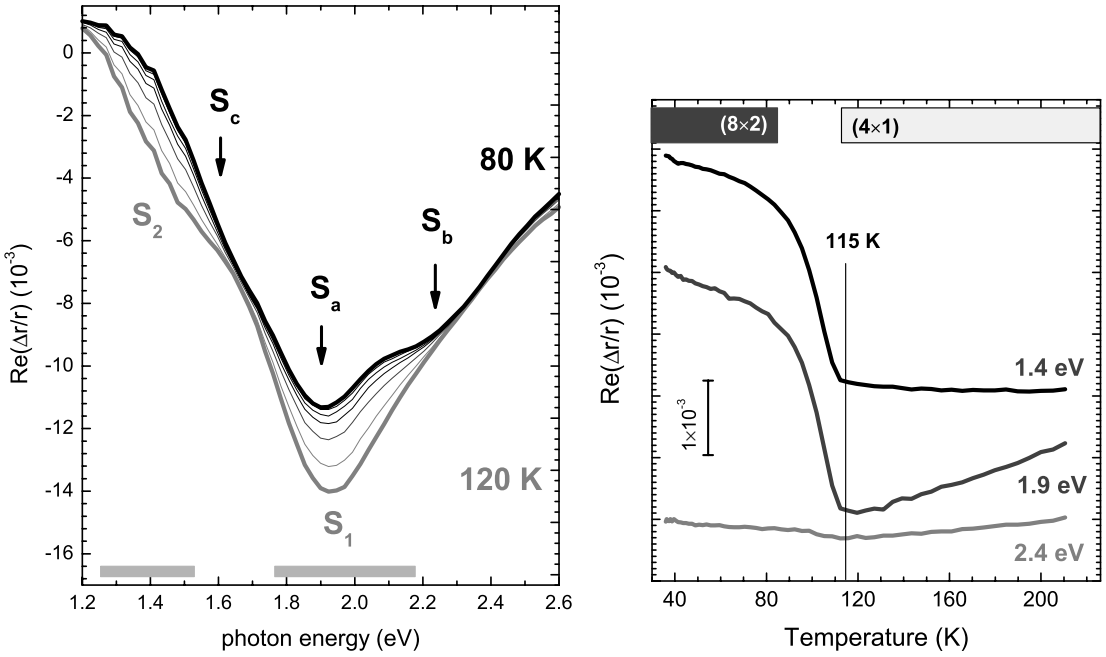

Figure 5.8: in situ *monitoring of the phase transition in Si(111)-In:(4×1). a) shows some spectra taken between 120 K and 80 K. Changes occur below 120 K leading to a double peak around 2 eV. b) shows transients taken at 1.4, 1.9 and 2.4 eV. The changes seen in the transient from 230 K to 120 K are related to the usual increase of RAS amplitudes upon cooling. The changes by the phase transition can clearly be distinguished.*

surface is fully (8×2) reconstructed at the lowest measured temperature of 30 K ± 10 K, the transient at 1.4 eV between 110 K and 30 K can be fitted by an exponential function of the form $y = y_0 + A\exp((T-T_c)/\tau)$, using fixed values[1] for y_0, A and T_c, the value τ which reflects the typical temperature range of the transition is found to be 17.5 K ± 0.3 K. The RAS transient can also be used to calculate the surface area which is still (4×1) reconstructed. Again assuming a 100% (8×2) surface at 30 K for instance, at 70 K 10% of the surface would still be (4×1) reconstructed. This compares well to the STM measurements of Yeom et al. where at 60 K individual rows still showed the ×1 periodicity [47]. In addition to RAS measurements LEED images were recorded for the same samples, which reveal that the phase transition is indeed responsible for the observed changes (see Fig. 5.5).

In a second step spectra were recorded at 30 K ± 10 K with the full available spectral region (0.5 - 3 eV and 0.75 - 6 eV). Again all relevant changes occur between 0.5 - 3 eV, so only this region is shown in Fig. 5.9. For comparison, spectra were also taken at 140 K – well above the transition temperature but already cold enough to resolve details in the broad minimum structure. By displaying the difference of two RAS spectra (here termed δRAS) small differences within larger, unchanged RAS structures can be seen more easily. One problem is that optical spectra taken at

[1] $y_0 = -0.5\times10^{-3}$ (RAS at 1.4 eV, 30 K), $A = -3.3\times10^{-3}$ (δRAS of 110 K and 30 K, 1.4 eV), T_c (110 K)

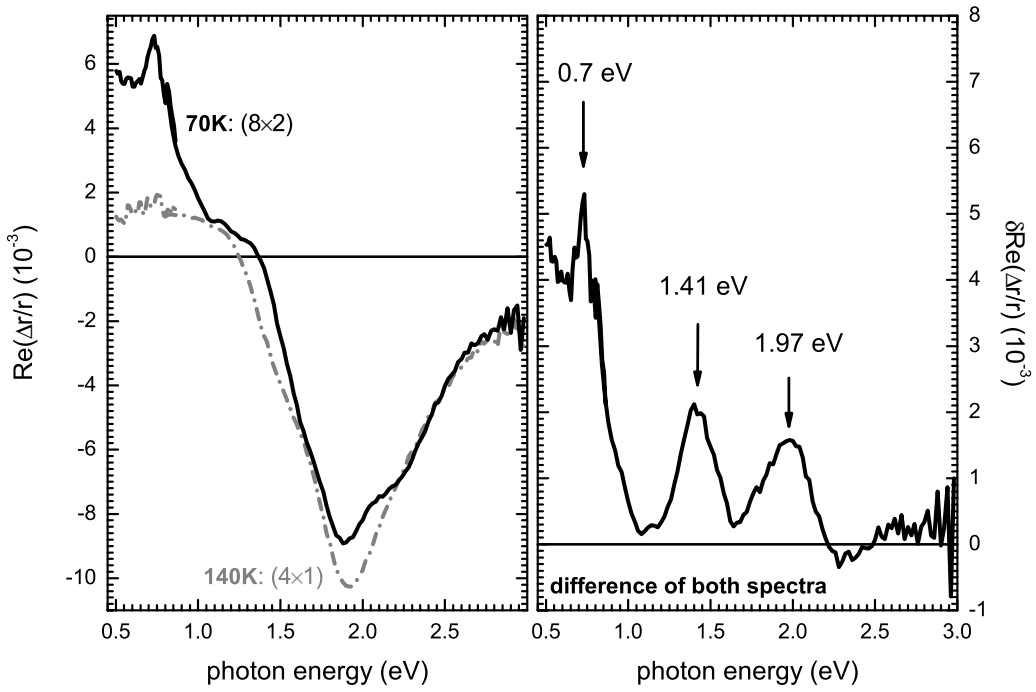

Figure 5.9: *RAS spectra of the indium terminated Si(111) surface at low temperatures. A spectra of the (4×1) at 140 K above the transition temperature is compared with one of the (8×2) phase at 60 K.*

different temperatures need to be subtracted. However the differences of RAS spectra taken at 140 K and 30 K are not as drastic as for similar ΔT at higher temperatures since changes by cooling usually saturate between 100 K and 0 K due to the zero point renormalisation [187]. Test measurements at 30 and 140 K with adsorbate stabilised (4×1) surfaces, which do not show the phase transition, have shown that the δRAS signal is less than 0.5 RAS units if only the temperature dependent shift and sharpening occurs (see also Fig. 5.26). All differences between (4×1) and (8×2) surface shown in Fig. 5.9 are much larger and can therefore be assigned to changes of the electronic states at the phase transition.

The low temperature (8×2) spectrum does show several new features. A broad structure in the infrared (below 1 eV) and a rather sharp peak at 0.7 eV. The main structures of the original (4×1) RAS spectrum are either completely quenched as the shoulder at 1.4 eV or changed. The change in the 2 eV minimum structure can be best explained by a splitting of the 2 eV minimum into two at 1.9 eV and 2.3 eV.

Before these changes can be discussed in terms of the conflicting models of the phase transition the origin of the optical anisotropy of the (4×1) surface itself has to be analysed in more detail.

5.3.1 Origin of spectral features in RAS

Recently Wang et al. calculated the optical anisotropy of the Si(111)-In:(4×1) surface [176]. In Fig. 5.10 the measured RAS spectra is compared to calculations for the (4×1) and (8×2) models introduced in Fig. 5.7. For comparison the calculated anisotropy

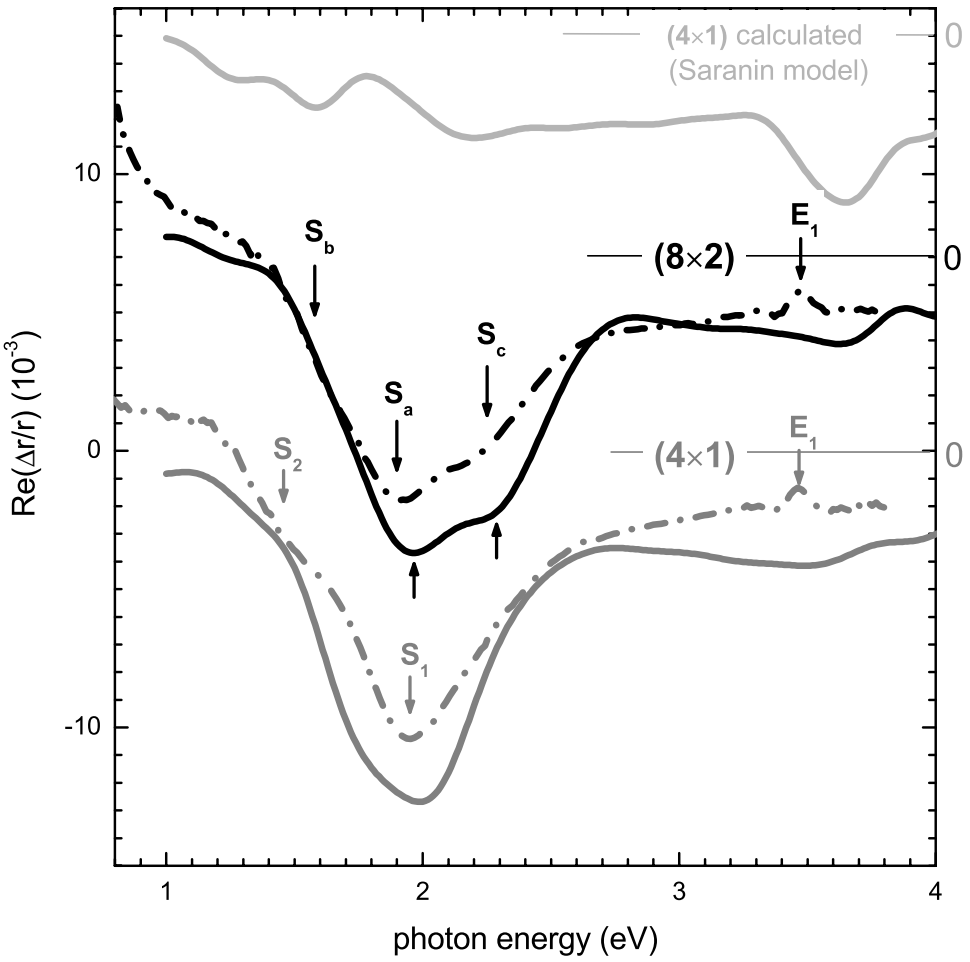

Figure 5.10: *Comparison of RAS spectra of the Si(111)-In:(4×1) and (8×2) surface. The calculated spectra of the zig-zag chain models can reproduce the measured spectra (dash-dotted) in amplitude and line shape. The alternative (4×1) model can be completely discarded, since no agreement with the measurement is found.*

of the π-bonded stacking fault model of Saranin et al. was calculated as well. It is obvious that the latter cannot explain the measurements. For the calculation of optical spectra from bandstructures derived by *ab-initio* calculation within the density functional theory in local density approximation (DFT-LDA), several approximations still have to be made which makes direct comparison to measurements difficult. DFT-LDA is a ground state theory. For the determination of optical spectra excited states have to be treated. Several corrections of the DFT-LDA result can be applied to treat the electron hole interaction or excitonic or local field effects [141, 190–192]. Such corrections are very time consuming and have not yet been performed for the surface of interest. In general such corrections lead to an enlargement of the gap energies always underestimated in DFT-LDA and in changes of the relative amplitude of the structures. Therefore the energetic position and relative peak intensities in the calculations shown in Fig. 5.10 are not expected to be accurate – for better comparison they were rigidly shifted to higher energies (scissors operator). What can be seen

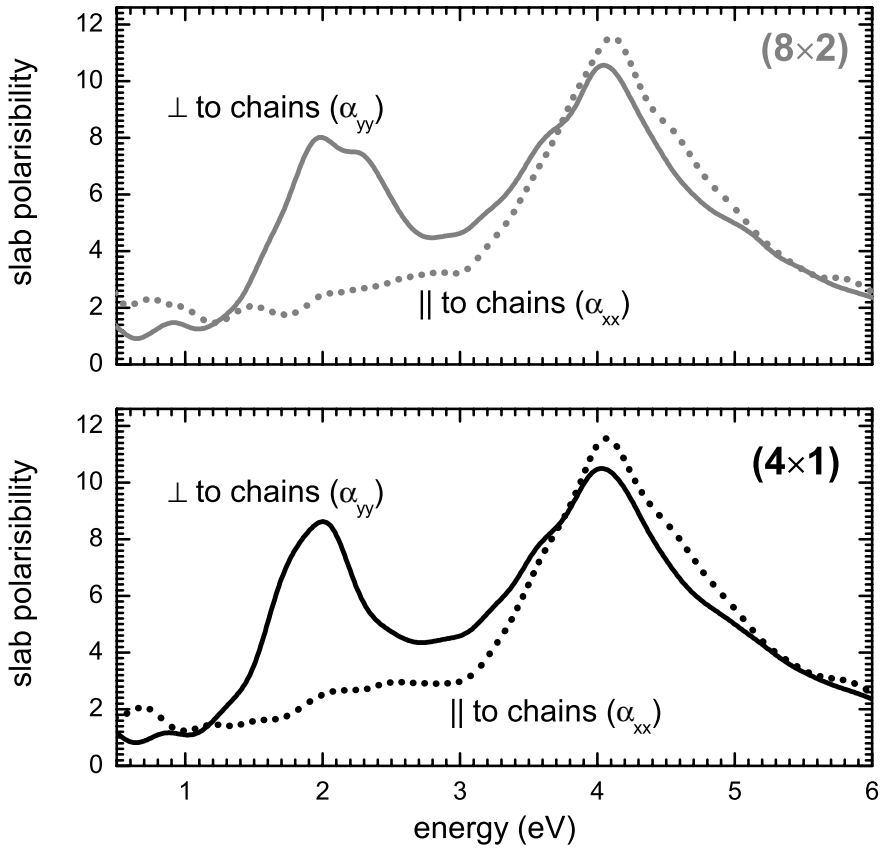

Figure 5.11: *Slab polarisabilities of the (4×1) and (8×2) surface (courtesy to Wang et al. [176]). The structure around 2 eV originates from an optical transition with no transition strength for light polarised along the chains. The structures at the Si bulk critical points originate by an anisotropy in the transition strength and energetic position.*

is that the calculation can already reproduce the main minimum structure at 2 eV (S_1) as well as the smaller structure (S_2) for the room temperature (4×1) phase. The three structures found for the (8×2) phase (S_a, S_b, S_c) are also reproduced. In order to calculate the RAS spectra the polarisability $\underline{\underline{\alpha}}$ of the surface slab is calculated. By analysing this value instead of the RAS spectrum one additional information can be gained. The minimum at 2 eV originates from a transition with almost no transition strength for light polarised parallel to the chain direction. This was already proposed by Pedreschi et al. [180] and can be clearly seen in the calculated slab polarisabilities in Fig. 5.11. This enables it to explain changes in the RAS peak energies directly with changes in the energy of the states involved and new appearing structures as new states.

Although the zig-zag chain model is confirmed by this calculation, particularly the underlying structural model for the (8×2) surface, no detailed information regarding the states involved in the optical anisotropy are yet available. In principle such an analysis can be done using RAS calculations as was shown with great success for other semiconductor surfaces such as the InP(001)-(2×4) reconstruction [190].

The good agreement of the calculated RAS spectra with the measured one can be

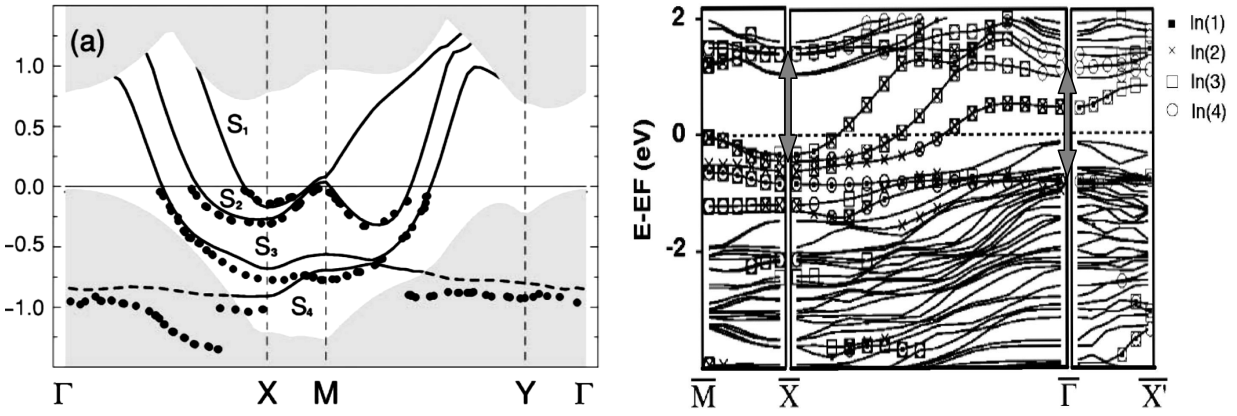

Figure 5.12: *Surface bandstructure calculations of Si(111)-In:(4×1) by Cho et al. [46] (left) and Nakamura et al. [193] (right). The grey shaded area in the left image shows projected bulk states. Only occupied surface states are found in the region without bulk states. In the right graph it can be seen that 2 eV transitions can occur around the $\overline{X}$ or $\overline{\Gamma}$ point. In both cases the three metallic states will be involved.*

used as a strong argument in favour of the model of Cho et al.; that the (8×2) is the real ground state surface, while the (4×1) surface is caused by a thermal disorder in the (8×2) unit cells leading to an effective (4×1) above the transition temperature.

Nevertheless there are other shortcomings of the disorder-order model as will become evident in the Raman measurements and in adsorption studies later in this chapter. I will therefore discuss now whether the model of the CDW formation can also explain the changes in the RAS spectra.

The argument starts with an analysis of the bandstructure of the (4×1) surface, in order to assign the main structures in the (4×1) RAS spectrum to certain electronic state transitions. Figure 5.12 shows two surface bandstructure calculations using DFT-GGA. As can be seen by the data from Cho et al. [46] there are no unoccupied states within the region of the bulk electronic gap. Another calculation by Nakamura et al. [193] shows that there are states localised at surface atoms – although energetically close to bulk states. Such states are also called surface resonances. The large anisotropic feature in the RAS must arise from transitions between surface states or surface resonances. Analysing the data of Nakamura et al. transitions with the right energetic difference may occur either around the $\overline{X}$ or $\overline{\Gamma}$ point. In both cases the three metallic surface states are involved either as ground state ($\overline{X}$) or final state ($\overline{\Gamma}$). The large number of likely states due to the large unit cell can also explain why the RAS structure is rather broad. Even upon cooling, the structure at 2 eV does not narrow considerably as was seen for RAS spectra of other surfaces at low temperatures. This indicates that many states with transition energies between 1.5 and 2.5 eV contribute to this minimum in RAS. Although the assignment to transitions at the $\overline{X}$ and $\overline{\Gamma}$ point needs to be confirmed by more detailed calculations some conclusions regarding the phase transition can already be drawn.

Within the model of the CDW formation, the doubling of the unit cell leads to a

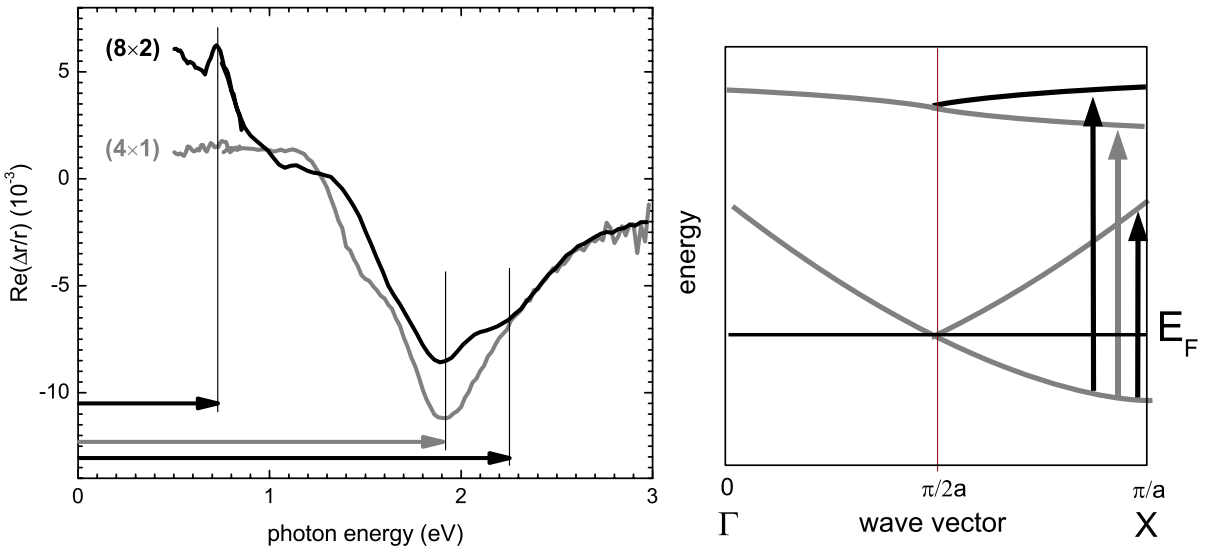

Figure 5.13: *Schematic explanation of the (8×2) RAS by backfolding of bands. If the main structure S_1 arises from a transition from the metallic surface state to a dispersive conduction band, after the phase transition two transitions with a small energy difference occur – the original S_1 now labelled S_a and Sb. The new structure at 0.7 eV S_c could then arise from a transition to the backfolded former metallic state.*

backfolding of the surface bandstructure. In Fig. 5.13 it is shown schematically how such a backfolding can explain the occurrence of the two peaks around 2 eV and the new peak at 0.7 eV as observed for the (8×2) phase. In this very simple picture the complicated bandstructure is reduced to one dispersive conduction band and one metallic surface state. Still the three main structures of the (8×2) RAS spectrum can be explained if the original structure S_1 arises from a transition between these two bands. Unfortunately no analysis of the states involved in the RAS minimum at 2 eV for the (4×1) surface exist so far, which could confirm this model. The situation is furthermore complicated by the numerous bands of this surface. The main point of this simple picture is therefore only, that in principle the backfolding of bands itself – using only the (4×1) bandstructure can explain the RAS spectra of the low temperature surface. This is particularly important for the discussion as to whether the good agreement of the calculated (8×2) surface can be used as an argument in favour of the structural phase transition. Assuming the calculated (4×1) model and its RAS spectrum is correct, it is not surprising that the calculated RAS spectra of a structure with a doubling of the periodicity and only small structural differences also matches the measurements.

I have shown that the differences in the RAS of the Si(111)-In:(4×1) and (8×2) surfaces can be explained in terms of a CDW formation, but also by the calculated structural models – no explanation can be favoured so far. In the next section I will therefore move to the discussion of the vibrational properties of the structure.

5.4 Raman spectra of the (4×1) and (8×2) surface

Concerning the vibrational modes of the Si(111)-In:(4×1) not much was known. A single report concerning surface vibrational modes by Sakamoto et al. showed one mode at 488 cm^{-1} for the (4×1) and two at 480 and 264 cm^{-1} for the (8×2) phase, which were assigned to surface phonons [194]. Since the resolution of HREELS is generally poor compared to Raman spectroscopy and particularly since, due to the high mass of indium, vibrational modes of the metal atoms are expected to be low in frequency, variable temperature Raman measurements were performed. In Fig. 5.14 the Raman spectra of a Si(111)-In:(4×1) surface is shown for two scattering configurations. All modes marked with arrows can be assigned to surface vibrational modes of the Si(111)-In:(4×1) surface, even though some of them occur in the range where bulk phonon modes exist. For comparison spectra of the clean Si(111)-(7×7) surface were measured which show no structures apart from the Si bulk phonon modes. By subtracting the spectra of the clean surface from the one of the Si(111)-In:(4×1), modes arising from surface vibrations only can be seen. The assignment of the observed surface phonon modes to certain atoms in the surface unit cell is also possible – at least for some vibrations. Particularly the strong mode at 427 cm^{-1} can be directly assigned to Si-Si vibrations either in the silicon chain or near surface Si

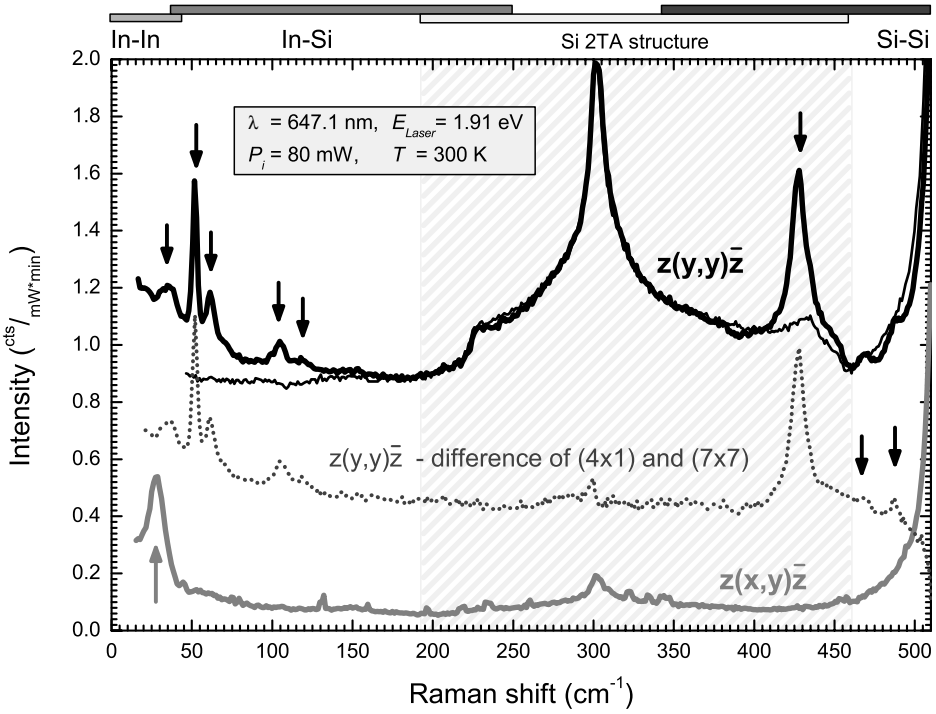

Figure 5.14: *Raman spectra of the Si(111)-In:(4×1) surface measured in two different geometries. For the upper incoming and measured polarisation was parallel to the indium chains and surface phonons are marked with arrows. The spectra of the clean Si(111)-(7×7) surface in the same scattering geometry is given by the thin line. The differences between the indium terminated and clean surface is given by the dotted line. In the case of the lowest curve* $\mathbf{e}_i$ *was rotated by 90°.*

symmetry	ω_0 in cm^{-1}	FWHM ($2w_L$) in cm^{-1}	comments
A''	28 ± 0.9	5.2 ± 1.3	
A'	31 ± 1	6 ± 4	1.91 and 1.83 eV only
	36 ± 2	14 ± 10	possibly two modes
	51.8 ± 0.6	3 ± 1	
	61 ± 1.3	5 ± 2	
	72 ± 3.3	11 ± 9	possibly two modes
	105 ± 1	8 ± 3	two phonon process
	118 ± 1	9 ± 2	
	148 ± 7	16 ± 12	possibly two modes
	428 ± 1	14 ± 4	
	467 ± 1.5	7 ± 7	1.91 and 1.83 eV only
	487 ± 2.6	10 ± 2	1.91 and 1.83 eV only
Γ'_{25}	520.0 ± 0.2	2.5 ± 0.2	silicon bulk

Table 5.1: *List of the identified surface phonon modes of the Si(111)-In:(4×1) surface. Some modes have unusually large FWHM and large errors in the frequency determination. It is possible in these cases that more than one mode is contributing, but since they are weak (148 cm^{-1}) or only shoulders in stronger modes (36, 72 cm^{-1}), no definite answer can be given.*

layers. For the Si(111)-(2×1) surface which only consists of π-bonded silicon chains, surface phonon modes were predicted at 435 cm^{-1} and 412 cm^{-1} [147]. The energy range where In-In or In-Si vibrations are expected can be approximated within the simple harmonic oscillator model ($\omega_0 \sim \sqrt{1/m}$) using the atomic mass of indium and silicon. In Fig. 5.14 these areas are marked. Stimulated by the Raman measurements, calculations of the vibrational properties of the Si(111)-In:(4×1) surface were performed by Bechstedt et al. [186]. Before I directly compare the calculations with the measurements shown in Fig. 5.14, measurements with different incident photon energies have to be analysed, since due to resonance certain modes are more pronounced at different laser energies. Figure 5.15 compares the normalised intensities $I/I_{Si,\Gamma'_{25}}$ with those corrected for penetration depth and the resonance of the silicon bulk mode as described in detail in section 3.4.4 by using the penetration depth calculated from the dielectric function in nm and the values for $S_{Si,\Gamma'_{25}}$ from [112]. With the corrected spectra, peak positions and amplitudes were derived with the fitting procedure described in 3.4.5.

In table 5.1 the result of this fit procedure is given for all identified surface modes. The given frequency of a mode ω_0 is the mean value of all fitted spectra at different incident laser energies. The error is estimated by the quadratic sum of the mean

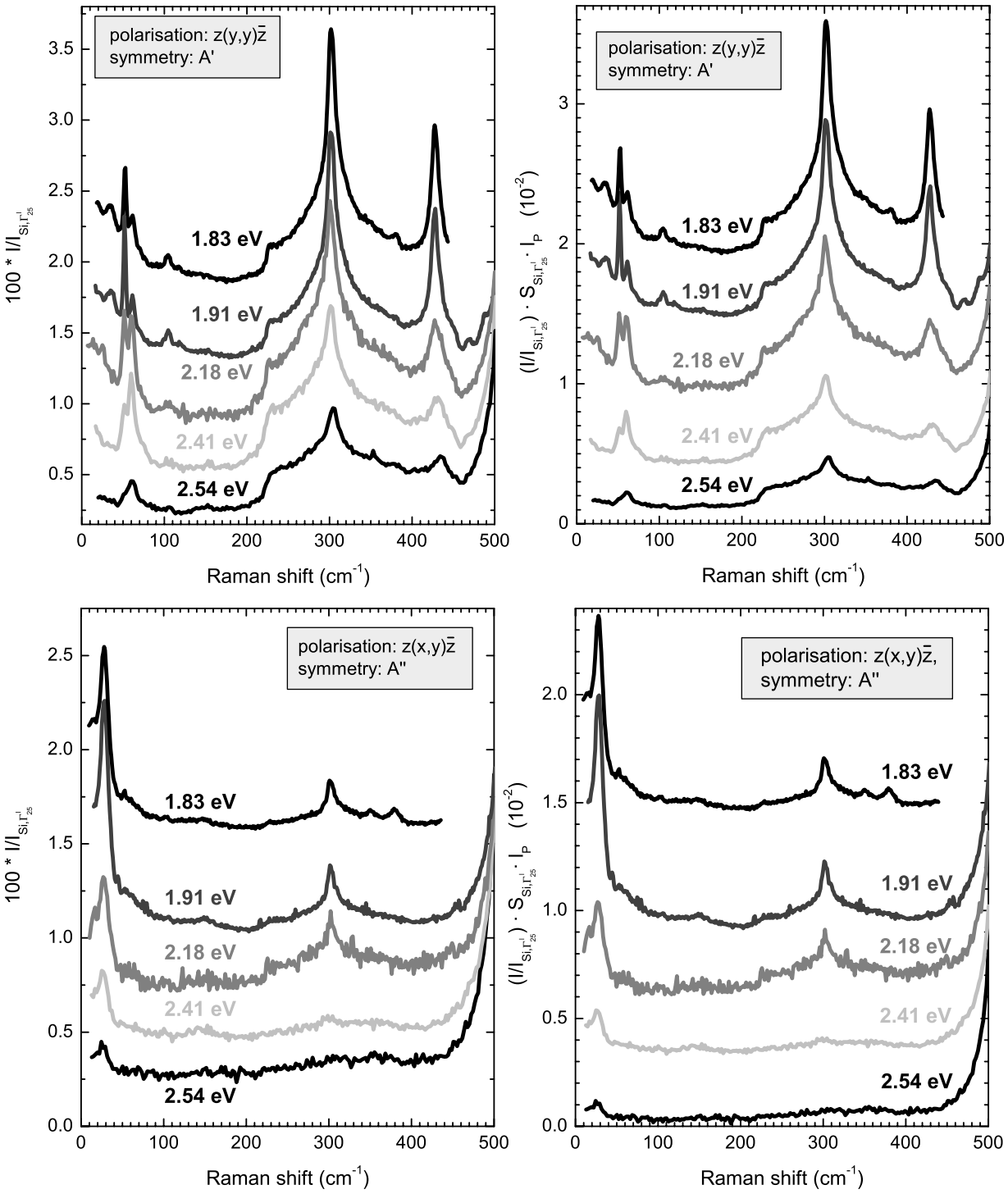

Figure 5.15: *Raman spectra of Si(111)-In:(4×1) for several photon energies. The left graphs shows the as measured spectra normalised to the Si* Γ'_{25} *mode. The right graph shows spectra corrected for the difference in the scattering volume for bulk and surface phonons and the resonance of the Si* Γ'_{25} *mode. The upper graphs show modes in A′ symmetry, where the polarisation vector of the incident* $\mathbf{e}_i$ *and scattered* $\mathbf{e}_s$ *light was perpendicular to the chain direction. For the lower graphs* $\mathbf{e}_i$ *was parallel to the chain direction, while* $\mathbf{e}_s$ *was perpendicular to the chains (A″ symmetry modes). All spectra were stacked for better visibility.*

individual error of the fit itself[2] and the standard deviation of the peak position for various measurements. The given width of the mode is the Lorentzian full width half maximum (FWHM). Again the error of this is estimated by the confidence interval of the fit itself and the standard deviation of the results for various incident laser energies. Most modes are not only much weaker but also broader than the silicon bulk mode. In some cases though the determined line width is unusually large (36, 72, 148, 487 cm^{-1}) an indication that more than one mode are close together. For the 487 cm^{-1} mode this was tested by high resolution measurements – but no difference in line shape was found. For the low energy range high resolution measurements could not be performed due to the increased elastic background by the reduced stray light reduction of this measurement configuration.

Another special case are the structures found at twice the energies of the strongest low energy modes at 52 and 61 cm^{-1}. It is likely that the structures at 105 and 118 cm^{-1} are no modes for themselves but two phonon processes. This explanation will be further supported by the low temperature measurements.

In addition to the peak positions and line widths the intensity was also derived from the fits. The corrected amplitudes of the modes are proportional to the Raman susceptibility. Figure 5.16 shows this value for several identified modes. It can be easily seen that most surface phonon modes are resonant below 2 eV – the same energy where also the strongest anisotropy in the reflectance of the surface occurs.

[2] Usually a confidence interval is given by the fit program – here "Peakfit V4"

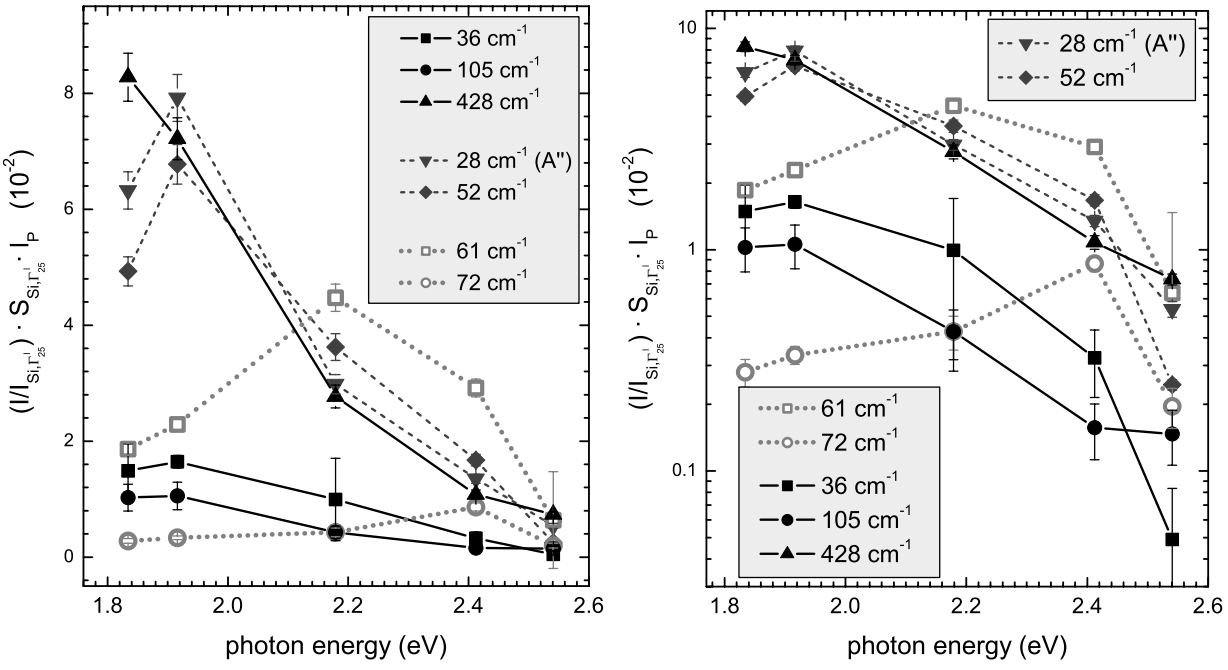

Figure 5.16: *Intensity of some surface phonon modes with incident photon energy. The left graph shows the intensity linearly scaled while the right graph uses a logarithmic axis. Most modes are strongest at 1.83 eV (solid curves). Some (28, 52 cm^{-1} – dashed) are strongest at 1.91 eV, while others (61, 72 rcm – dotted) are resonant above 2 eV.*

symmetry	measured (cm^{-1})	calculated modes (cm^{-1}) [186, 195]		
		surface	resonance	bulk
A″	28	**15**, **21**		
	–		51	55
	–	79		
	–		81, 109	114, 158
	–	*421*		435, 447
	–			457, 481
A′	31, 36	**31**, **42**		
	52	**54**		48
	61			67
	72			78
	105	104	93	
	118	109	129	
	148		129, 140	
	–			201, 211, 245
	–	255		274, 293
	–		303, 314	
	–		394	384, 401
	428	*411*		416, 430
	468			444, 459
	487			470

Table 5.2: *Comparison of measured Si(111)-In:(4×1) phonon modes with calculations from [186, 195]. The calculated modes with the strongest displacement within the first atomic layer are labelled "surface". Modes with no considerable displacement within the first layer are labelled "bulk", while those with displacement both in all layers are labelled "resonance". Surface modes with displacement patterns involving only indium atoms are additionally set in bold. If the silicon chain contributes dominantly the value is set in italic. A visualisation of all calculated modes is available at* `http://gift.physik.tu-berlin.de/pub/In-Si-modes/`. *The assignment to measured modes is not unique and is based only on the calculated energy and symmetry of the mode.*

Only the modes at 61 cm^{-1} and 72 cm^{-1} show different resonances at 2.2 eV or 2.4 eV respectively. Unfortunately the measurements for photon energies larger than 2 eV show a worse signal to noise ratio, caused by the low available laser power in the case of the 2.18 eV, yellow Kr^{+}-laser line and the poor quantum efficiency of the CCD array at higher energies. Nevertheless the resonance below 2 eV is evident and also the different behaviour of the 61 cm^{-1} mode.

After the determination of the frequencies of the surface phonons it is now possible to compare the measured modes with calculations. In Table 5.2 the frequency of all modes observed is given in comparison to calculations by Bechstedt et al. [186]. The ground state atomic positions were derived from DFT-GGA calculations and were comparable to the ones found by Cho et al. [46] and Wang et al. [176]. Details of the phonon mode calculations are given in [186]. Basically atomic force constants are derived by displacing each of the 14 topmost atoms of the slab by 0.01Å in each Cartesian direction. The restoring forces are then calculated. Together with the known atomic masses, the Eigenvalues of the resulting 42×42 dynamical matrix can then be calculated leading to 42 vibrational modes – 28 in A' and 14 in A'' symmetry. The latter ones can be seen in Raman spectra with crossed incoming and scattered polarisation, while the A' modes can be seen for parallel polarisation. However an assignment of the 42 calculated modes to the 12 measured ones is not straight forward, since there is a deviation from calculated energies and measured ones due to the small slab size. Additionally the large number of modes and, particularly for low energies, small energetic differences make an assignment difficult.

5.4.1 Monitoring of the phase transition

For the RAS measurements it was already shown that the phase transition can be monitored *in-situ*. For Raman measurements this is not as easy. The Raman setup used in this work was equipped with a CCD. Therefore it was not possible to measure transients for a certain Raman shift. Instead spectra were taken using the shortest integration time possible, but long enough to observe the weak surface phonon modes. Unfortunately the signal to noise ratio of these measurements is still rather poor. For technical reasons it was also impossible to stabilise the temperature with the inbuilt sample heating, since this produced a strong background illumination, which made Raman measurements impossible. The only possible measurement was to take spectra with 5 min integration time during cooling at the lowest possible stable cooling rate of -1 K/min. In Fig. 5.17 the spectra taken during these measurements are shown. All spectra shown in the plot taken were between 240 K and 60 K. The Raman intensity is coded in grey scales – the highest intensity in white, the lowest in black. Hence every horizontal line represents one spectrum. The peak position of the strongest modes of the (4×1) phase at 35, 52, 62 and 105 cm^{-1} are marked with white boxes.

Below 120 K the Raman spectra start to change. Again at around 80 K the changes are mostly completed, though the intensities of the new modes are still changed if the sample is cooled further. The temperature range in which the changes occur is the same as found in the RAS experiments. At low temperatures many more modes can be seen in comparison to the room temperature phase already for these short

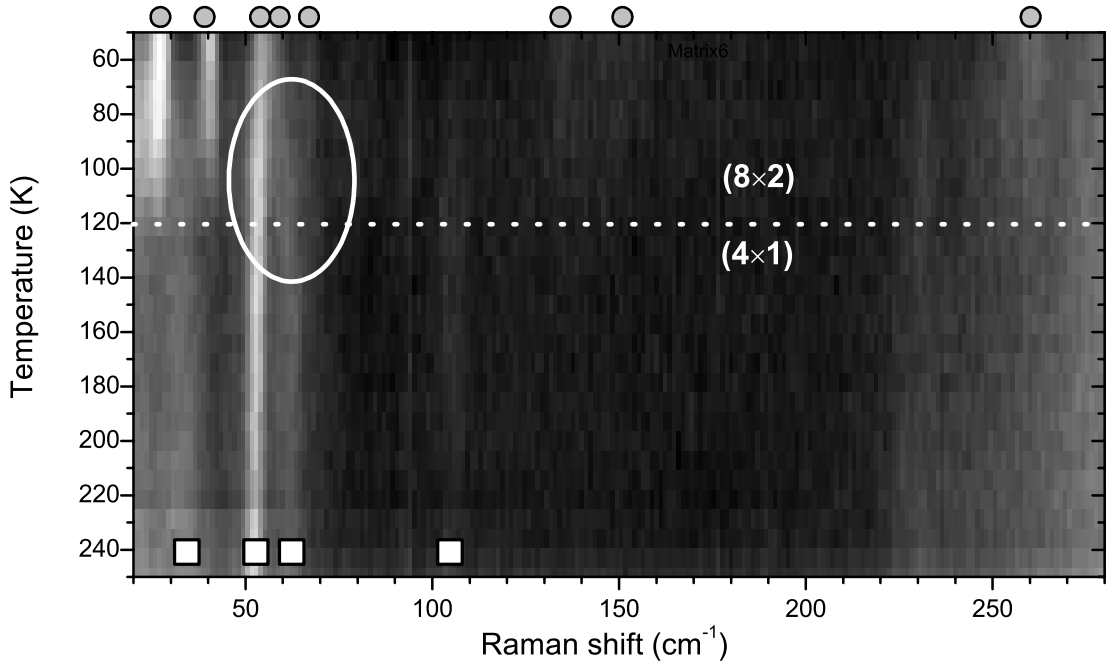

Figure 5.17: *Raman spectra of the Si(111)-In:(4×1) surface upon cooling. The spectra are shown coded in grayscales – the highest intensity in white, the lowest in black. Each horizontal line represents one spectrum, taken at the temperature as indicated in the y-axis. Around 120 K the Raman spectra change. Most prominent changes are the appearance of two strong modes at 28 and 40 cm^{-1} evolving out of the 35 cm^{-1} room temperature mode and the gradual shift of the mode at 62 cm^{-1} (white ellipse). The grey circles mark surface phonon modes found for the low temperature phase in these rather noisy spectra.*

integration time spectra. The new modes appearing will be discussed in detail in the next section, where spectra taken at 40 K and longer integration times will be analysed.

Although there are new modes appearing it is also noteworthy that the most dominant mode for the room temperature phase at 55 cm^{-1} is almost unchanged apart from a small blue shift. The same can be said for most of the weaker modes. Most interesting is the behaviour of the room temperature mode at 62 cm^{-1} (marked with the white ellipse in Fig. 5.17). Upon the phase transition it gradually shifts from 63 cm^{-1} at 120 K to 58 cm^{-1} at 60 K – showing therefore an unusual and unexpected red shift. As one will remember, this mode additionally shows an unexpected resonance at 2.2 eV – the energy where a structure in the low temperature RAS also occurs.

5.4.2 Raman spectra of the Si(111)-In:(8×2) surface

Before I discuss the differences of the (4×1) and (8×2) spectra and how they can be understood in terms of the formation of a CDW, the spectra of the low temperature phase needs to be analysed in the same detail as those of the room temperature phase.

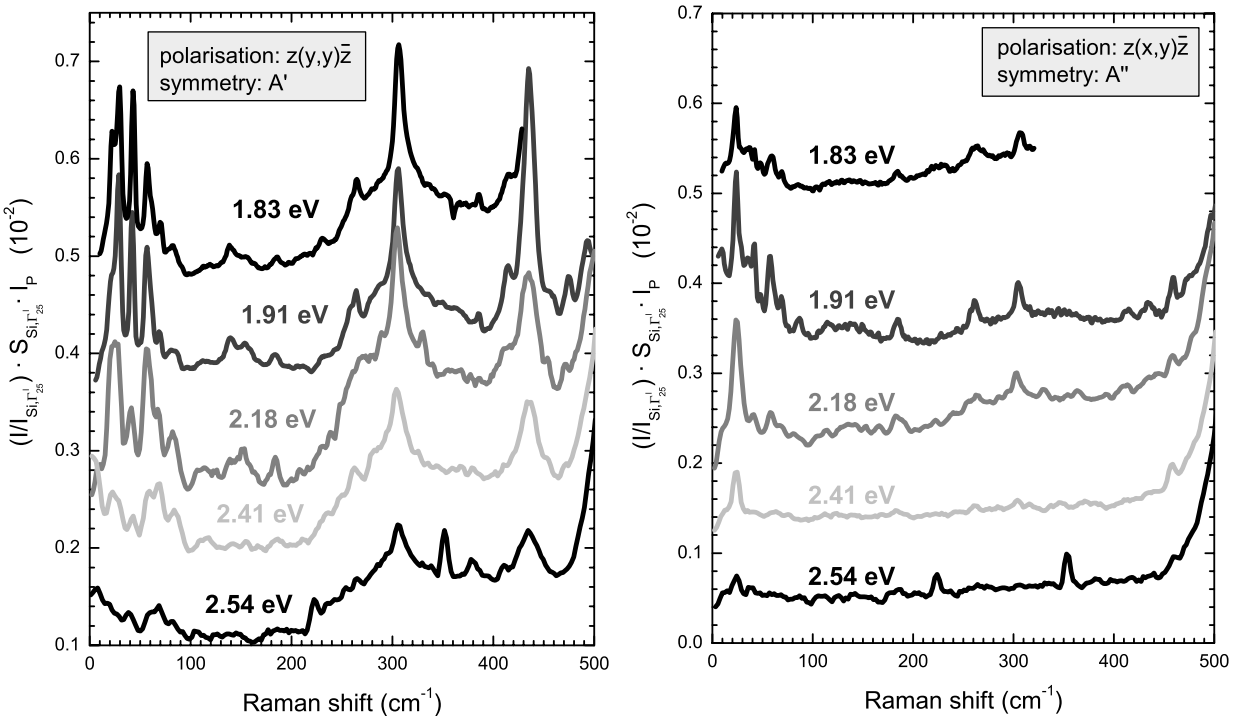

Figure 5.18: *Raman spectra of the (8×2) low temperature phase for A′ (left) and A″ symmetry (right). Several new modes are found for the low temperature phase, though most modes already found for the (4×1) surface still exist.*

Figure 5.18 shows the spectra taken for several incident photon energies. Many more modes are observed than for the room temperature phase, as expected for the larger unit cell. The most dominant change in the Raman spectra are two strong modes appearing at low frequencies at 29 cm^{-1} and 42 cm^{-1}. In this spectral region only two weak modes were found for the (4×1) surface (31, 36 cm^{-1}). Since the electronic surface states are changed upon the phase transition as well, one cannot exclude the possibility that these strong modes are resonantly enhanced for the (8×2) phase but not for the (4×1) phase. Therefore one has to analyse the resonance behaviour also for the low temperature phase.

In order to compare the intensities of the measured phonon modes for several incident photon energies a similar correction is done as was described for the room temperature measurements. Again the spectra are normalised for the Si bulk Γ'_{25} mode at 524 cm^{-1} and corrected for the resonance of the bulk phonon and the different scattering volume. Unfortunately there is no direct measurement of the Raman cross section for the Si bulk mode at low temperatures available. In Fig. 5.19 the measured Raman cross section for room temperature is compared to $|\partial\varepsilon/\partial\omega|^2$ calculated from ε as given in [74]. It can be seen that in this spectral range, there is a reasonable agreement with the measured cross section. Since the low temperature dielectric function for silicon is known as well [188], a similar quantity can be calculated for 30 K. To account for the deviation of the experimentally found cross section and the theoretical value from the macroscopic theory the calculated values for the low

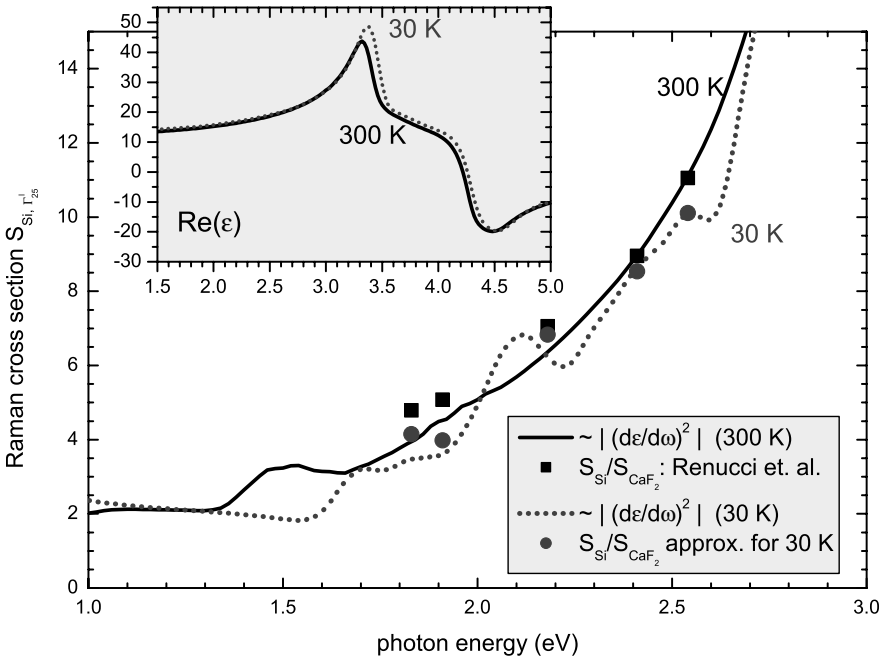

Figure 5.19: *In contrast to 300 K the Raman cross section for the Si Γ'_{25} was not found in the literature. The known values for 300 K are given in black squares (taken from [112]). The black line shows the $|\partial\varepsilon/\partial\omega|^2$ approximation for 30 K and the dotted line for 30 K (calculated from the dielectric function given in [74] and [188] (see inset). The grey circles denote the values used for correction of the LT Raman spectra as described in the text.*

temperature measurements were scaled by the same factor as the measured values deviate from the calculations for the room temperature case. The values found are shown in Fig. 5.19 as grey circles.

The spectra in Fig. 5.18 were corrected using $S_{Si,\Gamma'_{25}}$ for 30 K and the penetration depth (in nm) calculated from the low temperature dielectric function from [188]. The number of modes which can be identified for the (8×2) surface is huge. For A' symmetry 16 modes could be identified, since they were found for all incident laser energies, though there are indications of more modes in the spectra with the best signal to noise ration taken for ω_i = 1.91 eV. For the (4×1) only 8 modes were found. For the A'' symmetry the increase in the number of confirmed modes is even larger, since only one mode was found for the (4×1) but 9 for the low temperature (8×2) phase. For symmetry reasons the number of possible surface modes for the (8×2) should be 4 times larger, since the number of atoms per unit cell is increased likewise by the doubling of the unit cell in the two directions.

In table 5.3 the phonon modes derived from the fits of all measured spectra as shown in Fig. 5.18 are listed. Again for some structures it is likely that more than one mode is contributing. For the measurements with the best resolution and also highest available laser power (1.91 eV) the signal to noise ratio is considerably better than for most of the other measured laser energies. In this case even more modes can be identified. These cases are indicated by the comment “possibly 2 modes” in the

symmetry	ω_0 in cm^{-1}	FWHM ($2w_L$) in cm^{-1}	comments
A''	23.5 ± 0.8	4 ± 1.5	possibly 2 modes
	42 ± 3.5	8 ± 5	possibly 3 modes
	59 ± 3	8 ± 6	possibly 2 modes
	69 ± 1.5	4 ± 1.5	
	85 ± 1.7	8 ± 4	
	184 ± 0.7	7 ± 3	
	262 ± 2	12 ± 7	
	458 ± 1.2	3 ± 1.5	
A'	21 ± 1.6	4 ± 3	
	28 ± 1.3	4 ± 2	
	41 ± 2	4 ± 2	
	57.2 ± 0.7	5 ± 2	
	62 ± 1.5	3 ± 4	
	69 ± 1.1	5 ± 4	
	83 ± 2.3	7 ± 6	possibly 2 modes
	100-130	-	broad structure
	139 ± 1.2	11 ± 6	possibly 2 modes
	154 ± 2	7 ± 6	possibly 2 modes
	185 ± 2	12 ± 8	possibly 2 modes
	255 ± 4	7 ± 6	
	264 ± 3	7 ± 4	also in HREELS [194]
	412 ± 2.5	10 ± 8	
	435.1 ± 0.7	22 ± 10	
	473 ± 2	4 ± 4	also in HREELS [194]
	495 ± 5	18 ± 14	
Γ'_{25}	523.6 ± 0.8	0.9 ± 0.2	silicon bulk

Table 5.3: *List of the identified surface phonon modes of the Si(111)-In:(8×2) surface. For several modes more than one structure is likely to contribute, though they could be only resolved for the spectra with the highest resolution and signal to noise ratio (1.91 eV). The errors are given by the quadratic sum of the standard deviation of the measurements and the mean error of each fit itself (confidence interval). The Gaussian width of the Voigt profile was kept constant for all modes measured with the same incident laser energy, since the broadening of the experimental setup is quantified by w_G. The larger errors, compared to the RT measurements, in the determination of the energetic position but even more in the Lorentzian line width w_L, is caused by the large number of peaks which needed to be fitted. If two modes, separated by less than their own line width are fitted, the confidence intervals increase drastically.*

table.

Originally these experiments were performed to quantify the changes in the atomic positions upon the phase transitions. Due to some technical problems[3] Raman measurements with acceptable signal to noise ratio could not be performed at 140 K. For the majority of modes only room temperature spectral positions can be compared to the low temperature results. This complicates a discussion of energetic shifts in certain phonon modes upon the phase transition. Nevertheless a detailed comparison will be done.

5.4.3 The difference of the (4×1) and (8×2) Raman spectra

By analysing the modes found for the room temperature (4×1) and the low temperature (8×2) phase several similarities but also distinct differences can be seen. The question arises how this can be understood in terms of the charge density formation or, alternative, by the structural reordering.

Energetic shift

Whenever spectra taken at different temperatures are compared energetic shifts of the phonon modes are expected, since upon heating phonon modes are generally red shifted. This can be understood in terms of anharmonicities in the potential which lead also to thermal expansion and red shifts of critical point energies (see review article [187]). For bulk materials the expected shifts have long been known and can be described well by theory. The Γ'_{25} bulk mode of silicon for instance is found at 520 cm^{-1} at room temperature and at 524 cm^{-1} below 100 K. A similar shift is hence expected for the measured surface phonons. For the strongest modes, which can be found in both phases, the shift upon cooling is -4.5±1.2, 5.4±0.9 and 7±1.2 cm^{-1} for the 28, 52 and 428 cm^{-1} mode of the (4×1) surface respectively. The observed shift is larger than the one for the bulk silicon mode. The large shift is particularly surprising for the low energy surface phonons, especially for the 28 cm^{-1} phonon where a red shift is observed. If spectra taken upon cooling are analysed in more detail for the energy region of the In-In vibrations (below 80 cm^{-1}, Fig. 5.20) this discrepancy can be partly understood. The energetic shift due to the anharmonicity is expected to be saturated around 100 K [187, 196–198]. If spectra for various temperatures are again plotted in grayscales, the mode at 52 cm^{-1} appears as a straight white line in Fig. 5.17 and Fig. 5.20. In Fig. 5.20 it can be seen that this mode is already found at 54 cm^{-1} for 180 K. Further cooling does not change the energetic position anymore. The shift to 57 cm^{-1} occurs at temperatures well below 120 K, where no further temperature related shift is expected. One can therefore conclude that atoms involved in this vibrational mode do change their average position upon the phase transition. The shift nevertheless is gradual, since the phase transition is a gradual process, which is only fully completed below 60 K as one has already seen for the low temperature RAS measurements.

I have shown so far that the energetic shifts upon cooling and the phase transition for vibrational modes which are found on both phases are larger than expected for a

[3] background light due to the necessary heating of the samples

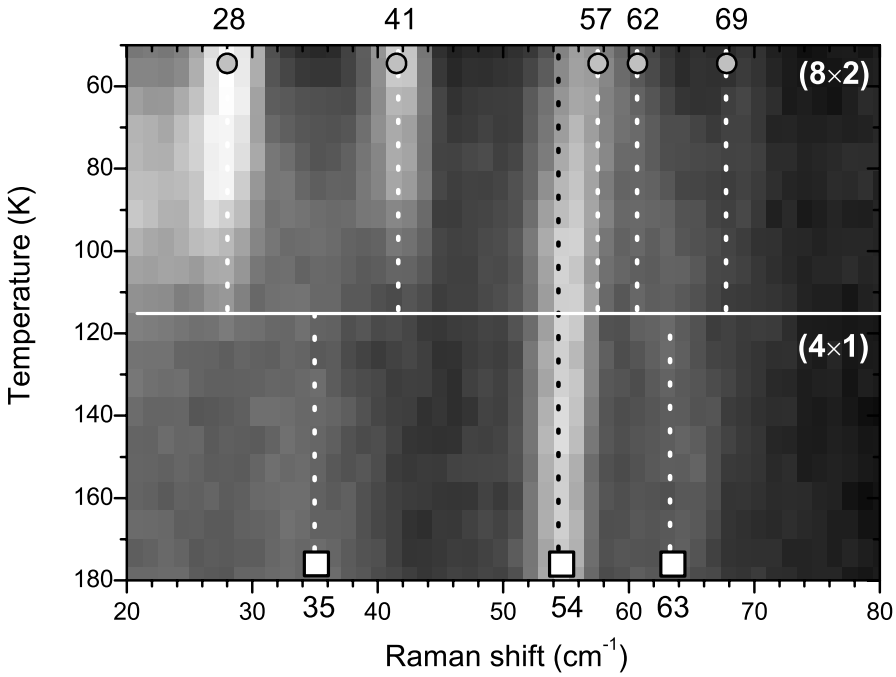

Figure 5.20: *Raman spectra of the Si(111)-In:(4×1) surface upon cooling. The spectra are shown coded in grayscales similar as in Fig. 5.17. Here only the modes related to In-In vibrations are shown below 80 cm^{-1}. The energetic shift of the 52 cm^{-1} below the transition temperature can be seen more clearly in this graph. Additionally the splitting of the 33 cm^{-1} and 62 cm^{-1} is indicated schematically by the white dotted lines.*

merely temperature related shift. In the case of the 52 cm^{-1} this can be even quantified. The temperature induced shift is approximately 2 cm^{-1}, while the shift introduced by the change of atomic positions upon the phase transition is 3 cm^{-1}. In a linear model this would correspond to changes of the In-In bond length of 5%. This is comparable to the reported changes in the atomic positions upon the phase transition [48] and also with the *ab-initio* calculations of the positions for both phases [46, 166, 176].

Another conclusion can be already drawn. A drastic change in the bonding configuration of the surface layer such as an In-trimer formation, as was suggested in [48], is unlikely. In such a case larger shifts or the complete disappearance of modes would be expected, since the local symmetry of the bonds would be changed.

Disappearing modes

As just mentioned the disappearance of modes would be a strong indication of drastic changes of the surface geometry upon the phase transition. In Fig. 5.21 the spectra of the (4×1) and (8×2) in the most interesting regions below 200 cm^{-1} and above 400 cm^{-1} is shown. Whenever there is a mode found for the (4×1) surface there is at least one, but usually more modes are found for the (8×2) surface at the same energy or near by. Only in the case of the two modes found at 105 and 118 cm^{-1} is this not true. A weak broad structure is found in this energetic region for the (8×2) surface. The two strongest modes of the (4×1) surface are found at 52 and 61 cm^{-1} which is exactly one half of the modes under discussion. There is the possibility

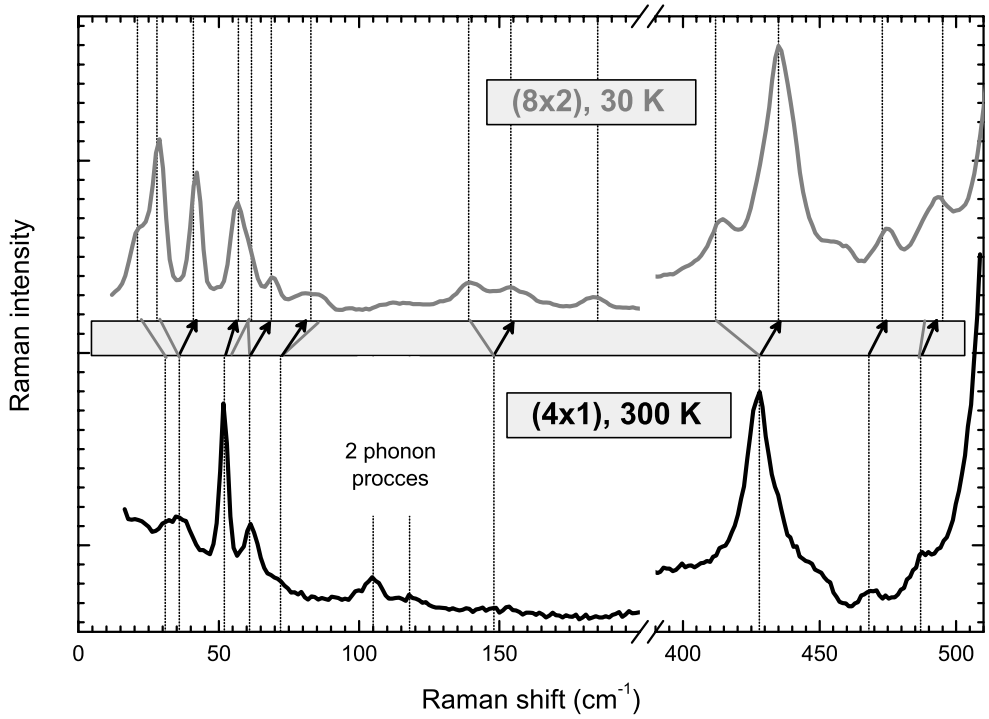

Figure 5.21: *Comparison of the A″ modes of the (4×1) and (8×2) phase. The shown spectra were taken with an incident laser energy of 1.91 eV, where the best resolution can be achieved and the laser power is high enough to achieve good signal to noise ratios. The energetic positions of the identified surface phonons are marked for both phases with vertical dotted lines. For the low temperature (8×2) phase the modes are usually blue shifted (black arrows) but new modes also appear, possibly due to backfolding of original modes (indicated by grey solid lines).*

that the structures at 105 and 118 cm^{-1} are caused by second order Raman scattering involving two phonons simultaneously. Such a process is unlikely and therefore weaker than the first order process. Even more important the process gets less likely at low temperatures, were the occupation numbers of the phonons are decreased [125, 199]. Two phonon structures are therefore much weaker at low temperatures as can be also seen for the 2TA silicon bulk structure in Fig. 5.15 for 300 K and Fig. 5.18 for 30 K. Assuming that the measured structures at 105 and 118 cm^{-1} are such second order processes it is therefore expected that they will be weaker at low temperatures. The broad and weak structure in the energy region of 100-130 cm^{-1} is most likely the remaining second order structure at low temperatures.

New modes and line broadening

The most prominent change of the Raman spectra of the Si(111)-In:(8×2) surface are the newly appearing modes. To some extent this can be explained by the better signal to noise ratio for low temperature measurements which makes the detection of weaker modes possible. Secondly the energetic shift in the bandstructure upon

cooling can change the resonance of certain modes. This will be discussed in detail later. The main reason though for new modes for the Si(111)-In:(8×2) is the increased number of atoms per unit cell. In the original Si(111)-In:(4×1) surface the top layer consist of 4 indium and 2 silicon atoms. The Si(111)-In:(8×2) unit cell contains 16 indium atoms and 8 silicon atoms – four times more. The number of microscopic surface modes should therefore be increased by the same factor.

The number of measured phonons is nevertheless much smaller than the theoretical maximum number of vibrational modes. The reasons for this are manifold. First the Raman cross section for the individual modes can differ greatly. There is always the possibility that a mode is just too weak to be observed with the available incident photon energies. The second and probably most important reason is the limited resolution of the measurements. By closing the entrance and exit slit of the monochromator to $d_{\mathrm{slit}} = 100\mu\mathrm{m}$ and using incident laser light close to the maximum of the sensitivity of the CCD array (E_i=1.91 eV) the best resolution of approximately 1.5 cm^{-1} was achieved. In the case of the Si(111)-In:(8×2) there is no reason why, for instance, microscopic In-In vibrations in the two adjacent rows spaced by the silicon zig-zag chain should differ. It is unlikely that an energetic difference due to the different phase of the lattice distortion for the (4×2) or (8×2) model (see Fig. 5.7, p. 62) can be measured. Consequently only a (4×2) unit cell need to be discussed for the measured spectra. The doubling of the number of surface phonons expected in that case is close to the observed numbers (10 for the (4×1) and >16 for the (8×2)).

Similar to the (4×1) surface, there exist calculations of the phonon frequencies for the low temperature phase by DFT-LDA [195]. Since the (8×2) unit cell is too large for such a calculation only a (4×2) unit cell was considered, though as already stated above, no great difference in the phonon energies between the (8×2) and (4×2) model are expected. Unfortunately the (4×2) was still to large for a calculation treating some subsurface silicon layers. This makes a comparison with the results for the (4×1) surface even more complicated. In table 5.4 the results of the calculation are compared with the measurements of the Si(111)-In:(8×2) Although the number of calculated modes is much smaller, since only vibrations in the top layer were considered, the assignment of calculated modes to measurements is rather complicated. By examining the calculated displacement patterns of the (4×2) surface one does not find many similarities with the calculations for the (4×1) surface. This is most likely only caused by the different number of layers treated in the calculations. For a meaningful comparison, calculations are necessary using the same number of atoms but different atomic positions for the two surfaces.

Some conclusions can be drawn from these calculations in any case. First no modes are calculated in the energy region above 410 cm^{-1}. But at least 4 were measured. For the (4×1) surface such modes were calculated, confirming that all measured modes in this energetic region are located in the near surface silicon layers. There is a good agreement of the (4×2) calculations only in the low energy region below 100 cm^{-1}. Most of these modes are In-In vibrations. This proves two points: *(i)* all changes in the energetic positions upon the phase transition as discussed above can indeed be attributed to changes in the indium position, *(ii)* the doubling of the periodicity perpendicular to the chain direction does not directly influence the measurable number of In-In vibrational modes.

symmetry	measured (cm^{-1})		calculated modes (cm^{-1}) [186, 195]	
	$(4\times1)_{300K}$	$(4\times2)_{30K}$	$(4\times1)_{surface}$	(4×2)
A″	28	23.5	**21**	20, 23
		42		
		59		60, 65
		69		68, 70, 74
		85		78, 99
		184		
		262		313, 323
		458	*421*	420
A′		21		
	31	28	**31**	31
	36	41	**42**	49, 53
	52	57.2	**54**	57
		62		64
	61	69		
	72	83		82, 87, 90
	105,108	100-130	104, 109	99, 105, 110, 117
		139		128, 144
	148	154		150, 164
		185		175
		255	255	221, 245
		264		263, 267
		–		316, 333
		412		
	428	435	*411*	408
	468	473		
	487	495		

Table 5.4: *Comparison of measured Si(111)-In:(8×2) phonon-modes with calculations from [195]. For comparison the measured modes of the (4×1) surface and calculated (4×1) modes which are located in the top surface layer only from table 5.2 are given as reference. A visualisation of all calculated modes is available at* `http://gift.physik.tu-berlin.de/pub/In-Si-modes/`. *In contrast to the calculations for the (4×1) surface no underlying silicon bulk layers was considered.*

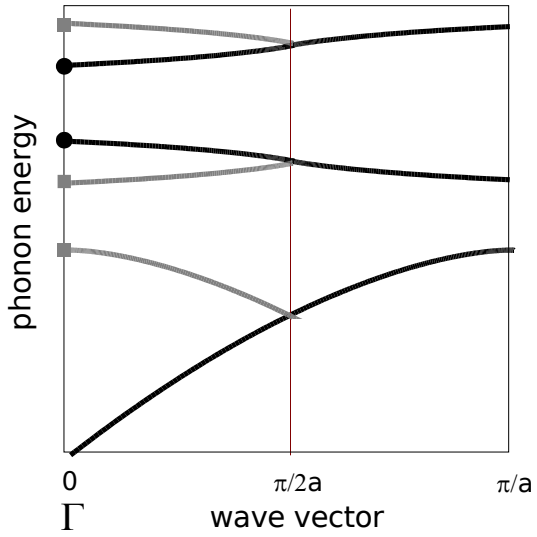

Figure 5.22:
Backfolding of phonon branches upon the doubling of the unit cell. Depending on the dispersion of the original phonon mode the new modes occur at higher and lower energies of the original mode. The stronger the dispersion the larger the energetic difference of the original and the newly appearing mode

Even without the calculations a simple model can be given, explaining the newly appearing modes but also the unusual broadening of some measured modes upon cooling. By the doubling of the unit cell in the chain direction a backfolding of the phonon branches is expected. In Fig. 5.22 this is shown schematically. Depending on the dispersion of the original mode new modes can appear either at higher or lower energies than the original mode. In the case of the Si(111)-In:(8×2) surface the Raman spectrum can be understood by the backfolding of phonon branches of the original Si(111)-In:(4×1) surface, first by the doubling of the unit cell along the chain direction and another by the doubling perpendicular to the indium chain direction. Since no detailed information about the dispersion of the Si(111)-In:(4×1) surface modes exist, the model cannot be tested directly. Nevertheless if the dispersion of the phonon branches is small the backfolding can explain the broadening of modes since the new mode is very close to the original mode. If the dispersion is stronger, particularly for acoustical phonons of the (4×1) surface, upon the phase transition new modes will appear, such as the strong low energy modes at 28 and 41 cm^{-1}.

Changes in measured amplitudes

The last difference of the (4×1) and (8×2) Raman spectra are the changes in the measured amplitudes. For certain modes there is a drastic increase in the measured amplitude as can be seen directly in Fig. 5.20 and 5.21. Other modes such as the one at 52 cm^{-1} are not changed. One possibility are resonance effects, since as already shown in the RAS measurements the surface bandstructure and also the optical transition energies are changed upon the phase transition. In Fig. 5.23 the intensity of the strongest modes is shown versus the incident photon energy for both the (4×1) and (8×2) surface. For both surfaces modes are found to be resonant not only in the red spectral region but also above 2.2 eV. In the case of the (4×1) surface only two modes are resonant above 2 eV while for the (8×2) surface many modes are resonant in this energy region (particularly the weaker modes which are omitted in Fig. 5.20 for clarity.

Within a classical macroscopic model the resonance of phonon modes in Raman spectroscopy can be related to the susceptibility of the sample, since the amplitude

was found to be proportional to $|\partial\chi/\partial\omega|^2$. For the surface modes a similar behaviour is expected. The only known quantity for the surface layer dielectric properties are the RAS measurements. But the RAS spectra can be related to the surface dielectric anisotropy only not to the dielectric function (and hence χ). Fortunately in the calculation of the RAS spectra based on the current models for the (4×1) and (8×2) spectra a quantity is calculated – the slab polarisability $\underline{\underline{\alpha}}$ – which is related to the dielectric function of the surface layer: $\varepsilon_{ij} = \delta_{ij} + 4\pi\alpha_{ij}$ [139, 200] (see also Fig. 5.11). $|\partial\alpha/\partial\omega|^2$ is proportional to $|\partial\chi/\partial\omega|^2$ and can therefore also be used to describe the resonance of the surface phonon modes. In Fig. 5.23 it can be seen that this approximation based on the DFT-LDA calculation gives only a qualitative agreement, explaining the resonance in the red spectral region. For the (8×2) surface a second resonance above 2 eV can also be seen. Nevertheless for the (4×1) surface, certain modes are resonant above 2 eV where no such resonance is calculated.

Until now the number of incident photon energies where Raman spectra were measured is too small to draw definite conclusions from this analysis. In principle these kinds of measurements, together with more detailed calculations which deconvolve the response from particular electronic states, can help to understand how the surface vibrations are coupled to the electronic states.

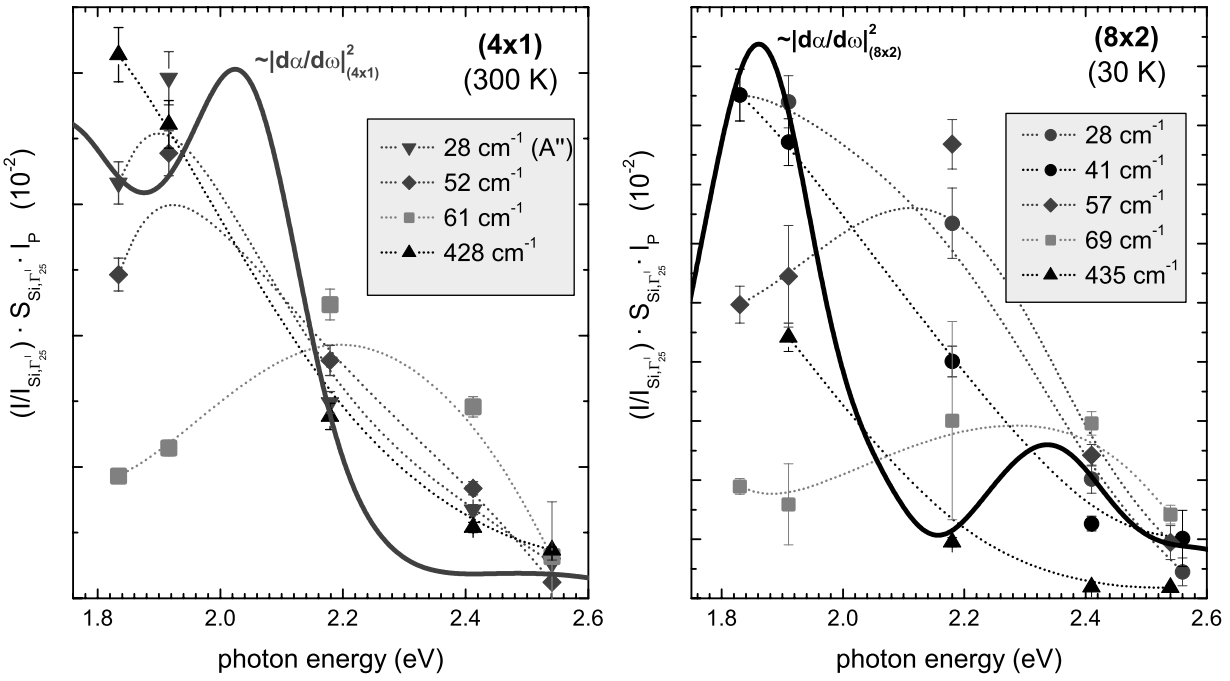

Figure 5.23: *Comparison of the surface phonon resonance of the (4×1) and (8×2) phase. For the (4×1) the resonance in the red spectral region can be well understood in a macroscopic model by using the first derivative of the surface polarisability α (solid lines). The only exception is the phonon at 61 cm^{-1} with a different resonance behaviour. For the low temperature surface the situation is more complex. Still there is a resonance below 2 eV for most modes but many are also enhanced around 2.2 eV. This can be at least qualitatively understood by the doubling of the main structure in the polarisability (see also 5.11).*

5.4.4 Consequences for the discussion of the conflicting models

To summarise this part I will shortly review the main conclusions which can be draw from the Raman measurements: *(i)* the two phases have very distinct Raman spectra. *(ii)* the phase transition can be monitored by observing the changes in the Raman modes of the surface phonons. *(iii)* for the low temperature phase many more modes are found and *(iv)* most modes of the (4×1) surface are found on the (8×2) phase as well, showing only changes in intensity and small changes in frequency. This fact rules out the proposed formation of trimers as the driving force of the phase transition since drastic changes are expected for a complete change of the In-In bonding configuration. Nevertheless the changes in the phonon frequencies upon the phase transition are in agreement with measured as well as calculated positional changes.

For the discussion as to whether the phase transition is driven by a CDW formation or whether an order–disorder transition occurs the Raman spectra cannot give a conclusive answer. In both cases the changes observed can be explained by the backfolding of phonon branches which are expected for both models. Some aspects though contradict an order–disorder transition. The occurrence of the two strong modes at 28 and 41 cm^{-1} for the (8×2) surface itself, where only a weak broad mode at 36 cm^{-1} is found for the (4×1) surface even at 150 K, can be easily understood if the atomic positions of the atoms involved in this transition do vary due to a thermally activated disorder. Nevertheless other modes on the (4×1) surface have exceptionally narrow line widths although the calculated displacement pattern show that the same indium atoms are involved in all these low energy modes. It is therefore hard to understand why some modes should be completely unaffected by the thermally induced disorder. Furthermore the most prominent modes of the (4×1) surface (52 and 428 cm^{-1}) are broadened at the phase transition which cannot be understood in the order–disorder picture at all.

The Raman measurements in the temperature region of the phase transition reveal changes in the phonon frequencies which confirm the changes in the atomic positions of the order of 5-10% changes in bond lengths of the indium atoms as found in GIXRD measurements [48, 178] and calculations of the (8×2) surface geometry [46, 166, 176]. The difference in the resonance of phonon modes of the (4×1) and (8×2) can also be qualitatively understood using the calculated slab polarisability of the two surfaces from [176]. This is another indication that the structural models for the (4×1) but also the (8×2) surface are quite accurate. Unfortunately the accuracy of the direct calculations of the phonon frequencies but also the signal to noise ratio of the measurements performed so far are not sufficient to enable a more detailed analysis of the obvious changes in the In-In related phonons upon the phase transition between 120 K and 80 K. More accurate measurements and calculations always using the same number of atoms in the unit cell could lead to a more definite answer as to which modes of the low temperature phase develop from the (4×1) modes.

The CDW formation on the other hand is in accordance with all the Raman measurements. The energetic shifts can be explained by the expected periodic lattice distortion due to the strong electron-phonon interaction in such systems. The resonance of the Raman intensity of the surface phonon modes in the spectral region

where structures are also seen in the RAS is another indication of the strong coupling of the lattice to the quasi 1D-electronic states. The unusual broadening and occurrence of new Raman modes for the low temperature phase is understood already in a simple backfolding picture.

In contrast to RAS spectra, Raman measurements do exist for the class of bulk one-dimensional conductors such as 2H-$TaSe_2$, 2H-$NbSe_2$ or $K_2Pt(CN)_4Br_{0.3} \cdot 3H_2O$ where a CDW formation driven by the Peierls instability is observed as well [201–204]. Similar to the observations for the indium chains the most dominant changes are the increase of measured phonons for the Peierls state, though in comparison the changes are even more pronounced since the CDW patterns are much more complicated. In the case of 1T-TaS_2 there is an increase in the number of Raman active modes from 2 to 348 in the presence of the CDW [204]. In some cases even the bulk symmetry is completely changed leading to even more irregular changes [203].

For some of these materials there are special modes observed which occur for the Peierls state only and drastically change their energy by further cooling. The so called “soft modes” are caused by a mode which transfers the atoms between the unperturbed positions and the positions in the Peierls distorted phase[4]. Above the phase transition temperature T_p these modes are acoustical modes and not seen in Raman spectra while below the transition temperature an optical mode occurs due to the backfolding of this soft phonon mode in the reduced Brillouin zone. In a mean field theory it was found that the energy of this mode Ω_{LO} varies with the temperature as follows: $\Omega_{LO}/\omega_0 = 1.4\lambda^{1/2}\sqrt{(T_P - T)/T}$. λ denotes the electron-phonon interaction parameter [51]. ω_0 is the frequency of the original acoustical mode at q_F, the wavevector of the distortion which depends on the number of atoms displaced and their masses. Such a mode can be found in measurements for some of the bulk materials [202, 203].

The occurrence of soft modes would be an additional proof of a Peierls state but were so far not observed for the Si(111)-In:(4×1) surface. The displacement pattern of soft modes should be in accordance to the changes in atomic positions. Since this displacement is almost only along the chain direction (see arrows in Fig. 5.7) a soft mode will have A'' symmetry. So far the temperature dependent measurements were only possible in A', due to the limitations of the setup. Without the observation of an energetic shift in some of the measured A'' modes any discussion as to whether one of these modes is a soft phonon mode is too speculative. If such modes are not observed in Raman spectroscopy it is, in reverse, no proof that there is no CDW, since the energy but also amplitude of the mode can be small and therefore out of the detectable range.

[4]Soft modes are general phenomena and occur not only for Peierls transitions but in many other structural phase transitions as well [205]

5.5 Influence of adsorbates

So far I have shown that all changes in the RAS and Raman spectra can be understood in terms of the CDW driven phase transition. On the other hand the calculation of these spectra based on the structural models can reproduce the measurements reasonably well. Yet there is another strong argument in favour of the CDW model. It was shown with RHEED studies by Ryjkov et al., that the (8×2) phase instantly reverts to a (4×1) phase upon adsorption of submonolayers of In, Ga, Al or Ag. Hence the (8×2) is unstable against perturbation of the surface. If the (8×2) is indeed the thermodynamically most stable surface as claimed by the calculations, this can hardly be understood.

The suppression of the phase transition was so far only seen by electron diffraction. Optical experiments, although integrating over the whole surface, are more sensitive to the local bond configuration than to long range surface order seen in electron diffraction experiments. It is therefore very interesting to study the adsorption also with optical techniques. Particularly it should be possible to distinguish whether the reversion to the (4×1) symmetry is caused by the pinning of the CDW at the adsorbate positions and distortion of the long range order, or whether the formation of the CDW is completely prevented. In the first case optical techniques should see no significant change in the spectral response, since the local symmetry will still be that of the (8×2) or (4×2). If instead there is a complete suppression of the CDW the optical response will also revert back to that of the (4×1) surface.

In adsorption

Several adsorbates were investigated to test the mechanisms of adsorbate – surface interactions. In order to compare the optical results to those of the RHEED study by Ryjkov et al. [206], adsorption of In was investigated first. In Fig. 5.24 the spectra of the (8×2) phase at 40 K is shown together with the one at the same temperature after additional deposition of 0.08±0.03 ML indium[5]. The adsorbed indium causes characteristic features of the (8×2) phase – the structure at 0.7 eV and the splitting of the 2 eV minimum – to disappear. Also smaller features such as the shoulders at 1.4 eV and 1.08 eV are quenched. Surprisingly the broad positive structure in the infrared remains. Since this structure is not present in a clean (4×1) spectrum it is obvious that this surface is different from the clean (4×1), although LEED images show the same (4×1) pattern. I will therefore label the (4×1) surface with additional adsorbates “stabilised (4×1)” and the initially prepared (4×1) surface “clean (4×1)”. The changes of RAS spectra upon adsorption are again best seen by plotting the difference of two spectra (δRAS).

Assuming the (8×2) is caused by a structural phase transition there was the possibility that additional In deposition will have different effects on a clean (4×1) than on the (8×2) since, with a modified geometry, adsorption sites might differ. In order to test this In was also deposited onto a clean (4×1) at temperatures above the transition temperature. In Fig. 5.25 RAS spectra for deposition of 0.04±0.02 ML indium at 150 K onto the (4×1) surface are shown. The most prominent change is the broad structure in the infrared as it was already seen for the low temperature (8×2)

[5] Details about the determination of submonolayer coverage of In can be found in the appendix A.1

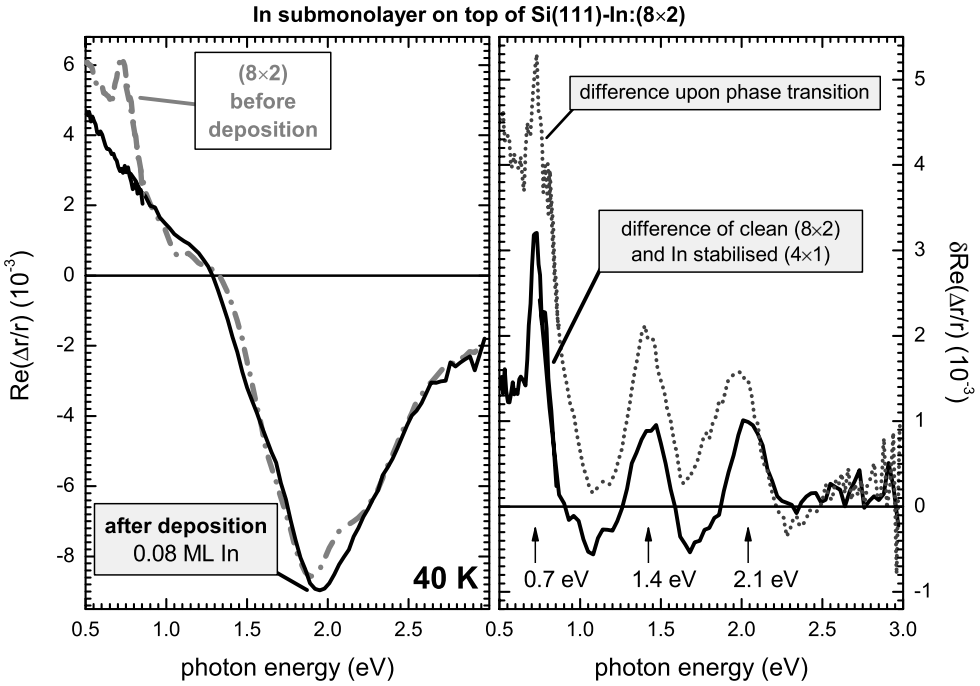

Figure 5.24: *RAS spectra of the indium terminated Si(111) surface at 40 K before and after quenching of the (8×2) phase by additional adsorption of 0.08±0.03 ML indium. In the right part the difference of both spectra is shown.*

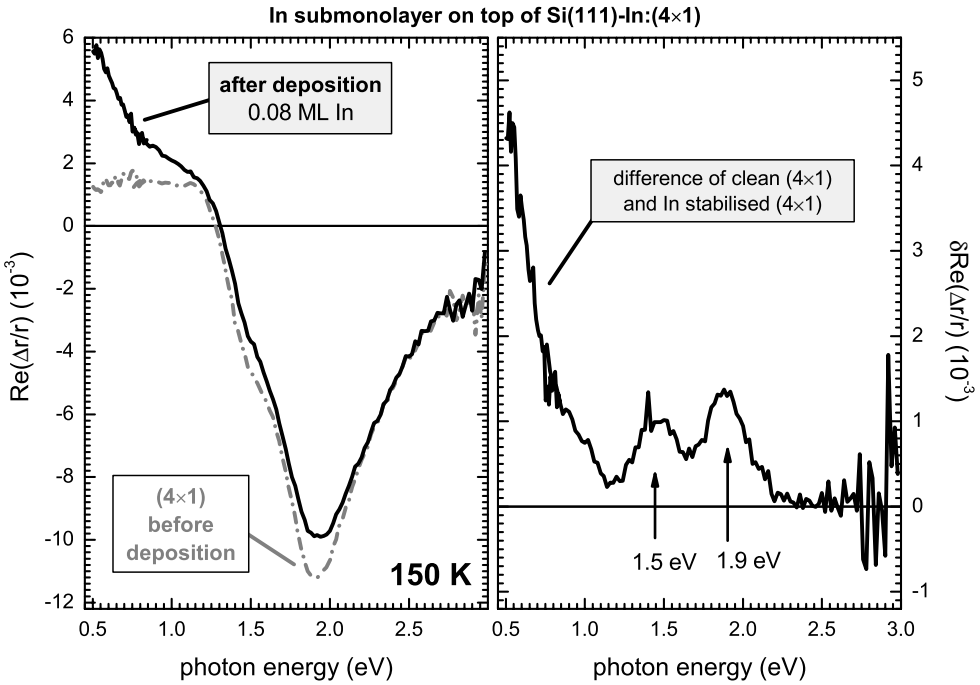

Figure 5.25: *RAS spectra of the indium terminated Si(111) surface at 150 K before and after changes of the (4×1) phase by additional adsorption of 0.04±0.02 ML indium.*

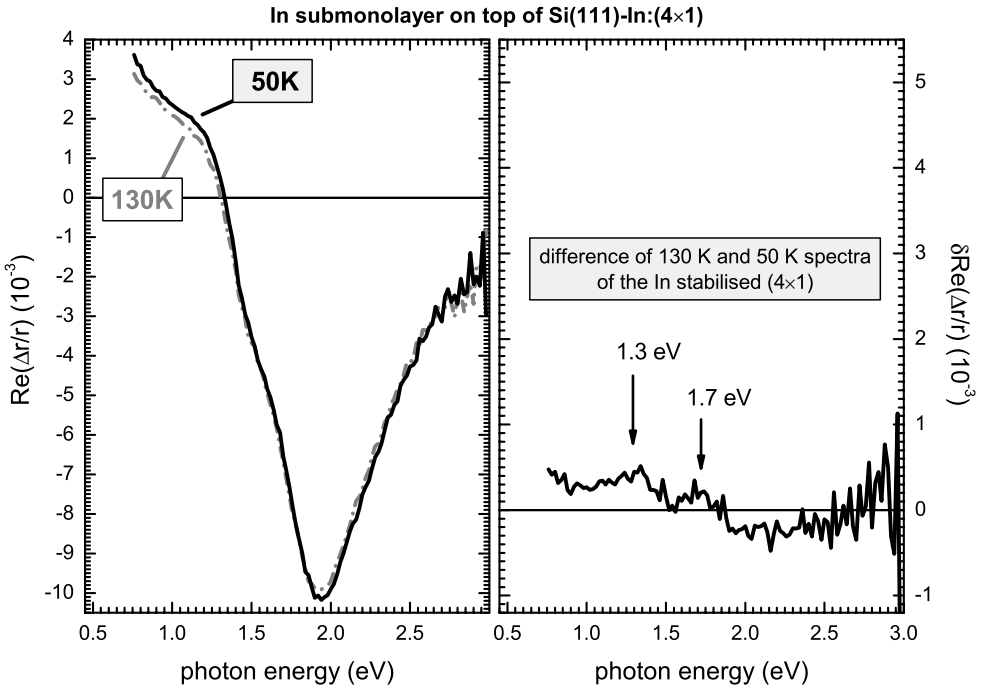

Figure 5.26: *RAS spectra of a Si(111)-(4×1):In surface quenched with additional 0.02 ML In. The surface is shown above the transition temperature and below. The small differences can be explained by temperature induced shifts only – a phase transition does not occur for this surface.*

phase and its indium stabilised surface in Fig. 5.25. There are also minor changes around 2 eV. The large anisotropy in that range is not quenched homogeneously, but at 1.47 eV and 1.88 eV structures in the δRAS spectra appear. This is an indication that defined states are affected by the adsorbed indium. As already discussed above the minimum structure around 2 eV cannot be explained as a single surface state transition. Adsorption leads to rather well defined changes, meaning that certain states involved in the 2 eV minimum are changed but the majority not. In what way these states are involved in the phase transition remains to be seen. In Fig. 5.26 it can be seen that the surface shown in Fig. 5.25 does not undergo a phase transition upon cooling below the transition temperature. All occurring changes in the spectrum are consistent with the usual blue shift and increase in amplitudes of optical spectra upon cooling.

As we have seen in section 5.1.2 during the initial preparation of the In chains around 450°C additional indium slowly desorbs or is otherwise incorporated into the original (4×1) structure. During the preparation the RAS amplitude still improves if the samples are kept at 300°C. The question therefore arises, whether the additional indium adsorbed at low temperatures can be either selectively desorbed or incorporated in the normal chain if such samples are annealed, thus leading to a “healing” of the surface. In Fig. 5.27 RAS spectra are shown of samples with additional 0.04 ML In before and after they were heated gradually to about 400°C. The total annealing time was about 5 min. Since the observed changes are small in comparison to the one shown for the low temperature measurements and the signal to noise ratio is

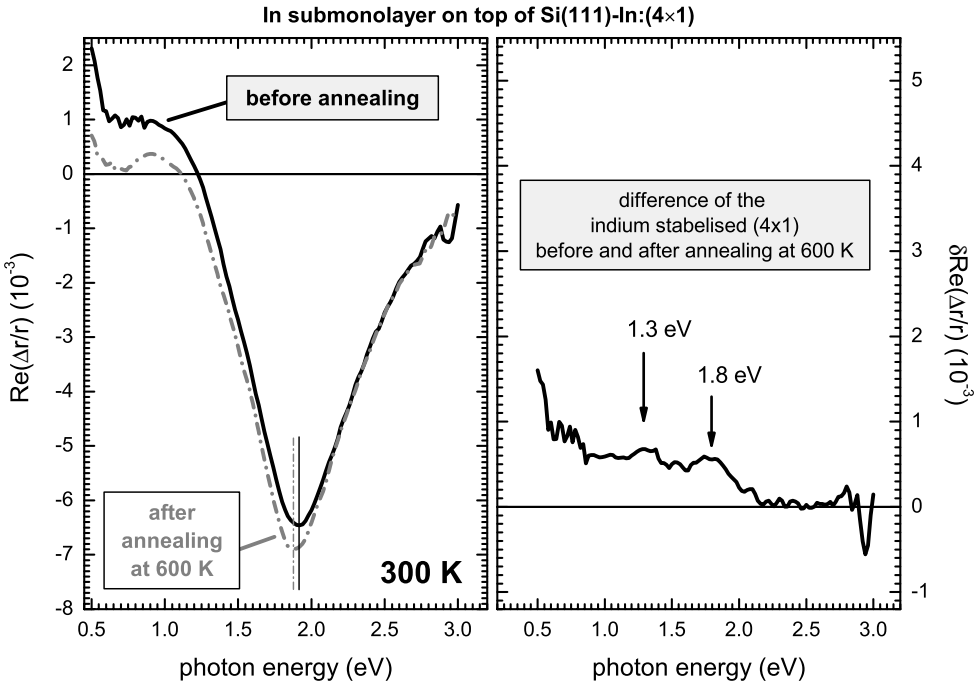

Figure 5.27: *RAS spectra of a stabilised Si(111)-(4×1):In, before and after annealing. The annealing of such samples partly reverts the changes introduced by the additional In. The obvious conclusion is that the adsorbate can be selectively removed at 600 K.*

higher, the spectra of three similar measurements were averaged. As one can see in the differences of the spectra before and after such annealing processes, the changes originally introduced by the additional In (see Fig. 5.25) can be partly undone. The anisotropy in the infrared can be reduced and the two shoulders reappear, though red shifted due to the temperature difference. Nevertheless the changes are not as pronounced as those during the stabilisation of the surface with additional indium. An annealing at higher temperatures was not performed, since it is already known from the preparation of the surfaces that indium within the chains starts to desorb above 450°C. Hence the (4×1) structure would be destroyed by such a heat treatment.

Since a reverting of the changes introduced by the quenching of the surface occurs, one question arises immediately: will the annealed surface undergo the phase transition again? To test this, one of the annealed surfaces was again cooled below the transition temperature. In Fig. 5.28 the result is shown. Indeed such a surface shows all features associated with the phase transition. In comparison to the changes observed with clean surfaces (see Fig. 5.9) the structures in the IR region, are less pronounced. In the visible range the difference spectra shows a mixture of the changes introduced by the phase transition at 1.4 and 2 eV and a broad structure at 1.8 eV because the overall anisotropy signal from the annealed samples is smaller than that of the original clean surface. Since RAS is a linear technique this just means that a smaller part of the surface is (4×1) reconstructed and an even smaller part is undergoing the phase transition. This shows clearly that the samples can only be partly recovered. Assuming the spectra of the clean surface represents a surface

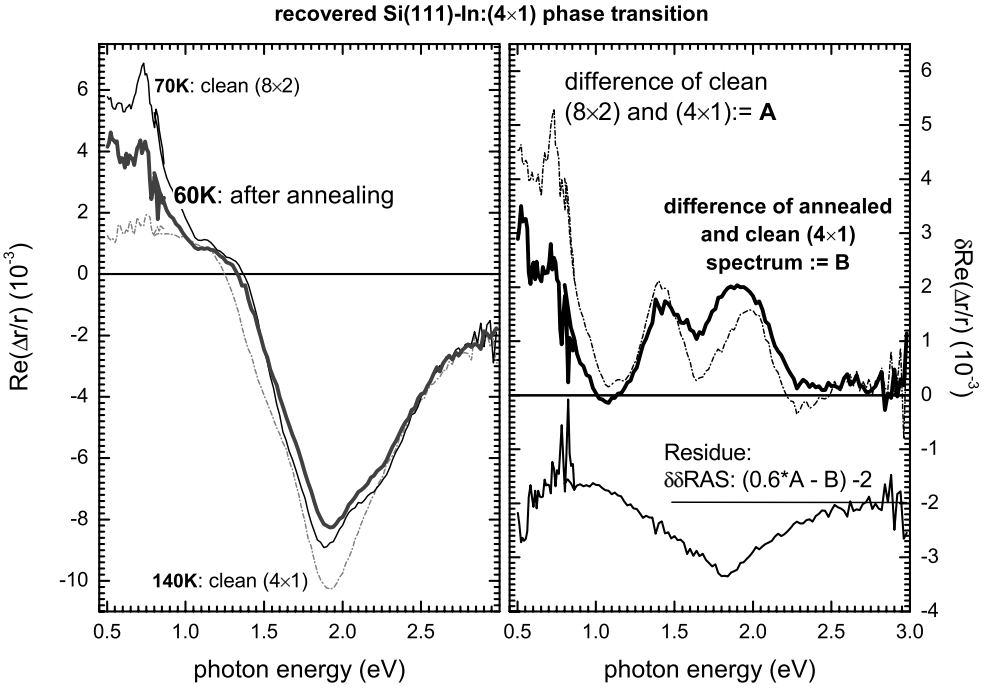

Figure 5.28: *RAS spectra of a recovered Si(111)-In:(4×1) surface at 60 K. The clean surface spectra for the (4×1) and (8×2) and their difference are shown for comparison. For the recovered sample δRAS is smaller in the IR but similar in amplitude in the visible range. This can be explained if δRAS is influenced by two different aspects: First only parts undergo the phase transition (≈ 60%) and second the overall RAS amplitude is smaller, since the surface is only partly (4×1) reconstructed (≈ 85%).*

which is not only fully single domain (4×1) reconstructed but also fully undergoes the phase transition, one can even quantify the changes within the annealed samples by analysing the RAS amplitudes in Fig. 5.28. In the IR, where the spectra of the (4×1) surface is flat one only sees about 60% of the changes as for the clean (8×2) surface. If one now tries to deconvolve the changes in the visible range one can determine in which way the overall surface quality is poorer for the annealed samples. By subtracting the δRAS of the clean (8×2) and (4×1) surface (A), scaled by 0.6 to account for the fact that only parts of the surface undergoes the phase transition, from the δRAS of the annealed sample (B) one can see that the residue ($\delta\delta$RAS) resembles the spectra of the clean (4×1) spectra – though with a much smaller amplitude. From this residue one can approximate the amount of the surface which is not (4×1) reconstructed anymore. The reduction in the overall amplitude between 1 and 1.8 eV to 9.8×10^{-3} compared to the clean surface (11.5×10^{-3}) shows that only 85% ± 5% are still (4×1) reconstructed after the annealing. The surface area which shows the (8×2) reconstruction at low temperatures is with only 60% even smaller.

Within this section I have shown the influence of additional indium to the RAS spectra of the Si(111)-In:(4×1) surface. Before I can discuss the underlying mechanisms of the observed changes the influence of other adsorbates has to be investigated as well.

Caesium adsorption

We have seen that additionally adsorbed indium can suppress the phase transition of the Si(111)-In:(4×1) surface. In order to get more information about the mechanism of this change in the surface and therefore additional information about the phase transition the adsorption of other materials was investigated.

Caesium was chosen as a test case for several reasons. Because of its size the caesium atom is believed to stick only on the surface without segregating into the chains or sub-surface layers. Additionally caesium could provide a doping mechanism into the indium-chains by transferring its valence electron.

As we have already seen for the additional indium adsorption, the differences between a surface which will undergo the phase transition and a clean surface can be already seen at room temperature. Since the characteristics of the caesium evaporator for room temperature deposition was very well known by the studies of Cs-wire formation on III-V surfaces (see section 6.1.2) it was the only case where the actual amount of adsorbed material was known exactly even for the submonolayer coverages (see also appendix A.1.

In Fig. 5.29 the RAS spectra of a clean surface and a surface with 0.1 ML Cs are shown. Similar to the case of additional indium the most dominant change is the reduction of RAS intensity at the 2 eV minimum. By cooling this surface to temperatures below the phase transition temperature, two things become clear. First even at 60 K there is no indication of spectral features associated with the (8×2) phase – the transition is suppressed again. On the other hand the differences between the clean surface become clearer than in the room temperature spectra. In Fig. 5.30 a

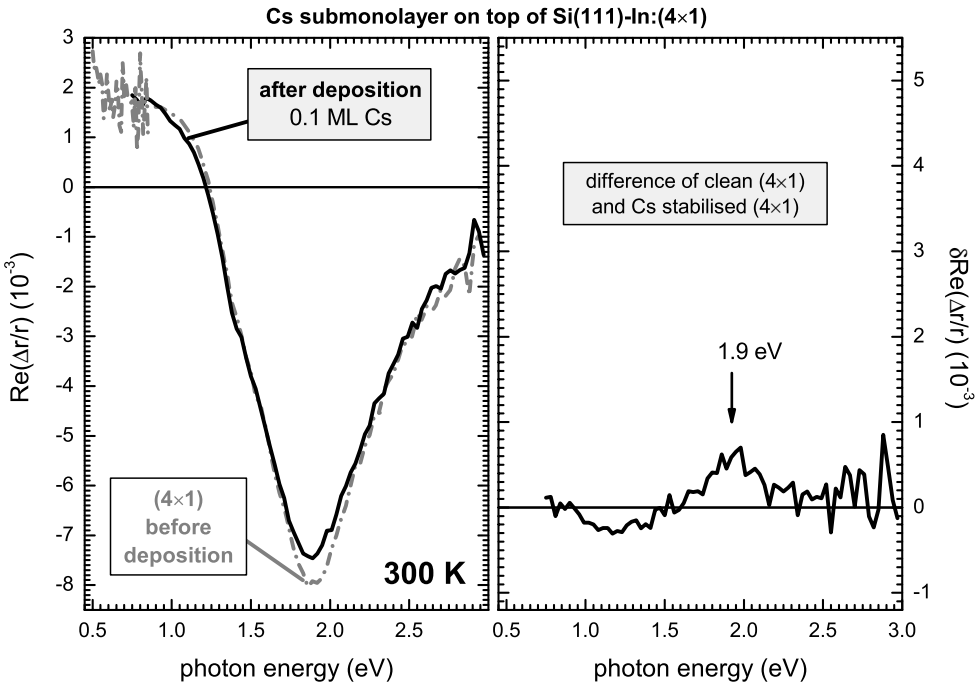

Figure 5.29: *Room Temperature RAS spectra of 0.1 ML Cs adsorbed on the Si(111)-In:(4×1) surface*

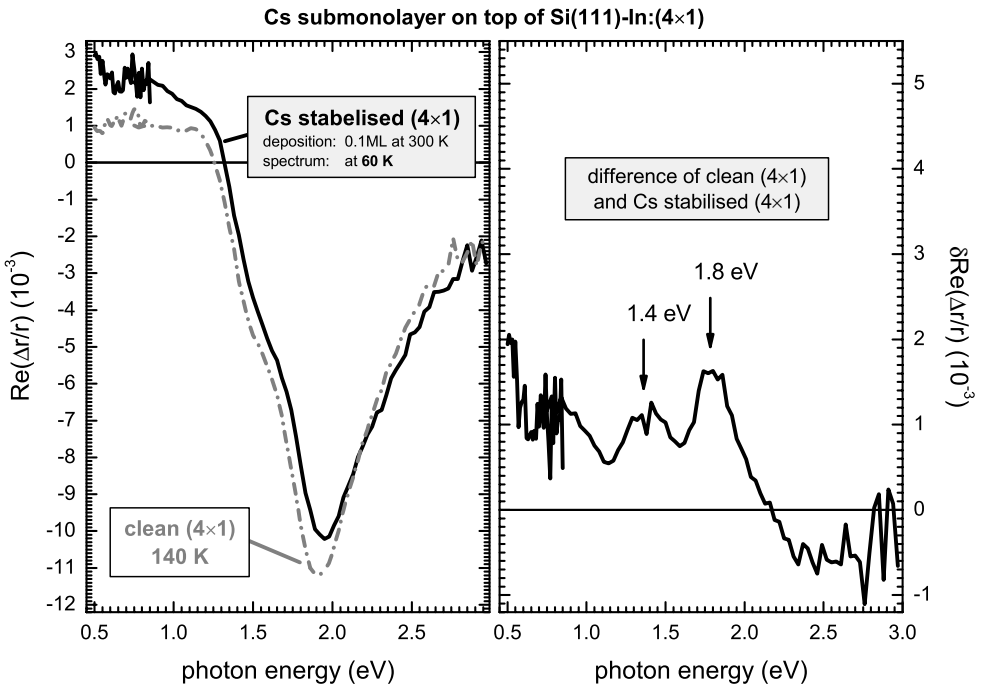

Figure 5.30: *Low Temperature RAS spectra of 0.1 ML Cs adsorbed on the Si(111)-In:(4×1) surface*

comparison of the clean Si(111)-In:(4×1) surface at 140 K and the Si(111)-In:(4×1)+Cs surface at 60 K is shown. It can be seen that again the fine structure of the large minimum structure is changed by the adsorbate and the anisotropy in the IR range is increased. Though in contrast to additional indium adsorption the increase in the IR is less pronounced.

In this section I have shown that the changes of the Si(111)-In:(4×1) introduced by additional Cs are very similar to the ones by indium as shown in the previous section. As one will see later the small differences between the In and Cs induced changes can provide a rather defined model of the adsorbate induced changes and also the phase transition of the clean surface. Before this will be discussed in more detail the results of another adsorption study is shown first.

Sodium adsorption

One of the few adsorption studies of other atoms other than indium or silver concerned the alkaline metal sodium. It was thought that by alkaline adsorption the electronic properties of the In chains can be deliberately changed. The alkaline atom was believed to give its electron to the chain, leading to an effective doping of the chain. In STM studies at room temperature by Lee et al. [207] it could be shown that at low Na coverages certain parts of the chains show the "×2" periodicity which was known for the low temperature state. At coverages of 0.4 ML they reported a weak but fully developed (4×2) LEED pattern of that surface at room temperature. This was explained by a pinning of the CDW between two adsorbed Na atoms in the low coverage range a complete stabilisation of the (4×2) phase for higher coverages. It was later proposed that this (4×2) surface is fundamentally different from the CDW

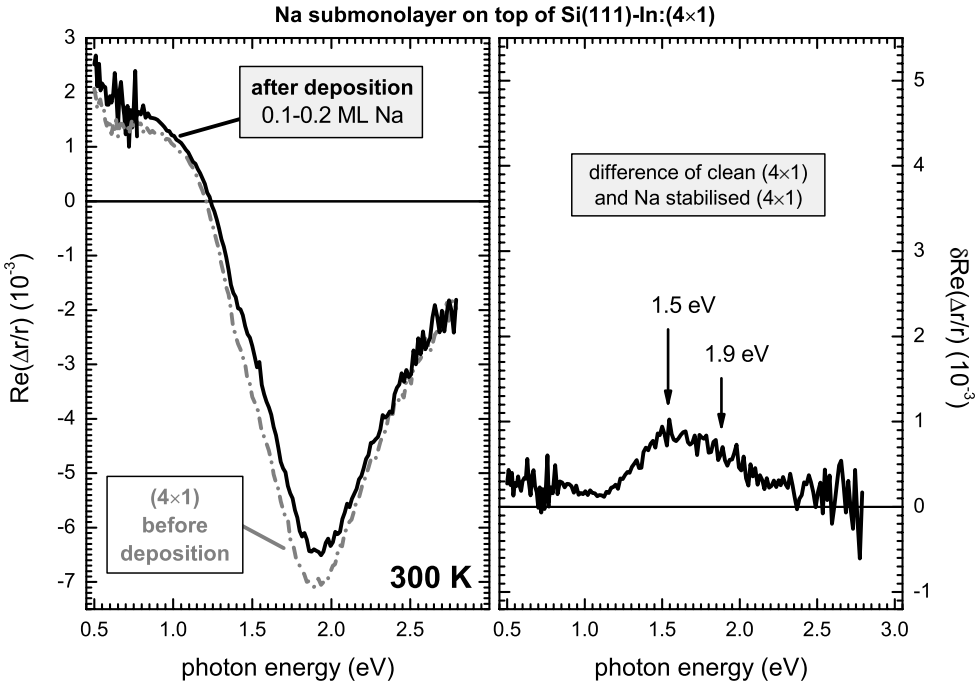

Figure 5.31: *Room temperature deposition of 0.1-0.2 ML Na on top of the Si(111)-In:(4×1) surface. In contrast to the adsorption of In changes occur in the whole range of the minima structure (1.3 – 2.1 eV). Similar to In adsorption an increase in the IR range was observed, though less pronounced.*

induced one discussed above but is instead a Na induced reconstruction. With DFT-GGA calculations by Cho et al. [208] it was shown that indeed a Na induced (4×2) reconstruction can be thermodynamically favourable. Since 0.4 ML corresponds to 4 Na atoms per (4×1) unit cell the latter explanation seems more likely.

Since the differences in the RAS spectra upon the phase transition were found to be very pronounced and by close examination of δRAS spectra one can even quantify the surface proportion which undergoes the phase transition, RAS measurements were done during adsorption of sodium, similar as the ones shown for indium and caesium adsorption. In Fig. 5.31 the room temperature spectra of a surface before and after Na deposition are shown. The exact amount of Na was not known, since the evaporation rate of the Na dispenser could not be fully calibrated as it was done for the caesium dispenser (see appendix A.1), though by an evaluation of the quenching of the 2 eV minimum a coverage between 0.1 and 0.2 ML is estimated.

It is obvious that the structures earlier related to the phase transition (maximum at 0.7 eV, doubling of the 2 eV minimum) are not found. It is therefore unlikely that the proposed stabilisation of the CDW at room temperature can be achieved with sodium adsorbates. Even at low temperatures no indication of the phase transition is observed, showing that instead of pinning the CDW sodium does also prevent the phase transition in the same way as indium or caesium. In Fig. 5.32 the low temperature spectra of the clean and a surface with additional adsorbed sodium is shown. No doubling of the 2 eV structure or the additional peak at 0.7 eV was found – the phase transition is, again, not occurring. Surprisingly the differences to

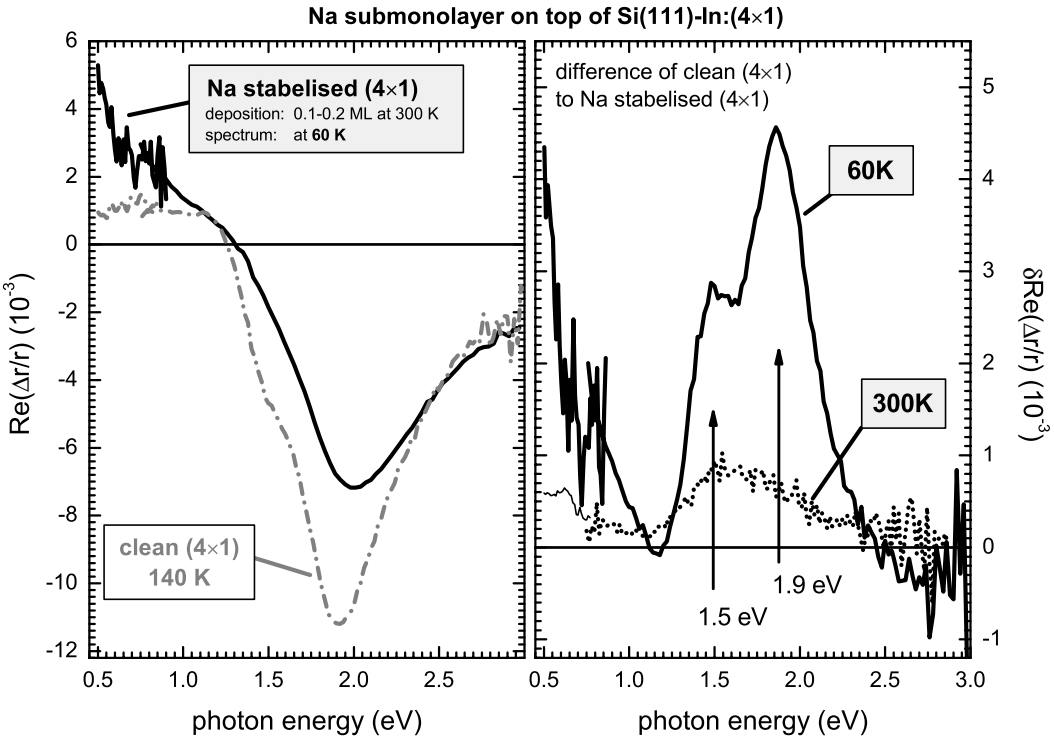

Figure 5.32: *Low temperature spectra of 0.3 ML Na on top of the Si(111)-In:(4×1) surface. The spectrum is compared to a low temperature spectrum of a clean surface. The difference of the two spectra is more pronounced but not significantly different to the room temperature difference (thin line). No obvious indication of a phase transition was found for this surface.*

the clean surface were found to be larger than expected from the room temperature data. Further analysis showed this to be an artifact, produced by an inhomogeneous sodium evaporation. Upon cooling, the manipulator bends and a different sample area is probed as for the room temperature spectrum. In Fig. 5.33 a set of spectra is shown, where the Na coverage is increased until saturation at room temperature. At high coverages the minimum structure is increasingly blue shifted and is almost not found for the saturated surface. The low temperature measurements in Fig. 5.32 is consistent with room temperature spectra of higher coverage.

The changes for the lowest coverage at room temperature are the ones most important for the discussion of the nature of the phase transition. The adsorption leads to a defined change in the 2 eV minimum structure as was observed for In and Cs as well. In the IR region a broad structure arises, though less pronounced than for indium.

Comparison of adsorbate induced changes

As seen so far all adsorbates investigated here prevent the phase transition of the Si(111)-In:(4×1) surface. In contrast to the earlier RHEED study by Ryjkov et al. [206] the study of the reflectance anisotropy also provides information of changes in the electronic properties of the surface upon the adsorption. If one compares the changes of the RAS signal for adsorption of Na, Cs and In as shown in Fig. 5.34, two structures

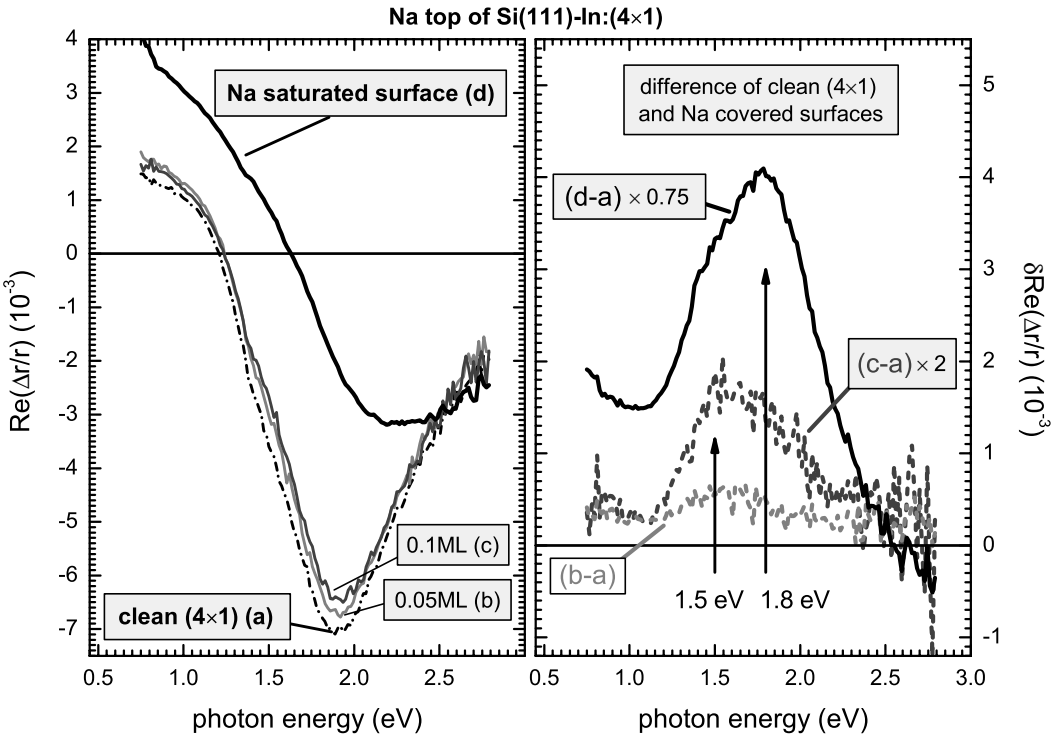

Figure 5.33: *Comparison of low Na coverages with a Na saturated surface. The δRAS spectra were scaled by the given factors to show the initial change at 1.5 eV more clearly.*

are noteworthy. First although the amount of adsorbate is comparable in the case of In and Cs, the RAS spectra and also the changes in comparison to a clean surface (δRAS) are different in the IR regime. In contrast to that the changes in the visible spectral range are very similar. In all cases the line shape of the broad minimum structure is changed. The shoulder around 1.5 eV and the RAS amplitude of the main structure at 1.9 eV is reduced upon addition of any adsorbate. As already described in 5.3.1 there are several surface state transitions involved in this minimum structure. The fact that all adsorbates used here introduce a similar change can be explained if the adsorption site is similar for all the substrates. The characteristic reduction of the RAS amplitude at 1.5 eV and 1.9 eV occurs already at an adsorbate coverage of 0.05 - 0.1 ML. With 6 atoms per unit cell in the case of the (4×1) surface this means that on average, at every 2nd or 3rd unit cell, an additional adsorbate atom is placed. This is already enough to change the RAS spectra at these two critical energies. If the adsorbate coverage is further increased the whole 2 eV RAS structure is quenched as expected if it originates from surface state transitions between localised states.

This behaviour is an indication that at least one of the states involved in the anisotropic transitions measured at 1.5 eV and 1.9 eV is not localised at a specific atom or bond. If that would be the case the structure should not be completely quenched if only half the surface unit cells are changed at all. Therefore a non-localised state must be involved. Unfortunately only calculations of the whole RAS spectra exists so far. A deconvolution of the spectrum into the transitions between selected individual states was not done so far. Such calculations can be useful to

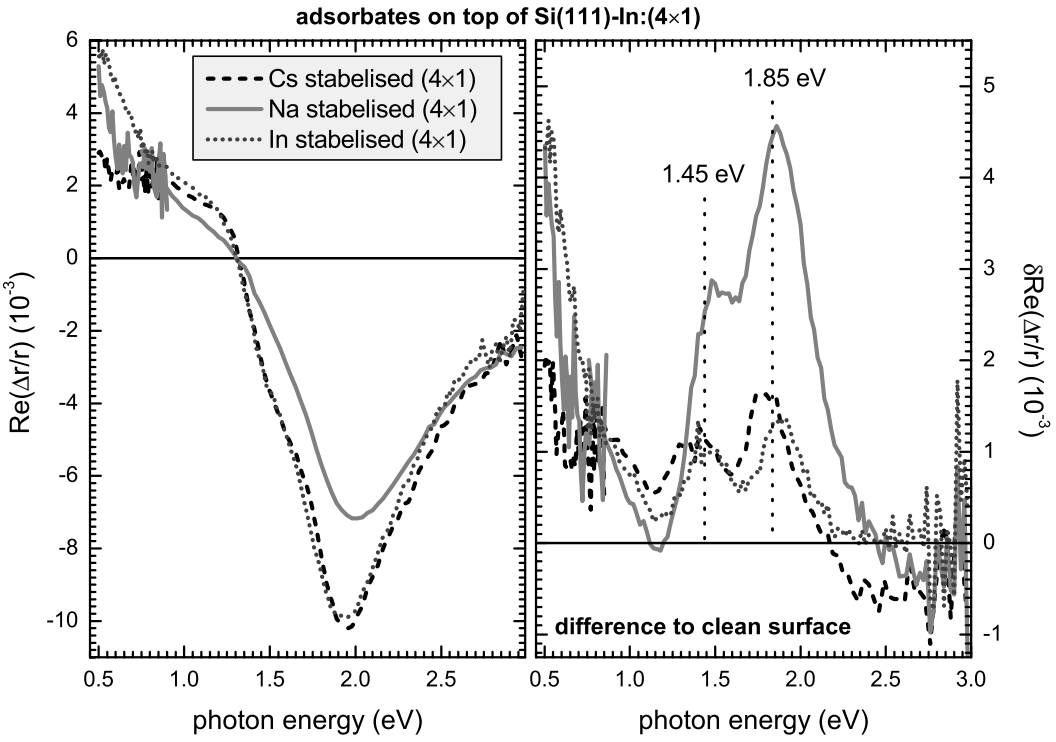

Figure 5.34: *Comparison of low temperature RAS Spectra of the Si(111)-In:(4×1) surface quenched with different adsorbates (additional 0.08 ML indium, 0.1 ML caesium, 0.3 ML sodium)*

correlate certain structures in the RAS to certain atoms or dimers within the real space surface structure as was shown for the InP surface by Schmidt et al. [190]. In the case of the Si(111)-In:(4×1) structure such an analysis can help to identify the states mostly changed by the adsorbates and possibly clarify in which way they relate to the suppression of the CDW.

What can be said is that all adsorbates do change the structure in a way that the phase transition is prevented. The fact that the RAS changes most prominently at 1.4 and 1.9 eV – exactly the range where also the main changes during the phase transition occurs, suggests that the geometry or certain electronic states differ for the room temperature clean (4×1) and the stabilised (4×1) reconstruction.

The response in the IR does vary significantly depending on the type of adsorbate even though the phase transition is always prevented. The IR anisotropy is therefore not directly related to the presence or suppression of the CDW. If this IR response originates from free carriers and if it is changed due to a doping by the adsorbate, this also shows that the doping itself does not directly prevent the phase transition by changing the Fermi level. Two possible scenarios remain – either the adsorbates act as scattering centres for the CDW, which can therefore not be established if the number of scattering centres is large enough. The other is that the adsorption site is similar for all adsorbates and it is directly changing the electronic states or vibrations needed for the formation of the CDW.

5.6 Model of the phase transition of Si(111)-In:(4×1)

Although there are still open questions as to how the different measurements and calculations can be put into a conclusive model I will describe one possible scenario in the next sections. First I would like to summarise the available information:

- The Si(111)-In:(4×1) undergoes a reversible phase transition around 110 K into the low temperature Si(111)-In:(8×2) phase.
- In contrast to the RT phase the low temperature phase is found to be semiconducting with a gap opening between 100 and 200 meV [47, 164, 182]
- STM measurements show that individual chains undergo the phase transition separately, the main feature being a doubling of the periodicity along the chain direction (→ ×2) [47]
- It was recently shown by STM that there can be a diffuse phase boundary of the ×2 bulges within one chain at low temperatures, which is moving along the chain [209]
- GIXRD shows changes in the atomic position along the chains leading to a doubling of the unit cell perpendicular to the chain direction (→ 8×) [48]
- RHEED and LEED measurements confirm the (8×“2”) symmetry of the LT surface
- The low temperature phase is unstable against perturbation of the surface by any kind of adsorbate [206].
- The measured anisotropies in the optical transitions between electronic states as well as the surface vibrational modes of both phases can be consistently explained by band backfolding due to a CDW formation accompanied with a periodic lattice distortion.
- The measured anisotropies in the optical transitions and the surface vibrational modes can be equally well described with DFT-LDA calculations based on two structurally different surfaces. The Si(111)-In:(8×2) is the thermodynamically most stable model – though it is generally found to be metallic [46, 165, 176]. (There are two recent calculations showing an electronic gap even for a (8×2) and slightly different atomic positions [166, 185].)
- The resonance of the surface phonons indicate a strong electron-phonon coupling.
- The narrow surface phonon modes found for the room temperature phase contradict the alternative model of a disorder–order transition.
- The Peierls instability and CDW formation is theoretically connected to a strong electron-phonon interaction. This interaction is **not** included in the DFT calculations.

The sensitivity to adsorbates, the fact that the ×2 seems to form only within one chain and the occurrence of moving phase boundaries within individual chains strongly supports that a collective electron mode – the CDW – is responsible for the phase transition. The observed changes in the atomic position is no contradiction of the CDW model, since due to the electron-phonon interaction a lattice distortion is expected.

It remains to be solved why the calculation predicts a more stable (8×2) surface. Since DFT is a ground state theory this should not be surprising. The ground state of the system at low temperature is also observed to be (8×2). Assuming the (4×1) model is correct and the good agreement of the calculated bandstructure with the ARPES measurements as well as the good agreement with calculations and the RAS measurements suggests this, almost any small distortion of the lattice which doubles the periodicity along the chains will result in a surface with lower energy. This is basically Peierls' argument why the 1D case should be unstable. The energy gain occurs due to the gap opening at the former crossing of the Fermi level (see 2.3). Hence the minimisation of total energy should lead to a surface as observed in the Peierls state below the phase transition. The calculated (8×2) surface therefore corresponds to the Peierls state, the calculated (4×1) to the state above the phase transition.

Using this basic assumption most details in the measurements can be explained. The 8× order originates from an inter-chain coupling. Such coupling mechanisms were already discussed for 1D-CDW found in bulk samples of $NbSe_3$ or $K_{0.3}MoO_3$ [210]. The most simple interaction is an out of phase coupling between two chains, which minimises the Coulomb interaction of the charge maxima of the CDW. In the case of the Si(111)-In:(4×1) surface this would lead to a 8× symmetry – as observed. The inter-chain interaction was found to be generally weak for CDWs in bulk samples. For the indium wires the distance between individual chains is smaller than for any of the metal trichalcogenides or MoO_3 based blue bronzes. Any coupling mechanisms should therefore also be more important.

With the model proposed so far, the changes in the optical response upon the phase transition can be completely explained by the backfolding of the bands. It was already discussed for RAS how this can explain the spectra. In the case of the Raman measurements the situation is more complex. First, because there are so many modes and second, since the phonon dispersion is not known. Currently it cannot be analysed whether and how the new modes in the (8×2) phase can be related to the original ones of the (4×1) phase. However the principal agreement of the phonon energies of the In-In modes with the calculations is a good indication – again assuming the calculations for the low temperature phase correspond to the Peierls state.

So far the dynamics of the changes upon the phase transitions have not been addressed. By a simple exponential fit of the changes in the RAS amplitudes a characteristic temperature range of the phase transition of $\Delta T = 17$ K was found. How this might be related to the coherence length of the CDW is not clear. Calculations of the dynamics of the CDW are so far not done in the case of the indium wires.

A more general discussion on CDW dynamics and the dynamics of the phase transitions can be found in the book "*Charge density waves in solids*" [49] and for instance in [211]. It was shown there that the measurements of CDW related peaks in

X-ray diffraction patterns can be understood and, for instance the width of such peaks can be related to the coherence length of the CDW. In the case of the indium wires a detailed analysis of the electron diffraction pattern could give similar information. The resolution of the LEED system used here was not good enough to perform such studies. With the, by now, very advanced spot profiling LEED systems (SPA-LEED) such studies may become possible in the future. The width of the ×2 streaks could provide direct information about the coherence of the CDW and also inter-chain interactions might be evaluated by distortions in the ×2 line or the width of the 8× spots.

Other measurements which could improve the understanding are adsorption studies for coverages much below the ones reported here, where effects of CDW pinning may be observable by STM or SPA-LEED.

5.6.1 The free electron response of the Si(111)-In:(4×1) surface

So far the changes in the optical response upon the phase transition and for the adsorption of In, Cs and Na were mostly discussed in terms of the interband transitions. In chapter 4 it was extensively discussed that intraband transitions, the so called free electron response, can also contribute to the RAS. A discussion of the indium wires was omitted at that point, since the RAS spectra are clearly dominated by interband transitions. However in this chapter we have seen that for the low temperature Si(111)-In:(8×2), the In stabilised (4×1) as well as for higher Na and Cs coverages, a broad structure in the infrared RAS occurred. It is possible that these structures do arise from quasi-free electrons.

Recently a calculation of the bandstructure for the Si(111)-In:(4×1) and (8×2) surface was analysed in detail with respect to the properties of the surface metallic bands [161]. An effective mass but also plasma frequencies were calculated for both surfaces. If one uses these calculated values for $\omega_{p,x}$, $\omega_{p,y}$ and the scattering rate ω_τ of 1 eV as given in [161], the free electron RAS response can be calculated. In Fig. 5.35 the result of this calculation, using a reasonable thickness d of 2 Å, is shown and compared to measured RAS spectra. In the measurements the broad IR structure does not occur for the clean Si(111)-In:(4×1) surface but appears for the low temperature phase and adsorbate stabilised surfaces. This is in clear contrast to the calculation by López-Lozano et al., where the plasma frequencies $\omega_{p,x}$, $\omega_{p,y}$, their difference and therefore also the RAS signal is larger for the (4×1) phase.

However the calculation so far always assumed an isotropic scattering rate ω_τ of 1 eV. By calculations within the DFT-LDA framework the dynamic properties such as the average scattering rate cannot be determined. Nevertheless the STM images in Fig. 5.1 already suggest that any scattering mechanisms and therefore also the scattering rate ω_τ should not only differ between the two phases but also between x and y. For larger wires such as Sn/InAs one has seen in chapter 4 that the free electron response can only be properly fitted if ω_τ is considered to be anisotropic as well. Such a fit was already shown for the (4×1) surface in Fig. 4.10. By using all available information such as the ratio between the effective mass along and perpendicular to the chains [160] or $\omega_{\tau,x}$ as derived from DC conductance measurements [148], the number of free parameters can be reduced. Additionally only the energy region below

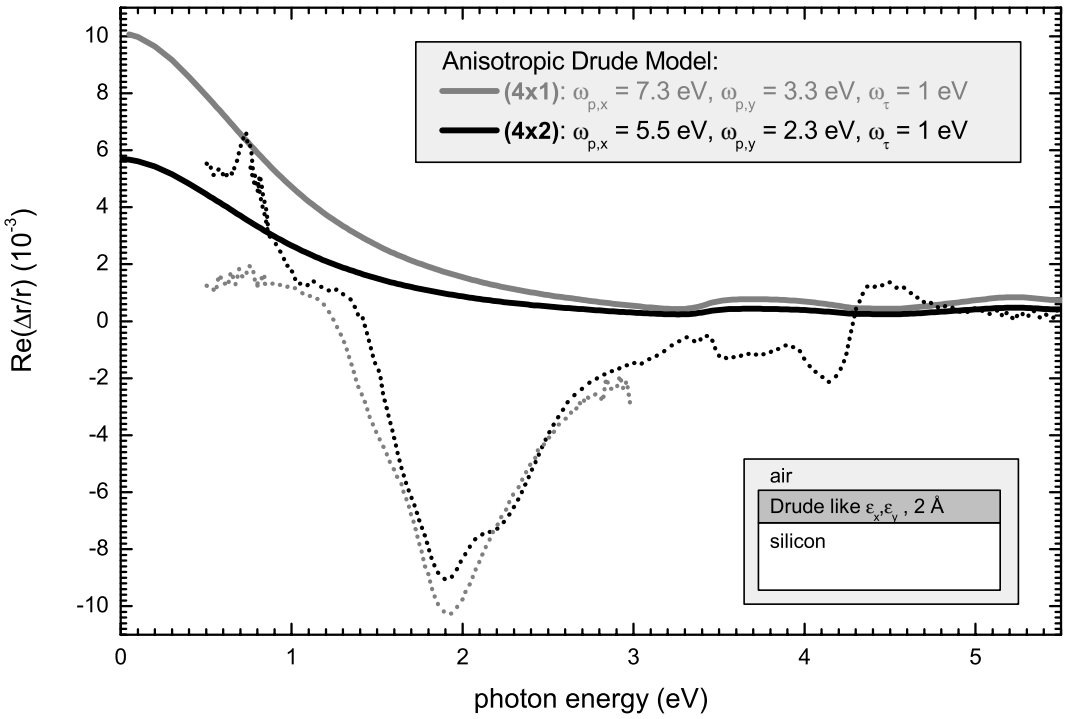

Figure 5.35: *Comparison of the simulated free electron optical response and the measurement for the (4×1) and (8×2) phase. A depth of the anisotropic surface layer of 0.2 nm was assumed. $\omega_{p,x}$, $\omega_{p,y}$ and the suggested isotropic ω_τ were taken from López-Lozano et al.. The RAS was calculated as described in section 3.3.3.*

1 eV and above 5 eV is considered to exclude the region of the interband transitions. Figure 5.36 shows such fits for both the (4×1) and (8×2) surface. In the case of the (4×1) surface the DC value calculated from the measured conductance anisotropy is given by a grey box for comparison [148]. In order to explain the larger IR anisotropy for the low temperature phase one has to either consider larger values of ω_p or lower values of ω_τ. The curve in Fig. 5.36 shows a fit with larger ω_p. To reproduce the RAS line shape it is furthermore necessary to assume a larger anisotropy in ω_τ. These fits can only be used as examples that the line shape can be understood in terms of a free electron response. The spectral region without significant interband transitions is to small for reliable fits and a physical interpretation of the results.

Nevertheless an anisotropic free electron response or intraband transitions as it should be better called in the case of the semiconducting low temperature phase can explain the different broad IR response for (4×1), (8×2) and all the different adsorbate stabilised (4×1) surface. The electron density and effective masses (hence ω_p) as well as the mean free path of an electron (hence ω_τ) does vary for all the surfaces resulting in different amplitudes of the IR response.

For the case of the low temperature (8×2) surface the strong IR anisotropy would contradict at first glance the fact that the surface was found to be semiconducting as was confirmed by STS or ARPES measurement [164, 182] and the DC conductance drops upon the phase transition [149]. Nevertheless one has to stress the point that not the conductance itself but a conductance anisotropy is measured in RAS. Second

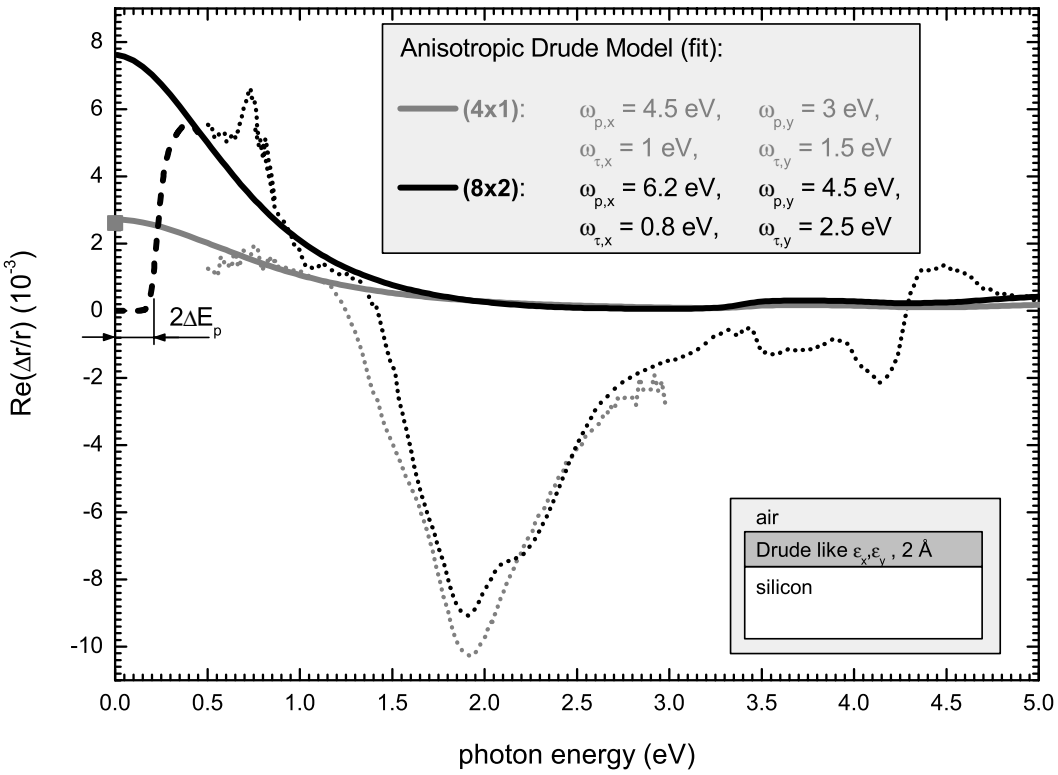

Figure 5.36: *Fit of the free electron response with an anisotropic ω_τ and fixed ratios of $\omega_{p,x}/\omega_{p,y} = 1.5 = \omega_{\tau,y}/\omega_{\tau,x}$ and d=2 Å for the (4×1) surface. The broad IR anisotropy for the (8×2) phase can only be explained by a considerably more anisotropic ω_τ and a larger ω_p. This does not necessarily mean that the DC anisotropy will be larger as well as is depicted with the dashed line showing a possible line shape assuming a Peierls gap of 0.1-0.2 eV (see text).*

there is the possibility that in the energy region of the Peierls gap ΔE_p reported between 0.1 and 0.2 eV, the RAS and also the conductance drops. This was already seen in reflectance measurements of bulk quasi one-dimensional structures such as $K_{0.3}MoO_3$ [212]. A calculation in [213] shows that above $2\Delta E_p$ the conductivity can be single particle like again, hence showing the Drude tail. In the case of the Si(111)-In:(8×2) surface this is expected at 0.1-0.4 eV just outside the spectral range of the setup. In Fig. 5.36 such a possible line shape is depicted with the dashed curve.

So far the explanation of the broad IR structures as a free electron contribution remains speculative, though in agreement with the limited measurements. A further extension of the RAS into the IR may solve this issue since the energetic region for the fits would be improved or in the case of the (8×2) phase the Peierls gap might be seen directly.

5.7 Concluding remarks

In this chapter it was shown how the formation of a charge density wave can be seen in optical spectra for atomic nanowires on surfaces. The backfolding of the bands leads to characteristic changes in the measured spectra. Details as to whether new structures arise, changes in amplitude occur or existing structures are shifted in energy or even split into two, depend on the electronic surface bandstructure in the case of RAS spectra and the surface phonon dispersion in the case of the Raman spectra. It was shown for the particular system of indium wires on Si(111) that the surface phase transition can be optically monitored and that additional perturbation of the system by adsorbates prevent the phase transition – again the changes in the electronic transitions can be seen by RAS.

Whether RAS is able to measure the changes of the conductivity upon the phase transition is not as clear. In the spectral range above 0.5 eV there is only an indication that this is the case. The spectral range needs to be considerably enhanced. One approach would be to use an FTIR-ellipsometer [94], providing the signals from the surface layer are large enough. In [213] it was predicted, that upon the phase transition the optical conductance is decreased drastically in the region of the Peierls gap. In the case of the indium nanowires the Peierls gap is supposed to be around 100 to 200 meV. To directly observe this with optical techniques, the available spectral range must be below 300 meV (2400 cm^{-1}). With conventional RAS setups this is not possible.

For the system discussed here, it was not as clear whether the phase transition is caused by the Peierls instability of the one-dimensional metallic surface state. For other one-dimensional conductors this is not questioned. For a further understanding of the Si(111)-In:(4×1) surface it would be useful to compare the RAS and Raman spectra – and the changes upon the phase transition – with other one-dimensional systems where a CDW formation is discussed or confirmed. Particularly a comparison to the bulk anisotropic inorganic compounds (transition metal trichalcogenides, pentachalcogenides or molybdenum blue bronzes [214]) where numerous other measurements exist and for instance CDW correlation lengths are known for all temperatures, will be helpful in interpreting the measurements in the case of the indium wires. A second class of systems which should be investigated in a similar way are other anisotropic surfaces such as the Si(111)-(K,Na,Li,Ag):(3×1) and Si(111)-Au:(5×2). For all these structures surface phase transitions are found and discussed also in terms of possible Peierls instabilities [4, 25, 26, 29, 215]. In some cases such as the system of gold on silicon the inter chain distance can even be tailored by varying the sample offcut [17].

6. Mott-Hubbard correlated systems

In the last chapter the optical response of a quasi 1D metallic system with strong electron-phonon coupling was discussed. The metal-insulator transition was driven by a charge density wave and occurred at a temperature defined by the energetic gain upon the formation of the insulating phase. It was discussed in detail in chapter 2.4.3 that there is another interaction which can drive a metal insulator transition – the electron-electron interaction. Formulated by Mott it was shown that if the electron density is lowered below a critical density, it is energetically more favourable to form an insulating material [52]. The so called Mott-Hubbard transition was able to explain the insulating behaviour of liquid alkaline metals, where the solid phase is metallic. By showing that due to the increased atomic distances at high temperatures, the electron distances are sufficiently enlarged to force the Mott-Hubbard transition this behaviour was explained. In contrast to Peierls unstable systems discussed in the previous chapter the Mott insulator does not revert to the metallic state at elevated temperatures.

For alkaline wires, which can be prepared on different III-V(110) surfaces the Mott-Hubbard mechanism was also discussed to explain the semiconducting nature, since the distance between adsorbed Cs atoms depends on the substrate lattice constant and is larger than in the bulk metal. It was shown in 1989 that caesium adsorption at room temperature leads to the formation of wire-like structures on the GaAs(110) surface [216, 217]. Later similar structures were also found on InAs(110) and InSb(110) surfaces [218, 219].

From STM (scanning tunnelling microscopy) studies one knows that on all the

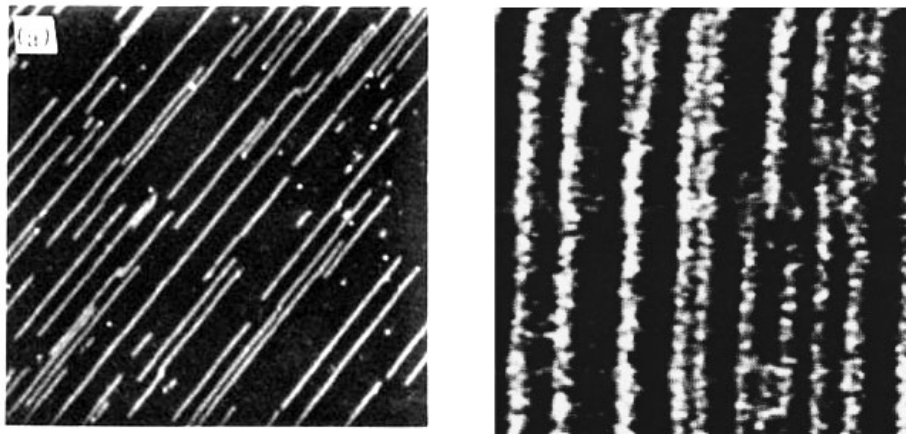

0.03 ML Cs on GaAs, 137×137 nm 0.2 ML Cs on InAs, 20×20 nm

Figure 6.1: *STM images of Cs wires on GaAs(110) (left, taken form [217]) and InAs(110) (right, taken from [218]). On both surfaces isolated Cs wires form for room temperature deposition and submonolayer coverage.*

III–V(110) cleaved (1×1) surfaces Cs forms isolated wires along the [1$\bar{1}$0] direction at small coverages (< 0.3 ML). In the coverage region around 0.3 ML (GaAs), Cs forms a closed two dimensional adlayer. For InAs and InSb this 2D phase is completed at a coverage of 0.5 ML, which is one Cs atom per III–V(110) unit cell. At even higher coverages deposition of Cs at room temperature leads to the formation of a second Cs layer which shows no local order. It is therefore often called the 3D disordered layer or Cs bi-layer.

Both the 1D and 2D Cs covered surfaces were found to be insulating by STS (scanning tunnelling spectroscopy) and PES (photo emission spectroscopy) investigations [67, 217]. In the case of the 2D closed layer this result was rather surprising since a metallic surface was expected by using the electron counting rule. Several models for this unusual behaviour were suggested namely that the surfaces are Mott-Hubbard insulators or that bipolaron formation leads to a gap opening [4, 66, 67, 220, 221]. Therefore the caesium covered III–V(110) surfaces are not only ideal systems for studying the formation of nanowires but can also be used to study the states of correlated electrons of 1D and 2D Mott Hubbard insulators.

6.1 RAS of alkaline 1D and 2D structures

The method of choice for the analysis of the wire formation on III-V(110) surfaces was again reflectance anisotropy spectroscopy. In contrast to the other systems discussed so far, no response from the free electrons is expected. The structures under discussion are semiconducting. An interesting subject is the determination of the Mott-Hubbard gap in these wires, but it was unlikely from the beginning that optical probes can provide information on that, since direct optical transitions between the two collective electron states are dipole forbidden [52]. Nevertheless RAS can give an insight to the wire-formation process itself. The main point will be whether differences in the actual wire geometry, the 1D-2D structural transition and finally also the 2D-3D structural transition can be analysed optically. The comparison with wires on different III-V(110) surfaces will also help to understand in which way observable changes in the RAS spectra originate from changes of the wire electronic structure or of the near surface bulk region.

6.1.1 The RAS of the III-V(110) clean surfaces

In comparison to the structures discussed in the previous chapters the analysis of the optical anisotropy of the nanowires is complicated by the fact that the surface on which the metal is deposited itself is optically anisotropic. In the case of the larger tin wires on InAs(110) the clean surface response was small compared to the anisotropy of the wires. In the case of the indium wires on silicon (111) the substrate surface itself was isotropic, hence the measured anisotropy was directly attributed to the wire. For the caesium wires the situation is different. The wires occur at submonolayer coverages – the unchanged surface region will therefore still contribute to the RAS. In a first step I will therefore shortly review the optical anisotropy of the clean surface.

The III-V(110), in particular the GaAs(110) surface, have long been studied with RAS. One of the first RAS study by Berkovits et al. was measuring the optical anisotropy of GaAs(110) [88]. In later years it became the test system in particular for theoretical approaches to calculate RAS spectra, either with tight-binding calculations [222–224] and within *ab-initio* DFT theory [191, 192, 225, 226].

In the case of GaAs two prominent structures (at 2.5 and 2.7 eV), caused by surface states below the E_1 critical point, are observed (**S** in Fig. 6.2). Similar transitions between surface states in the case of InP and InAs are less evident at room temperature, but clearly seen in low temperature spectra [227]. For the GaAs(110) another surface related maximum structure nearly coincides with a minimum structure around the E_0' which leads to an almost flat curve in the spectral region between 4 and 4.7 eV for the clean surface. In the case of the InP(110) and InAs(110) these two structures are separated.

Considering GaAs(110), InAs(110) and InP(110) the RAS spectral features evidently common to all III–V(110) clean surfaces are: *(i)* maxima related to surface

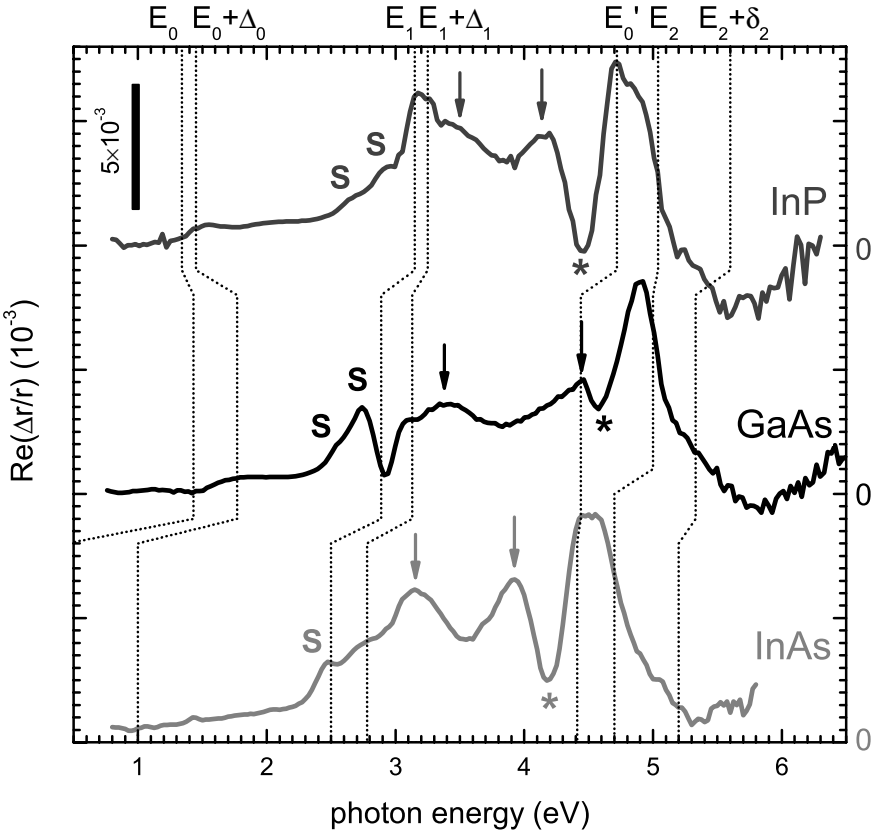

Figure 6.2: *(a) Comparison of the RAS spectra of clean III–V cleaved surfaces. The (1×1) bulk truncated structure is characteristic for these surfaces and also the RAS spectra are similar. Structures related to surface states are labelled with* ***S****, structures due to surface to bulk transitions with an arrow and the minimum below the* E_0' *bulk critical point with* *******. The energies of the bulk critical points are marked with dotted lines and taken from [228].*

state transitions below the E_1 critical point (**S** in Fig. 6.2); *(ii)* maxima due to transitions between surface states and bulk-like states in the energy range between the E_1 and E_2 bulk critical points (marked with arrows in Fig. 6.2); *(iii)* a minimum below the E_0' bulk critical point (***** in Fig. 6.2); and *(iv)* a maximum between the E_0' and E_2. Both transitions from surface to bulk and from bulk to bulk states contribute to *(iv)*.

In some earlier measurements the large structure around 4.9 eV, 4.5 eV and 4.7 eV for GaAs, InAs and InP respectively was not seen due to limitations in the spectral range of the RAS setup [88, 222] Nevertheless calculations already predicted a strong maximum in this energy region [192].

It remains to be seen in the following section how these clean spectra are modified during the wire formation and in which way these changes are characteristic, since the quenching of structures related to transitions involving true surface state are expected to be reduced in any case – independent of the geometry formed by the adsorbate.

6.1.2 Sample preparation

The samples were cleaved in UHV with a base pressure below 8×10^{-11} mbar. Cs was evaporated from SAES Getter alkali dispensers without any significant pressure rise. RAS and Auger spectra, as well as LEED images, were taken after each evaporation step for the first experiments, in order to calibrate the adsorption and link certain RAS spectra to their corresponding LEED images and Auger spectra. The coverage was determined by Auger electron spectroscopy using a VG instruments LEED/Auger system. The relative Auger intensity of the Cs NOO line at 47 eV to the substrate Auger lines (As: LMM at 1230 eV, Ga: LMM at 1070 eV, In: MNN at 404 eV) saturates upon completion of the 3D layer. It is already known that for room temperature deposition, not more than one monolayer can be deposited [217]. In order to get an approximation of the coverage, one can therefore normalise the relative Auger intensities of Cs for each evaporation step with respect to the relative intensity at saturation. The procedure is described in more detail in the appendix A.1.

Please note that there have been some differences in the literature concerning the classification of one monolayer in the case of alkali adsorption. I use the definition of one monolayer as the number of atoms on the clean III–V substrate surface. The coverage calibration has to be done for each of the substrate material because the sticking coefficient of Cs differs on the substrates investigated here. Since the evaporation rate for each Cs source is also slightly different, a re-calibration is necessary for each individual dispenser. The details of this calibration process can be found in A.1.

The RAS spectra itself were taken during Cs evaporation using a minimised Cs flux without stopping for additional measurements in order to avoid any changes in the spectra introduced by otherwise necessary optical readjustments.

6.1.3 Cs on GaAs(110)

GaAs(110) was the first material investigated, since it is the most studied system so far. It was already known that wire formation occurs immediately after adsorption.

For a coverage of 0.3 ML a 2D closed layer with a c(4×4) symmetry was found using STM [217]. For even higher coverages a disordered second Cs layer forms. At the saturation coverage of 1 ML the surface is metallic.

The RAS spectra of the clean GaAs(110) surface is shown in Fig. 6.2 and 6.3. Upon Cs adsorption, structures related to surface states of the clean surface are quenched. Already at 0.15 ML the features at 2.7 eV and 3.4 eV are not seen anymore. The structure at 4.9 eV is quenched as well, though it can still be seen even at a fully saturated surface. This feature therefore originates from transitions involving surface states and transitions involving only perturbed bulk states. This conclusion is consistent with a deconvolution of the calculated optical anisotropy where it is shown that both bulk-bulk and bulk-surface transitions contribute to the large structure [192, 223]. A similar interpretation has been recently proposed for the clean InAs(110) surface [191].

Apart from changes of RAS structures of the clean surface upon Cs adsorption a minimum at 1.9 eV evolves. Since the clean surface does not have a structure in this energy region and no GaAs bulk critical point is near 2.0 eV this structure can be directly attributed to the presence of Cs wires. In the coverage range below 0.1 ML it was reported that a single zig-zag chain of Cs dominates the surface while above that Cs triple chains are formed [216, 217]. So far RAS is not able to observe features which could be directly related to such a change of wire geometry. In the coverage

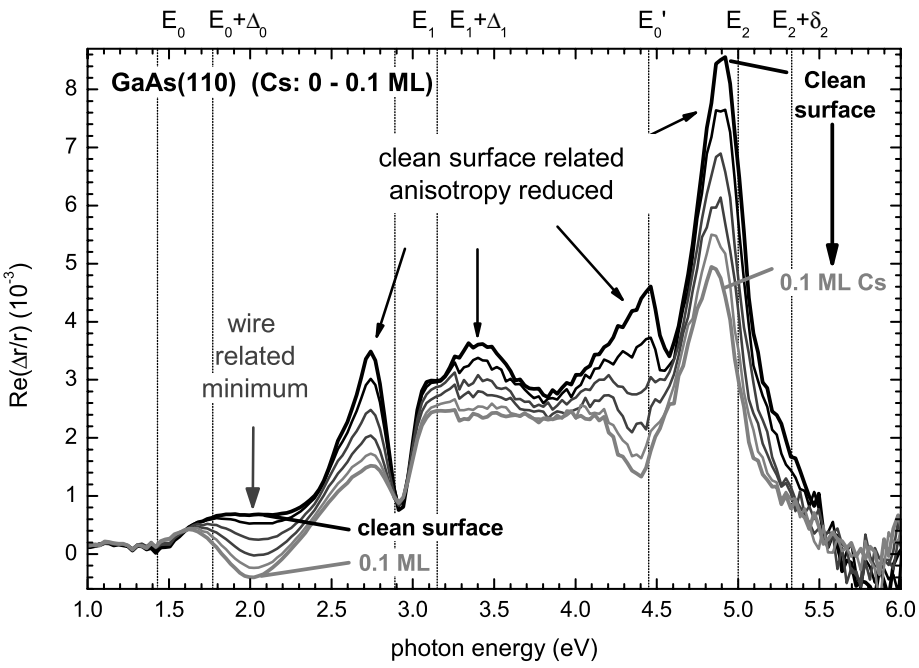

Figure 6.3: *RAS spectra of the GaAs(110) surface with growing Cs coverage from zero to 0.1 ML. The coverage difference between the individual spectra is 0.02 ML. At these low coverages a minimum at 2 eV emerges, while the clean surface structures related to electronic transitions involving true surface states are quenched.*

region below 0.1 ML the wire related minimum structure is not pronounced enough to observe possible differences due to the different wire types.

Another prominent change in the RAS spectra is the "inversion" of the small maximum structure at 4.5 eV (around the GaAs E_0') into a minimum. Since this structure is close to a bulk critical point of GaAs, it is not possible to interpret this finding directly as new optical anisotropy within the evolving Cs chain. The nature of this feature is better understood assuming the flat RAS line shape around the GaAs E_0' is caused by the coinciding of the usual surface related maximum structure below the E_0' and the minimum structure at the E_0', which originates from perturbed bulk states. Upon adsorption of various materials (Cs, Sn, Sb) and the quenching of surface states the minimum around the E_0' appears, since initially only the surface related term is reduced upon adsorption. This would lead to the apparent inversion of the line shape around E_0' (see Fig. 6.3 in the case of Cs adsorption but also Fig. 4.5 for Sn adsorption). As an alternative explanation for such a reversal of sign one could consider strain [229], possibly modified upon Cs adsorption. However, since from theoretical calculations it is expected that Cs introduces different strain fields for GaAs and InAs [230], but similar changes are observed in RAS spectra challenges this explanation. Moreover, additional strain should affect the anisotropies at all critical points [229], while only changes around the E_0' bulk critical point are observed. It is then not plausible that strain is responsible for the development of the RAS in this spectral region.

Upon further Cs adsorption, exceeding 0.1 ML the amplitude of the wire related minimum at 2 eV still increases, but it is accompanied with a gradual shift of the structure to 1.75 eV at a coverage of 0.2 ML (Fig. 6.4). It was already reported that the surface undergoes a structural transition into a c(4×4) reconstructed surface [217]. This shift can therefore be attributed to the formation of the closed 2D Cs layer. The shift is gradual since RAS is sensitive to the local bonding configuration but nevertheless integrates over the whole illuminated area of the sample. Parts of the sample are already in the c(4×4) symmetry, while other parts still have wires. In this transition regime, a linear combination of the structures related to wires (at 2 eV) and to the c(4×4) phase (at 1.75 eV) results in a gradual shift of the minimum in the intermediate coverage region. LEED images taken in this coverage range from 0.1 to 0.25 ML show a transition from a weak and streaky c(2×2) symmetry (wires) to a (2×1) symmetry (closed layer) at 0.2 ML (see Fig. 6.5), though the closed 2D layer was reported to be c(4×4) reconstructed [217]. The latter symmetry was derived from STM images and might differ from the symmetry observed in LEED images. For other systems, namely Li on GaAs(110) [231] and Cs on InAs(110) [232], a (2×1) symmetry in LEED for the 2D closed layer was also recently reported. This strongly supports the correlation between the changes in RAS and the variation of the surface reconstruction upon the formation of the closed layer. At the moment, the slight difference between these measurements and the STM data where the 2D closed layer occurs (0.2 ML here, 0.3 ML in [219]) cannot be explained. Though a difference in the calibration of coverage could be the origin, further STM/RAS experiments will be needed clarify this point.

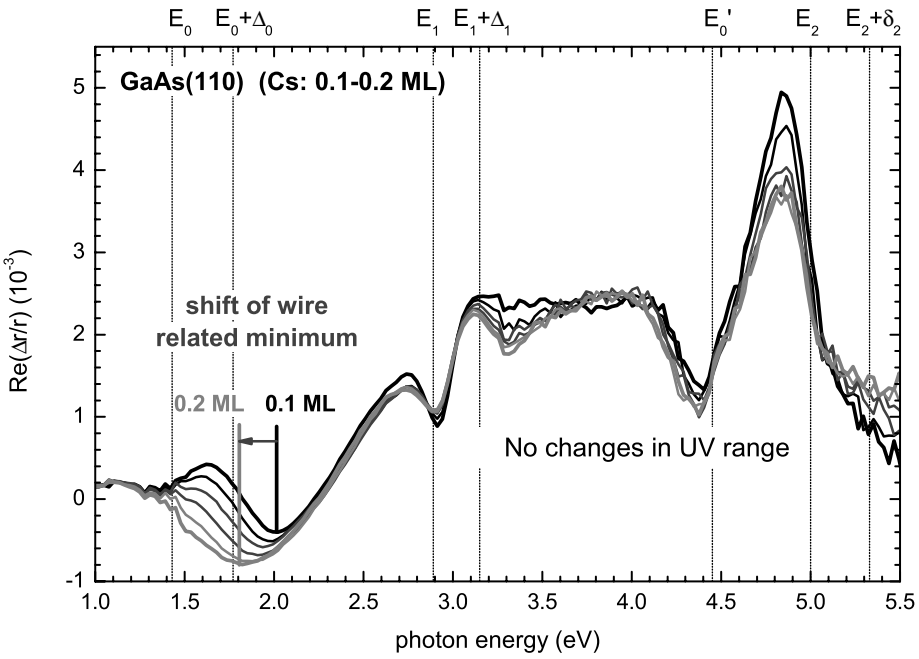

Figure 6.4: *With growing coverage (0.1 – 0.2 ML) the wire related RAS minimum is shifted towards lower energies (to 1.75 eV) and broadened. The coverage difference between subsequent spectra is again 0.02 ML.*

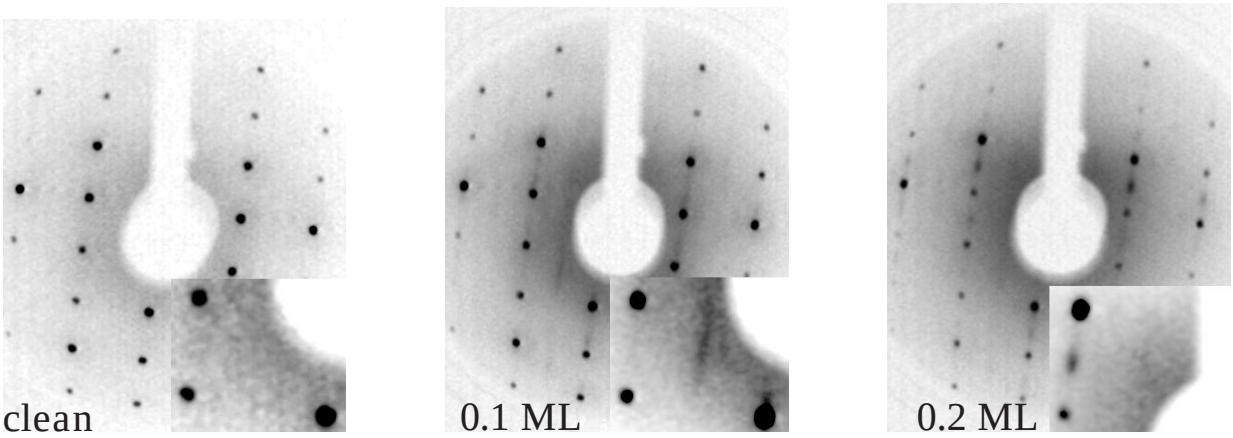

Figure 6.5: *LEED images taken at 150 eV electron energy showing the clean surface (left), the streaky c(2×2) at 0.1 ML (middle) and the (2×1) symmetry at 0.2 ML (right). The inset always shows one (1×1) unit cell with enhanced contrast.*

6.1.4 Cs on InAs(110)

The adsorption of Cs on the InAs(110) surface has already been studied by STM and STS [217, 218]. Cs was found to form similar wire structures as on GaAs, although certain peculiarities were reported. In STM images two different wires are visible, distinguishable by their different widths (measured along a line perpendicular to the wire axis) [218]. The "narrow" type (single atom zig-zag chains along $[1\bar{1}0]$ direction) occurs at coverages below 0.2 ML, while the "broad" type (1D triple line of atoms along $[1\bar{1}0]$) appear above 0.2 ML. In contrast to GaAs(110), the formation of the 2D phase found at 0.5 ML is not accompanied with a reordering of the Cs surface layer, but consists of a closed package of the broader chain type. For larger coverages, a disordered 3D phase similar to GaAs was found [218].

In Fig. 6.6 RAS spectra of the clean surface and spectra taken for the two wire geometries are shown. Similar to GaAs the initial quenching of all structures related to the clean surface (2.47, 3.15, 3.9 and 4.5 eV) is observed. The negative structure, which develops at low coverages at about 1.5 eV, can, by analogy to GaAs, be related to the presence of wires. This minimum is broadened to higher photon energy upon reaching 0.3 ML. In this case, the two different line shapes of the minimum can be attributed to the presence of two different Cs wires at the surface. Since above 0.3 ML – apart from the gradual quenching of the minimum below 2 eV – no further variations are detected in this energy region, the RAS measurements confirm that there is no difference in the local Cs geometry going from the broad wires to the 2D layer. As for GaAs, an additional maximum develops at 3.75 eV for the closed 2D layer.

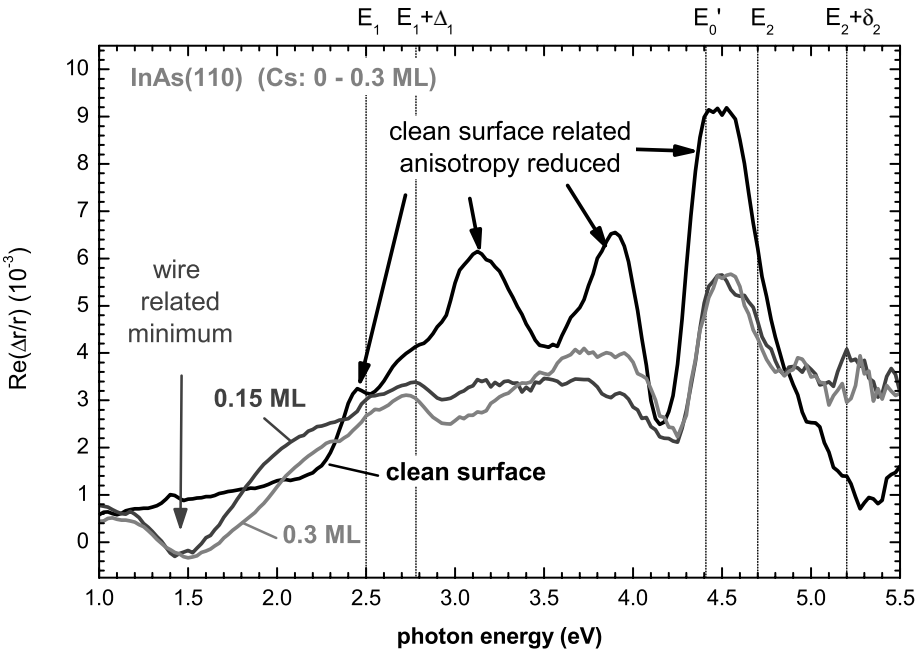

Figure 6.6: *RAS spectra of different Cs coverages on the InAs(110) surface. The spectra of the clean surface, 0.15 ML and 0.3 ML coverage are shown.*

6.2 Cs on InP(110)

Although no other experimental results for alkali adsorption on InP(110) exist so far, one expects a similar Cs adsorption behaviour, since the atomic geometry and electronic properties of the InP(110) surface are comparable to those of GaAs and InAs [233]. Even bulk critical point energies of InP are similar to GaAs, though with a smaller spin orbit splitting [228]

Upon the initial Cs adsorption as seen for GaAs and InAs, a minimum structure below the E_1 bulk critical point occurs. The minimum structure is more pronounced than in the InAs or GaAs case. Above 0.2 ML a blue shift of the minimum structure is observed.

If all RAS spectra are plotted in one graph by using a colour code (Fig. 6.8), it can be easily seen that the shift of the minimum is a gradual transition from one adsorbate configuration to another (indicated by the vertical lines in Fig. 6.8a). One structure, leading to the minimum at 1.8 eV can be found from the early stages of adsorption, but only up to 0.35 ML, while the other (minimum at 2.1 eV) occurs for coverages above 0.1 ML and vanishes only on formation of the disordered 3D layer. Although no experimental confirmation exists (e.g. STM), it is likely that a similar transition from one wire type to another happens on InP(110) as on InAs.

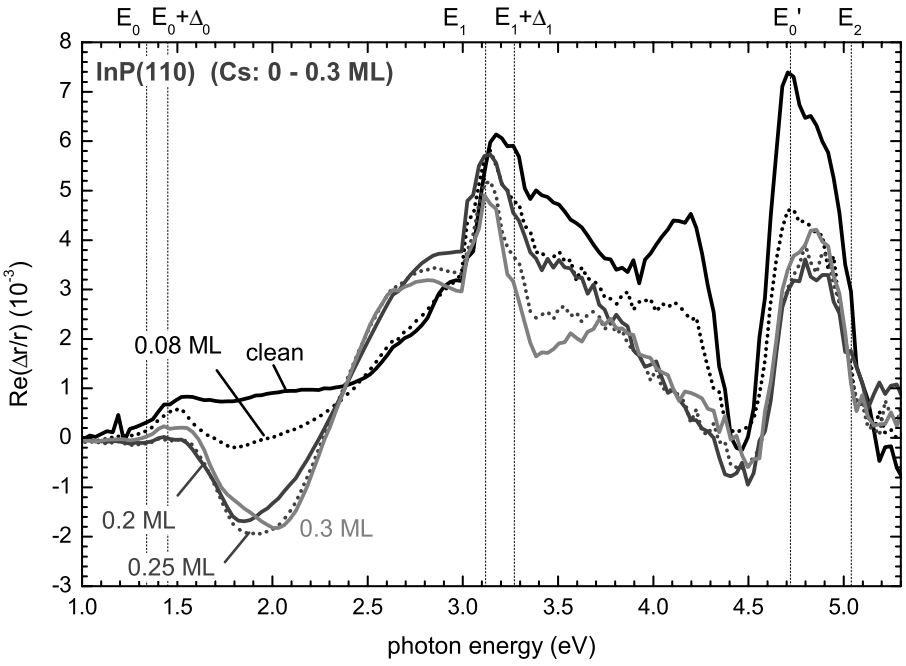

Figure 6.7: *RAS spectra for initial Cs adsorption on InP(110): Similar to the case of GaAs and InAs a minimum structure evolves upon Cs adsorption. Above 0.2 ML the minimum is blue shifted as it was observed for InAs, indicating the presence of a second wire geometry as is already confirmed for InAs.*

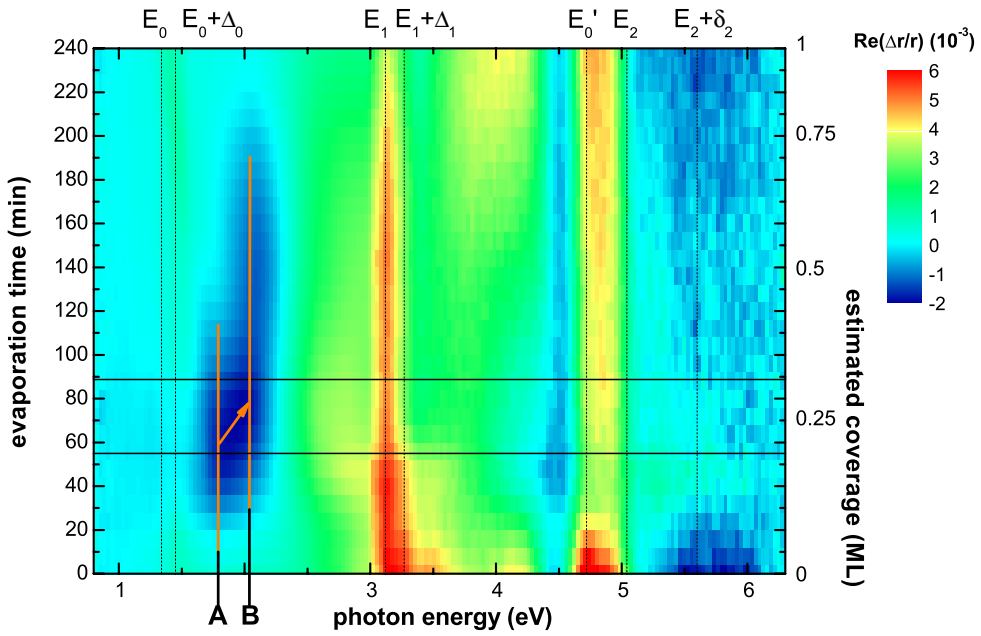

Figure 6.8: *RAS colour plot of caesium adsorption on InP. The RAS signal is colour coded (blue: -2, red: +6) and all spectra from the clean surface to complete saturation are shown. The two coverages shown in Fig. 6.7 (0.2 and 0.3 ML) are marked with a horizontal line. If plotted this way the two characteristic structures, which can be attributed to two different wire geometries, can be easily seen. The minima marked as **A** occurs for lower coverages. The second structure **B** appears above 0.2 ML and at a complete surface coverage (0.5 ML) only the minimum **B** is found.*

6.3 Comparative analysis of the wire regime

Generally upon adsorption of Cs the clean surface structures involving transitions from or to surface states disappear. Structures at bulk critical points, even visible for completely saturated or oxidised samples, remain. In all cases a minimum structure at low energies can be directly attributed to the Cs wires. It is evident that the energetic position of this minimum is substrate dependent (arrows in 6.9). It is therefore unlikely that the minimum is caused by transitions between states localised at the Cs-Cs bonds only, which are expected to be similar for all substrate materials [230]. For GaAs the minimum is located at 2 eV, which is exactly in the same energy region as a structure seen for Cs adsorption on GaAs(001) [234–236]. Although the atomic configuration is different in that case, this suggests the involvement of states localised at Cs-Ga or Cs-As bonds in the minima structure. The idea that such states are responsible for the minima around 2 eV is also strongly supported by an early combined photo emission and inverse photo emission study [237]. It was shown that upon Cs adsorption on GaAs(110) new surface states evolve, but all of them are above the conduction band minimum. Anisotropic transitions involving these states will therefore occur above the fundamental band gap of GaAs of 1.45 eV.

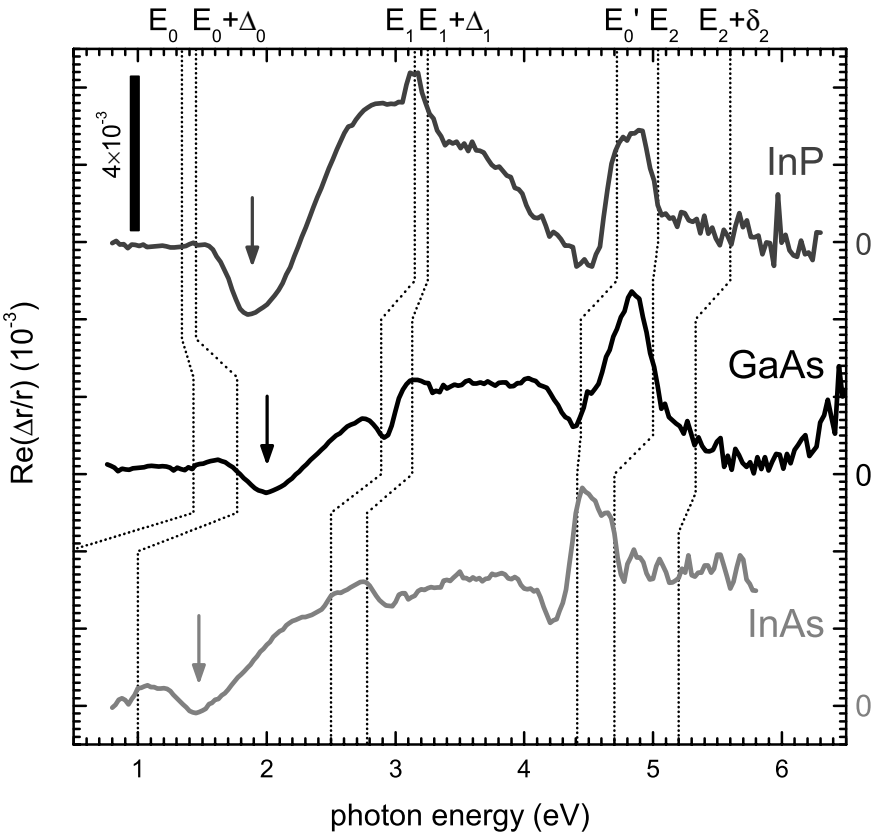

Figure 6.9: *Comparison of the RAS spectra of Cs wires on III–V cleaved surfaces. The characteristic feature is the minimum structure (arrows) above the $E_0 + \Delta_0$ bulk critical point.*

Another possibility would be that strain, introduced by the Cs chains, modifies bulk states and produces the characteristic anisotropies. This would be consistent with the fact that the energetic position of the minimum scales with the bulk critical points of the different substrates. This model is supported by the fact that other adsorbates forming chains along the [1$\bar{1}$0] direction (such as Sb) lead to a minimum in the RAS around 2 eV as well [238, 239]. In Fig. 6.10 submonolayer coverages of Sb on GaAs and Sn on InAs are compared to corresponding coverages of Cs. For the case of Sn on InAs, where no wires are formed in this coverage region, no minimum structure is found. In the case of Sb on GaAs, where a Sb zig-zag chain is formed a similar minimum is found. This comparison would suggest that the formation of an adsorbate zig-zag chain leads to a minimum structure above the $E_0 + \Delta_0$ bulk critical point due to introduction of a strain field.

On the other hand it is hard to understand why strain should effect the RAS spectra in a region away from bulk critical points. I think the second scenario of surface states localised at adsorbate–group V or adsorbate–group III bonds contribute is more likely. If the adsorbate forms a zig-zag chain the orientation of the bonds will be always similar and if the involved states are closer to the group V or group III atom the energetic difference can only vary slightly with adsorbate and is also linked to the band structure of the substrate. In this picture it can also be understood

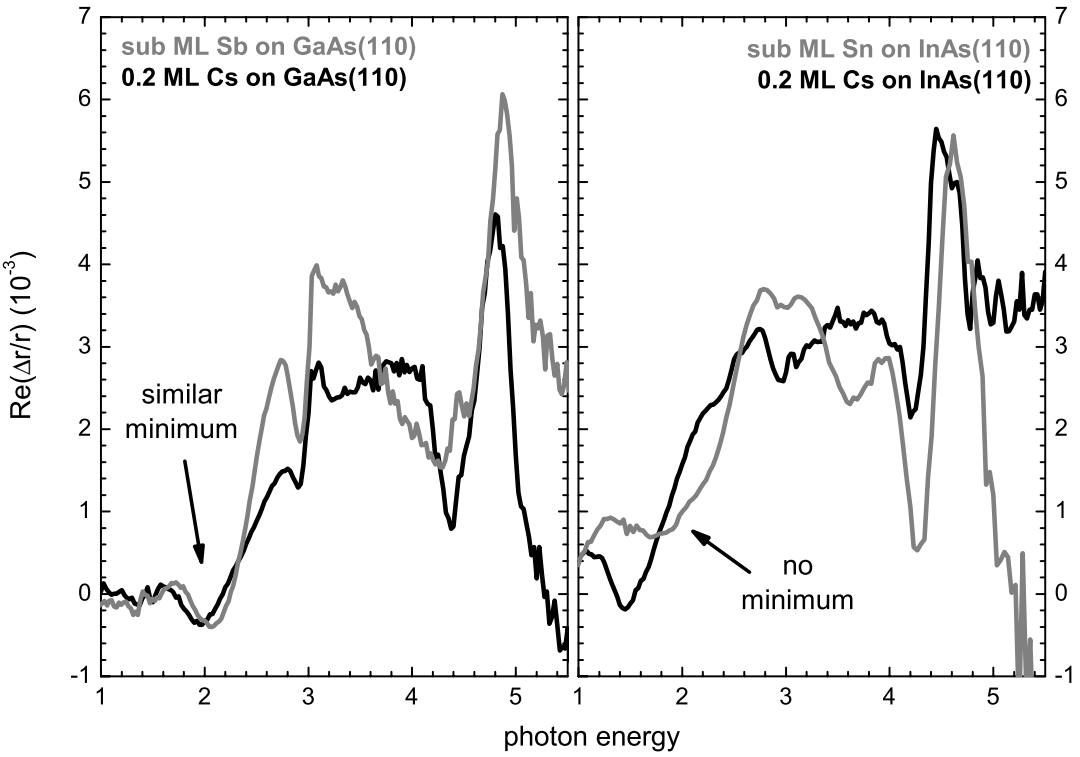

Figure 6.10: *Comparison of RAS spectra of Cs wires on GaAs(110) and InAs(110) with other adsorbates. For Sb/GaAs(110) the formation of a zig-zag chain was observed. In the RAS again a minimum structure is observed. For the case of Sn/InAs a disordered (1×1) was found – the characteristic minimum does not appear. The number of studied systems though is at the moment too small to conclude that the minimum does occur for every 1D adsorbate structure.*

how other chain structures of Cs or Sb on GaAs(001) surface lead to similar minima around 2 eV [234, 240].

Currently no final answer can be given concerning the origin of the minimum structure itself. Either *ab-initio* calculations of these surfaces or additional measurements are needed. One possible measurement to gain new insight in the origin of the wire induced anisotropy would be an adsorption experiment with Na or K. On the (110) surface it is known that K and Na form similar wires but strain the underlying substrate in different ways than Cs [230].

6.4 Structural transition towards a 3D metallic surface

For room temperature deposition, alkaline adsorption above 0.5 ML leads to the formation of a disordered metallic surface, saturating at a coverage of about 1 ML. This second Cs adlayer was always reported to be locally disordered and isotropic in STM images [217]. One therefore expects a quenching of all RAS feature which were attributed to the ordered 2D phase. The disorder is also seen in LEED images, where one observes only a weak (1×1) pattern.

In Fig. 6.11 the development of the RAS spectra for the case of Cs adsorption on GaAs(110) is shown. The quenching of RAS features related to the ordered phase (minimum at 1.75 eV) is clearly observed. The reduction of the minimum is accompanied with the development of a new structure at 4 eV. This structure is already present in the spectra of the 2D ordered layer, though less intense. To prove whether these structures originate from the Cs layer, the samples were oxidised at ambient conditions for 5 min. The maxima at 4.0 eV and 2.6 eV and the remaining minimum structure at 2 eV disappear completely upon oxidation (see Fig. 6.12), while all the remaining anisotropies are close to the bulk critical points and are therefore likely related to surface modified bulk states. These structures are always present in the spectra independent of Cs coverage. The characteristic structures of

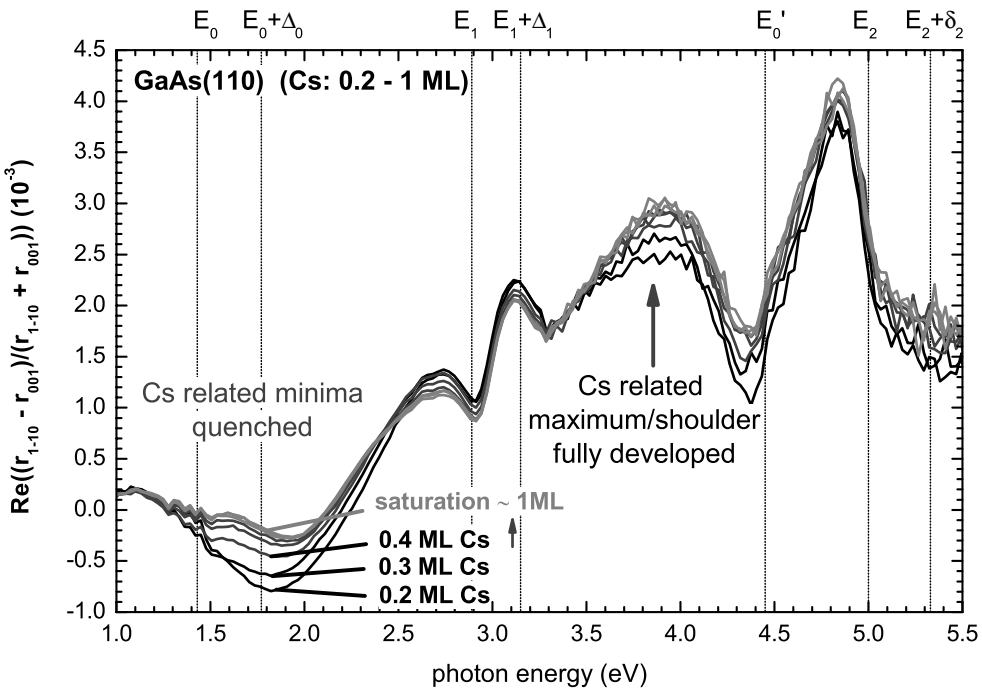

Figure 6.11: *RAS spectra of the caesium covered GaAs(110) surface upon saturation. The minimum related to the two dimensional phase vanishes, while the maximum at 4.0 eV gets more pronounced. The spectra were taken during evaporation. The time difference between the individual spectra was 30 min. Since the coverage is not linear with time in this region there is no constant coverage difference between the spectra.*

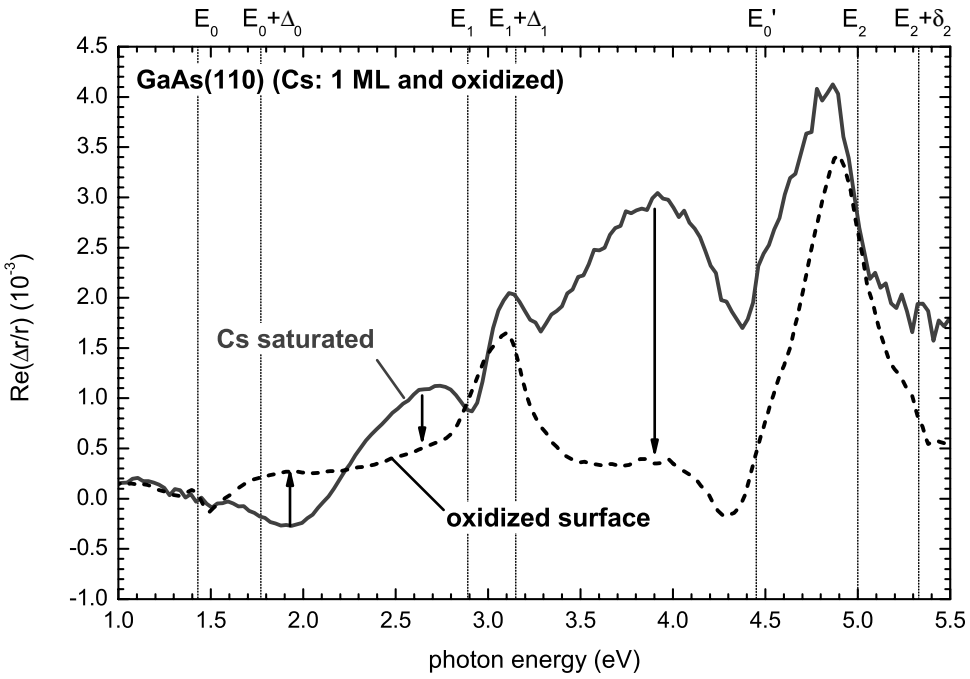

Figure 6.12: *Oxidation of the Cs/GaAs(110) saturated surface. By putting the saturated surface into ambient conditions the Cs related anisotropies vanish. In the vicinity of bulk critical points anisotropies remain most likely caused by strain in the near surface bulk layers.*

the disordered metallic phase are therefore: *(i)* a remaining minimum, *(ii)* a shoulder below the E_1 bulk critical point and *(iii)* the broad maximum between the $E_1 + \Delta_1$ and E_0' bulk critical points. In Fig. 6.13 the spectra of the Cs saturated GaAs, InAs and InP surface are shown. The characteristic structures *(i,ii,iii)* are seen for all substrates.

The second and more pronounced maximum *(iii)* at 4.0 eV for InP, 3.9 eV for GaAs and 3.75 eV for InAs appears already in the 2D phase but is fully developed at 1 ML when the second disordered Cs layer is completed. The question arises whether this structure originates from anisotropic Cs-Cs or Cs-substrate bonds in the interface layer, since it starts to evolve already for the 2D closed layer around 0.5 ML coverage. To remove the influence of the substrate reflectivity on the RAS spectra on can calculate the surface dielectric anisotropy (SDA), which describes the anisotropy in the dielectric tensor components directly (see 3.2.1). In Fig. 6.14 the SDA is calculated for saturated GaAs, InAs and InP (110)-surfaces. The SDA for the Cs disordered layer is very similar for all surfaces and can be described by only two contributions. The oscillatory structures at the bulk critical points usually originate from an uni-axial strained near-surface-layer and are quite well understood [229]. The structure in this case can be explained in a simple model where the bulk dielectric function is slightly shifted in energy for one direction. The SDA will then show the characteristic derivative like structures at **all** critical point energies. Additionally the changed surface electric field upon the formation of the metallic overlayer can influence the RAS and SDA of the sample, since an electric field gradient at the

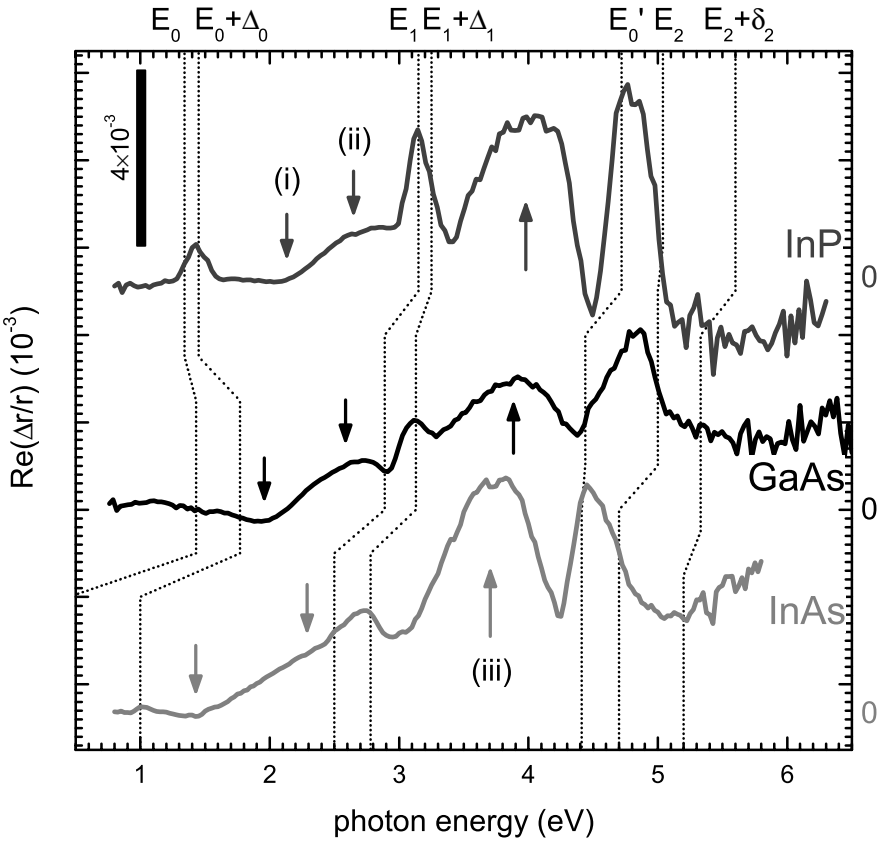

Figure 6.13: *Comparison of the fully saturated III–V (110) surfaces, the structures related to the Cs-Cs or Cs-bulk bonds are marked with arrows. For all surfaces a remaining minimum* (i)*, a shoulder below the* E_1 *critical point* (ii) *and a broad maximum* (iii) *are found*

surface layer can also produce an optical anisotropy [241, 242].

The second prominent structure in the SDA is a broad structure, which is centred around 3 eV (see guide lines in Fig. 6.14) Being almost independent from the substrate, it probably originates from Cs-Cs bonds between the first and the disordered second Cs adlayer. However one cannot exclude the possibility that bulk like states are involved, since they also vary only slightly in this energy region for the substrates used in this study [228]. This scenario is be supported by recent results of Cs adsorbed on the GaAs(001) surface where a structure at 4 eV has been explained by transitions from bulk-like and surface states into states located in the Cs layer [234]. An additional experiment with InSb(110) could clarify this assignment, since for InSb the E_1 bulk critical point is at lower energies than the E_1 of GaAs, InAs and InP.

Experimentally there is one strong indication that the broad structure originates from the substrate-Cs interface. For Cs/GaAs(110) the structure is already fully developed for the 2D closed surface while on InP and InAs it is clearly maximised upon formation of the 3D disordered layer. If one assumes that states localised at the caesium/substrate interface are involved, this might suggest that a rearrangement of

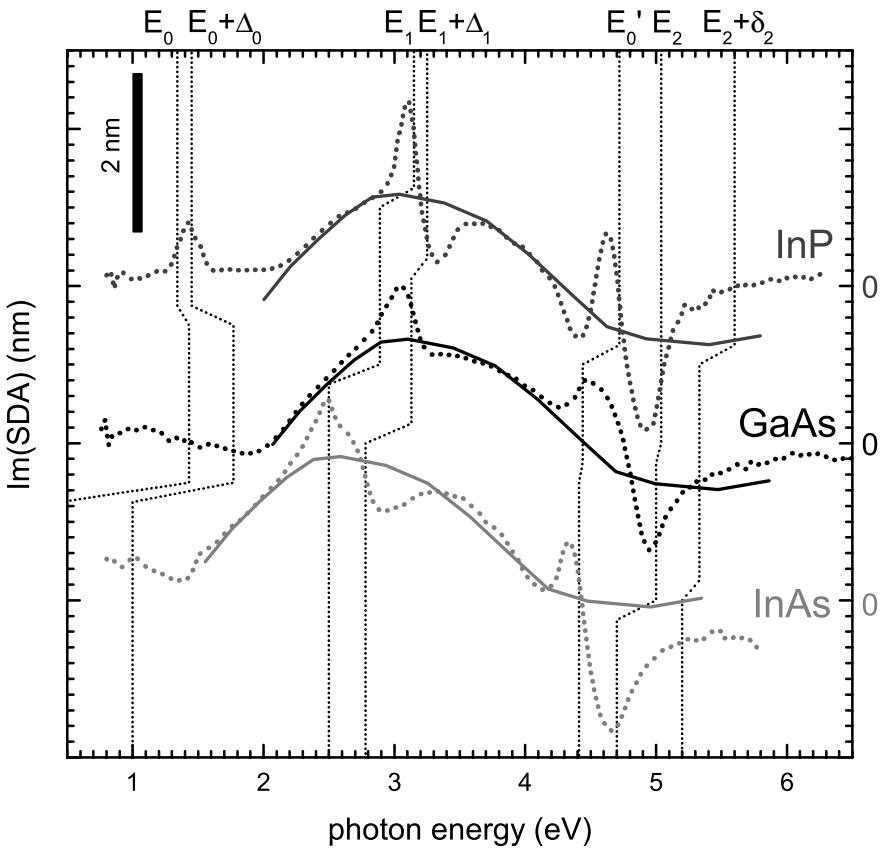

Figure 6.14: *Surface dielectric anisotropy of the metallic Cs overlayer (dotted), calculated from the RAS spectra of Fig. 6.13 and the dielectric function of the substrate material from [74]. All surfaces show oscillatory structures around the bulk critical point and a broad structure around 3 eV (see the solid guide to the eye).*

the interface upon saturation occurs in the case of InAs and InP. It would be interesting to have calculations of the formation energies of different interface geometries as well as calculations of the optical anisotropy to explain these differences between the substrates.

6.5 Concluding remarks

The wires of caesium atoms on III-V cleaved surface discussed in this chapter do not show any anisotropic metallic properties as the other wires discussed in previous chapters. However a one dimensional character in real space is clearly observed and by electron counting (at least for the 2D closed layer) a metallic surface is expected [67, 217]. The reason of the insulating behaviour of the Cs wires is so far not fully understood. It is likely though that the lateral spacing of the caesium atoms and therefore also the average electron distance are larger than the critical spacing d_0 for a Mott-Hubbard transition. The electronic band gap, which was measured by STS, is

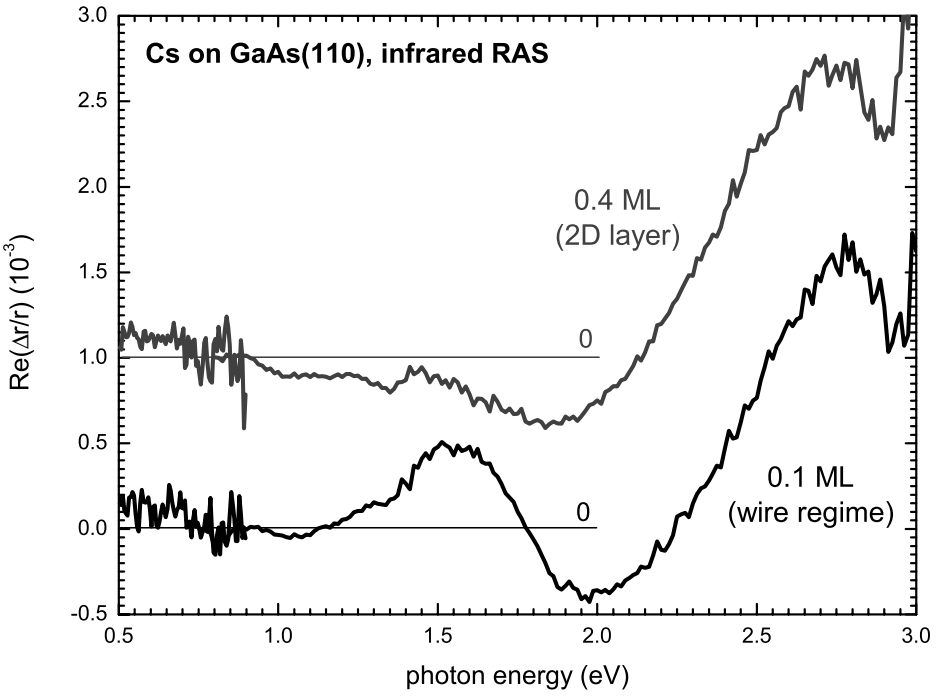

Figure 6.15: *Infrared RAS measurements for the Cs/GaAs(110) system. The spectra for the 1D regime as well as for the 2D regime do not show any structures above the noise level. Hence RAS is unsuited to directly measure the Mott-Hubbard gap.*

for instance, in the case of Cs/GaAs with 1.1 eV for the 1D regime and 0.65 eV for the 2D regime, smaller than the clean surface band gap of 1.45 eV [217].

Figure 6.15 shows infrared RAS spectra in the region between 0.5 and 3 eV. No structures are found in the RAS in the case of Cs wires or for closed 2D layers. At least no structures above the noise level and uncertainty of the zero line (0.2×10^{-3}). For a geometrical anisotropic system optical transitions between the surface fundamental gap are possible and can result in particularly strong RAS signals also in the infrared (see for instance the Si(111)-(2×1) reconstructed surface [92] or the Si(111)-In:(8×2) in section 5.3.1). For the fundamental gap of a Mott-Hubbard correlated system optical transitions between the empty and occupied states are disallowed. Consequently RAS should show no structures at these transition energies – and none are measured (see Fig. 6.15).

Nevertheless the RAS spectra of the clean surfaces are changed in a characteristic way upon the formation of the wires. Structures arising from transitions involving true surface states of the clean surface are quenched with increasing coverage. This behaviour though is unspecific regarding kind of adsorbate or whether wires are formed.

What is characteristic is the formation of a minimum structure between the $E_0+\Delta_0$ and E_1 bulk critical point. The changes in the line shape of this minimum can be directly attributed to changes in the geometric structure of the Cs wires. Hence RAS can be used to monitor the wire formation. So far no *ab-initio* calculation of the

optical anisotropy or the bandstructure of these surfaces exist, therefore the origin is only speculative. Since the bulk joint density of states is comparably small in this spectral region it is likely that surface states or resonances located at the back bonds are involved in this minimum structure.

For the broad positive structure which arises for all surfaces upon completion of the 2D closed Cs layer and formation of the 3D disordered phase (see Fig. 6.14) the same argument would suggest that Cs-Cs bonds in the still anisotropic interface region contribute. Nevertheless this assignment is preliminary and awaits confirmation by calculations or additional measurements such as core level spectroscopy. The RAS measurements with the disordered metallic overlayer also show that the characteristic minimum structure of the wire regime (or 2D layer) though reduced is not completely quenched. This is a promising sign that the interface geometry still has similar characteristics as the original wire itself. For a technical implementation of nanowires only some atoms wide, structures need to be protected by additional layers. Whether the properties of the wires will be unaffected by such caps is in doubt. With RAS it will be possible to test these effects of capping in more detail since as is shown here, the uncapped as well as the capped wires can be measured with the same technique.

7. Conclusions

In this work the optical properties of nanowires, composed of atoms which are metallic in their bulk phase, were investigated. The measured structures itself varied not only in material but also in size. Common to all was that the nanowires were formed by a self organising process of the adsorbed metal atoms on clean semiconductor surfaces.

It was shown that for the largest investigated wires (or better anisotropic islands), effective media theories are sufficient to describe the optical anisotropy of the nanowire with the properties of the bulk metal. This description fails for wires with diameters smaller than 40 nm. Instead the optical anisotropy is dominated by a free electron like response. It was shown that this response can be described by anisotropies in the plasma frequency ω_p and the scattering frequency ω_τ and is directly related to the conductance anisotropy $\Delta\sigma$. For the two test systems Sn/InAs(110) and Pb/Si(335) it was found that mainly the anisotropy in the scattering rate leads to strong RAS signals. The anisotropy dominantly occurs below 1 eV and only by the development of an IR enhanced RAS setup these measurements were possible.

In the case of even smaller nanowires (< 5 nm) such as indium wires on Si(111) the free electron like response becomes negligible and interband transitions dominate the RAS spectra. Nevertheless one particular system – the Si(111)-In:(4×1) surface – was studied since it undergoes a reversible phase transition below 120 K which was attributed to the inherent instability of an one-dimensional metallic system to periodic lattice distortions – the Peierls instability. Although other models than the formation of a charge density wave (CDW) driven by this instability are discussed the combined RAS and Raman spectroscopy study performed here could show that only the CDW formation can explain all experimental data. The suggested alternative – a structural disorder–order transition, cannot explain the narrow line widths of surface phonons in the supposed disordered phase, which are broadened in the supposed ordered low temperature phase. Other measurements such as the adsorption experiments, where the room temperature (4×1) phase was stabilised at 30 K also confirm the CDW model. With a detailed analysis of the infrared RAS measurements it could be furthermore shown that, although small, a contribution of the quasi free electrons can be seen. Unfortunately a direct observation of a Peierls gap, as it is expected in the CDW model, was due to the limitations of the spectral range of the RAS not possible.

The last wire system which was extensively studied were Cs wires formed on different III–V(110) surfaces. In this case the electron density is already small enough that the wires are non-metallic. The system is believed to be a Mott-Hubbard insulator. In this work it could be shown that – as expected – no free electron contribution is found but that the formation of such wires still can be optically monitored since surface states or surface resonances located at the Cs-group III or Cs-group V atoms

and transitions are sensitive to the wire geometry and can be seen in RAS.

In conclusion it was shown that surface sensitive optical techniques can be used not only to monitor the formation of nanowires but can also help to test competing models of the wire structure itself. The direct observation of a surface phase transition with RAS but also Raman spectroscopy was proven to be a valuable tool in understanding such complex phenomena. For larger nanowires it was also possible to measure the conductance anisotropy of metallic nanowires in a contactless way.

A. Experimental details

A.1 Calibration of submonolayer coverages

Within this study different metals were deposited on to clean surfaces to obtain self-assembled metallic nanowires. In the case of Sn/GaAs the quantities of tin deposited were large enough to use rather classical approaches for thickness calibration of the adsorbed material such as growth monitoring with quartz microbalances – which itself were calibrated with growing thick samples through masks and determination of thickness by *ex-situ* atomic force microscopy (AFM).

However in all other cases this direct approach was not feasible for various reasons. In the case of the alkaline adsorption this method could not be used. Due to the slow growth rates quartz-micro balances were not stable enough and adsorption was limited to 1 ML in any case, since that was found as the saturation coverage of alkali metals on silicon and the III-V semiconductors used in this study. Also for the indium deposition on silicon only 1 ML was needed to grow the wire structures and therefore other methods of adsorbate coverage determination had to be used. In the next sections they are described in detail for all adsorbates used.

Caesium evaporation

Caesium was evaporated out of dispensers from SAES-Getter. In contrast to Knudsen-like evaporators no bulk material is thermally desorbed but a salt of Cs (here CsJ) is thermally decomposed. The dispensers are heated with direct current and mounted on a two-pin UHV feedthrough. The deposition rates can be varied by the heating power, but are low compared to Knudsen-type evaporators. An additional problem is that the characteristics of each dispenser varies – hence each had to be calibrated individually.

The adsorption on the surfaces studied here saturates at about 1 ML and is therefore highly non-linear in time. Classical approaches such as flux and evaporation time measurements cannot be applied because of the low fluxes but also because of the inherent nonlinearity of the adsorption.

To overcome this problem and to have a reliable calibration which can be done *in-situ* without need of additional measurements the adsorption of caesium was first investigated for several substrates with Auger electron spectroscopy. In this first step for each coverage LEED images were taken and RAS measurements performed. The relative Auger intensity of the Cs NOO line at 47 eV to the substrate Auger lines (As: LMM at 1230 eV, Ga: LMM at 1070 eV, In: MNN at 404 eV) saturates upon completion of the 3D layer. It is already known that for room temperature deposition, not more than one monolayer can be deposited [217]. In order to get an approximation of the

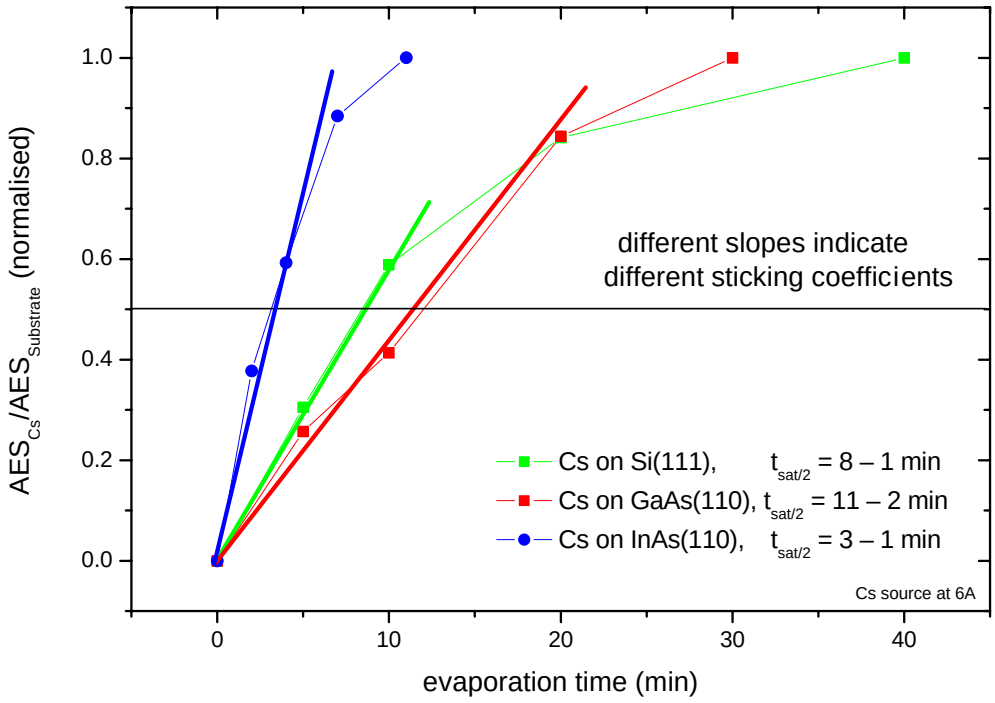

Figure A.1: *Normalised Auger intensity ratios of the Cs NOO Auger line and a substrate Auger line for different Cs coverages. Since saturation means 1 ML in the case of alkaline adsorption this quantity can be directly interpreted as coverage. It is already obvious that adsorption rates vary with each substrate material due to different sticking coefficients. It is seen that for coverages much below 0.5 ML coverage versus evaporation time shows a linear behaviour. For later adsorption studies a linear behaviour was therefore always assumed in this coverage range. The Cs flux of other evaporators was determined by measuring the time until the RAS spectrum of Cs/GaAs(110) was similar to the one measured for the 10 min spectra of this first study.*

coverage, one can therefore normalise the relative Auger intensities of Cs for each evaporation step with respect to the relative intensity at saturation.

Please note that there have been some differences in the literature concerning the classification of one monolayer in the case of alkali adsorption. We use the definition of one monolayer as the number of atoms on the clean III–V substrate surface. The coverage calibration has to be done for each of the substrate material since the sticking coefficient of Cs differs on the substrates investigated here. Using the same condition on the Cs cell one finds saturation after 2 hours for GaAs but already after 45 minutes for InAs (for minimised Cs flux).

In Fig. A.1 the results of these measurements are shown for different substrate materials. Since such a study can only be done if an Auger electron spectrometer is available it could not be applied for all the studies shown in this work. But what could be done was using this coverage calibration to establish a set of “calibrated”

RAS spectra. Since only the Cs-flux varies between different chambers, different dispensers, and applied heating power, the general adsorption behaviour as seen in Fig. A.1 is only scaled in time. By utilising certain key features in the RAS spectra of Cs/GaAs(110) such as the energetic shift of the 2 eV minimum (see Fig. 6.4), or the beginning quenching of the minimum structure (see Fig. 6.11) evaporation time was linked to coverage. Hence by always using the same nominal evaporation conditions and a calibration measurement of the well known Cs/GaAs(110) system the flux rate of each individual Cs dispenser was determined. By scaling the adsorption characteristics of Fig. A.1 by this flux rate the actual coverage could be estimated for all other evaporation times.

This procedure works fine for all surfaces where this first Auger measurement was performed: GaAs(110), InAs(110) and Si(111). For other surfaces additional assumptions had to be made. For the measurements of Cs on InP(110) the coverage was estimated by assuming the principal changes in the RAS spectra of Cs/InP(110) occur at the same Cs coverages as for Cs/InAs(110). Since the RAS spectra are very similar this assumption can be justified. For the measurements of Cs on Si(111)-In:(4×1) surfaces the estimation was based on the assumption that the sticking coefficient of Cs on clean Si(111) and on Si(111)-In:(4×1) does not differ significantly and the results of Fig. A.1 are therefore valid.

Sodium evaporation

All measurements using sodium were performed in a vacuum chamber were no Auger analysis was possible. The evaporation of sodium was done again with dispensers from SAES-Getter as in the case of caesium evaporation. Similar to Cs also for sodium a saturation of GaAs(110) or Si(111) surfaces was found. The calibration of the sodium coverage was therefore based on the RAS measurements of the Cs/GaAs(110) system. Assuming that the coverage is similar linear in the low coverage region and that structures of the clean surface are equally quenched by sodium adsorption the development of the clean surface GaAs(110) RAS spectra upon sodium adsorption was used for calibration.

This approximation of the coverage was consistent with the reduction of the 2 eV RAS minimum of the Si(111)-In:(4×1) upon sodium adsorption – again compared to the changes introduced by caesium where the actual coverage was calibrated with Auger measurements.

Indium evaporation

Indium was needed for the preparation of the Si(111)-In:(4×1) surface, which has a nominal coverage of 0.75 ML indium. Since the preparation was controlled *in-situ* by RAS as described in detail in section 5.1.2 the effective indium flux at the surface was very well known for each sample at a temperature of 450°C. Since the evaporation time for 0.75 ML was known, submonolayer coverages which are needed for the prevention of the phase transition of the Si(111)-In:(4×1) can be achieved by much shorter evaporation times.

Tin evaporation

Tin was evaporated in larger quantities from regular Knudsen type cells. The cell characteristics were well known, since the evaporator was already used and calibrated with AFM measurements of thick samples in previous studies of tin adsorption [154, 155]. With the given geometry of the UHV chamber, sample- , Sn-cell- and quartz micro balance position a growth rate of 1 ML/min was achieved if the Sn-cell was set to 960°C. Cell temperature was controlled by the inbuilt Pt-RhPt thermocouple and evaporation was only started when the flux was stable at a change of oscillator frequency of 6 Hz/min. Since RAS spectra were taken at growth interruptions and closed evaporator shutters the Sn layer thickness was known for each spectrum. In later studies these "calibrated" RAS spectra were utilised to determine the coverage of samples grown in other chambers, where no micro balance was available.

A.2 Calibration of the temperature measurement

Low temperatures

The low temperature RAS and Raman measurements were performed in a UHV chamber equipped with a liquid Helium evaporator type cryostat. Attached to the cooling stage without shielding was a home built preparation stage with direct heating capability as well as resistive heating. To prevent heat transfer to the copper cooling stage during the sample preparation the molybdenum heating stage was separated from the cooling stage by 1 mm thick sapphire plates.

With such a setup the lowest sample temperature possible was found to be 20±10 K. The temperature was measured with three independent Platinum resistors (Pt100 and Pt1000) with a three point measurement to account for the resistance of the connecting wire. Other type of temperature sensors could not be used, since not only low but also high temperatures (900 K) are needed to be measured in this particular setup, which will destroy commonly used Si diode temperature sensors.

In the range of 70-800 K the Pt100 resistors are specified with an temperature error of ±1 K. Below 70 K each resistor is needed to be calibrated individually since the zero temperature reading depends on the defect density of the platinum resistor itself and not on temperature alone. Such a calibration would need a known low temperature reference, which was not available. Using the interpolation of the standard *R-T* dependence of a Pt100 at temperatures below 70 K will lead to a systematical overestimation of the temperature. The temperatures given here are always mean values of all three detectors. For the lowest achievable temperature (highest He flux) a typical reading was 10 K, 15 K and 30 K, the temperature is therefore given as 20±10 K, which is a reasonable value for a liquid Helium cooled stage without cooling shields, though due to the systematic overestimation, the true temperature will be probably at the lower end of the confidence interval.

At higher temperatures the errors get smaller and above 70 K all resistors showed the same reading within the 1 K error range.

In order to test whether the true sample temperature deviates from the reading of the temperature sensors two different test experiments were performed. First a

Pt100 resistor was mounted on top of a sample during cooling, which showed a 10 K higher minimum temperature than the ones mounted at the manipulator, though this is within the errors of the resistors used and since the thermal contact to the sample was not ideal the small difference was believed to be irrelevant. Above 100 K the difference was smaller than 2 K.

The second test was to measure the shift in the phonon mode of a silicon sample during cooling. The Γ'_{25} mode shifts from 520 cm^{-1} at room temperature to 524 cm^{-1} at low temperatures and is very well known (see for instance [198]. The error of this method is given by the error of the frequency determination by Raman spectroscopy which was about 0.1 cm^{-1} which corresponds to a temperature deviation of 5 K. Within this error there was no deviation from the temperature reading of the Pt100 elements, though due to the saturation of the frequency shift of the silicon phonon below 100 K (see zero point renormalisation effects in [187, 198]) this method could not be used to evaluate the minimum temperature.

High temperatures

During the preparation of the vicinal Si(111)-(7×7) surface with defined monoatomic steps and regular terraces the samples need to be heated to 1100°C. The heating was by direct current heating and it was necessary to calibrate the current vs. temperature curves for each individual sample, since sample size, contact resistance and if samples with different offcuts were used, the doping level also varies. The temperature of the sample was measured with a commercial pyrometer (Keller HCW, Pz20 AF1) measuring in the wavelength region of 1.1–1.7 μm through the optical viewport normally used for the RAS measurements. The emissivity of silicon was set to 0.65, which, in this spectral region, is only valid for temperatures above 800°C [243]. Since the temperature for the preparation of the indium nanowires (400-450°C) was not as critical because the wire formation was monitored with RAS, the systematic deviations of the pyrometer reading below 800°C were neglected.

For the high temperatures the measured spot was systematically varied, showing temperature gradients of up to 50 K on the samples. For the *I-T* calibration curves the highest reading was always taken to prevent accidental melting of the samples.

B. Visualisation of surface phonons

Vibrations of single molecules or clusters and other isolated structures can be calculated with freely available packages such as GAUSSIAN[1]. The software packages also include mechanisms to visualise the calculated vibrational modes.

In the case of indium nanowires the calculations are more complicated, since for proper treatment of the surface many unit cells need to be considered. There are other packages used for DFT calculations in such repeated slab geometries. Some groups also analyse the vibrational properties of surfaces with such packages (see calculation details in [145–147, 186]). The calculated Eigenvector of the vibration is then usually plotted by indicating the maximum displacement of the atoms from their equilibrium positions. An example of this is given in Fig. B.1. The displacement

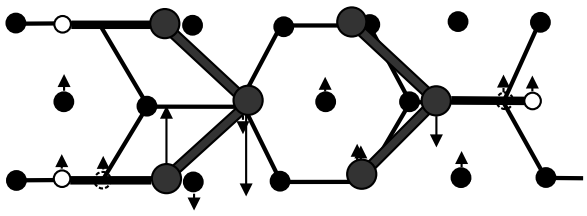

Figure B.1:
Example of a calculated displacement pattern of the Si(111)-In:(4×1) surface taken from [186]. This particular mode is the A″ mode at 55 cm^{-1}.

pattern is shown in one unit cell and if more than one layer is considered the projected views are not very intuitive.

Since the available packages for visualisation of phonons were not prepared to display structures in a periodic continuation, which is necessary for intuitive animations of a surface phonon starting with the unit cell, a new approach was made. To simplify the problem the graphics are not generated by the new program itself. Instead description files for the free ray-tracing program Povray are created. The individual images are then put together into a single animation by standard graphic packages. The program itself is written in a script language (perl). To use it a perl interpreter, povray and an image processing program which can be used in batch mode is additionally needed.

The atomic positions and the Eigenvector of the vibration need to be calculated first by the theorists and are then given in normal coordinates in a single configuration file (`unitcell.conf`). In a second file (`atoms.conf`) for each type of atom a colour is defined. In the last configuration file (`povray.conf`) all other information necessary for the animation is given. This includes some details for the ray tracing program (camera position, light source, . . .). For convenience these should be tested in modelling programs for povray. The second class of information given in `povray.conf` are the number of frames for a single period, how many periods and unit cells should

[1] see: `http://www.gaussian.com/gv_plat.htm`

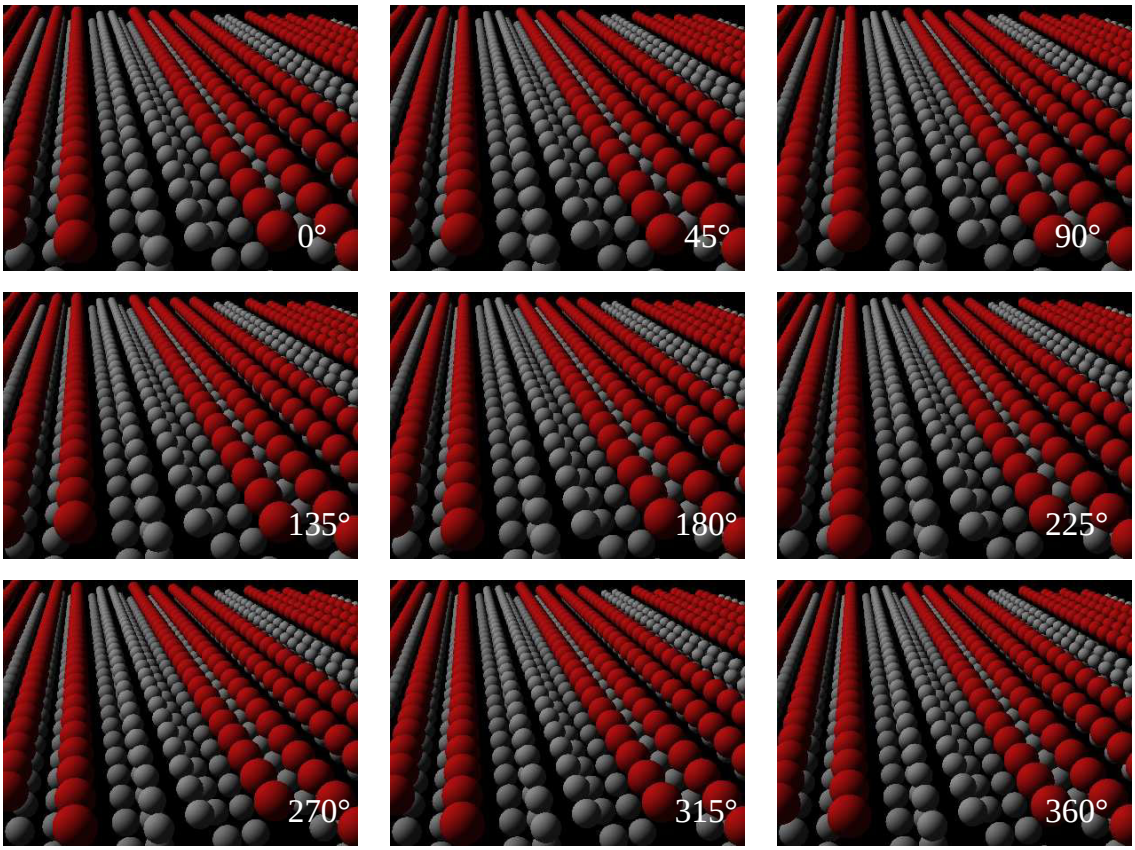

Figure B.2: *Snapshots of a phonon animation for the 55 cm^{-1} A'' mode of the Si(111)-In:(4×1) surface. The darker (red) atoms depict indium atoms while the lighter ones depict silicon. In this static view the vibration is not very obvious. It is therefore recommended to look at the animation at:* `http://gift.physik.tu-berlin.de/pub/In-Si-modes/`

be considered and the exact commands as to how povray and graphic converter are to be called to finish the animation.

Finally some physical information is set in `povray.conf`: first of all the size of the unit cell and phonon amplitude in nm. To animate propagating waves a phase shift can be defined between adjacent unit cells in x and y direction. Lastly there is the possibility to simulate elevated temperatures by applying additional random displacements for each atom. Currently no physical models are included for the temperature dependence, amplitude of vibration or wavevectors, since in a first step only the visualisation of the displacement pattern itself was of interest.

In Fig. B.2 a set of images for visualising the same vibrational mode as in Fig. B.1 is given. The full animation can be found, together with all other calculated modes of the Si(111)-In:(4×1) surface at the given website.

Bibliography

[1] Mauro J. Kobrinsky, Bruce A. Block, Jun-Fei Zheng, Brandon C. Barnett, Edris Mohammed, Miriam Reshotko, Frank Robertson, Scott List, Ian Young, and Kenneth Cadien, *On-Chip Optical Interconnects*, *Intel Techn. Journal* **8**, 129 (2004).

[2] R. E. Peierls, *Quantum theory of solids*, At the Clarendon Press, Oxford, 1955.

[3] T. Abukawa, M. Sasaki, F. Hisamatsu, T. Goto, T. Kinoshita, A. Kakizaki, and S. Kono, *Surface electronic structure of a single-domain Si(111)4x1-In surface: a synchrotron radiation photoemission study*, *Surf. Sci.* **325**, 33 (1995).

[4] F. J. Himpsel, K. N. Altmann, R. Bennewitz, J. N. Crain, A. Kirakosian, J. L. Lin, and J. L. McChesney, *One-dimensional electronic states at surfaces*, *J. Phys. Cond. Mat.* **13**, 11097 (2001), and references therein.

[5] Q. Tang, S. Q. Shi, and L. M. Zhou, *Nanofabrication with atomic force microscopy*, *J. Nanosci. Nanotechnol.* **4**, 948 (2004).

[6] B. Fay, *Advanced optical lithography development, from UV to EUV*, *Microelectron. Eng.* **61-62**, 11 (2002).

[7] J. C. Hulteen and C. R. Martin, *A general template-based method for the preparation of nanomaterials*, *J. Mat. Chem.* **7**, 1075 (1997).

[8] B. R. Martin, D. J. Dermody, B. D. Reiss, M. M. Fang, L. A. Lyon, M. J. Natan, and T. E. Mallouk, *Orthogonal self-assembly on colloidal gold-platinum nanorods*, *Adv. Mater.* **11**, 1021 (1999).

[9] M. Wirtz and C. R. Martin, *Template-fabricated gold nanowires and nanotubes*, *Adv. Mater.* **15**, 455 (2003).

[10] N. I. Kovtyukhova and T. E. Mallouk, *Nanowires as building blocks for self-assembling logic and memory circuits*, *Chemistry-A European Journal* **8**, 4355 (2002).

[11] R. M. Dickson and L. A. Lyon, *Unidirectional plasmon propagation in metallic nanowires*, *J. Phys. Chem. B* **104**, 6095 (2000).

[12] W. K. Hsu, S. Trasobares, H. Terrones, M. Terrones, N. Grobert, Y. Q. Zhu, W. Z. Li, R. Escudero, J. P. Hare, H. W. Kroto, and D. RM. Walton, *Electrolytic formation of carbon-sheathed mixed Sn-Pb nanowires*, *Chem. Mat.* **11**, 1747 (1999).

[13] C. J. Murphy and N. R. Jana, *Controlling the aspect ratio of inorganic nanorods and nanowires*, *Adv. Mater.* **14**, 80 (2002).

[14] Marian A. Herman, Wolfgang Richter, and Helmut Sitter, *Epitaxy*, Number 62 in Springer Series in Materials Science. Sringer-Verlag, Berlin, Heidelberg, 2004.

[15] P. Gambardella, M. Blanc, H. Brune, K. Kuhnke, and K. Kern, *One-dimensional metal chains on Pt vicinal surfaces, Phys. Rev. B* **61**, 2254 (2000).

[16] J. E. Yater, A. Shih, and Y. U. Idzerda, *Structural Characterization Of Stepped Ga/Si(112) Surfaces, Phys. Rev. B* **51**, 7365 (1995).

[17] J. N. Crain, J. L. McChesney, F. Zheng, M. C. Gallagher, P. C. Snijders, M. Bissen, C. Gundelach, S. C. Erwin, and F. J. Himpsel, *Chains of gold atoms with tailored electronic states, Phys. Rev. B* **69**, 125401 (2004).

[18] P. Segovia, D. Purdie, M. Hengsberger, and Y. Baer, *Observation of spin and charge collective modes in one- dimensional metallic chains, Nature* **402**, 504 (1999).

[19] H. H. Song, K. M. Jones, and A. A. Baski, *Growth of Ag rows on Si(5512), J. Vac. Sci. Technol. A-Vac. Surf. Films* **17**, 1696 (1999).

[20] J.L. Lin, D. Y. Petrovykh, Viernow J., F. K. Men, Seo D. J., and F. J. Himpsel, *Formation of regular step arrays on Si(111)7x7, J. Appl. Phys.* **84**, 255 (1998).

[21] J. Viernow, J. L. Lin, D. Y. Petrovykh, F. M. Leibsle, F. K. Men, and F. J. Himpsel, *Regular step arrays on silicon, Appl. Phys. Lett.* **72**, 948 (1998).

[22] S. Folsch, G. Meyer, K. H. Rieder, M. Horn-von Hoegen, T. Schmidt, and M. Henzler, *Ag-mediated step-bunching instability on vicinal Si(100), Surf. Sci.* **394**, 60 (1997).

[23] M. Shinohara and N. Inoue, *Behavior And Mechanism Of Step Bunching During Metalorganic Vapor-Phase Epitaxy Of Gaas, Appl. Phys. Lett.* **66**, 1936 (1995).

[24] M. Kasu and N. Kobayashi, *Equilibrium Multiatomic Step Structure Of Gaas(001) Vicinal Surfaces Grown By Metalorganic Chemical Vapor-Deposition, Appl. Phys. Lett.* **62**, 1262 (1993).

[25] J. N. Crain, A. Kirakosian, K. N. Altmann, C. Bromberger, S. C. Erwin, J. L. McChesney, J. L. Lin, and F. J. Himpsel, *Fractional band filling in an atomic chain structure, Phys. Rev. Lett.* **90**, 176805 (2003).

[26] I. Matsuda, M. Hengsberger, F. Baumberger, T. Greber, H. W. Yeom, and J. Osterwalder, *Reinvestigation of the band structure of the Si(111)5 X 2-Au surface, Phys. Rev. B* **68**, 195319 (2003).

[27] M. G. Betti, V. Corradini, U. del Pennino, V. De Renzi, P. Fantini, and C. Mariani, *Gap-state formation in two-dimensional ordered Bi layers on InAs(110), Phys. Rev. B* **58**, R4231 (1998).

[28] P. Martensson and R. M. Feenstra, *Geometric And Electronic-Structure Of Antimony On The Gaas(110) Surface Studied By Scanning Tunneling Microscopy*, *Phys. Rev. B* **39**, 7744 (1989).

[29] J. M. Carpinelli and H. H. Weitering, *Scanning-Tunneling-Microscopy Study Of The Metal-Induced Si(111)3X1 Reconstruction - Evidence For Dimerized Chain Formation*, *Surf. Sci.* **333**, 1015 (1995).

[30] X. S. Zhang, C. Y. Fan, Y. B. Xu, H. Sui, S. Bao, S. H. Xu, H. B. Pan, and P. S. Xu, *Study of the Na-Si(111) 3x1 interface using core-level photoemission spectroscopy*, *J. Phys.-Condes. Matter* **8**, 699 (1996).

[31] M. Stròżak, V. Hnatyuk, and M. Jałochowski, *Optical properties of Pb nanowires on Si(335)*, *Vacuum* **74**, 241 (2004).

[32] Mildred S. Dresselhaus, G. Dresselhaus, and Ph. Avouvis, editors, *Carbon nanotubes: synthesis, structure, properties, and applications*, volume 80 of *Topics in applied physics*, Springer Verlag, Berlin, Heidelberg, 2001.

[33] Y. N. Xia, P. D. Yang, Y. G. Sun, Y. Y. Wu, B. Mayers, B. Gates, Y. D. Yin, F. Kim, and Y. Q. Yan, *One-dimensional nanostructures: Synthesis, characterization, and applications*, *Adv. Mater.* **15**, 353 (2003).

[34] M. Zacharias and P. Werner, *Das Wachstum von Nanodrähten*, *Physik Journal* **4**, 29 (2005).

[35] Paul K. L. Drude, *Zur Elektronentheorie*, *Ann. d. Phys.* **1**, 556 (1900).

[36] Arnold Sommerfeld, *Zur Elektronentheorie der Metalle aufgrund der Fermischen Statistik*, *Z. f. Physik* **47**, 1 (1928).

[37] Felix Bloch, *Über die Quantenmechanik der Elektronen in Kristallgittern*, *Z. f. Physik* **52**, 555 (1928).

[38] A. H. Wilson, *Theory of electronic semi-conductors*, *Proc. Roy. Soc. A* **133**, 458 (1931).

[39] Neil W. Ashcroft and N. David Mermin, *Solid state physics*, Thomson Learning, Inc., 1976.

[40] C. Kittel, *Einführung ind die Festkörperphysik*, R. Oldenbourg, München, 5 edition, 1980.

[41] C. Kittel, *Quantentheorie der Festkörper*, R. Oldenbourg, München, 1970.

[42] L. D. Landau, *On the theory of the Fermi liquid*, *Soviet Physics JETP-USSR* **8**, 70 (1959), and references therein.

[43] Johannes Voit, *One-dimensional Fermi liquids*, *Rep. Prog. Phys.* **57**, 977 (1994), and references therein.

[44] H. Fröhlich, *On The Theory Of Superconductivity - The One-Dimensional Case, 296* **223**, 296 (1954).

[45] J. Bardeen, L. N. Cooper, and J. R. Schrieffer, *Theory of superconductivity, Phys. Rev.* **108**, 1175 (1957).

[46] Jun-Hyung Cho, Dong-Hwa Oh, Kwang S. Kim, and Leonard Kleinman, *Weakly correlated one-dimensional indium chains on Si(111), Phys. Rev. B* **64**, 235302 (2001).

[47] H. W. Yeom, S. Takeda, E. Rotenberg, I. Matsuda, K. Horikoshi, J. Schaefer, C. M. Lee, S. D. Kevan, T. Ohta, T. Nagao, and S. Hasegawa, *Instability and charge density wave of metallic quantum chains on a silicon surface, Phys. Rev. Lett.* **82**, 4898 (1999).

[48] C. Kumpf, O. Bunk, J. H. Zeysing, Y. Su, M. Nielsen, R. L. Johnson, R. Feidenhans'l, and K. Bechgaard, *Low-temperature structure of indium quantum chains on silicon, Phys. Rev. Lett.* **85**, 4916 (2000).

[49] L. P. Gor'kov and G. Grüner, editors, *Charge Density Waves in Solids*, volume 25 of *Modern Problems in Condensed Matter Sciences*, North-Holland, Elsevier Science Publishers B.V., Amsterdam, 1989.

[50] J. Wosnitza, *Fermi Surfaces of Low- Dimensional Organic Metals and Superconductors*, volume 134 of *Springer Tracts in Modern Physics*, Springer Verlag, Heidelberg, 1998.

[51] M. J. Rice and S. Strässler, *Effects Of Fluctuations And Interchain Coupling On Peierls Transition, Solid State Commun.* **13**, 1389 (1973).

[52] N. F. Mott, *Metal-Insulator transition, Rev. Mod. Phys.* **40**, 677 (1968), and references therein.

[53] S Tomonaga, *Remarks on Blochs method of sound waves applied to many-Fermion problems, Prog. Theor. Phys.* **5**, 1153 (1950).

[54] J. M. Luttinger, *Fermi Surface And Some Simple Equilibrium Properties Of A System Of Interacting Fermions, Phys. Rev.* **119**, 1153 (1960).

[55] J. M. Luttinger, *An Exactly Soluble Model Of A Many-Fermion System, J. Math. Phys.* **4**, 1154 (1963).

[56] F. Zwick, D. Jerome, G. Margaritondo, M. Onellion, J. Voit, and M. Grioni, *Band mapping and quasiparticle suppression in the one- dimensional organic conductor TTF-TCNQ, Phys. Rev. Lett.* **81**, 2974 (1998).

[57] M. Grioni, I. Vobornik, F. Zwick, and G. Margaritondo, *High-resolution photoemission in low-dimensional conductors and superconductors, J. Elect. Spectr. Rel. Phen.* **100**, 313 (1999).

[58] M. G. Zacher, E. Arrigoni, W. Hanke, and J. R. Schrieffer, *Systematic numerical study of spin-charge separation in one dimension, Phys. Rev. B* **57**, 6370 (1998).

[59] F. K. Men, Feng Liu, P. J. Wang, C. H. Chen, D. L. Cheng, J. L. Lin, and F. J. Himpsel, *Self-Organized Nanoscale Pattern Formation on Vicinal Si(111) Surfaces via a Two-Stage Faceting Transition*, *Phys. Rev. Lett.* **88**, 096105 (2002).

[60] N. F. Mott, *The Basis Of The Electron Theory Of Metals, With Special Reference To The Transition Metals*, *Proc. Roy. Soc. A* **62**, 416 (1949).

[61] J. Hubbard, *Electron Correlations In Narrow Energy Bands .3. Improved Solution*, *Proc. Roy. Soc. A* **281**, 401 (1964).

[62] J. Hubbard, *Electron Correlations In Narrow Energy Bands .2. Degenerate Band Case*, *Proc. Roy. Soc. A* **277**, 237 (1964).

[63] M. Knupfer, H. Peisert, and T. Schwieger, *Band-gap and correlation effects in the organic semiconductor Alq(3)*, *Phys. Rev. B* **6503**, 033204 (2002).

[64] A. V. Puchkov, M. C. Schabel, D. N. Basov, T. Startseva, G. Cao, T. Timusk, and Z. X. Shen, *Layered ruthenium oxides: From band metal to Mott insulator*, *Phys. Rev. Lett.* **81**, 2747 (1998).

[65] D. Jeon, T. Hashizume, T. Sakurai, and R. F. Willis, *Structural And Electronic-Properties Of Ordered Single And Multiple Layers Of Na On The Si(111) Surface*, *Phys. Rev. Lett.* **69**, 1419 (1992).

[66] O. Pankratov and M. Scheffler, *Hubbard Correlations and charge transfer at the GaAs(110) surface with alkali adsorbates*, *Phys. Rev. Lett.* **70**, 351 (1992).

[67] U. del Pennino, B. Savarani, and R. Compañò, *Evidence of a bipolaronic, insulating state of Na submonolayer on GaAs(110)*, *Phys. Rev. B* **52**, 10717 (1990).

[68] Paul Harrison, *Quantum Wells, Wires and Dots: Theoretical and Computational Physics*, John Wiley & Son Ltd, Chichester, 2000.

[69] C. Z. Li and N. J. Tao, *Quantum transport in metallic nanowires fabricated by electrochemical deposition/dissolution*, *Appl. Phys. Lett.* **72**, 894 (1998).

[70] H. Mehrez and S. Ciraci, *Yielding and fracture mechanisms of nanowires*, *Phys. Rev. B* **56**, 12632 (1997).

[71] C. Yannouleas and U. Landman, *On mesoscopic forces and quantized conductance in model metallic nanowires*, *J. Phys. Chem. B* **101**, 5780 (1997).

[72] Peter Y. Yu and Manuel Cardona, *Fundamentals of Semiconductors*, Sringer-Verlag, Berlin, Heidelberg, 2 edition, 1999.

[73] Günther Bauer and Wolfgang Richter, editors, *Optical Characterization of Epitaxial Semiconductor Layers*, Sringer-Verlag, Berlin, Heidelberg, 1996.

[74] E. D. Palik, editor, *Handbook of Optical Constants of Solids*, Academic Press, New York, 1985.

[75] E. D. Palik, editor, *Handbook of Optical Constants of Solids*, Academic Press, New York, 1991.

[76] Harland G. Tomkins, *A user's guide to Ellipsometry*, Academic Press, San Diego, 1993.

[77] J.-T. Zettler, *Lay_TEX 2.0: Modellierung und Auswertung zur linear-optischen Spektroskopie an Schichtstrukturen*, 1995, short manual.

[78] R. H. Ritchie, *Plasma losses by fast electrons in thin films*, *Phys. Rev.* **106**, 874 (1957).

[79] M. Rocca, *Low-energy EELS investigation of surface electronic excitations on metals*, *Surf. Sci. Rep.* **22**, 1 (1995).

[80] C.K. Chen, A. R. B. de Castro, and Y. R. Shen, *Surface-enhanced Second-Harmonic Generation*, *Phys. Rev. Lett.* **46**, 145 (1981).

[81] Uwe Kreibig and Michael Vollmer, *Optical properties of Metal Clusters*, volume 25 of *Springer Series in Materials Science*, Springer verlag, Berlin, Heidelberg, 1995.

[82] W. L. Mochan, R. G. Barrera, Y. Borensztein, and Tadjeddine A., *Optical reflectance anisotropy of Ag and Au (110) single-crystals*, *Physica A* **207**, 334 (1994).

[83] R. Wiesendanger, *Scanning probe microscopy and spectroscopy*, Cambridge University Press, 1994.

[84] G. Fahsold, A. Priebe, N. Magg, and A. Pucci, *Non-contact measurements of conductivity during growth of metal ultrathin films*, *Thin Solid Films* **428**, 107 (2003).

[85] M. Cardona, F. H. Pollak, and K. L. Shaklee, *Electroreflectance In Semiconductors*, *J. Phys. Soc. Jap.* **S 21**, 89 (1966).

[86] J. D. Mcintyre and D. E. Aspnes, *Differential Reflection Spectroscopy Of Very Thin Surface Films*, *Surf. Sci.* **24**, 417 (1971).

[87] D. E. Aspnes and A. A. Studna, *Anisotropies in the above-band-gap optical spectra of cubic semiconductors*, *Phys. Rev. Lett.* **54**, 1956 (1985).

[88] V. I. Berkovits, I. V. Makarenko, T. A. Minashvili, and V. I. Safarov, *Optical transitions on GaAs(110) surface*, *Solid. State. Commun.* **56**, 449 (1985).

[89] D. E. Aspnes, J. P. Harbison, A. A. Studna, and L. T. Florez, *Application of reflectance difference spectroscopy to molecular-beam epitaxy growth of GaAs and AlAs*, *J. Vac. Sci. Technol. A* **6**, 1327 (1988).

[90] A. Salvati and P. Chiaradia, *Analysis of reflectometers for surface anisotropy*, *Applied Optics* **39**, 5820 (2000).

[91] O. Hunderi, J.-T. Zettler, and K. Haberland, *On the AlAs/GaAs (001) interface dielectric anisotropy*, *Thin Solid Films* **472**, 261 (2005).

[92] C. Goletti, G. Bussetti, F. Arciprete, P. Chiaradia, and G. Chiarotti, *Infrared surface absorption in Si(111)2x1 observed with reflectance anisotropy spectroscopy*, *Phys. Rev. B* **66**, 153307 (2002).

[93] Th. Herrmann, *Optische Spektroskopie an Metallen und ferromagnetischen Filmen*, 2005, Dissertation, Fakultät II. Technische Universität Berlin.

[94] K. Hinrichs, M. Gensch, A. Roseler, E. H. Korte, K. Sahre, K. J. Eichhorn, N Esser, and U. Schade, *Fourier transform infrared synchrotron ellipsometry for studying the anisotropy of small organic samples*, *Applied Spectroscopy* **57**, 1250 (2003).

[95] K. Stahrenberg, T. Herrmann, N. Esser, J. Sahm, W. Richter, S. V. Hoffmann, and P. Hofmann, *Surface-state contribution to the optical anisotropy of Ag(110) surfaces: A reflectance-anisotropy-spectroscopy and photoemission study*, *Phys. Rev. B* **58**, R10207 (1998).

[96] Th. Herrmann, M. Gensch, M. J. G. Lee, A. I. Shkrebtii, N. Esser, W. Richter, and Ph. Hofmann, *Optical reflectance anisotropy of Al(110): Experiment and ab initio calculation*, *Phys. Rev. B* **69**, 165406 (2004).

[97] J. Bremer, J. K. Hansen, K. Stahrenberg, and T. Worren, *The influence of surface steps on the optical and electronic anisotropy of Ag(110)*, *Surf. Sci.* **459**, 39 (2000).

[98] J. Bremer and O. Hunderi, *RAS studies of laterally nanostructured surfaces*, *phys. stat. sol. (a)* **184**, 89 (2001).

[99] J. C. Maxwell Garnett, *Colours in Metal Glasses and in Metallic Films*, *Phil. Trans. Royal. Soc. London* **203**, 385 (1904).

[100] J. C. Maxwell Garnett, *Colours in Metal Glasses, in Metallic Films and in Metallic Solutions – II*, *Phil. Trans. Royal. Soc. London* **205**, 237 (1906).

[101] D. E. Aspnes and J. B. Theeten, *Investigation of effective-medium models of microscopic surface roughness by spectroscopic ellipsometry*, *Phys. Rev. B* **20**, 3292 (1979).

[102] Serge Berthier, *Anisotropic effective medium theories*, *J. Phys. I. France* **4**, 303 (1994).

[103] J.-T. Zettler, J. Rumberg, K. Ploska, K. Stahrenberg, M. Pristovsek, W. Richter, M. Wassermeier, P. Schutzendube, J. Behrend, and L. Däweritz, *Reflectance anisotropy oscillations during MOCVD and MBE growth of GaAs (001)*, *phys. stat. sol. (a)* **152**, 35 (1995).

[104] D. E. Aspnes, *Optical response of microscopically rough surfaces*, *Phys. Rev. B* **41**, 10334 (1990).

[105] M. Gluodenis and Jr. C. A. Foss, *The effect of mutual orientation on the spectra of metal nanoparticle rod-rod and rod-sphere pairs, J. Phys. Chem. B* **106**, 9484 (2002).

[106] H. C. F. Martens, J. A. Reedijk, Brom H. B., de Leeuw D. M., and Menon R., *Metallic state in disordered quasi-one-dimensional conductors, Phys. Rev. B* **63**, 73203 (2001).

[107] C. V. Raman, *A new radiation, Ind. J. Phys.* **2**, 387 (1928).

[108] G. Landsberg and L. Mandestam, *A novel effect of light scattering, Naturwissenschaften* **16**, 57 (1928).

[109] M. Cardona, editor, *Light Scattering in Solids I: Introductory Concepts*, volume 8 of *Topics in Applied Physics*, Springer-Verlag, Berlin, Heidelberg, 2 edition, 1982.

[110] M. Cardona, editor, *Light Scattering in Solids II: Basic concepts and Instrumentation*, volume 50 of *Topics in Applied Physics*, Springer-Verlag, Berlin, Heidelberg, 2 edition, 1982.

[111] T. Ruf, *Phonon Raman Scattering in Semiconductors, Quantum Wells and Superlattices, Basic Results and Applications*, volume 142 of *Springer Tracts in Modern Physics*, Springer-Verlag, Berlin, Heidelber, 1998.

[112] J. B. Renucci, R. N. Tyte, and M. Cardona, *Resonant Raman scattering in silicon, Phys. Rev. B* **11**, 3885 (1975).

[113] A. Compaan and H.J. Trodahl, *Resonance Raman scattering in Si at elevated temperatures, Phys. Rev. B* **29**, 793 (1984).

[114] R Trommer and M CardonA, *Resonant Raman-scattering in GaAs, Phys. Rev. B* **17**, 1865 (1978).

[115] L. Y. Ching, S. Buchner, E. Burstein, and H. Wieder, *Resonant Raman-scattering at InAs surfaces in air and in MOS junctions, Bulletin of the APS* **23**, 410 (1978).

[116] Lord Rayleigh, *On the scattering of light by small particles, Phil. Mag.* **41**, 107 (1871).

[117] W. Kress and F.W. de Wette, editors, *Surface Phonons*, volume 21 of *Springer Series in Surface Sciences*, Sringer-Verlag, Berlin, Heidelberg, 1991.

[118] Karsten Hinrichs, *Ramanspektroskopie an Oberflächenphononen von InP(110) und Si(001)-Sb*, PhD thesis, Technische Universität Berlin, 1999.

[119] R. Fuchs, K. L. Kliewer, and W. J. Pardee, *Optical Properties of an Ionic Crystal Slab, Phys. Rev.* **150**, 589 (1966).

[120] R. F. Wallis, *Theory of Surface Modes of Vibration in Two- and Three-Dimensional Crystal Lattices, Phys. Rev.* **116**, 302 (1959).

[121] K Hinrichs, A Schierhorn, P Haier, N Esser, W Richter, and Sahm J, *Surface phonons of InP(110) studied by Raman spectroscopy, Phys. Rev. Lett.* **79**, 1094 (1997).

[122] N Esser, M Kopp, P Haier, A Kelnberger, and Richter W, *Electronic-properties of Sb monolayers on III-V(110) surfaces determined by resonance Raman-scattering, J. Vac. Sci. Technol. B* **11**, 1481 (1993).

[123] N Esser, M Kopp, P Haier, and Richter W, *Optical characterization of surface electronic and vibrational properties of epitaxial antimony monolayers on III-V (110) surfaces, phys. stat. sol. (a)* **152**, 191 (1995).

[124] M. A. Hines, Y. J. Chabal, T. D. Harris, and A. L. Harris, *Raman studies of steric hindrance and surface relaxation of stepped H-terminated silicon surfaces, Phys. Rev. Lett.* **71**, 2280 (1993).

[125] P. A. Temple and C. E. Hathaway, *Multiphonon Raman spectrum of silicon, Phys. Rev. B* **7**, 3685 (1973).

[126] Claudia Andrzejak, *Ramanspektroskopische Untersuchungen an porösen Silicium-Schichten,* Diplomarbeit an der RWTH Aachen, 1991.

[127] J. Zhang and L. D. Zhang, *Morphology and Raman scattering spectrum of GaN nanowires embedded in nanochannels of template, J. Phys. D* **35**, 1481 (2002).

[128] L. Q. Jing, Z. L. Xu, J. Shang, X. J. Sun, W. M. Cai, and H. C. Guo, *The preparation and characterization of ZnO ultrafine particles, Mat. Sci. Engin. A* **332**, 356 (2002).

[129] K. Nakamura, M. Fujitsuka, and M. Kitajima, *Finite Size Effect On Raman-Scattering Of Graphite Microcrystals, Chem. Phys. Lett.* **172**, 205 (1990).

[130] S. Piscanec, M. Cantoro, A. C. Ferrari, J. A. Zapien, Y. Lifshitz, S. T. Lee, S. Hofmann, and J. Robertson, *Raman spectroscopy of silicon nanowires, Phys. Rev. B* **68**, 241312 (2003).

[131] D. T. Wang, A. Göbel, J. Zegenhagen, and M. Cardona, *Raman scattering on α-tin: Dependence on isotopic composition, Phys. Rev. B* **56**, 13167 (1997).

[132] P. Hohenberg and W. Kohn, *Inhomogeneous Electron Gas, Phys. Rev. B* **136**, B864 (1964).

[133] W. Kohn and L. J. Sham, *Self-Consistent Equations Including Exchange And Correlation Effects, Phys. Rev.* **140**, 1133 (1965).

[134] J. M. Thijssen, *Computational Physics,* Cambridge University Press, 1999.

[135] L. Hedin, *New Method For Calculating 1-Particle Greens Function With Application To Electron-Gas Problem, Phys. Rev.* **139**, A796 (1965).

[136] X. J. Zhu and S. G. Louie, *Quasi-Particle Band-Structure Of 13 Semiconductors And Insulators*, *Phys. Rev. B* **43**, 14142 (1991).

[137] G. Onida, L. Reining, R. W. Godby, R. Delsole, and W. Andreoni, *Ab-Initio Calculations Of The Quasi-Particle And Absorption- Spectra Of Clusters - The Sodium Tetramer*, *Phys. Rev. Lett.* **75**, 818 (1995).

[138] M. Marsili and O. Pulci, *to be published* (2005).

[139] R. Delsole and E. Fiorino, *Macroscopic Dielectric Tensor At Crystal-Surfaces*, *Phys. Rev. B* **29**, 4631 (1984).

[140] G. Onida, L. Reining, and A. Rubio, *Electronic excitations: density-functional versus many-body Green's-function approaches*, *Rev. Mod. Phys.* **74**, 601 (2002).

[141] W. G. Schmidt, K. Seino, P. H. Hahn, E. Bechstedt, W. Lu, S. Wang, and J. Bernholc, *Calculation of surface optical properties: from qualitative understanding to quantitative predictions*, *Thin Solid Films* **455-56**, 764 (2004).

[142] H. Wendel and R. M. Martin, *Theory Of Structural-Properties Of Covalent Semiconductors*, *Phys. Rev. B* **19**, 5251 (1979).

[143] M. T. Yin and M. L. Cohen, *Theory of lattice-dynamical properties of solids - application to Si and Ge*, *Phys. Rev. B* **26**, 3259 (1982).

[144] R. C. Yu, D. Singh, and H. Krakauer, *All-Electron And Pseudopotential Force Calculations Using The Linearized-Augmented-Plane-Wave Method*, *Phys. Rev. B* **43**, 6411 (1991).

[145] W. G. Schmidt, F. Bechstedt, and G. P. Srivastava, *Iii-V(110) Surface Dynamics From An Ab-Initio Frozen-Phonon Approach*, *Phys. Rev. B* **52**, 2001 (1995).

[146] W. G. Schmidt, F. Bechstedt, and G. P. Srivastava, *Phonons at III-V (110) surfaces*, *Surf. Sci.* **352**, 83 (1996).

[147] J. Fritsch and P. Pavone, *Ab initio calculation of the structure, electronic states, and the phonon dispersion of the Si(100) surface*, *Surf. Sci.* **344**, 159 (1995).

[148] T. Kanagawa, R. Hobara, I. Matsuda, T. Tanikawa, A. Natori, and S. Hasegawa, *Anisotropy in conductance of a quasi-one-dimensional metallic surface state measured by a square micro-four-point probe method*, *Phys. Rev. Lett.* **91**, 036805 (2003).

[149] T. Uchihashi and U. Ramsperger, *Electron conduction through quasi-one-dimensional indium wires on silicon*, *Appl. Phys. Lett.* **80**, 4169 (2002).

[150] T. López-Ríos, A. Briggs, S. Guillet, A. M. Baro, and M. Luna, *Anisotropic conductivity of silver thin films grown on silicon (100) vicinal surfaces*, *Appl. Phys. Lett.* **66**, 529 (1995).

[151] J. Kircher, M.K. Kelly, S. Rashkeev, M. Alouani, D. Fuchs, and M. Cardona, *Anisotropy and oxygen-stoichiometry dependence of the dielectric tensor of* $YBa_2Cu_3O_{7-\delta}$ *(*$0 \leq \delta \leq 1$*), Phys. Rev. B* **44**, 217 (1991).

[152] A. Bruchhausen, S. Bahrs, K. Fleischer, A. R. Goñi, A. Fainstein, G. Nieva, A. A. Aligia, W. Richter, and C. Thomsen, *Photoinduced chain-oxygen ordering in detwinned* $YBa_2Cu_3O_{6.7}$ *single crystals studied by reflectance-anisotropy spectroscopy, Phys. Rev. B* **69**, 224508 (2004).

[153] Thomas W. Ebbesen, editor, *Carbon nanotubes: preparation and properties*, CRC Press Inc., Boca Raton, 1997.

[154] Holger Eisele, *Strukturuntersuchungen an Sb- und Sn-Schichten auf III-V-Halbleitern*, Diplomarbeit an der TU Berlin, 1996.

[155] Karsten Fleischer, *Epitaxial metal layers on semiconductor surfaces*, Diplomarbeit an der TU Berlin, 1999.

[156] R. A. MacRae and E. T. Arakawa, *Optical properties of vacuum-evaporated white tin, Phys. Rev.* **162**, 162 (1967).

[157] N. Esser, A. M. Frisch, A. Roseler, S. Schintke, C. Goletti, and B. O. Fimland, *Optical resonances of indium islands on GaAs(001) observed by reflectance anisotropy spectroscopy, Phys. Rev. B* **67**, 125306 (2003).

[158] D. Stroud, *Percolation effects and sum rules in the optical properties of composities, Phys. Rev. B* **19**, 1783 (1979).

[159] Wen Chu Huang and Juh Tzeng Lue, *Quantum size effect on the optical properties of small metallic particles, Phys. Rev. B* **49**, 17279 (1994).

[160] I. G. Hill and A. B. McLean, *Strongly Anisotropic Band Dispersion of an Image State Located above Metallic Nanowires, Phys. Rev. Lett.* **82**, 2155 (1999).

[161] X. López-Lozano, A.A. Stekolnikov, J. Furthmüller, and F. Bechstedt, *Properties of electron gas in In chains on Si(111), publication in preparation* (2005).

[162] M. Jałochowski, M. Stròżak, , and R. Zdyb, *Optical recognition of structural and electronic transformation of Pb ultrathin films, J. Phys.: Cond. Matter* **16**, S4352 (2004).

[163] H. W. Yeom, K. Horikoshi, H. M. Zhang, K. Ono, and R. I. G. Uhrberg, *Nature of the broken-symmetry phase of the one-dimensional metallic In/Si(111) surface, Phys. Rev. B* **65**, 241307 R (2002).

[164] S. J. Park, H. W. Yeom, S. H. Min, D. H. Park, and I.-W. Lyo, *Direct Evidence of the Charge Ordered Phase Transition of Indium Nanowires on Si(111), Phys. Rev. Lett.* **93**, 106402 (2004).

[165] J. H. Cho, J.Y. Lee, and L Kleinman, *Electronic structure of one-dimensional indium chains on Si(111), Phys. Rev. B* **71**, 081310 (2005).

[166] S.F. Tsay, *Atomic and electronic structure of the (4x1) and (8x2) In/Si(111) surfaces, Phys. Rev. B* **71**, 035207 (2005).

[167] J. J. Lander and J. Morrison, *Surface Reactions Of Silicon With Aluminum And With Indium, Surf. Sci.* **2**, 553 (1964).

[168] T. Aiyama and S. Ino, *Rheed observation of the Si(111)($\sqrt{31}\times\sqrt{31}$)-In structure, Surf. Sci.* **82**, L585 (1979).

[169] M. Kawaji, S. Baba, and A. Kinbara, *Superstructures of submonolayer Indium films on Silicon(111) surfaces, Appl. Phys. Lett.* **34**, 748 (1979).

[170] S. Baba, M. Kawaji, and A. Kinbara, *Isothermal desorption of indium from $\sqrt{31}$-In and $\sqrt{3}$3-In on Silicon (111) surfaces, Surf. Sci.* **85**, 29 (1979).

[171] J. Nogami, S. I. Park, and C. F. Quate, *Indium-induced reconstructions of the Si(111) surface studied by scanning tunneling microscopy, Phys. Rev. B* **36**, 6221 (1987).

[172] J. Nogami, S. I. Park, and C. F. Quate, *Behavior of Indium on the Si(111)7x7 surface at low-metal coverage, J. Vac. Sci. Technol. B* **6**, 1479 (1988).

[173] N. Nakamura, K. Anno, and S. Kono, *Structure-Analysis Of The Single-Domain Si(111)4 X 1-In Surface By Mu-Probe Auger-Electron Diffraction And Mu-Probe Reflection High-Energy Electron-Diffraction, Surf. Sci.* **256**, 129 (1991).

[174] J. L. Stevens, M. S. Worthington, and I. ST. Tsong, *4x1 reconstruction of Indium deposited on vicinal Si(111) surfaces, Phys. Rev. B* **47**, 1453 (1993).

[175] A. A. Saranin, E. A. Khramtsova, K. V. Ignatovich, V. G. Lifshits, T. Numata, O. Kubo, M. Katayama, I. Katayama, and K. Oura, *Indium-induced Si(111)4x1 silicon substrate atom reconstruction, Phys. Rev. B-Condens Matter* **55**, 5353 (1997).

[176] S. Wang, W. Lu, W. G. Schmidt, and J. Bernholc, *Nanowire-induced optical anisotropy of the Si(111)-In surface, Phys. Rev. B* **68**, 035329 (2003).

[177] M. K. Kelly, G. Margaritondo, J. Anderson, D. J. Frankel, and G. J. Lapeyre, *Reconstruction of Aluminum and Indium overlayers on Si(111) - A systematic study with High-Resolution Electron-Energy Loss Spectroscopy and Low-Energy Electron-Diffraction, J. Vac. Sci. Technol. A* **4**, 1396 (1986).

[178] O. Bunk, G. Falkenberg, J. H. Zeysing, L. Lottermoser, R. L. Johnson, M. Nielsen, F. Berg-Rasmussen, J. Baker, and R. Feidenhans'l, *Structure determination of the indium-induced Si(111)-(4 x 1) reconstruction by surface x-ray diffraction, Phys. Rev. B* **59**, 12228 (1999).

[179] S. Baba, H. Hirayama, J. M. Zhou, and A. Kinbara, *Adatoms Of Indium On Si(111) Surfaces - Application Of Reflection High-Energy Electron-Diffraction To Desorption Experiments, Thin Solid Films* **90**, 57 (1982).

[180] F. Pedreschi, J. D. O'Mahony, P. Weightman, and J. R. Power, *Evidence of electron confinement in the single-domain, (4x1)-In superstructure on vicinal Si(111), Appl. Phys. Lett.* **73**, 2152 (1998).

[181] U. Rossow, L. Mantese, T. Yasuda, and D. E. Aspnes, *Hydrogenated and oxidized vicinal Si(001) surfaces investigated by reflectance-difference spectroscopy, Appl. Surf. Sci.* **104/105**, 137 (1996).

[182] J. R. Ahn, J. H. Byun, H. Koh, E. Rotenberg, S. D. Kevan, and H. W. Yeom, *Mechanism of Gap Opening in a Triple-Band Peierls System: In Atomic Wires on Si, Phys, Rev. Lett.* **93**, 106401 (2004).

[183] Kenji Hata, Shoji Yoshida, and Hidemi Shigekawa, *p(2×2) Phase of Buckled Dimers of Si(100) Observed on n-Type Substrates below 40 K by Scanning Tunneling Microscopy, Phys. Rev. Lett.* **89**, 286104 (2002), and references therein.

[184] 藤田大介・鷲坂恵介, 低温ＳＴＭによるＳｉ(001)非対称ダイマー相の操作, *Oyo Buturi* **74**, 208 (2005), and references therein.

[185] C. González, J. Ortega, and F. Flores, *Metal–insulator transition in one-dimensional In-chains on Si(111): combination of a soft shear distortion and a double-band Peierls instability, New J. Phys.* **7**, 100 (2005).

[186] F. Bechstedt, A. Krivosheeva, J. Furthmüller, and A.A. Stekolnikov, *Vibrational properties of the quasi-one-dimensional In/Si(111)-(4x1) system, Phys. Rev. B* **68**, 193406 (2003).

[187] M. Cardona, *Renormalization of the optical response of semiconductors by electron-phonon interaction, phys. stat. sol. (a)* **188**, 1209 (2001).

[188] P. Lautenschlager, M. Garriga, L. Vi na, and M. Cardona, *Temperature dependence of the dielectric function and interband critical points in silicon, Phys. Rev. B* **36**, 4821 (1987).

[189] N. Esser, W. G. Schmidt, C. Cobet, K. Fleischer, A. I. Shkrebtii, B. O. Fimland, and W. Richter, *Atomic structure and optical anisotropy of III-V (001) surfaces, J. Vac. Science & Techn. B* **19**, 1756 (2001).

[190] W. G. Schmidt, N. Esser, A. M. Frisch, P. Vogt, J. Bernholc, F. Bechstedt, M. Zorn, T. Hannappel, S. Visbeck, F. Willig, and W. Richter, *Understanding reflectance anisotropy: Surface-state signatures and bulk-related features in the optical spectrum of InP(001)(2×4), Phys. Rev. B* **61**, 16335 (2000).

[191] X. Lopez-Lozano, O. Pulci, C. Noguez, K. Fleischer, and W. Richter, *Electronic structure and reflectance anisotropy spectrum of InAs(110), Phys. Rev. B* **71**, 125337 (2005).

[192] O. Pulci, G. Onida, R. Del Sole, and L. Reining, *Ab Initio Calculation of Self-Energy Effects on Optical Properties of GaAs(110), Phys. Rev. Lett.* **81**, 5374 (1998).

[193] J. Nakamura, S. Watanabe, and M. Aono, *Anisotropic electronic structure of the Si(111)/(4x1)-In surface, Phys. Rev. B* **63**, 193307 (2001).

[194] K. Sakamoto, H. Ashima, H. W. Yeom, and Wakio Uchida, *Angle-resolved high-resolution electron-energy-loss study of In-adsorbed Si(111)-(4x1) and -(8x2) surfaces, Phys. Rev. B* **62**, 9923 (2000).

[195] A. Krivosheeva and F. Bechstedt, 2004, private communication.

[196] A. Debernardi, *Anharmonic effects in the phonons of III-V semiconductors: first principles calculations, Solid State Commun.* **113**, 1 (1999).

[197] T. R. Hart, R. L. Aggarwal, and B. Lax, *Temperature Dependence Of Raman Scattering In Silicon, Phys. Rev. B* **1**, 638 (1970).

[198] G. Lang, K. Karch, M. Schmitt, P. Pavone, A. P. Mayer, R. K. Wehner, and D. Strauch, *Anharmonic line shift and linewidth of the Raman mode in covalent semiconductors, Phys. Rev. B* **59**, 6182 (1999).

[199] V. V. Brazhkin, S. G. Lyapin, I. A. Trojan, R. N. Voloshin, A. G. Lyapin, and N. N. Mel'nik, *Anharmonicity of short-wavelength acoustic phonons in silicon at high temperatures, Jetp Lett.* **72**, 195 (2000).

[200] F. Manghi, R. Delsole, A. Selloni, and E. Molinari, *Anisotropy Of Surface Optical-Properties From 1St-Principles Calculations, Phys. Rev. B* **41**, 9935 (1990).

[201] T. Nakashizu, T. Sekine, K. Uchinokura, and E. Matsuura, *Raman-Study Of Charge-Density-Wave Excitations In 4Hb-Tas2, Phys. Rev. B* **29**, 3090 (1984).

[202] J. C. Tsang, J. E. Smith, and M. W. Shafer, *Raman-Spectroscopy Of Soft Modes At Charge-Density-Wave Phase- Transition In 2H-Nbse2, Phys. Rev. Lett.* **37**, 1407 (1976).

[203] E. F. Steigmeier, R. Loudon, G. Harbeke, H. Auderset, and G. Scheiber, *Raman-Scattering In K2Pt(Cn)4Br0.3 3H2O, Solid State Commun.* **17**, 1447 (1975).

[204] J. E. Smith, J. C. Tsang, and M. W. Shafer, *Raman-Spectra Of Several Layer Compounds With Charge-Density Waves, Solid State Commun.* **19**, 283 (1976).

[205] J. F. Scott, *Soft-mode spectroscopy - experimental studies of structural phase-transitions, Rev. Mod. Phys.* **46**, 83 (1974).

[206] S. V. Ryjkov, T. Nagao, V. G. Lifshits, and S. Hasegawa, *Phase transition and stability of Si(111)-8x'2'-In surface phase at low temperatures, Surf. Sci.* **488**, 15 (2001).

[207] S. S. Lee, J. R. Ahn, N. D. Kim, J. H. Min, C. G. Hwang, J. W. Chung, H. W. Yeom, S. V. Ryjkov, and S. Hasegawa, *Adsorbate-induced pinning of a charge-density wave in a quasi- 1D metallic chains: Na on the In/Si(111)-(4 x 1) surface, Phys. Rev. Lett.* **88**, art. no. (2002).

[208] J. H. Cho, D. H. Oh, and L. Kleinman, *Theoretical study of Na adsorption on top of In chains on the Si(111) surface*, *Phys. Rev. B* **66**, art. no. (2002).

[209] Harumo Morikawa, Iwao Matsuda, and Shuji Hasegawa, *Direct observation of soliton dynamics in charge-density waves on a quasi-one-dimensional metallic surface*, *Phys. Rev. B* **70**, 085412 (2004).

[210] J. P. Pouget and R. Comes, *The CDW Transition: Structural Studies*, Chapter 3 in [49].

[211] A. W. Overhaus, *Observability of charge-density waves by neutron differaction*, *Phys. Rev. B* **3**, 3173 (1971).

[212] G. Travaglini, P. Wachter, J. Marcus, and C. Schlenker, *The Blue Bronze K0.3Moo3 - A New One-Dimensional Conductor*, *Solid State Commun.* **37**, 599 (1981).

[213] G. Grüner and P. Monceau, *Dynamical Properties of Charge Density Waves*, Chapter 4 in [49].

[214] J. Rouxel and C. Schlenker, *Structural, Electronic Properties and Design of Quasi-One-Dimensional Inorganic Conductors*, Chapter 2 in [49].

[215] H. H. Weitering, N. J. Dinardo, R. Perezsandoz, J. Chen, and E. J. Mele, *Structural Model For The Metal-Induced Si(111)3X1 Reconstruction*, *Phys. Rev. B* **49**, 16837 (1994).

[216] P. N. First, R. A. Dragoset, J. A. Stroscio, R. J. Celotta, and R. M. Feenstra, *Structure of Cs on GaAs(110) as determined by scanning tunneling microscopy*, *J. Vac. Sci. Technol. A* **7**, 2868 (1989).

[217] L. J. Whitman, J. A. Stroscio, R. A. Dragoset, and R. J. Celotta, *Geometric and Electronic Properties of Cs Structures on III–V Surfaces: From 1D and 2D Insulators to 3D Metals*, *Phys. Rev. Lett.* **66**, 1338 (1991).

[218] S. Modesti, A. Falasca, M. Polentarutti, M. G. Betti, V. De Renzi, and C. Mariani, *Evolution of one-dimensional Cs chains on InAs (110) as determined by scanning-tunneling microscopy and core-level spectroscopy*, *Surf. Sci.* **447**, 133 (2000).

[219] L. J. Whitman, J. A. Stroscio, R. A. Dragoset, and R. J. Celotta, *Insulating Cs overlayer on InSb(110)*, *Phys. Rev. B* **44**, 5951 (1991).

[220] O. Pankratov and M. Scheffler, *Bound bipolaron at the surface: The negative-U behaviour of GaAs(110) with adsorbed alkali metals*, *Phys. Rev. Lett.* **71**, 2797 (1993).

[221] N. J. DiNardo, T. Maeda Wong, and E. W. Plummer, *Semiconductor-to-Metal Transition in an Ultrathin Interface: Cs/GaAs(110)*, *Phys. Rev. Lett.* **65**, 2177 (1990).

[222] N. Esser, R. Hunger, J. Rumberg, W. Richter, R. Del Sole, and A. I. Shkrebtii, *Reflectance anisotropy spectroscopy of ordered Sb overlayers on GaAs(110) and InP(110), Surf. Sci.* **307-309**, 1045 (1994).

[223] B. Mendoza, N. Esser, and W. Richter, *Model for the effects of surface disorder on reflectance anisotropy spectroscopy, Phys. Rev. B* **67**, 165319 (2003).

[224] T. Nakayama and M. Murayama, *Tight-binding-calculation method and physical origin of reflectance difference spectra, Jap. J. Appl. Phys.* **38**, 3497 (1999).

[225] P. V. Santos, B. Koopmans, N. Esser, W. G. Schmidt, and F. Bechstedt, *Optical properties of ordered as layers on InP(110) surfaces, Phys. Rev. Lett.* **77**, 759 (1996).

[226] C. MJ. Wijers, R. Delsole, and F. Manghi, *Surface Local-Field Effect On The Optical-Properties Of Gaas(110) And Gap(110), Phys. Rev. B* **44**, 1825 (1991).

[227] V. I. Berkovits, L. F. Ivantsov, I. V. Makarenko, T. A. Minashvili, and V. I. Safarov, *Optical transitions on (110) surfaces of III–V compounds, Solid. State. Commun.* **64**, 767 (1987).

[228] M. Cardona, K. L. Shaklee, and F. H. Pollak, *Electroreflectance at a semiconductor-electrolyte interface, Phys. Rev.* **154**, 696 (1967).

[229] L. F. Lastras-Martinez, R. E. Balderas-Navarro, M. Chavira-Rodriguez, J. M. Flores-Camacho, and A. Lastras-Martinez, *Strain induced optical anisotropies in zincblende semiconductors, pys. stat. sol. (b)* **240**, 500 (2003).

[230] A. Calzolari, C. A. Pignedoli, R. Di Felice, C. M. Bertoni, and A. Catellani, *Theory of Cs adsorption on InAs(110), Surf. Sci.* **491**, 265 (2001).

[231] Hongsuk Yi, Hanchul Kim, Beena Kuruvilla, and Jinwook Chung, *Atomic structure and theoretical scanning tunneling microscopy images of Li zigzag chains on the GaAs(110) surface, Phys. Rev. B* **67**, 195302 (2003).

[232] M. G. Betti, V. Corradini, M. Sauvage-Simkin, and R. Pinchaux, *Atomic geometry and the probability distribution of self-assembled Cs nanowires at the InAs(110) surface, Phys. Rev. B* **66**, 085335 (2002).

[233] C. B. Duke, *Surface structures of tetrahedrally coordinated semiconductors: principles, practice, and universality, Appl. Surf. Sci.* **65-66**, 543 (1994).

[234] C. Hogan, D. Paget, O. E. Tereshchenko, and R. Del Sole, *Effect of adsorption of the electronegative and electropositive elements on the surface optical anisotropy of GaAs(001), phys. stat. sol. (c)* **0**, 2976 (2003).

[235] C. Hogan, D. Paget, Y. Garreau, M. Sauvage, G. Onida, L. Reining, P. Chiaradia, and V. Corradini, *Early stages of cesium adsorption on the As-rich c(2x8) reconstruction of GaAs(001): Adsorption sites and Cs-induced chemical bonds, Phys. Rev. B* **68**, 205313 (2003).

[236] C. Hogan, D. Paget, O. E. Tereshchenko, L. Reining, and G. Onida, *Optical anisotropy induced by cesium adsorption on the As-rich c(2X8) reconstruction of GaAs(001), Phys. Rev. B* **69**, 125332 (2004).

[237] K. O. Magnusson and B. Reihl, *Surface electronic structure of submonolayer to full-monolayer coverages of alkali metals on GaAs(110): K and Cs, Phys. Rev. B* **40**, 7814 (1989).

[238] V. L. Berkovits, V. A. Kiselev, and V. I. Safarov, *Optical spectroscopy of (110) surfaces of III-V semiconductors, Surf. Sci.* **211-212**, 489 (1989).

[239] N. Esser, W. Richter, U. Resch-Esser, P. Chiaradia, C. Goletti, and L. Moretti, *Optical anisotropy of ordered Sb layers on III-V (110) surfaces, Phil. Mag. B* **70**, 507 (1994).

[240] N. Esser, A. I. Shkrebtii, U. ReschEsser, C. Springer, W. Richter, W. G. Schmidt, F. Bechstedt, and R. DelSole, *Atomic structure of the Sb-stabilized GaAs(100)-(2x4) surface, Phys. Rev. Lett.* **77**, 4402 (1996).

[241] M. Pristovsek, S. Tsukamoto, N. Koguchi, B. Han, K. Haberland, J.-T. Zettler, W. Richter, M. Zorn, and M. Weyers, *In-situ determination of the carrier concentration of (001) GaAs by Reflectance Anisotropy Spectroscopy, phys. stat. sol (a)* **188**, 1423 (2001).

[242] N. Kumagai, T. Yasuda, T. Hanada, and T. Yao, *In situ measurement of carrier concentration in n-ZnSe by reflectance difference spectroscopy (RDS), J. Cryst. Growth* **214/215**, 547 (2000), and references therein.

[243] P. J. Timans, *Emissivity of silicon at elevated temperatures, J. App. Phys* **74**, 6353 (1993).

List of abbreviations and symbols

1D	one-dimensional
2D	two-dimensional
3D	three-dimensional
α	polarisability, sometimes absorption coefficient
AC	alternating current
AFM	atomic force microscopy
ARPES	angle resolved photo emmision spectroscopy
CCD	charge coupled device
CDW	charge density wave
$\underline{\underline{\tilde{\chi}}}$	complex dielectric susceptibility
cm^{-1}	reciprocal centimeter, 1 meV $\approx$ 8cm^{-1}
DC	direct current
d	thickness, distance
ΔE_p	Peierls gap
δRAS	difference of two RAS spectra
$\Delta r/r$	reflectance anisotropy
ε_0	electric field constant
e	electron charge
$\underline{\underline{\tilde{\varepsilon}}}$	complex dielectric function, tensor components: $\tilde{\varepsilon}_{ij}$
$<\varepsilon>$	effective dielectric function
e	unit vector
E	electric field, energy (with numerical indices: critical point energy)
E_F	Fermi energy
EMA	effective medium approximation
f	volume fraction
FTIR	Fourier transform infrared spectroscopy
FWHM	full width half maximum
GGA	generalised gradient approximation
GIXRD	grazing incidence X-ray diffraction
GW	derived from: Greens function G, Coulomb Potential W
HREELS	high resolution electron energy loss spectroscopy
IR	infra red
k_F	Fermi vector
k	wave vector (photons)
LDA	local density approximation
LEED	low energy electron diffraction
λ	wavelenght, sometimes interaction parameter
l_P	penetration depth (of light)
ML	monolayer

PEM	photo elastic modulator
$\mathbf{q}$	wave vector (phonons)
RAS	reflectance anisotropy spectroscopy
RHEED	reflection high energy electron diffraction
R	reflectance, $R = \|\tilde{r}\|^2$
$\tilde{r}$	complex (Fresnel) reflectivity
SDA	surface dielectric anisotropy
SDR	surface differential reflectivity
CDW	spin density wave
σ	conductivity
S	Raman cross section
STM	scanning tunneling microscopy
τ	relaxation time, average scattering time
T	temperature
UHV	ultra high vacuum
UV	ultra violet
ω_p	plasma frequency
ω_τ	scattering frequency

Index

Acknowledgements

I would like to express my thanks to many people. Without their energetic support this work would not have been possible.

Prof. Wolfgang Richter for the possibility to work in his group, all his support, fruitful discussions, but also for the nice evenings in Frascati.

Dr. Norbert Esser for his open door to discuss the recent results and always being interested even after he had left the group.

Prof. Piero Chiaradia and Dr. Claudio Goletti for initiating the Marie-Curie project which made my visit to Rome possible and of course all the things I learnt about infrared RAS, alkaline adsorption and the lively discussions.

Prof. Christian Thomsen for his willingness to referee this work.

Prof. John McGilp for his patience and good ideas about the indium wires.

Dr. Sandhya Chandola for many things. The help in the preparation and RAS measurements of the indium wires, patient proofreading and the nice evenings in the “Hardenberg”.

Christoph Cobet for his initial work to get our infrared RAS setup on its way, his usefuls scripts and crash courses in Origin programming and help during the first low temperature RAS measurements.

Theo Herrmann for the first multidetector RAS. Most of the spectra were measured with it.

Dr. Markus Pristovsek, Christian Kaspari and Matthias Wahl for their support in solving the teething troubles of the infrared RAS.

Gianlorenzo Bussetti for the LEED images of the Cs/GaAs(110) system, all the help in the initial measurements of that system and the good times in the “dark” laboratory and its surroundings – bib.

Dr. Wolf Gero Schmidt, Dr. Olivia Pulci and Prof. Friedhelm Bechstedt for sharing their calculations fresh out of the printer and for giving me at least an idea what DFT can and cannot do.

Eugen Speiser for keeping the Raman spectrometer alive even during hard times of the “Asbestsanierung” but also for the discussions about the Raman results.

Dr. Patrick Vogt and all other members of the workgroup for good and always interesting times, the opportunities to learn a lot about subjects related to mine, but also those far removed, particularly during lunchtime.

Torsten Schmidtling for his ability to smell technical problems even before they happen and his ready help to fix them.

Engelbert Eder for his efforts to keep 20 year old electronics alive and all the support in building new things.

Bert Rähmer for moral support, funny times in the office and all those hours playing badminton.

Everyone who had the opportunity to cross my way, whenever I had to lift the cryostat in and out of the chamber

The workshop of the institute and Norbert Zielinski for the realisation of the weird things I needed out of molybdenum and sapphire

Finally I would also thank my parents Dr. Jürgen Fleischer and Dr. Gerburg Fleischer for always being there. Special thanks also to all other members of the family particular Jens, Anja, Hannah, Marie and last but not least Clara for getting me out of the lab from time to time.